Title
Selective Encapsulation of Metal and Metal Oxide Nanoparticles within Microporous Zeotype Frameworks via Hydrothermal Assembly in the Presence of Ligand-Protected Metal Cations

Author
Otto, Trenton

Publication Date
2019

Peer reviewed|Thesis/dissertation

Selective Encapsulation of Metal and Metal Oxide Nanoparticles within Microporous Zeotype Frameworks via Hydrothermal Assembly in the Presence of Ligand-Protected Metal Cations

by

Trenton Otto

A dissertation submitted in partial satisfaction of the

requirements for the degree of

Doctor of Philosophy

in

Chemical Engineering

in the

Graduate Division

of the

University of California, Berkeley

Committee in charge:

Professor Enrique Iglesia, Chair
Professor T. Don Tilley
Professor Alexis Bell

Spring 2019

Selective Encapsulation of Metal and Metal Oxide Nanoparticles within Microporous Zeotype Frameworks via Hydrothermal Assembly in the Presence of Ligand-Protected Metal Cations

by

Trenton Otto

Abstract

Selective Encapsulation of Metal and Metal Oxide Nanoparticles within Microporous Zeotype Frameworks via Hydrothermal Assembly in the Presence of Ligand-Protected Metal Cations

by

Trenton Otto

Doctor of Philosophy in Chemical Engineering

University of California, Berkeley

Professor Enrique Iglesia, Chair

The encapsulation of metal nanoparticles within zeolitic voids of molecular dimensions protects metal surfaces from contact by reactant or poison species that are too large to enter framework apertures, and confers sinter-stability to confined metal domains via intervening channels that prevent cluster coalescence. Such channels can also stabilize specific transition states or retain undesired products until they fragment into smaller molecules capable of egress by diffusion. These size-selective properties are governed, in each instance, by the size of the microporous channels and voids in a specific framework. The encapsulation of noble metal (e.g., Au, Pd, Pt) clusters within small-pore (8-member ring (8-MR) apertures) and medium-pore (10-MR) zeolites, however, often cannot be achieved through established post-synthetic exchange or impregnation techniques, because solvated metal cations may be too large to enter the apertures of these zeolites. Base metal cations (e.g., Ni^{2+}, Co^{2+}, Fe^{2+}), though generally small enough to enter even small-pore zeolites, tend to form highly refractory complexes when ion-exchanged, thus precluding their conversion into catalytically active metal or metal oxide particles by reductive or oxidative treatments. We have developed synthetic strategies and guiding principles for the successful preparation of Au and bimetallic (AuPd, AuPt, PdPt) nanoparticles within the microporous voids of zeolite or zeotype materials with medium (MFI, TS-1) and small (LTA) sized pores. Synthetic techniques have also been devised for the encapsulation of base metal oxide (NiO, Co_3O_4, Fe_2O_3) nanoparticles within large (FAU; 12-MR), medium (MFI), and small-pore (LTA) zeolites.

The encapsulation of Au and bimetallic clusters within LTA and MFI was achieved via hydrothermal self-assembly of crystalline frameworks around ligated metal cation precursors (Au^{3+}, Pd^{2+}, Pt^{2+}). Bifunctional ligands containing a thiol moiety are used to coordinate with and protect metal cations, thus preventing their premature precipitation or reduction in alkaline synthesis gels at elevated temperature. Such ligands also contain alkoxysilane moieties that form covalent linkages with nucleating silicate oligomers to enforce metal uptake into crystallizing frameworks. The controlled deprotection of ligated cations with sequential oxidative and reductive treatments forms encapsulated clusters that are small (<2 nm), uniform in size, and sinter-stable at temperatures as high as 870 K. The simple incorporation of two ligated metal precursors into

zeolite synthesis gels leads to the encapsulation of bimetallic clusters that are uniform in size and composition.

The encapsulation of Au clusters within zeotype frameworks via hydrothermal assembly around ligated Au cation precursors poses a greater challenge for TS-1 than MFI or LTA, because the high temperature typically required for the crystallization of TS-1 (448 K; LTA: 373 K; MFI: 393 K) strongly promotes the deprotection of even ligand-protected Au precursors. TS-1 was successfully crystallized at much milder conditions than previously reported in order to prevent decomposition (or reaction with alkanols formed during hydrolysis of Ti or Si precursors) of Au-ligand complexes in the synthesis gels without adversely affecting Ti incorporation into the framework or sample crystallinity. The changes made to the established synthesis procedures for TS-1 include much lower crystallization temperatures (393 K vs. 448 K) compensated by longer crystallization times (120 h vs 48 h). Post-synthetic oxidative treatment procedures were developed in order to remove ligand species and organic structure-directing agents from the crystallized Au/TS-1 solids while minimizing the generation of local exotherms; these procedures led to the formation of small (~3.8 nm in diameter) Au nanoparticles embedded within TS-1 crystals.

Techniques developed for the encapsulation of base metals (Ni, Co, Fe) differ from those used for noble metals in (i) the types of ligands used for metal cation stabilization in synthesis gels (thiol ligands for noble metals; bidentate amine ligands for base metals), (ii) the precise order of reagent addition to zeolite synthesis gels needed to ensure ligand attachment and the prevention of metal precipitation, and (iii) the post-synthetic treatments that are most effective at removing ligand residues and subsequently forming encapsulated nanoparticles. It is critically important to prevent the attachment of base metal cations to zeolite exchange sites during both the zeolite assembly process and post-synthetic treatments, because the conditions required to convert such exchanged cations into clusters (>1100 K in H_2) are so prohibitively extreme as to cause degradation of the host zeolite frameworks. Base metals were successfully encapsulated by adding Ni^{2+}, Co^{2+}, or Fe^{2+} cations protected by chelating amine ligands to LTA, MFI, or FAU synthesis gels. Such ligands protect metal cations from precipitation as metal hydroxides or oxides in the alkaline gels and form siloxane bridges with nucleating aluminosilicate oligomers, thereby enforcing metal uptake into zeolite crystallites during framework assembly. The amine ligands also sterically preclude the direct attachment of base metal cations to zeolite exchange sites, thus allowing the conversion of occluded base metal species into metal or metal oxide clusters at conditions that do not incur damage to the zeolite frameworks. Oxidative treatment of the crystallized zeolites removes ligand species occluded within the zeolite pores and forms encapsulated metal oxide clusters.

The selectivity of metal encapsulation within zeotype crystals was quantified by examining rates of probe reactions involving small molecules (e.g., ethanol, O_2) on metal-zeotype samples exposed to bulky organosulfur compounds (e.g., dibenzothiophene) that are too large to enter framework apertures. Such organosulfur compounds selectively titrate and deactivate extracrystalline metal surfaces, leading to probe reaction rates that exclusively or predominantly reflect turnover events occurring on encapsulated metal surfaces. These experiments indicate that >95% of active metal surfaces reside within framework crystals for each metal-zeotype sample, confirming the efficacy of the encapsulation methods and demonstrating the size-selective properties conferred by confinement.

The synthesis strategies presented in this work, which demonstrate the requirements for successful syntheses, provide guiding principles for the selective encapsulation of metal and oxide nanoparticles within a wide variety of crystalline environments through simple one-step hydrothermal assembly routes. Such strategies provide versatile and broadly applicable alternatives to the limited or system-specific schemes for nanoparticle encapsulation that have been developed previously. These encapsulated clusters have potential uses in diverse applications that exploit the catalytic benefits conferred by metal encapsulation within microporous solids, including stability against sintering during reactions, reactant or product shape selectivity, and the protection of catalytic surfaces from contact with poisons that block their active sites.

Table of Contents

List of Figures

Chapter 2

Chapter 4

Chapter 5

List of Tables

Chapter 2

Chapter 3

Chapter 4

Chapter 5

Chapter 6

List of Schemes

Chapter 2

Chapter 3

Chapter 4

Chapter 5

Acknowledgements

My sincerest gratitude goes out to my advisor, Professor Enrique Iglesia, for his scientific and professional counsel throughout my graduate studies. His extensive experience with and knowledge of catalysis arguably situate him as the world's premier research scientist in his field of study, and I count myself incredibly fortunate to have conducted research under his tutelage. Professor Iglesia's continued stalwart pursuit of new knowledge, even after decades of focused work that has garnered nearly every imaginable accolade, speaks to his dedication to his science and has inspired me in my own research. My thanks also go out to Dr. Stacey Zones, who has taken on a co-advisor role and helped to move my research forward with critical insights or advice on countless occasions when progress on my work was stalled. Access to Dr. Zones' knowledge of zeolites together with Professor Iglesia's expertise in catalysis over the course of my studies has made for an inimitable experience and set me up with ample opportunities for success, and for that I am extremely grateful.

Next, I acknowledge my undergraduate research advisor, Professor Louis Bouchard. The formative years I spent conducting research under Professor Bouchard's guidance were critical to cultivating my interests and skills in scientific research, and laid the groundwork for my graduate work later on. Professor Bouchard has taught me much and opened many doors for me, and for that I will always be grateful.

I am thankful to my LSAC colleagues, including current and former members, for their professional and technical support and cooperation throughout my studies at UC Berkeley. Special thanks go out to Derek De Mornay, an undergraduate student with whom I have worked, for his contributions to my research projects. I would also like to thank "the quadruplets," Sam Leung, Ari Fischer, Marianne Sleiman, and Haefa Mansour, for their help in managing the tasks necessary to maintain a large research lab. Many thanks go out to Gina Noh, Allie Landry, Neelay Phadke, and Jianwei Liu for their roles in easing my transition into conducting research in LSAC. My gratitude also goes out to Bi-Zeng Zhan for his counsel and key role in guiding my post-graduation professional path.

I acknowledge the organizations and individuals who supported me financially during my dissertation work, including the ARCS Foundation, the National Science Foundation, and the Chevron Energy Technology Company. I am especially grateful to the staff at Chevron for their material support of my research, graduate fellowship, and technical guidance throughout my studies.

Finally, I would like to thank my mother, brother, and Walt for their love and support. They have moved heaven and earth for me and supported me unconditionally despite my many self-imposed periods of seclusion in esoteric academic pursuits. They have made everything I've done in my academic journey possible.

Chapter 1

Introduction to Metal Cluster Encapsulation within Microporous Zeotypes

1.1 Introduction

Metal nanoparticles encapsulated within microporous solids benefit from sinter stability as a consequence of their confinement within voids that prevent their coalescence with adjacent nanoclusters, and are limited in the size to which they can grow by spatial constraints [1,2]. Nanocluster sequestration within such solids also prevents certain reactant or titrant molecules from accessing active metal surfaces residing within intracrystalline regions, stabilizes specific transition states, and leads to the retention of large undesired products until they can fragment and egress by diffusion. These effects are governed, in each case, by the size of the intracrystalline pores and cavities within a distinct microporous framework [2]. The encapsulation of noble metals (e.g., Pt, Pd, Au) within large-pore zeolites (12-member ring (12-MR) or larger) is relatively straightforward, because solvated cation precursors (e.g., Pt^{2+}, Pd^{2+}) can be impregnated or ion-exchanged into the frameworks and subsequently reduced by H_2 to form metal clusters [3]. Such exchange techniques are generally unsuitable for small-pore (8-MR or smaller) and some medium-pore (10-MR) zeolites, however, because solvated or gaseous noble metal precursors are often too large to enter their narrow apertures [4]. Most base metals (e.g., Ni, Co, Fe) also cannot be encapsulated via exchange techniques because their cationic precursors, though small enough to enter even 8-MR zeolites, are highly refractory when exchanged and can only be reduced at temperatures (>1000 K) that damage zeolite frameworks [5,6,7]. A subset of the noble metal species, including Pt, Pd, Ir, Rh, and Ru, have been successfully encapsulated within small-pore zeolites (e.g., LTA, ANA, GIS) via hydrothermal self-assembly of crystalline frameworks around ligated metal cations added to zeolite synthesis gels [4,8]. Such techniques utilize organic ligand species which protect base metal cations from precipitation at the high temperatures (>373 K) and pH values (>12) typically required for zeolite crystallization. Sequential oxidative and reductive treatments applied subsequent to framework crystallization then remove the attached ligand species from the metal cations, and lead to the formation of metal nanoparticles embedded within the assembled framework crystals [4,8].

In chapters 2 and 3 of this work, general synthetic techniques and guiding principles are presented for the encapsulation of Au (Chapter 2) and bimetallic (AuPd, AuPt, PdPt; Chapter 3) nanoparticles within small-pore (LTA) and medium pore (MFI) zeolites. Encapsulation is achieved, in each case, via hydrothermal synthesis of zeolite frameworks around ligand-protected metal cations (i.e., Au^{3+}, Pd^{2+}, Pt^{2+}). The encapsulation of Au nanoparticles through this approach is particularly challenging because the high reduction potential of Au^{3+} (1.50 V; [9]) relative to other noble metals (e.g., Pt^{2+}: 1.18 V, Pd^{2+}: 0.915 V; [9]) results in a strong driving force for the reduction of ligated Au^{3+} cations and the premature agglomeration of Au^0 species as large, inactive colloidal particles [10]. The relatively low Tamman temperature of Au (668 K; [11]) relative to other metals (Pd: 914 K; Pt: 1014 K; [11]) also renders Au agglomerates particularly prone to excessive sintering during the critical periods of ligand removal and subsequent cluster nucleation, necessitating the use of carefully controlled post-synthetic treatment procedures that remove ligand species at relatively mild conditions. Techniques for the encapsulation of bimetallic clusters

(Chapter 3) via the hydrothermal assembly approach, as with Au clusters, constitute an innovation that expands upon previously developed methods for the encapsulation of monometallic noble metal species.

The encapsulation of Au and bimetallic clusters within LTA (0.42 nm apertures; [12]) and MFI (0.55 nm apertures; [12]) frameworks was achieved by incorporating metal cations stabilized by 3-mercaptopropyl-trimethoxysilane (MPS) ligands into zeolite synthesis gels. Such ligands bind with the metal cations through their terminal thiol groups and protect said cations from premature reduction or precipitation during zeolite framework nucleation and assembly. Alkoxysilane moieties in these ligands concurrently form siloxane linkages with nucleating silicate oligomers, thus enforcing the incorporation of metal precursors throughout each crystal and the ultimate composition and size homogeneity of the confined nanoparticles after post-synthetic application of thermal treatments to remove the ligands. In-situ diffuse-reflectance UV-visible spectra collected on as-synthesized Au/LTA samples showed that ligated Au^{3+} cations occluded within zeolite crystals are deprotected, reduced to Au^0, and form metal clusters during treatments in O_2 or H_2 over a narrow temperature range that dictates the dynamics of nanoparticle nucleation and growth. Treatments in H_2 at relatively mild temperatures (540-623 K) lead to the formation of highly dispersed nanoparticles (1.0-2.0 nm) visible in electron micrographs. Such clusters are also free of ligand residues or synthetic debris, as indicated by infrared spectra of CO chemisorbed onto Au metal surfaces. The small and uniform sizes of the Au clusters formed are preserved even after treatments in O_2 or H_2 at temperatures (>773 K) that would typically lead to the sintering of metal clusters dispersed on mesoporous supports [13,14]. Such thermal stability reflects the sequestration of metal clusters within microporous voids, which imposes barriers to the coalescence of adjacent nanoparticles. X-Ray diffractograms of crystallized and post-synthetically treated Au/LTA and Au/MFI samples showed that the targeted zeolite frameworks were formed with high crystallinity despite the addition of metal coordination complexes to synthesis gels. Elemental analysis measurements further indicated that metal uptake into the product frameworks (up to 2% wt.) was essentially complete, confirming the efficacy of the MPS ligands in enforcing metal incorporation.

Bimetallic clusters (AuPd, AuPt, PdPt), prepared within LTA through the addition of two different metal precursors protected by MPS ligands to synthesis gels, were small (<2 nm), uniform in size, and thermally stable (up to 823 K), similar to the monometallic Au nanoparticles synthesized in a similar fashion. The compositional uniformity of such clusters was probed through infrared spectra of CO adsorbed on bimetallic cluster surfaces and X-ray absorption measurements with accompanying extended fine structure analysis. Results from both characterization techniques indicated the prevalence of intracluster metal mixing and significant heteroatomic coordination, with cluster-scale metal compositions reflecting the overall ratio of metal species in the bulk samples. The relatively uniform compositions of such clusters indicate that precursor metal species are distributed uniformly throughout assembled zeolite crystals, which would tend to favor the formation of homogeneous nanoparticles subsequent to thermal treatments that remove ligand species, reduce metal cations, and lead to the agglomeration of denuded metal adatoms. The implementation of the bimetallic encapsulation technique therefore allows for the preparation of compositionally uniform metal clusters, which is challenging to achieve using more common impregnation techniques with mesoporous supports [15], while also pairing the unique catalytic chemistries of bimetallic clusters with the benefits conferred by encapsulation.

Chapters 4 and 5 of this work demonstrate how small base metal oxide (NiO, Co_3O_4, Fe_2O_3) nanoparticles, uniformly distributed in size and thermally stable, can be selectively placed throughout the microporous frameworks of LTA, MFI, and FAU crystals by their nucleation and growth around ligated Ni^{2+}, Co^{2+}, or Fe^{2+} precursors at conditions of hydrothermal synthesis. Chapter 4 focuses narrowly on the development of synthetic techniques for the preparation of Co_3O_4 clusters within LTA, including the screening and identification of effective ligand species, the impact of metal loading on product zeolite crystallinity, and the design of post-synthetic treatment procedures that remove ligand species while promoting the formation of small and uniform clusters. Chapter 5 extends the techniques and analysis explored in Chapter 4 to a wider variety of metal species (Ni, Co, Fe) and zeolite frameworks (LTA, MFI, FAU) in order to examine the versatility of the synthetic protocol. The protective ligands used for base metal encapsulation (N-[3-(trimethoxysilyl)propyl]ethylenediamine; TPE) contain an amine and an alkoxysilane function that concurrently stabilize metal cations against precipitation as oxyhydroxides in alkaline media while promoting the encapsulation of the ligated precursors within zeolite crystals via the formation of ligand-framework linkages. Oxidative treatments of ligated compounds occluded within zeolites remove the ligands and form metal oxide nanoparticles (<2.0 nm) uniformly dispersed throughout crystals and stable up to 870 K. Such stability and homogeneity reflect, in turn, the uniform dispersion of metal precursors throughout LTA, MFI, or FAU crystals as such crystals form and the diffusional obstacles to coalescence imposed by the intervening apertures present between clusters. The reduction temperatures and stoichiometry of such clusters (NiO, Co_3O_4, Fe_2O_3) and the infrared spectra of adsorbed CO confirm the selective formation of metal oxide clusters, without the concomitant formation of less reducible metal aluminosilicates or exchanged cations. Co_3O_4 nanoparticles encapsulated within LTA, in contrast with Co^{2+}-exchanged LTA and Co aluminosilicates, were active for CO and NO oxidation, a consequence of their more reducible character and of their ability to undergo Co^{3+}/Co^{2+} redox cycles and to dissociate molecular O_2. Turnover rates normalized per surface Co atom, however, were lower than bulk Co_3O_4 powders, as a result of the diffusional constraints imposed by small LTA apertures and the less facile redox cycle characteristic of small clusters.

These synthetic protocols provide a route to prepare small, stable, and encapsulated base metal oxide clusters, which cannot be prepared via sequential ion exchange of metal cations (M^{n+}), reduction to M^0, and re-oxidation to MO_x, because the thermal treatments required to detach exchanged base metal cations lead to the destruction of the confining crystalline microporous frameworks [5,6,7]. These methods and the demonstration of the requirements for successful syntheses also build a practical platform for selectively encapsulating nanoparticles of base metals and early transition metals in their oxide or metal forms within a broad range of confining crystalline environments and using simple one-step hydrothermal assembly routes.

Chapter 6 details synthetic techniques for the encapsulation of Au nanoparticles within titanium silicalite-1 (TS-1) via hydrothermal synthesis in the presence of ligated Au^{3+} cations. Au encapsulation techniques developed for LTA and MFI frameworks (Chapter 2) cannot be analogously applied to TS-1 or other zeotype frameworks with high Si content because the crystallization temperatures typically required (443-448 K; 48 h; [16,17]) are substantially higher (LTA: 373 K; MFI: 393 K). Such synthesis conditions lead to the premature deprotection and subsequent reduction of Au^{3+} cations even when they are protected by MPS (thiol) ligands. Au/TS-1 was prepared by systematically varying the TS-1 crystallization parameters in order to identify

conditions (393 K; 120 h; 10% wt. seed crystals) which preclude the premature decomposition of Au^{3+} coordination complexes without adversely affecting the TS-1 framework crystallinity or Ti incorporation. The formation of small Au nanoparticles within Au/TS-1 is particularly challenging because oxidative removal of organic ligand and templating species present in the as-synthesized TS-1 frameworks leads to local exotherms that sinter Au clusters during critical periods of nanoparticle nucleation. Gradual heating (0.01 K s^{-1} to 773 K) in air leads to the formation of fairly small Au nanoparticles (3.8 nm) via the slow removal organic species that minimizes local exotherms.

Hydrothermal assembly of Au/TS-1 at the modified synthesis conditions led to the formation of crystalline frameworks (determined by X-ray diffraction) with nearly full metal uptake (0.2-1.0% wt. Au). Infrared spectra of Au/TS-1 showed an absorption band at 960 cm^{-1} corresponding to framework Ti species [18]; the normalized intensity of this band was commensurate with that of a standard TS-1 sample ($I_{Au/TS-1}/I_{TS-1}$=0.9), indicating that the atypical crystallization conditions for Au/TS-1 did not adversely affect framework assembly. Au/TS-1 exposed to CO showed an infrared band associated with CO adsorbed onto Au surfaces (~2100 cm^{-1}; [19]); the integrated intensity of this band was similar to that of a standard Au/SiO_2 sample with clean Au surfaces ($I_{Au/zeotype}/I_{Au/SiO2}$=0.9-1.2), indicating that the post-synthetic air treatments remove ligand residues from Au surfaces.

The synthetic technique developed for the encapsulation of Au nanoparticles within TS-1 provides a guiding template for the synthesis of Au and other metal species within TS-1 or other high-Si zeotype frameworks, which often require crystallization at conditions that typically lead to the premature precipitation or reduction of even ligand-protected metal species. Au nanoparticles encapsulated within TS-1 crystals reside within molecular distances of framework Ti species; consequently, the Au/TS-1 systems prepared via the techniques shown in Chapter 6, or improved versions thereof, have potential future applications as alkene epoxidation catalysts with H_2/O_2 or H_2O/O_2 reactants because of the close proximity between Au and Ti active sites required for such reactions [20,21].

The selectivity of metal placement within zeolite and zeotype crystals was determined, in all cases (Chapters 2-6), by measuring oxidative dehydrogenation (ODH) turnover rates of ethanol (0.40 nm kinetic diameter, [4]) on metal-zeolite samples exposed to bulky organosulfur titrants that selectively titrate and deactivate extracrystalline metal or metal oxide surfaces. Sulfur poisons that are too large to appreciably enter LTA (0.42 nm aperture, [12]), MFI (0.55 nm, [12]), TS-1 (0.55 nm, [12]), or FAU (0.74 nm [12]) apertures are sterically limited to binding with active metal or oxide surfaces that reside in freely accessible locations on outer crystal surfaces; consequently, the degree to which large poison molecules decrease ethanol turnover rates gives a quantitative measure of the fraction of metal surfaces that are not embedded within microporous zeotype voids. Thiophene (0.46 nm kinetic diameter, [22]), dibenzothiophene (0.9 nm, [22]), or 2,4,6-trimethylbenzyl mercaptan (>0.86 nm, [23]) titrants were used to poison extracrystalline metal or metal oxide surfaces either during or before measurements of ethanol ODH rates. Analogous rate measurements were also conducted on metal or metal oxide clusters dispersed on mesoporous SiO_2 in order to evaluate the effects of the sulfur titrants on unprotected metal or metal oxide surfaces. Ethanol ODH rates on nanoparticles supported by mesoporous SiO_2 were either fully or substantially suppressed (typically <15% residual activity) by exposure to the organosulfur titrants,

reflecting the near unrestricted access of the sulfur species to these unprotected particles. Zeotype-encapsulated metal or metal oxide nanoparticles, by contrast, retained >95% of their ethanol ODH activity upon exposure to the organosulfur titrants. Quantitative comparisons between the extent of deactivation on metal/zeotype and metal/SiO_2 samples suggest that a similarly high fraction of active metal or metal oxide surfaces (>95%) reside within zeotype crystals in all cases, reflecting the efficacy of the synthesis techniques in enforcing metal uptake within nucleating zeotype frameworks.

The synthetic methods described here explicate generally applicable procedures to prepare a diverse array of nanoparticle catalysts confined within an equally wide variety of zeotype frameworks. The synthetic approach, utilizing ligand-protected metal cation precursors incorporated into zeotype synthesis gels, circumvents common limitations to metal encapsulation imposed by the inability of metal precursors to enter narrow apertures, or by the irreducibility of certain exchanged metal species. The nanoparticles ultimately formed are small, stable, and size-selective during catalysis as a consequence of their confinement. The size selectivity of such nanoparticles results from the molecular sieving properties of microporous frameworks that have led to their widespread use in catalysis, and is coupled with the unique catalytic properties of small noble metal, alloy, or metal oxide domains.

1.2 References

[1] Weisz, P.; Frilette, V.; Maatman, R.; Mower, E. *J. Catal*. **1962**, *1*, 307.
[2] Wu, J. C. S.; Goodwin, J. G.; Davis, M. *J. Catal*. **1990**, *125*, 488.
[3] Sebastian, V.; Irusta, S.; Mallada, R.; Santamaría, J. *Appl. Catal. A* **2009**, *366*, 242.
[4] Wu, Z.; Goel, S.; Choi, M.; Iglesia, E. *J. Catal.* **2014**, *311*, 458.
[5] Asedegbega-Nieto, E.; Díaz, E.; Vega, A.; Ordóñez, S. *Catal. Today* **2010**, *157*, 425.
[6] Borqschulte, A.; Callini, E.; Stadie, N.; Arroyo, Y.; Rossell, M. D.; Erni, R.; Geerlings, H.; Züttel, A.; Ferri, D. *Catal. Sci. Technol*. **2015**, *5*, 4613.
[7] Otto, T.; Zones, S. I., Iglesia, E. *Microporous Mesoporous Mater*. **2018**, *270*, 10.
[8] Goel, S.; Wu, Z.; Zones, S.; Iglesia, E. *J. Am. Chem. Soc*. **2012**, *134*, 17688.
[9] Bratsch, S. G. *J. Phys. Chem. Ref. Data* **1989**, *18*, 1.
[10] Horvath, D.; Polisset-Thfoin, M.; Fraissard, J.; Guczi, L. *Solid State Ionics* **2001**, *141-142*, 153.
[11] Argyle, M. D.; Bartholomew, C. H. *Catalysts* **2015**, *5*, 145.
[12] C. M. Baerlocher, Database of Zeolite Structures. http://www.iza-structure.org/databases/, 2017 (accessed February 2018).
[13] Otto, T.; Zones, S. I.; Iglesia, E. *J. Catal*. **2016**, *339*, 195.
[14] Veith, G. M.; Lupini, A. R.; Pennycook, S. J.; Mullins, D. R.; Schwartz, V.; Bridges, C. A.; Dudney, N. J. *J. Catal.* **2009**, *262*, 92.
[15] Alexeev, O. S.; Gates, B. C. *Ind. Eng. Chem. Res.* **2003**, *42*, 1571.
[16] van der Pol, A. J. H. P.; van Hooff, J. H. C. *Appl. Catal. A* **1992**, *92*, 93.
[17] Wang, M.; Zhou, J.; Mao, G.; Zheng, X. *Ind. Eng. Chem. Res*. **2012**, *51*, 12730.
[18] Dartt, C. B.; Khouw, C. B.; Li, H.-X.; Davis, M. E. *Microporous Mater*. **1994**, *2*, 425.
[19] Venkov, T.; Fajerwerg, K.; Delannoy, L.; Klimev, H.; Hadjiivanov, K.; Louis, C. *Appl. Catal. A* **2006**, *301*, 106.
[20] Ojeda, M.; Iglesia, E. *Chem. Commun.* **2009**, *3*, 352.

[21] Lee, W.-S.; Akatay, M. C.; Stach, E. A.; Ribeiro, F. H.; Delgass, W. N. *J. Catal*. **2012**, *287*, 178.
[22] Van de Voorde, B.; Hezinova, M.; Lannoeye, J.; Vandekerkhove, A.; Marszalek, B.; Gil, B.; Beurroies, I.; Nachtiqall, P.; De Vos, D. *Phys. Chem. Chem. Phys.* **2015**, *17*, 10759.
[23] Tukur, N. M.; Al-Khattaf, S. *Energy Fuels* **2007**, *21*, 2499.

Chapter 2

Challenges and Strategies in the Encapsulation and Stabilization of Monodisperse Au Clusters within Zeolites

Abstract

This study describes successful strategies and guiding principles for the synthesis of small and monodisperse Au clusters protected against coalescence and poisoning by their uniform dispersion throughout the void space of LTA and MFI zeolites. These protocols involve hydrothermal zeolite crystallization around Au^{3+} precursors stabilized by mercaptosilane ligands, which prevent their premature reduction and enforce connectivity with incipient crystalline frameworks. The confining nanometer scale voids restrict cluster mobility during thermal treatment and allow the selection of reactants, products, and transition states and the exclusion of organosulfur poisons in catalytic applications based on molecular size. UV-visible spectra show that Au^{3+} forms Au^0 clusters in O_2 or H_2 in a narrow temperature range that sets the dynamics of nucleation and growth and thus cluster size. Reduction protocols that maintain stable temperatures at the lower end of this range lead to small clusters uniform in size (LTA: 1.3 nm, MFI: 2.0 nm; 1.06-1.09 dispersity indices) with clean and accessible surfaces, as shown by their infrared spectra upon chemisorption of CO. Their unprecedented size and monodispersity are retained during oxidative treatments (773-823 K) that sinter Au clusters on mesoporous supports. Oxidative dehydrogenation rates of small (ethanol) and large (isobutanol) alkanols and the poisoning of unprotected clusters by organosulfur titrants show that >90% of the Au surfaces reside within intracrystalline LTA and MFI voids. Their very different structures, compositions, and synthesis protocols suggest that these encapsulation strategies can be adapted readily to other zeolite frameworks with apertures too small for post-synthesis exchange of Au precursors. This study illustrates how confinement favors small, uniquely stable, and monodisperse clusters, even for Au, a metal prone to cluster growth at conditions often required for its catalytic use.

2.1 Introduction

The synthesis and the mechanistic interpretation of the reactivity of Au nanoparticles have attracted significant attention because of their unique catalytic properties and adsorbate binding characteristics, which resemble those of less noble Pt group metals in reactions as diverse as alkene epoxidation, CO oxidation, hydrogenation, and alcohol oxidation [1-3]. Preserving their monodisperse and small sizes (<5 nm) during thermal treatments and catalysis remains essential, because their unique properties are often conferred by coordinatively unsaturated surface atoms that prevail in small clusters [4,5]. These requirements present formidable challenges because of the low Tammann temperature of Au (620 K) [6] and also because cluster melting points decrease markedly with decreasing particle size [7].

The encapsulation of nanoparticles within microporous solids may improve the inherent instability of Au nanoclusters by sequestering them within voids that prevent their coalescence with other clusters, while also restricting the size to which they can grow through spatial constraints. Confinement within such voids can also preclude access by reactants or poisons to Au

surfaces, retain undesired products until they can convert and then diffuse as smaller species, or stabilize specific transition states, in all cases dictated by the size of the voids or channels in a specific microporous framework [8,9]. Strategies to confine Au within zeolites, however, often face synthetic challenges that prevent selective and efficient encapsulation.

Encapsulation within large-pore zeolites (12-member ring (12-MR) or larger) is relatively straightforward, because solvated metal cations can enter via exchange, impregnation, or adsorption methods after the framework has formed [10]. Au clusters within such zeolites, however, often do not show greater stability than those prepared by colloidal precipitation methods and subsequent dispersion of clusters onto mesoporous scaffolds. For example, Au nanoparticles with ~3 nm mean diameter are present in FAU after exchange with Au(III)-ethylenediamine, but treatment in O_2 or H_2 at 473 K causes their growth to ~10 nm clusters [11]. Similar strategies in LTL zeolites initially form ~2 nm clusters that coalesce and grow to ~5 nm after treatment in air at 498 K [12]. The sputtering of Au metal onto SiO_2, in contrast, forms clusters with 3.2 nm mean diameter after treatment in O_2 at 773 K [6], while deposition-precipitation methods on γ-Al_2O_3 lead to 4 nm Au clusters after treatment at 873 K in O_2 [13]. Au can be simply encapsulated into large-pore zeolites, but these previous studies show that the clusters in these zeolites are often less stable than those on mesoporous scaffolds, in spite of the posited benefits of encapsulation.

Medium-pore (10-MR) zeolites with more constrained apertures, such as MFI, confer greater stability than large-pore materials, but reported synthetic procedures typically lead to bimodal size distributions, with a significant fraction of the clusters (>10 nm in size) at external MFI crystal surfaces [14,15]. The introduction of ligand-stabilized colloidal Au into an MFI synthesis gel led to the intact encapsulation of only a subset of these particles; the encapsulated clusters are stable at 823 K in air, but those excluded from the intracrystalline voids sinter to very large Au crystals (>20 nm) [15]. The impregnation of aqueous cationic Pt or Au precursors onto alkali-treated MFI (to form mesopores that enhance imbibition by these solutions) gave metal clusters with ~3 nm mean diameter after O_2 (823 K) or H_2 (623 K) treatments [5,16], but the significant fraction of the clusters present at external zeolite surfaces again formed large (>10 nm) clusters [16]. These diverse techniques have led to improved encapsulation and greater size stability of Au clusters, but they do not form encapsulated clusters of unimodal size or allow extensions to zeolites with even smaller apertures, for which impregnation or exchange are impossible because solvated precursors are much larger than the intracrystalline passages [8].

Here, we report the selective encapsulation of Au clusters into LTA (small-pore) and MFI (medium-pore) zeolites by incorporating ligand-stabilized monomeric Au^{3+} precursors into hydrothermal synthesis gels and decomposing such precursors after zeolite crystalllization using protocols that lead to small and nearly monodisperse clusters (1-2 nm) with clean surfaces; these clusters remain stable against growth at 773 K in both H_2 and O_2 environments. Transmission electron microscopy (TEM), X-ray diffraction (XRD), and infrared (IR) spectroscopy of chemisorbed CO are used to determine the size and dispersity of Au clusters, the zeolite crystallinity, and the Au surface cleanliness, respectively. The bifunctional 3-mercaptopropyl-trimethoxysilane ligands provide chemical protection from reduction or precipitation of Au^{3+} precursors in strongly alkaline synthesis gels, while also promoting the nucleation of silicate oligomers around ligated metal precursors. The thiol group binds to Au^{3+} cations to form stable Au-S adducts [17,18] and the alkoxysilane moiety forms siloxane bridges with the silica precursors

in alkaline conditions [19], thus encouraging the uniform dispersion of Au precursors throughout the zeolite crystals formed. Treatment in O_2 and then H_2 leads to 1-2 nm particles that are narrowly distributed in size (as determined by their dispersity index [8,9] (DI) values) and expose surfaces free of synthetic debris. Their mean diameter can be systematically varied without loss in monodispersity by varying the temperature of the post-synthetic H_2 treatment, which is shown by UV-vis spectroscopy to represent the most consequential synthesis stage for the formation of Au^0 and its nucleation and growth into clusters. These reduced clusters, once formed, do not coalesce during later treatments in O_2 or H_2 environments up to 773 K, consistent with their encapsulation and protection by the intervening windows and cages within zeolite crystals.

The oxidative dehydrogenation (ODH) of large and small alkanols confirmed the extent and consequences of confinement. Ethanol (0.40 nm kinetic diameter) [9] ODH turnover rates are much higher than for isobutanol (0.55 nm) [9] on Au/CaLTA (0.50 nm apertures) [20], consistent with the exclusion of isobutanol from Au clusters within intracrystalline regions. Ethanol ODH rates after exposing AuNaLTA (0.42 nm apertures) [20] to thiophene (0.46 nm) [9] and AuNaMFI (0.55 nm apertures) [21] to dibenzothiophene (DBT, 0.9 nm kinetic diameter) [22] confirmed that active Au surfaces are protected from large titrants and predominantly confined within LTA and MFI voids.

2.2 Methods

2.2.1 Reagents

Ludox AS-30 colloidal silica (30% wt. suspension in H_2O, Sigma-Aldrich), tetraethyl orthosilicate (TEOS; 98%, Sigma-Aldrich), fumed SiO_2 (Cab-O-Sil, HS-5, 310 m^2 g^{-1}), 3-mercaptopropyl-trimethoxysilane (95%, Sigma-Aldrich), $NaAlO_2$ (53% Al_2O_3, 42.5% Na_2O, Riedel-de Haën), NaOH (99.99%, Sigma-Aldrich), 1 M tetrapropylammonium hydroxide (TPAOH; 98%, Sigma-Aldrich), $HAuCl_4 \cdot 3H_2O$ (99.999%, Sigma-Aldrich), calcium chloride dihydrate (EMD Millipore), ethanol (99.9%, Sigma-Aldrich), isobutanol (99.9%, Sigma-Aldrich), thiophene (99%, Alfa Aesar), dibenzothiophene (98%, Sigma-Aldrich), ethylenediamine (98%, Sigma-Aldrich), acetone (99.9%, Sigma-Aldrich), He (99.999%, Praxair), 25% O_2/He (99.999%, Praxair), air (extra dry; 99.999%, Praxair), H_2 (99.999%, Praxair), and 1.0% CO/He (99.999%, Praxair) were used as received.

2.2.2 Synthesis of Au cluster catalysts in LTA, MFI, and mesoporous SiO_2

2.2.2.1. Au cluster encapsulation within LTA

Au-encapsulated Na-LTA zeolite (AuNaLTA) was prepared by adding 3-mercaptopropyl-trimethoxysilane to a synthesis gel using hydrothermal synthesis techniques [8] that were modified to allow the incorporation and persistence of Au^{3+} cations in the gel at the conditions of synthesis. In a typical synthesis, NaOH (4.8 g) and 3-mercaptopropyl-trimethoxysilane (0.82 g) were added to deionized H_2O (17.9 MΩ resistance; 18 cm^3) in an open 125 cm^3 polypropylene container and stirred by a magnetic bar (6.7 Hz; 8 h); during this process the methanol formed by hydrolysis of the ligands (Section 2.3.1) evaporates, thus preventing methanol from reducing the Au^{3+} precursors when they are added later. An aqueous solution of $HAuCl_4 \cdot 3H_2O$ (0.26 g) in deionized H_2O (18

cm^3) was added dropwise to the basic methanol-free ligand solution under agitation by a magnetic bar (6.7 Hz) over a period of 0.5 h. Colloidal silica (10.67 g, Ludox AS-30) was added to the polypropylene container, which was capped and sealed and heated to 353 K under agitation by a magnetic bar (6.7 Hz) for 0.5 h. Finally, $NaAlO_2$ (6.0 g) dissolved in deionized H_2O (18 cm^3) was added dropwise to the Au^{3+}, ligand, and silica solution and mixed by magnetic stirring (6.7 Hz) for 2 h at ambient temperature; this led to a homogeneous synthesis gel with a molar ratios of 1.7 SiO_2/1 Al_2O_3/3.2 Na_2O/110 H_2O/0.02 Au/0.12 ligand. The gel was heated at 373 K while magnetically stirring (6.7 Hz) for 12 h under its autogenous pressure to form AuNaLTA. The Au content in the final solids (as measured by optical emission spectroscopy, discussed in Section 2.2.3) was adjusted by increasing or decreasing the amount of added Au to achieve 0.5-1.0% wt. theoretical loadings, while keeping a constant 3-mercaptopropyl-trimethoxysilane to Au molar ratio of 6. The solids formed were filtered (Pyrex 3606 fritted funnel, 4-5.5 μm), washed with deionized water until the rinse liquids reached a pH 7-8, and treated in a convection oven at 373 K for 8 h. The solids were heated in flowing dry air (1.67 $cm^3\ g^{-1}\ s^{-1}$) from ambient to 623 K (or 573 K; at 0.033 K s^{-1}) and held for 2 h, cooled to ambient temperature, and then heated to 623 K (or 573 K; at 0.033 K s^{-1}) in flowing H_2 (1.67 $cm^3\ g^{-1}\ s^{-1}$) and held for 2 h.

The air and H_2 treated AuNaLTA zeolites were Ca^{2+} ion exchanged [20] to convert them into AuCaLTA before use in catalytic or characterization studies. AuCaLTA was prepared by adding AuNaLTA (1-5 g) to an aqueous 1 M solution of $CaCl_2$•$2H_2O$ (1 g AuNaLTA per 100 cm^3) and stirring magnetically (6.7 Hz) at ambient temperature for 8 h. The exchange was repeated ten times (to achieve complete exchange, Section 2.3.4.2) and the solids were filtered and washed with deionized water (1500 $cm^3\ g^{-1}$), then treated in stagnant ambient air at 373 K for 12 h.

2.2.2.2. Au cluster encapsulation within MFI

A hydrothermal MFI synthesis technique [23] which uses TPAOH as a structure-directing agent (SDA) was modified with the addition of Au^{3+} and 3-mercaptopropyl-trimethoxysilane to form AuNaMFI. TPAOH (16.5 g of 1 M solution) and 3-mercaptopropyl-trimethoxysilane (0.28 g) were mixed in a 100 cm^3 polypropylene bottle and stirred magnetically (6.7 Hz) for 8 h in ambient stagnant air. A solution containing $HAuCl_4$•$3H_2O$ (0.088 g) in deionized H_2O (1.88 cm^3) was added dropwise to the ligand/TPAOH solution under agitation by a magnetic bar (6.7 Hz) over a period of 0.5 h, followed by the addition of TEOS (17.3 g). The resulting mixture was sealed with the bottle's cap and further agitated for 13 h at ambient temperature, after which a mixture of TPAOH (13.2 g of 1 M solution), $NaAlO_2$ (0.189 g) and deionized H_2O (1.88 cm^3) was added to it in order to prepare the synthesis gel (6.5 TEOS/2.3 TPAOH/0.18 $NaAlO_2$/120 H_2O/0.035 Au/0.20 ligand molar ratios). The gel was heated to 371 K while magnetically stirring (6.7 Hz) and held for 2 h under its autogenous pressure, then cooled to ambient temperature and transferred to a Teflon-lined stainless steel autoclave (125 cm^3, Parr), in which the gel was held at 393 K for 15 h to form AuNaMFI. The Au content in AuNaMFI was varied by changing the concentrations of the Au precursor and the 3-mercaptopropyl-trimethoxysilane ligand in the synthesis gel (1:6 molar ratio) to obtain 0.2-2.0% wt. theoretical loadings. AuNaMFI solids were recovered by filtration (Pyrex 3606 fritted funnel, 4-5.5 μm), washed with deionized water to a rinse pH of 7-8, and treated for 8 h at 373 K in ambient air.

Thermal treatments of these AuNaMFI catalysts in dry air and H_2 were varied to establish protocols that form small (~2 nm) and monodisperse Au clusters free of synthetic debris—the characterization of these clusters is discussed in Sections 2.2.3, 2.3.1 and 2.3.3. Changes in the Au particle size and surface cleanliness that resulted from incremental increases in treatment temperature and duration, or the application of multiple treatment steps in succession, were evaluated to find the optimal conditions that were then used throughout this study. In the most effective procedure, the AuNaMFI sample was first treated in flowing dry air (1.67 $cm^3\ g^{-1}\ s^{-1}$) and heated from ambient temperature to 546 K (at 0.033 K s^{-1}) and held for 2 h, then cooled to ambient temperature; it was then treated in flowing H_2 (1.67 $cm^3\ g^{-1}\ s^{-1}$) by heating to 546 K (at 0.033 K s^{-1}) and held for 2 h, then allowed to cool to ambient temperature a second time. The sample was further treated in flowing dry air (1.67 $cm^3\ g^{-1}\ s^{-1}$) under a ramped heating procedure in which the temperature was raised to 573 K and held for 2 h, then increased to 648 K and held for 2 h, and finally heated to 723 K and held for 4 h, with a ramp rate of 0.017 K s^{-1} between each step. The Au cluster accessibility and size distribution achieved in AuNaMFI (discussed in Section 2.3) required the identification and use of these treatment protocols.

2.2.2.3. Synthesis of silica-supported Au clusters

Au clusters dispersed on SiO_2 (Cab-O-Sil, HS-5, 310 $m^2\ g^{-1}$) were prepared using an $Au(en)_2Cl_3$ (en=ethylenediamine) complex previously shown to lead to small clusters [24]. $Au(en)_2Cl_3$ was prepared by dissolving $HAuCl_4 \bullet 3H_2O$ (1.0 g) in deionized H_2O (10 cm^3) and ethylenediamine (0.40 g) was then added. The solution was agitated by magnetic stirring (6.7 Hz) at ambient temperature for 0.5 h, and ethanol (70 cm^3) was then added to cause precipitation; the slurry was stirred for an additional 0.33 h and the solids were recovered by filtration and treated in ambient stagnant air at 313 K for 12 h.

Au/SiO_2 was prepared by dissolving $Au(en)_2Cl_3$ (0.03 g) in deionized H_2O (50 cm^3) and raising the pH to 10 by adding 1.0 M NaOH; SiO_2 (1.0 g) was added to the solution and 1.0 M NaOH was again used to adjust the pH to 10. The suspension was heated to 338 K while stirring for 2 h, filtered and washed with 1500 cm^3 deionized H_2O, and treated in stagnant ambient air at 343 K for 5 h. These Au/SiO_2 samples were heated from ambient to 423 K (at 0.033 K s^{-1}) in flowing H_2 (1.67 $cm^3\ g^{-1}\ s^{-1}$) and held for 2 h. The samples were then cooled to ambient temperature, and finally heated to 673 K (at 0.033 K s^{-1}) in flowing dry air (1.67 $cm^3\ g^{-1}\ s^{-1}$) and held for 2 h. These procedures were previously shown to form active Au clusters free of C and N residues from the ethylenediamine ligands [24]. Brønsted acid sites originating from the silica support can form acid-catalyzed products or secondary alkanol ODH products [25]. A small number of experiments intended to detect the presence of Brønsted acid sites on the silica support (Section 2.3.4.1) were therefore conducted, before which the Au/SiO_2 catalysts were further treated in 0.05 M NaOH (100 $cm^3\ g^{-1}$) at ambient temperature for 2 h with magnetic stir bar agitation (6.7 Hz), and finally recovered by filtration (Pyrex 3606 fritted funnel, 4-5.5 μm) then washed with 500 $cm^3\ g^{-1}$ of deionized H_2O.

2.2.3 Characterization of zeolite structures and embedded Au clusters

Au contents were measured by inductively coupled plasma optical emission spectroscopy (ICP-OES) using a Perkin Elmer 5300 DV optical emission ICP analyzer. X-Ray diffractograms

(XRD) were used to determine the phase purity of zeolites and to confirm the absence of large (>10 nm) Au clusters. Diffractograms were measured with a D8 Discover GADDS Powder Diffractometer using Cu-Kα radiation (λ=0.15418 nm, 40 kV, 40 mA). Samples were mounted on quartz slides by placing and leveling finely-ground powders; diffractograms were measured for 2θ values between 5-50° with a scan rate of 0.00625 degrees s^{-1}.

UV-visible spectra were used to monitor the Au localized surface plasmon resonance (LSPR) band during or following treatment of AuNaLTA and Au/SiO_2 in air or H_2. Spectra were acquired using a Varian-Cary 6000i spectrometer and a Harrick scientific diffuse reflectance accessory (DRP-XXX) with a reaction chamber add-on (DRA-2CR); the latter was modified with a fritted stainless steel disc at the sample cup to eliminate temperature gradients and to ensure uniform gas flow through the packed powder samples. A heater held underneath the sample holder and a temperature controller (Watlow Series 982) were used to adjust temperatures, which were measured with a type K thermocouple (Omega) embedded in the sample holder wall. UV-vis spectra were acquired on AuNaLTA and Au/SiO_2 samples (0.1 g; <100 μm aggregates), which were heated to 623 K (at 0.033 K s^{-1}) in flowing dry air (1.67 $cm^3\ g^{-1}\ s^{-1}$) and held for 2 h; they were then cooled to ambient temperature, and treated in flowing H_2 (1.67 $cm^3\ g^{-1}\ s^{-1}$) by heating to 623 K (at 0.067 K s^{-1}) and holding for 2.67 h. Background spectra were used to isolate the effect of Au on the UV-vis spectra and were collected after identical treatment procedures on NaLTA or SiO_2 samples synthesized as AuNaLTA or Au/SiO_2 but without adding Au precursors.

Transmission electron micrographs (TEM) were collected at 120 kV with a Philips/FEI Technai 12 microscope. Samples were prepared by suspending ground powders in acetone and dispersing them onto holey carbon films mounted on 400 mesh copper grids (Ted Pella Inc.). Cluster size distributions were measured using >300 particles for each sample to determine surface-averaged cluster diameters $\langle d_{\mathrm{TEM}} \rangle$ [26]:

$$\langle d_{\mathrm{TEM}} \rangle = \frac{\sum n_i d_i^3}{\sum n_i d_i^2} \qquad (1)$$

where n_i is the number of clusters with diameter d_i. Metal dispersions (D), defined as the fraction of Au atoms exposed at cluster surfaces, were estimated from $\langle d_{\mathrm{TEM}} \rangle$ [26]:

$$D = 6\frac{\nu_m / a_m}{\langle d_{\mathrm{TEM}} \rangle} \qquad (2)$$

where ν_m is the bulk atomic density of Au (16.49×10^{-3} nm^3) and a_m is the area occupied by an Au atom (8.75×10^{-2} nm^2) on a polycrystalline surface [27]. Size distributions were also used to calculate the dispersity index (DI), given by the ratio of the surface-averaged ($\langle d_{\mathrm{TEM}} \rangle$) to the number-averaged ($\langle d_n \rangle$) diameter [26]:

$$\mathrm{DI} = \frac{\langle d_{\mathrm{TEM}} \rangle}{\langle d_n \rangle} = \frac{\left(\frac{\sum n_i d_i^3}{\sum n_i d_i^2}\right)}{\left(\frac{\sum n_i d_i}{\sum n_i}\right)} \qquad (3)$$

The DI value provides a metric for particle size uniformity, with unity denoting perfect monodispersity and values <1.5 typically taken as monodisperse distributions [26,28]. Standard deviations of the mean particle diameters are also computed to provide more commonly recognized metrics of the uniformity of particle size distributions.

Infrared (IR) spectra of CO adsorbed on AuCaLTA, AuNaMFI, and Au/SiO_2 wafers (40 mg cm^{-2}) were collected to determine the surface cleanliness of Au clusters. Spectra were measured with a Thermo Nicolet 8700 spectrometer equipped with an in situ flow cell. The wafers were treated in flowing H_2/He mixtures (8.4 cm^3 g^{-1} s^{-1} H_2, 33.6 cm^3 g^{-1} s^{-1} He) by heating to 573 K (at 0.033 K s^{-1}) and holding for 1 h. After cooling in He flow (42.0 cm^3 g^{-1} s^{-1}) to 263 K, the samples were exposed to flowing CO/He mixtures (42.0 cm^3 g^{-1} s^{-1}; 0.1-1.0 kPa CO). Spectral contributions from CO(g) were subtracted from all reported spectra. Each spectrum was normalized by the number of exposed surface Au atoms, calculated from $\langle d_{\mathrm{TEM}} \rangle$ and Au contents.

2.2.4 Catalytic assessment of reactivity and encapsulation

Oxidative dehydrogenation (ODH) turnover rates of ethanol and isobutanol were measured on powders pelleted and sieved to retain 180-250 μm aggregates and held on a porous quartz frit within a quartz tube (10 mm O.D.). Samples were treated in flowing 20% O_2/He (1.67 cm^3 g^{-1} s^{-1}) by heating to 673 K (at 0.033 K s^{-1}) and holding for 1 h, then cooled to 393 K before catalytic measurements. Liquid alkanols (ethanol, isobutanol) and deionized water were evaporated into flowing O_2/He streams at 393 K using liquid syringe pumps (Cole Parmer, 60061 Series). He and O_2 flow rates were adjusted with mass flow controllers (Porter Instrument) to achieve the desired pressures (4 kPa alkanol, 9 kPa O_2, 87.5 kPa He, and 0.5 kPa H_2O). H_2O forms as an ODH product and can act as a co-catalyst (discussed in Section 2.3.4.1); thus it was added to maintain a constant concentration throughout the catalyst bed. Alkanol conversions were kept below 3%, and transfer lines were maintained at 393 K to avoid condensation. Ethanol but not isobutanol can diffuse through the apertures of AuNaLTA and AuCaLTA; thus, their relative rates provide an assessment of the extent to which Au surfaces reside within the protected environment of LTA voids [8,9] (Section 2.3.4). Comparison of these rates to those measured on Au/SiO_2 confirms that the effects of alkanol size on reactivity reflect the confinement of Au clusters. Both alkanols can enter MFI channels; as a result, the ability of AuNaMFI to protect Au surfaces from titration by large poison molecules was used instead to assess encapsulation.

Ethanol ODH on AuNaLTA and Au/SiO_2 was also carried out in the presence and absence of thiophene in the reactant stream (0 vs 0.1 kPa thiophene) to probe the fraction of the Au surfaces protected from contact with thiophene, as a result of their confinement within LTA voids. AuNaMFI, in contrast, was treated ex-situ with dibenzothiophene and then used in ethanol ODH to examine the fraction of the Au surface accessible to DBT. These treatments exposed AuNaMFI and the Au/SiO_2 reference (0.1 g) to DBT dissolved in liquid ethanol (30 cm^3; DBT/Au=6 molar) for 4 h with magnetic stirring (6.7 Hz) at ambient temperature. Samples were then filtered and

treated in stagnant dry air at 343 K for 12 h, and used in ethanol ODH reactions at 393 K without further pre-treatment (to avoid DBT desorption/decomposition). AuNaMFI and Au/SiO_2 control samples were prepared through an analogous procedure without DBT, then used for ethanol ODH. The controls were next heated to 673 K with 0.033 K s^{-1} for 1 h under 20% O_2/He (1.67 cm^3 g^{-1} s^{-1}), then cooled back to 393 K for use in ethanol ODH a second time. These controls were used to distinguish the effects of DBT on the measured rate from effects caused by the absence of high temperature pretreatment (673 K O_2/He) (Section 2.3.4.3).

Selectivities are reported on a carbon basis as the fraction of converted alkanol appearing as a particular product. Turnover rates are defined as the molar alkanol conversion rates per surface Au atom (from Au content and $\langle d_{TEM} \rangle$). NaLTA, CaLTA, NaMFI, fumed silica, and empty reactors did not lead to detectable product formation. Measured turnover rates were unaffected by dilution (10:1 mass acid-washed fumed SiO_2:Au catalyst) within aggregates or within the packed bed (10:1 mass acid-washed quartz:Au catalyst); thus, measured rates are not corrupted by concentration or temperature effects. Deactivation was not detected over the time scale of these experiments (~5 h), except on Au/SiO_2, which exhibited half-lives of 14 and 11 h during ethanol and isobutanol ODH, respectively. Turnover rates on Au/SiO_2 were extrapolated to the start of each experiment. Effluent concentrations were measured by gas chromatography (Shimadzu GC-2014) using a methyl-silicone capillary column (HP-1; 50 m × 0.32 mm, 1.05 μm film thickness) and a flame ionization detector.

2.3 Results and Discussion

2.3.1 Zeolite-encapsulated Au nanoparticle synthesis and characterization

X-Ray diffractograms confirmed the presence of the intended zeolite frameworks in AuNaLTA and AuNaMFI samples after treatment in flowing dry air and then H_2 (up to 623 K for AuNaLTA, 723 K for AuNaMFI) (Fig. 2.1). Their crystallinities were 98% and 96% for AuNaLTA (1.1% wt. Au) and AuNaMFI (1.9% wt. Au), respectively, as determined from the integrated intensities of the three most intense Bragg lines, using Au-free NaLTA and NaMFI as standards. Diffraction lines for Au metal were not detected in these samples and their crystallinity was unchanged by thermal treatments as high as 823 K in air or H_2. These zeolite materials are crystalline, stable during thermal treatments, and do not contain large Au crystallites (>10 nm), which would have been evident in the diffractograms.

AuNaLTA and AuNaMFI samples were white powders after treatment in ambient air at 373 K and did not exhibit detectable LSPR bands (at 500-600 nm) [29] or ligand-to-metal charge transfer bands (LMCT, 300-500 nm) [30] in their UV-visible spectra. These data show that Au^0 clusters larger than 2 nm are not present [31] and suggest the presence of intact Au-S adducts, which do not exhibit LMCT or LSPR bands [32-33]. Also, Au clusters were not detected by TEM in as-synthesized AuNaLTA or AuNaMFI after treatment at 373 K in ambient air. Thus, we conclude that Au^{3+} centers in the ligated complexes do not reduce to form Au^0 during the hydrothermal synthesis protocols or the crystallization of MFI or LTA frameworks. Such permanence at the pH and temperature of these hydrothermal syntheses indicates that Au^{3+} complexes are effectively stabilized by mercaptosilane ligands. The ethylenediamine ligands in the $Au(en)_2Cl_3$ chelate complex, in contrast, reduce Au^{3+} even in inert atmospheres at temperatures

as low as 343 K [12], making such ligands unsuitable as stabilizing species during hydrothermal synthesis.

The mercaptosilane ligands form CH_3OH molecules in alkaline solution during the displacement of their methoxy groups with hydroxyl groups via hydrolysis:

$$HS(CH_2)_3Si(OCH_3)_3 + nH_2O \xrightarrow{OH^-} HS(CH_2)_3Si(OCH_3)_{3-n}(OH)_n + nCH_3OH \qquad (4)$$

The evaporative removal of the CH_3OH formed in these reactions is required before hydrothermal synthesis, because CH_3OH acts as a reductant for Au^{3+} precursors, even when stabilized by mercaptosilane ligands. Analogous AuNaLTA synthesis protocols using ethylenediamine ligands (to form $Au(en)_2Cl_3$) led to large Au^0 crystallites during zeolite crystallization; such species were evident from the marked changes in the color of the synthesis gels (from clear to blue to mauve) as the temperature increased from 300 K to 373 K. These changes, indicative of the formation of Au^0 colloids [7], were confirmed by the presence of large Au clusters (>6 nm) in micrographs of the LTA solids formed via hydrothermal synthesis (Fig. 2.S1, SI).

The presence of Au^{3+} cations uniformly dispersed within LTA or MFI crystals, enforced by the stabilization conferred by mercaptosilane ligands and by the pre-emptive removal of CH_3OH reductants, allows their systematic reduction to Au^0 via post-synthetic thermal or chemical treatments, specifically designed to preserve the encapsulation and monodispersity of small (~1 nm) clusters. Such treatments and their consequences for the size and location of Au clusters were examined by UV-visible spectroscopy and TEM microscopy, as well as by probe reactions that determine the extent to which host zeolites prevent molecules larger than their apertures from accessing active Au surfaces (Section 2.3.4).

The intensity of the LSPR band in the UV-visible spectra of AuNaLTA (1.1% wt.) was monitored during heating in flowing dry air and then in flowing H_2 (from ambient temperature to 623 K in both cases) to track the formation and growth of Au^0 clusters from the cationic Au precursors (Fig. 2.2). The LSPR intensity serves as a diagnostic of Au^0 clusters larger than 2 nm, the diameter at which they incipiently exhibit plasmon resonance [31]. These LSPR bands were centered at 506 nm; this wavelength is characteristic of Au^0 clusters smaller than 5 nm, but it is not otherwise sensitive to cluster size [31].

A weak and barely detectable LSPR band emerged during thermal treatments in air between ambient temperature and 623 K, a procedure shown to combust and remove C-atoms from the mercaptosilane ligands (Fig. 2.2) [8]; these data show that this treatment did not form Au^0 clusters, apparently because strong Au-S bonds prevent Au^{3+} reduction at these conditions. As-synthesized Au/SiO_2, consisting of mesoporous SiO_2 with deposited $Au(en)_2Cl_3$ (Section 2.2.2.3), in contrast, exhibited an intense plasmon resonance after similar treatments in air (Fig. 2.S2, SI). Such plasmon resonances demonstrate the strong tendency of Au^{3+} to reduce to Au^0, even with protecting ligands and in oxidizing environments, and provides compelling evidence for the greater stability conferred to Au^{3+} by mercaptosilane ligands. Exposing AuNaLTA to pure H_2 after air treatment at 623 K led to a sharp increase in the intensity of the LSPR band at 540-623 K (Fig. 2.2). This increase in intensity reflects the reduction of Au^{3+} by H_2 after the oxidative removal of C-atoms from occluded mercaptosilane ligands, which may obstruct H_2 from accessing Au^{3+}

cations. Treatment of as-synthesized AuNaLTA in pure H_2 at 623 K (1.67 cm^3 g^{-1}; 0.067 K s^{-1}) for 2 h without a preceding air treatment at 623 K, however, also led to nearly identical increases in the plasmon band intensity in the same temperature range (540-623 K; Fig. 2.S3, SI). These data show that the protecting ligands do not obstruct H_2 access to Au^{3+} cations and that the H_2 treatment is solely responsible for decomposing Au-S adducts and for forming Au^0 species, which subsequently migrate throughout the zeolite crystal to form metal clusters. Au plasmon resonance bands are also evident in AuNaLTA after only treatment in air at 723 K (1.67 cm^3 g^{-1}; 0.067 K s^{-1}) for 2 h (Fig. 2.S4, SI), indicating that Au-S adducts decompose and form Au^0 (even without H_2 treatment) at sufficiently high temperatures. Air treatment alone can reduce Au^{3+} cations, but the use of H_2 allows reduction at lower temperatures, an important requirement to preserve Au dispersion, monodispersity, and encapsulation during the critical reduction process.

The strong effects of H_2 treatment temperature (540-623 K) on the intensity of LSPR bands (Fig. 2.2), and on the Au^0 cluster size that such features reflect, were examined to determine whether the mean particle diameter in AuNaLTA could be systematically varied through changes in the H_2 treatment temperature protocols. AuNaLTA was first treated in air (to remove C residues) and then in H_2 at several temperatures within the critical range for Au^{3+} reduction (540-623 K) evident from UV-vis spectra (Fig. 2.2), and the resulting Au particle size distributions were measured using TEM micrographs. Post-synthetic treatment of AuNaLTA (1.1% wt.) in flowing air at 573 K (or 623 K) and then in pure H_2 at 573 K (or 623 K) (each for 2 h) gives Au clusters with surface-averaged diameters of 1.3 nm (or 2.3 nm) (Fig. 2.3, Table 2.1). These clusters were nearly monodisperse in both cases (1.07 and 1.09 DI), indicating that cluster growth occurred without detectable loss of uniformity.

We surmise that such size uniformity reflects the condensation of silanols with the protecting ligands attached to Au^{3+} cations to form siloxane bridges within the synthesis gel or within the structural building units involved in the nucleation and growth of the zeolite framework. Such chemical linkages would favor the uniform incorporation of Au^{3+} precursors throughout the zeolite crystals [8] and the ultimate orderly migration of Au^0 species as such precursors reduce to form clusters uniform in size and dispersed throughout the zeolite void space. The smaller clusters evident at lower treatment temperatures in H_2 may reflect the less mobile nature of incipiently-reduced Au precursors, denuded of some mercaptosilane ligands, at these temperatures, thus favoring the formation of a larger number of nucleation points and, consequently, of smaller Au^0 clusters. The small Au clusters (1.3 nm) formed by H_2 treatment at 573 K are similar or slightly larger than the NaLTA α-cages (1.1 nm) [8], and occupy approximately 1.5% of these α-cages for the 1.1% wt. Au loading sample (calculations in SI; Section 2.S5, Eq. S1) [9]. The 2.3 nm clusters formed by H_2 treatment at 623 K occupy approximately 0.26% of these α-cages. These clusters exceed the size of the LTA α-cages, indicating that they locally disrupt the LTA framework, but the small number and extent of such disruptions preclude their detection in diffractograms [9]. In spite of these local disruptions, such Au clusters are protected by the large number of intervening windows and cages among clusters and between the clusters and the external crystal surfaces, thereby conferring stability against coalescence, as well as reactant shape selectivity in catalytic reactions (Section 2.3.4.2). The mean size, but not the dispersity of these clusters, is sensitive to the temperature at which their cationic precursors are reduced; thus, their dispersion can be systematically controlled through variations in the H_2 treatment temperature.

The precise control of Au cluster size is more challenging for MFI than LTA frameworks, because organic SDA species (TPAOH) occluded within the zeolite must be removed to allow access to intracrystalline voids and to any active surfaces therein. Air treatments for 2-3 h above 720 K completely combust and remove TPAOH [34]. Treating as-synthesized AuNaMFI (1.9% wt.) in flowing dry air (1.67 $cm^3\ g^{-1}\ s^{-1}$) from ambient temperature to 723 K (0.033 $K\ s^{-1}$) and holding for 3 h, however, led to the formation of relatively large Au particles (3.2 nm; 1.12 DI; Fig. 2.S5, SI). A similar treatment with a slower temperature ramp (0.016 $K\ s^{-1}$) formed slightly smaller clusters (3.0 nm; 1.09 DI; Fig. 2.S6, SI). It seems plausible that oxidation of intracrystalline SDA moieties causes local exotherms, thus precluding precise local temperature control as Au^0 forms and favoring cluster growth. Such effects were minimized using a stepped temperature ramping protocol (Section 2.2.2.2) to 723 K in air, intended to decrease SDA oxidation rates and allow heat dissipation; this strategy led to much smaller (2.0 nm) and nearly monodisperse (1.09 DI) Au clusters (TEM; Fig. 2.3, Table 2.1). As in the case of Au clusters in LTA, these clusters are larger than the largest voids in MFI (channel intersections; 0.64 nm) [21]; yet, they are thermally stable (Section 2.3.2), reside within the zeolite crystals (Section 2.3.4.3), and are protected against sintering and access by large molecules by many intervening channels among clusters and between the clusters and the external zeolite surfaces.

The size and dispersity of Au clusters in AuNaMFI and AuNaLTA prepared using these treatment protocols were essentially unaffected by Au loading (0.5-1.1% wt. in LTA; 0.2-1.9% wt. in MFI; Table 2.1). Syntheses with higher Au loading (≥6% wt.) led to amorphous materials (Fig. 2.S7, SI) apparently because of competition for the intracrystalline void space within incipiently formed nuclei between the SDA species (Na^+ for LTA or TPAOH for MFI), needed to template the crystalline voids, and the mercaptosilane ligands needed to protect and disperse the Au^{3+}. AuNaLTA treated in air at 623 K then H_2 at 623 K gave clusters with 2.3 nm surface-averaged diameter and DI values of 1.08 and 1.09 for 0.5% wt. and 1.1% wt. Au contents, respectively. Similarly, AuNaMFI with 0.2% wt. and 1.9% wt. Au gave clusters with diameters of 2.1 nm (1.06 DI) and 2.0 nm (1.09 DI), respectively. Au clusters occupy <0.5% of the intracrystalline void volume in these LTA and MFI samples [9,21], and TEM micrographs (Fig. 2.3) suggest that the Au clusters are uniformly dispersed throughout LTA and MFI crystals.

We therefore conclude that the uniform dispersion of the ligand-stabilized precursors throughout the synthesis gel, and ultimately throughout the zeolite crystals, lead to large and uniform spacing among precursors and to limited cluster growth processes. The driving force for such cluster growth, reflecting the tendency of small particles to minimize their surface energy, tends to weaken in magnitude as the cluster size increases and is likely resisted sterically by the surrounding framework. Such resistance probably includes the kinetic hurdles imposed by large numbers and small sizes of the intervening apertures and the thermodynamic barriers imposed by the energy required to locally disrupt the zeolite framework to accommodate larger clusters. We surmise that the clusters continue to grow until the driving force for their expansion is balanced by these barriers against further disruption of the framework.

2.3.2 Thermal stability of Au clusters in LTA and MFI

The stability of Au^0 clusters in AuNaLTA (1.1% wt.) and AuNaMFI (1.9% wt.) (prepared as described in Sections 2.2.2.1 and 2.2.2.2, respectively) were then examined during treatment in

flowing dry air by heating to a final temperature between 623 and 873 K at 0.033 K s^{-1} and holding for 5 h. Their surface-averaged cluster diameters and DI values, derived from TEM micrographs, are shown in Figure 2.4 as a function of this final temperature. The cluster diameters were unchanged by treatment temperatures below 773 K (1.3 nm NaLTA; 2.0 nm NaMFI); their size and dispersity increased slightly between 773 K and 823 K and then significantly at temperatures above 823 K (2.1 nm AuNaLTA; 2.6 nm AuNaMFI). Similar treatment protocols using pure H_2 instead of air at 773 K did not cause detectable cluster growth in AuNaMFI or AuNaLTA, but some slight growth was detected after treatments between 773 K and 823 K and became more evident above 823 K (1.9 nm AuNaLTA; 2.5 nm AuNaMFI) (Table 2.S1, SI). The treatment atmosphere (air or pure H_2) did not have any detectable effects on the stability of the Au clusters, apparently because Au surfaces remain essentially bare above 600 K in both environments [35], thus preventing adsorbed species from altering surface energies or atomic mobility, which influence, in turn, coalescence and Ostwald ripening. The stability of Au clusters in AuCaLTA, the Ca^{2+} exchanged form of AuNaLTA (Section 2.2.2.1), were also examined using analogous air or H_2 treatments at 773 K. The Ca^{2+} exchange was performed to enlarge the apertures in NaLTA [20] before using it in CO adsorption (Section 2.3.3; Section 2.S9, SI) or catalytic reaction studies (Section 2.3.4.1), so as to improve the access of diffusing molecules to Au cluster surfaces. The Au cluster size (1.3 nm) and dispersity index (1.07) in AuCaLTA also did not change following these air or H_2 treatments, indicating that the ion exchange process did not adversely affect Au cluster size or stability.

The size, stability, and dispersity of these Au clusters within AuNaLTA, AuCaLTA, and AuNaMFI represent significant improvements over those reported for clusters dispersed on mesoporous supports. Deposition-precipitation or impregnation of Au onto TiO_2 gives Au^0 particles as small as 3.2 nm [36], but treatment in 8% O_2/He for 2 h at 773 K causes extensive cluster agglomeration to form particles >10 nm in diameter [6]. Deposition-precipitation techniques on γ-Al_2O_3 supports form slightly larger 3.5 nm particles, which grow to 4.0 nm after treatment for 2 h at 873 K in 25% O_2/He [13]. Au clusters deposited onto mesoporous silicas (SBA-11, SBA-12, SBA-15, HMM-2, and MCM-41) functionalized with amines sinter to form 4.3-7.9 nm particles after treatment in pure H_2 at 473 K for 2 h [37]. Metal sputter deposition techniques, although difficult to implement at practical scales [38,39], form Au clusters that are among the smallest and most stable [6]. For example, sputtering Au metal onto fumed SiO_2 gives particles with 2.5 nm mean diameter (but also several large (>10 nm) clusters), which grow to 3.2 nm after annealing at 773 K in 8% O_2/He for 2 h [6]. AuNaLTA (1.3 nm) and AuNaMFI (2.0 nm), by contrast, maintain smaller and nearly monodisperse clusters after similar treatments. The size stability conferred to Au clusters by encapsulation appears to reflect their uniform dispersion throughout crystals and their inhibited migration and coalescence caused by the small apertures connecting LTA and MFI voids. The Au metal clusters within these voids do not coalesce up to 773 K, temperatures well above those used during the post-synthetic H_2 reduction (573-623 K) that forms them, showing that desirable dispersions can be maintained at higher temperatures after Au metal clusters form, as long as the critical Au^{3+} reduction step is systematically controlled.

2.3.3 Assessment of exposed Au surfaces by chemisorbed CO

Infrared absorption bands of CO adsorbed on AuCaLTA, AuNaMFI, and Au/SiO_2 were examined to assess the cleanliness and accessibility of their Au metal surfaces. This technique was

used instead of chemisorptive titrations that are challenging or infeasible for Au^0 particles in zeolites. The chemisorption of H_2 and O_2 onto Au^0, for instance, is slow and seldom equilibrated at temperatures required for significant coverages because of high dissociation activation barriers [35]. The molecular adsorption of CO occurs on both Au clusters and zeolite counterions [40] and cannot be distinguished from volumetric uptakes.

The IR spectra of CO adsorbed on the Au clusters in AuNaMFI (1.9% wt.; $\langle d_{TEM} \rangle$=2.0 nm), AuCaLTA (1.1% wt.; $\langle d_{TEM} \rangle$=2.3 nm), and Au/SiO_2 (2.2% wt.; $\langle d_{TEM} \rangle$=2.7 nm) at 263 K under 1 kPa CO are shown in Figure 2.5a. Spectral intensities are normalized by the number of surface Au atoms.

AuNaMFI and Au/SiO_2 samples exhibit absorption bands at 2108 cm^{-1} and 2109 cm^{-1} respectively, which correspond to atop adsorption of CO on Au^0 [41]. AuCaLTA showed two separate bands, both at higher frequencies than those for CO-Au^0 in AuNaMFI and Au/SiO_2. The more intense band at 2177 cm^{-1} corresponds to CO adsorbed onto charge-balancing Ca^{2+} cations in LTA [40,42]. The second band at 2123 cm^{-1} corresponds to CO on Au sites in AuCaLTA. The contributions to this spectrum from Ca^{2+}-CO species were subtracted using the CO infrared bands on CaLTA (Fig. 2.S8, SI) to obtain accurate intensities and frequencies for the Au-CO bands. The Au-CO band in AuCaLTA is shifted to higher frequencies (by 14 cm^{-1}) relative to that for CO-Au^0 in Au/SiO_2. This shift likely reflects slightly electron-deficient Au surfaces ($Au^{\delta+}$) [41,43,44], which decrease back-donation from Au to $2\pi^*$ orbitals in adsorbed CO, thus increasing the C-O bond force constant and increasing its vibrational frequency [43]. Such effects have been reported for Pt, Pd, and Au clusters within FAU, and reflect electron withdrawal from metal centers by the electropositive charge-balancing zeolite cations [43,45,46]. We consider this to add circumstantial evidence indicating that the Au clusters are located within LTA voids, where the Ca^{2+} cations must reside. The absence of similar shifts (relative to Au/SiO_2) on AuNaMFI reflects the higher valence of Ca^{2+} (in LTA) relative to Na^+ (in MFI), and also the higher density of cations in LTA (0.24 Ca^{2+}/T atom, where T=Si, Al; Si/Al=1.1 vs. 0.03 Na^+/T atom; Si/Al=31).

In what follows, we measure the effects of CO pressure on Au-CO band intensities for AuCaLTA, AuNaMFI, and Au/SiO_2 to determine the number and relative binding strength of CO binding sites. In doing so, we compare the number of exposed Au atoms in these materials to determine whether the Au clusters evident in their TEM micrographs exhibit clean surfaces available for CO chemisorption.

The integrated intensities of the Au-CO bands in AuCaLTA, AuNaMFI, and Au/SiO_2 are shown in Figure 2.5b (263 K, 0.1-1.0 kPa CO). These normalized intensities (by saturation values at 1.0 kPa) reflect the CO fractional coverage at accessible Au surface atoms, but not the absolute amounts of chemisorbed CO. The Au-CO bands in all samples shift to slightly lower frequencies as pressure increases from 0.1 to 1.0 kPa CO (~4.2 cm^{-1}; Fig. 2.S9, SI), a result of weakening Au-CO interactions as CO coverage increases [47]. Increases in the Au-CO band intensities with pressure are significantly weaker at the high end of the pressure range (~7% increase from 0.8 to 1.0 kPa) than the low end (~21% increase from 0.1 to 0.2 kPa) for all samples, suggesting that coverages are near to saturation values at 1.0 kPa. CO fractional coverages are similar on these samples in spite of the slightly electron-deficient cluster surfaces in AuCaLTA, indicating that the higher CO vibrational frequencies (relative to Au^0) do not lead to detectable effects on CO binding

energies. Density functional theory calculations of chemisorbed CO on Pt(111) surfaces with a mathematically imposed slight positive charge show a 20 cm^{-1} increase in frequency, but a small decrease in CO binding energy (< 5 kJ mol^{-1}) at 0.25 fractional coverages, which becomes even smaller as coverages increase [48]. Physical mechanisms and magnitudes of such shifts in frequencies and binding energies are expected to be similar for other metals, including Au [48]. The similar CO fractional coverages on AuCaLTA, AuNaMFI, and Au/SiO_2 suggest that CO interacts similarly with their respective surfaces, indicating that binding stoichiometries and infrared absorption cross-sections are also similar, thus allowing absolute comparisons of band intensities to determine the number of surface atoms that are able to bind CO for each sample. These comparisons of the CO binding provide a measure of the surface cleanliness of samples prepared by mercaptosilane-stabilized precursors.

The surface cleanliness of Au clusters in AuCaLTA and AuNaMFI is quantified by a factor Ω_i:

$$\Omega_i = \frac{\tilde{I}_i}{\tilde{I}_{Au/SiO_2}} \qquad (5)$$

where $\tilde{I}_i$ is the integrated Au-CO band intensity for catalyst i (i= AuCaLTA, AuNaMFI, Au/SiO_2) normalized by the number of surface Au atoms in the sample. $\tilde{I}_{Au/SiO_2}$ is used as the reference because the oxidative treatments (673 K, 2 h, Section 2.2.2.3) we apply to Au/SiO_2 are known to remove all synthetic debris from the sample, as shown conclusively by temperature programmed oxidation experiments and thermal gravimetric analysis [24]. Consequently, Ω_i values near unity reflect similarly clean and accessible Au surfaces in AuCaLTA or AuNaMFI. The Ω_i values were computed using normalized CO IR spectra collected at 1 kPa and are shown in Table 2.1. Errors in these values are estimated as ±10% based on the standard deviation of three unique measurements of $\Omega_{AuCaLTA}$ (for 1.1% wt. AuCaLTA; $\langle d_{TEM} \rangle$=2.3 nm), computed using three measurements of $\tilde{I}_{Au/SiO_2}$ and $\tilde{I}_{AuCaLTA}$. All Ω_i values are close to unity (0.9-1.2), confirming the cleanliness and accessibility of the Au clusters in AuCaLTA and AuNaMFI. These Ω_i values indicate that the air and H_2 treatments applied to the Au-zeolite catalysts (to 673 K in air; 573 K in H_2) are effective at removing S species, derived from mercaptosilane ligands, from Au cluster surfaces. Indeed, mercaptosilane ligands can be removed from Au^0 clusters at even lower temperatures (573 K, 1 h, air flow) [49] and even from Pt, Pd, and Ir clusters (623 K, 2 h flowing H_2 treatment) [8] in spite of stronger S binding on these metals than on Au (Pt-S: 233 kJ mol^{-1}; Pd-S: 183 kJ mol^{-1}; Ir-S: 206 kJ mol^{-1}; Au-S: 126 kJ mol^{-1}) [50,51]. The data shown in this section provide compelling evidence that the post-synthesis treatments used here lead to accessible and clean Au clusters.

2.3.4 Consequences of encapsulation for catalysis and the use of turnover rates and large titrants to determine encapsulation selectivities

Our evidence for the presence of Au clusters within zeolite voids in AuNaLTA, AuCaLTA, and AuNaMFI based on their size (Section 2.3.1), stability (Section 2.3.2), and CO binding properties (Section 2.3.3) seems compelling. They are small in size (1.3-2.0 nm), similar to the dimensions of zeolite voids (1.1 nm LTA; 0.64 nm MFI), and seem uniformly dispersed throughout zeolite crystals (TEM; Fig. 2.3). They are exceptionally resistant to sintering by comparison with Au clusters dispersed on mesoporous supports, a property that we infer must reflect their restricted

mobility through confinement and the thermodynamic hurdles imposed by the need to disrupt LTA and MFI frameworks to grow. The $Au^{\delta+}$-CO IR bands in AuCaLTA suggest a proximity between Au clusters and Ca^{2+} counterions that can only be reconciled with confinement. Yet, their catalytic properties remain the ultimate arbiter of surface cleanliness and the raison d'etre for the effort spent in their synthesis. Reactivity, in the form of turnover rates, depends sensitively on the amount and cleanliness of the exposed Au surfaces; the selective preference for reactions of smaller molecules and a resistance to poisoning by large titrants, in turn, would provide the quantitative measures of encapsulation.

2.3.4.1 Alkanol oxidative dehydrogenation (ODH) on Au-zeolite catalysts

Zeolites bring forth remarkable diversity into the catalytic chemistries of encapsulated metal clusters through their ability to select reactants, products, and transition states based on their molecular size and shape [8,9]. Here, we exploit such zeolite shape selectivity effects by measuring ODH turnover rates of ethanol (0.40 nm kinetic diameter) [9] and isobutanol (0.55 nm kinetic diameter) [9] on AuNaLTA (0.42 nm aperture) [9] and AuCaLTA (0.50 nm aperture) [20] to quantify the extent to which active Au surfaces reside within zeolite voids. The windows in NaLTA and CaLTA allow ethanol diffusion into the void space but essentially exclude isobutanol; thus, comparison of ODH turnover rates for small and large alkanols on unrestricted surfaces (e.g. Au/SiO_2) and on AuCaLTA or AuNaLTA allows rigorous estimates of the fraction of the exposed metal atoms that reside within the LTA void space.

The slow diffusion of reactants in small-pore zeolites, such as LTA, can be enhanced by replacing the resident cations with ions that have smaller atomic radii or higher valence [52]. Ca^{2+} exchange into NaLTA decreases the total number of counterions in the framework and leads to larger effective window apertures that increase diffusion rates [52]; therefore, ODH rates on AuNaLTA and AuCaLTA can be used to determine the extent to which intracrystalline concentration gradients of alkanol reactants affect measured rates. NaMFI channels (0.55 nm apertures) cannot exclude isobutanol from intracrystalline voids. Consequently, the relative rates of ethanol and isobutanol ODH cannot be used to determine the extent of encapsulation in AuNaMFI. Instead, encapsulation is probed by determining the fraction of Au cluster surfaces that are protected from titration by a poison (dibenzothiophene; DBT, 0.9 nm kinetic diameter) that cannot enter MFI crystals (Section 2.3.4.3).

Alkanol ODH reactions form water and alkanals as primary products [25,53]. These alkanals can undergo oxidation to carboxylic acids, which, in turn, can react with alkanols in esterification reactions [53] on Brønsted acids to form hemiacetals that dehydrogenate oxidatively on Au to form esters [54]. These Brønsted acid sites can also catalyze elimination reactions of alkanols to form ethers and alkenes [25,53]. H_2O, formed as an ODH co-product, increases the rate of kinetically-relevant O_2 activation steps in ODH reactions via the formation of peroxide or hydroperoxide species, thus acting as an ODH co-catalyst [55]. In doing so, H_2O circumvents difficult O_2 dissociation steps, which exhibit high activation barriers on Au surfaces [13], and removes the requirement for coordinatively unsaturated Au atoms prevalent on small clusters [55], making even large Au clusters remarkably active in alkanol oxidations [55,56]. These effects of H_2O make reactivity comparisons among catalysts difficult because axial H_2O gradients lead to non-uniform reactivity along the catalyst bed, even at low alkanol conversions. These effects are

eliminated here by adding H_2O to the reactant stream at concentrations 5-10 times larger than those imposed by ODH reactions and by operating at low alkanol conversions (<3.0%), which also minimize secondary reactions.

Secondary ODH products (esters, carboxylic acids, ethers) were not detected on any Au-zeolite catalysts, but Au/SiO_2 formed ethyl acetate from ethanol (10.0% selectivity at 2.4% conversion) and isobutyl-isobutyrate from isobutanol (8.7% selectivity at 2.1% conversion). These secondary reactions do not affect measured turnover rates, because the formation of each product requires one initial ODH event, in which an alkanal forms via kinetically-relevant β-H abstraction from an adsorbed alkoxide by chemisorbed oxygen atoms [57]. Exposure of Au/SiO_2 to 0.05 M NaOH (as described in Section 2.2.2.3) to titrate H^+ species by Na^+ led to much lower ethyl acetate selectivies (4.8% vs. 10.0%) without detectably influencing ODH turnover rates. These data show that esters form on Au/SiO_2 because of the presence of Brønsted acid sites.

2.3.4.2 ODH catalytic evidence for cluster encapsulation within LTA

The selectivity of Au encapsulation in AuNaLTA and AuCaLTA can be measured from the ratio of ODH turnover rates for ethanol (r_{ethanol}) and isobutanol ($r_{\text{isobutanol}}$) reactants, defined as:

$$\chi_{\text{ODH,i}} = \frac{r_{\text{ethanol}}}{r_{\text{isobutanol}}} \qquad (6)$$

where i represents a given sample (AuNaLTA, AuCaLTA, AuNaMFI). These χ_{ODH} values are expected to be larger on AuNaLTA and AuCaLTA than on AuNaMFI or Au/SiO_2, because the former two samples but not the latter two prevent access to intracrystalline Au clusters by isobutanol reactants. The χ_{ODH} value for Au/SiO_2 ($\chi_{\text{ODH, Au/SiO}_2}$) reflects the relative intrinsic reactivities of ethanol and isobutanol in the absence of diffusional constraints for either alkanol, because SiO_2 mesopores do not selectively exclude the larger alkanol. The ratio of these χ_{ODH} values for each Au-zeolite sample to that of Au/SiO_2 defines an encapsulation selectivity parameter ϕ:

$$\phi = \frac{\chi_{\text{ODH,i}}}{\chi_{\text{ODH, Au/SiO}_2}} \qquad (7)$$

which determines, in turn, the extent to which active Au surface atoms reside within microporous voids that ethanol, but not isobutanol, can access. ϕ values approach unity for Au clusters that are freely accessible to both alkanols, such as those dispersed in MFI or mesoporous SiO_2. Large ϕ values, by contrast, suggest that Au clusters are predominantly secluded from contact by isobutanol. Clusters encapsulated within LTA should be completely inactive in isobutanol ODH, because LTA apertures are small enough to fully exclude isobutanol from its void structure. As a result, ϕ values for AuNaLTA and AuCaLTA represent the ratio of the total active Au surface area in the sample to that of fully accessible Au clusters at external zeolite crystal surfaces. The selectivity parameters then give the fraction of the Au surface area contained within voids (*F*) as:

$$F = 1 - \frac{1}{\phi} \qquad (8)$$

Large ϕ values (e.g. ϕ>10, which implies F>0.90; Eq. 8) thus provide evidence that Au clusters predominantly reside within zeolite voids, and are taken here as evidence of successful encapsulation.

Table 2.2 shows ethanol and isobutanol ODH turnover rates, χ_{ODH} values, and the resulting encapsulation selectivity parameters for Au/SiO_2 and Au-zeolite catalysts. The ratios of ethanol to isobutanol ODH rates on AuNaLTA and AuCaLTA (33-133) are much larger than on AuNaMFI (1.8) or Au/SiO_2 (1.5), consistent with Au clusters predominantly residing within LTA crystals, which in contrast with Au clusters in MFI or SiO_2 structures, are prevented from contact with isobutanol. The resulting encapsulation selectivities (ϕ, Eq. 7) are large (22-57). These ϕ values correspond to >95% (F>0.95; Eq. 8) of the Au surface area in AuNaLTA and AuCaLTA residing within the protected microporous voids of LTA crystals.

Ethanol ODH turnover rates varied somewhat among LTA-based Au catalysts with changes in Au content and cluster size, and as Na^+ was replaced with Ca^{2+} via post-synthesis exchange. AuCaLTA (2.3 nm clusters; 1.1% wt. Au; 0.017 s^{-1}) gave larger ODH turnover rates than AuNaLTA (2.3 nm; 1.1% wt.; 0.004 s^{-1}) (Table 2.2), apparently because slight ethanol concentration gradients were weakened as diffusivities increased when Ca^{2+} replaced Na^+ cations. Ethanol ODH turnover rates increased monotonically as Ca^{2+} ions replaced two Na^+ ions with each additional exchange cycle (Section 2.2.2.1) (Fig. 2.S10, SI) and then reached constant values after ten exchange cycles. The Ca/Al ratio (measured by ICP) after ten exchange cycles was 0.47, similar to the value expected from complete exchange (0.50). These monotonic changes continue up to the point of full exchange, suggesting that Ca^{2+} weakens, but does not remove, ethanol concentration gradients that lead to turnover rates lower than their kinetic limit.

The AuCaLTA sample with larger Au particles (1.1% wt.; 2.3 nm) gave slightly higher ethanol ODH turnover rates (0.017 s^{-1}; Table 2.2) than that with smaller Au clusters (1.1% wt. 1.3 nm; 0.012 s^{-1}), an unexpected finding in view of ethanol ODH turnover rates that depend only weakly on Au cluster size [58]. These trends do not reflect residues derived from protecting ligands, because the intensity of their respective CO infrared bands are proportional to their TEM-derived cluster dispersions (see Ω_i values; Eq. 5; Table 2.1; Section 2.3.3). Their different rates reflect instead ethanol concentration gradients that become steeper as the number of Au surface atoms, and therefore the kinetic load, increase with increasing dispersion. Indeed, ethanol turnover rates on AuCaLTA samples (0.022 s^{-1}, 0.017 s^{-1}, 0.012 s^{-1}; Table 2.2) decrease monotonically as the volumetric density of Au surface atoms increases (0.015, 0.033, 0.057; units $(1000Å^3)^{-1}$; Eq. S2, SI); these trends are consistent with intrazeolite ethanol concentration gradients that cause measured rates to be lower than those expected from the (higher) extrazeolite concentrations. The monotonic increase in turnover rates with the number of Ca^{2+} exchange cycles (Fig. 2.S10, SI) further confirms that these ethanol gradients persist even in fully exchanged samples. In contrast with encapsulated Au clusters, Au surfaces in extrazeolitic regions or in mesoporous solids are exposed to the prevalent concentrations of ethanol in the fluid phase, thus operating at the higher alkanol turnover rates characteristic of their kinetic limit. The lower ODH turnover rates on intracrystalline clusters lead, in turn, to ϕ values (Eq. 7) that underestimate the extent to which Au

surfaces reside within the confining voids in LTA samples. The reported encapsulation selectivity parameters (Table 2.2) must therefore be considered conservative lower limits of their true values.

2.3.4.3 Evidence of metal cluster encapsulation in MFI

The encapsulation selectivity of Au clusters in AuNaMFI was determined from measurements of ethanol ODH turnover rates on Au/SiO_2 and AuNaMFI samples with and without preceding exposure to dibenzothiophene (DBT) dissolved in ethanol (Section 2.2.4). Organosulfur compounds, such as thiophene and DBT, irreversibly adsorb onto Au surfaces, both as molecular species and after C-S hydrogenolysis, to form unreactive species that block active surfaces [59]. As a result, ODH turnover rates on Au/SiO_2 and on extrazeolite Au clusters in AuNaMFI should be strongly suppressed by DBT, while Au surfaces within intracrystalline MFI regions, which are inaccessible to DBT, should preserve their ODH reactivity in the presence of DBT, thus providing a reliable account of the extent to which Au cluster surfaces lie within the intracrystalline space.

In these experiments, untreated and DBT-treated samples were exposed to air at mild conditions (343 K, Section 2.2.4) before use in ethanol ODH to remove adsorbed ethanol but to avoid desorbing DBT or its hydrogenolysis products from Au surfaces; such mild treatments may allow samples to retain other residues from the ethanol solvent used to dissolve DBT (Section 2.2.4). These effects led to only small changes in ODH rates (Table 2.3), but were taken into account by comparing ODH turnover rates on samples exposed to liquid ethanol with and without dissolved DBT (the latter denoted below as the "control sample") and otherwise identically treated in air at 343 K before catalysis. Turnover rates measured on control samples (AuNaMFI: 0.0094 s^{-1}; Au/SiO_2: 0.012 s^{-1}) (Table 2.3) were slightly lower than those on samples pretreated at higher temperature (673 K; AuNaMFI: 0.016 s^{-1}; Au/SiO_2: 0.033 s^{-1}). Treatment of the control samples at this higher temperature leads to full recovery in the ODH rates (Table 2.3), consistent with the desorption of contaminants that could not be removed by the milder air treatment.

ODH turnover rates measured on the control samples (r_{ODH}) and on those exposed to DBT ($r_{ODH,\ DBT}$) are used to define a parameter Λ_{DBT}:

$$\Lambda_{DBT,i} = \frac{r_{ODH,\ DBT}}{r_{ODH}} \qquad (9)$$

where i identifies the specific sample (e.g., Au/SiO_2, AuNaMFI). A fraction of the Au surfaces exposed to DBT will retain some detectable ODH reactivity, because the binding and surface reactivity of DBT-derived species decreases as surfaces reach near-saturation coverages [60]. As a result, $\Lambda_{DBT,Au/SiO_2}$ reflects the fraction of the Au surface in Au/SiO_2 that remains vacant after DBT exposure. $\Lambda_{DBT,AuNaMFI}$ similarly represents the fraction of the Au surfaces that remain active in ODH for AuNaMFI, which would include those cluster surfaces confined within MFI crystals. These ratios are used to define an encapsulation selectivity parameter (ϕ_{DBT}) as:

$$\phi_{DBT} = \frac{\Lambda_{DBT,AuNaMFI}}{\Lambda_{DBT,\ Au/SiO_2}} \qquad (10)$$

As in the case of similar parameters for LTA samples (Eq. 7; Section 2.3.4.2), a ϕ_{DBT} value of unity would reflect Au clusters that are fully accessible to DBT in MFI samples, thus indicating their exclusive presence at extracrystalline regions. Values of ϕ_{DBT} much larger than unity are taken as a measure of successful encapsulation procedures. ϕ_{DBT} values, similar to the values of ϕ (Eq. 7), give the ratio of the total Au surface area to that present at extrazeolite Au clusters, thus allowing the determination of the fraction of the Au surface area that is encapsulated (*F*):

$$F = 1 - \frac{1}{\phi_{DBT}} \qquad (11)$$

The ethanol ODH turnover rates and their associated $\Lambda_{DBT,i}$ values for AuNaMFI (1.9% wt.; $\langle d_{TEM} \rangle$=2.0 nm) and Au/SiO_2 (1.1% wt.; $\langle d_{TEM} \rangle$=2.7 nm), as well as the treatment conditions for these catalysts, are shown in Table 2.3. The ODH turnover rates on AuNaMFI exposed to DBT (0.0089 s^{-1}) and on the DBT-free control sample (0.0094 s^{-1}) were similar, thus resulting in a $\Lambda_{DBT,AuNaMFI}$ value near unity (0.95). The turnover rate on the DBT-treated Au/SiO_2 sample (0.0013 s^{-1}), in contrast, was about ten times smaller than that on the DBT-free Au/SiO_2 control (0.012 s^{-1}), resulting in a small $\Lambda_{DBT,Au/SiO_2}$ value (0.11) (Eq. 9). These data lead in turn to an encapsulation selectivity parameter of 8.6 (ϕ_{DBT}, Eq. 10) for AuNaMFI, and to the conclusion that ~90% of its Au surface area resides within the protected voids of MFI crystals (Eq. 11).

Ethanol ODH turnover rates on samples treated at 673 K were slightly lower for AuNaMFI (0.016 s^{-1}; Table 2.3) than Au/SiO_2 (0.033 s^{-1}); this difference does not reflect Au surface contamination derived from mercaptosilane ligand residues, because the surface-normalized CO IR bands for these samples (Ω_i; Eq. 5; Table 2.1) are of equal intensity. We attribute these different rates instead to diffusional constraints for ethanol within MFI crystals. Such constraints may result from relatively slow rates of intracrystalline diffusion, or from pore blockage at the crystallite outer surface by a layer of silicates [61-64], which may be formed as by-products during MFI crystallization through the action of the organic templates [64].

2.3.5 Protection of LTA-encapsulated Au clusters from thiophene poisoning

The selective encapsulation of Au clusters within LTA, evident from the relative rates of ethanol and isobutanol ODH (Section 2.3.4.2), should also protect such clusters from thiophene, which, as in the case of isobutanol, cannot diffuse within LTA voids. This is shown here from ethanol ODH rates on AuNaLTA and Au/SiO_2 in the presence or absence of thiophene. NaLTA is used, because its apertures (0.42 nm) are smaller than those of CaLTA (0.50 nm) and thus more effectively exclude thiophene poisons (0.46 nm kinetic diameter) [9]. These data are used to confirm the high encapsulation selectivities determined from ethanol and isobutanol ODH turnover rates.

Ethanol ODH rates (divided by their initial value) are shown in Figure 2.6 as a function of time for AuNaLTA and Au/SiO_2 with 0 kPa and 1 kPa of thiophene in the reactor feed. ODH rates on AuNaLTA gradually decreased to 80% of their initial value after 2 h of exposure to thiophene, without detectable changes upon thiophene removal from the inlet stream. On Au/SiO_2, rates decreased to 6% of their initial value over 2 h of exposure, then recovered slightly (to 11%) upon thiophene removal, likely because some thiophene desorbed from Au clusters [65], an effect that

was not evident in AuNaLTA apparently because of the relatively small fraction of the Au surface in unprotected extracrystalline regions.

These data can be used to confirm the encapsulation selectivities reported in Section 2.3.4.2 from ethanol and isobutanol ODH rates, using a formalism similar to that developed for AuNaMFI using DBT poisons (Section 2.3.4.3). Ethanol turnover rates on AuNaLTA and Au/SiO_2 before (r_{ODH}) and after ($r_{ODH,\ TP}$) thiophene poisoning for 2.0 h are defined as:

$$\Lambda_{TP,i} = \frac{r_{ODH,\ TP}}{r_{ODH}} \qquad (12)$$

where i represents a given sample (Au/SiO_2, AuNaLTA). This $\Lambda_{TP,i}$ parameter accounts for the fraction of the Au surfaces that are inaccessible to thiophene in each sample. Similar to ϕ_{DBT} (Eq. 10), an encapsulation selectivity parameter (ϕ_{TP}) is defined as:

$$\phi_{TP} = \frac{\Lambda_{TP,AuNaLTA}}{\Lambda_{TP,\ Au/SiO_2}} \qquad (13)$$

which gives the ratio of the total Au surface area in AuNaLTA to that residing in unprotected extrazeolite environments. As in the case of ϕ (Eq. 7), this selectivity parameter underestimate the true extent of encapsulation, because intracrystalline ethanol concentration gradients cause ODH rates on encapsulated Au clusters to be smaller than those on Au surfaces at fully accessible locations. The measured $\Lambda_{TP,AuNaLTA}$ and $\Lambda_{TP,\ Au/SiO_2}$ values were 0.77 and 0.063 respectively, giving a ϕ_{TP} value of 12.8 and an F value of 0.92, consistent with the conclusions reached from the relative turnover rates of ethanol and isobutanol ODH on these samples (F>0.95, Section 2.3.4.2).

These data, taken together, provide compelling evidence for the selective encapsulation of Au clusters within zeolites. Encapsulation was achieved in both LTA and MFI, zeolites with significantly different aperture sizes (8-MR, 0.42 nm; 10-MR, 0.55 nm), Si/Al ratios (1.1; 31), void environments (supercages; channel intersections), synthesis templates (Na^+, inorganic SDA; TPAOH, organic SDA), and silica sources (colloidal SiO_2; TEOS). In spite of this diversity in framework structure, composition, and required synthesis reagents, Au precursors were confined within zeolites and subsequent thermal treatments led to their reduction and the nucleation of nearly monodisperse clusters ~1-2 nm in size and with clean surfaces using the same mercaptosilane ligands and synthesis protocols. These ligands disperse Au^{3+} precursors throughout zeolite crystals as they incipiently form and prevent their premature reduction and agglomeration at the pH and temperatures required for crystallization of the microporous frameworks. The small and monodisperse nature of these clusters reflects the uniform dispersion and the restricted mobility of their ligand-stabilized precursors, imposed by the small interconnecting channels in the microporous networks and the systematic control of the rates of reduction and of ligand removal from these precursors. Such protocols and mechanistic insights can be translated broadly into successful general strategies for the encapsulation of Au clusters within diverse frameworks, within which, as shown in this study, they can be protected structurally and chemically and used to catalyze reactions only of those reactant molecules that can access their surfaces via diffusion through their intracrystalline voids.

2.4 Conclusion

A broadly applicable procedure was developed for the encapsulation of small (1-2 nm) and nearly monodisperse Au clusters within zeolites using a ligand-assisted hydrothermal synthesis protocol. The encapsulation of Au particles in LTA and MFI zeolites are demonstrated as specific examples of the proposed technique. The synthetic procedure employs mercaptosilane ligands, which bind to and chemically protect Au^{3+} cations against reduction as they are introduced into zeolite synthesis gels. These ligands simultaneously form siloxane bridges with silicate precursors to promote the uniform incorporation of Au into the zeolite host. Treatment of the crystallized zeolites in O_2 and then H_2 reduces the Au^{3+} cations, which form dispersed and encapsulated clusters. The mean size of these clusters can be systematically adjusted, without losses in monodispersity, through simple modifications in the reduction temperature. The Au particles remain sinter-stable to 773 K in air or H_2 as a result of their confinement in zeolite voids, which restrict their mobility and the size to which they can grow. The encapsulated clusters also show high size selectivity during catalytic oxidative alkanol dehydrogenation or exposure to organosulfur poisons, because they are secluded from contact by molecules larger than the zeolite apertures. The encapsulated Au surfaces were free of synthetic debris and accessible to CO, as determined by the analysis of adsorbed CO IR bands. The present work outlines the synthesis of Au clusters whose average size can be controlled while maintaining stability and a narrow size distribution, allowing the systematic study of Au clusters at reaction conditions which strongly favor Au particle sintering into large, inactive agglomerates. We predict that the proposed strategy will have wide applicability for the encapsulation of Au into zeolites with different framework topologies, compositions, and void environments. The proposed method extends the currently available Au encapsulation techniques to include small-pore ($\leq$8 MR) zeolites, for which the use of cation-exchange or impregnation techniques are not feasible.

2.5 Acknowledgments

We gratefully acknowledge the generous financial support of the Chevron Energy Technology Co., and an ARCS Foundation Fellowship (for TO). We thank Dr. Reena Zalpuri (Electron Microscope Lab) for help with TEM instrumentation, Dr. Antonio DiPasquale (X-Ray Facility) for assistance with XRD, Professor Prashant Deshlahra for discussions on IR spectroscopy, as well as Stanley Herrmann and Alexandra Landry for review of the manuscript.

2.6 Figures, Tables, and Scheme(s)

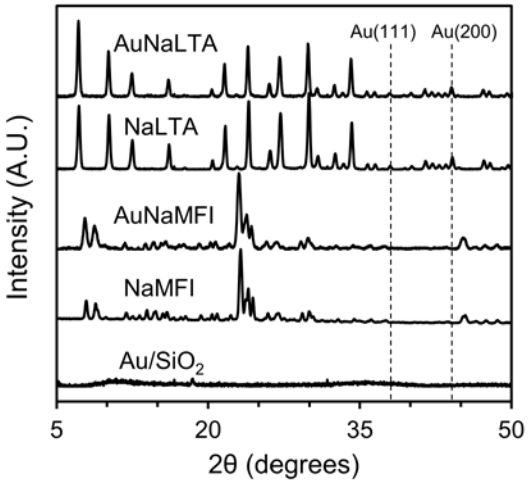

Figure 2.1. XRD patterns of AuNaLTA, AuNaMFI, and Au/SiO_2 samples.

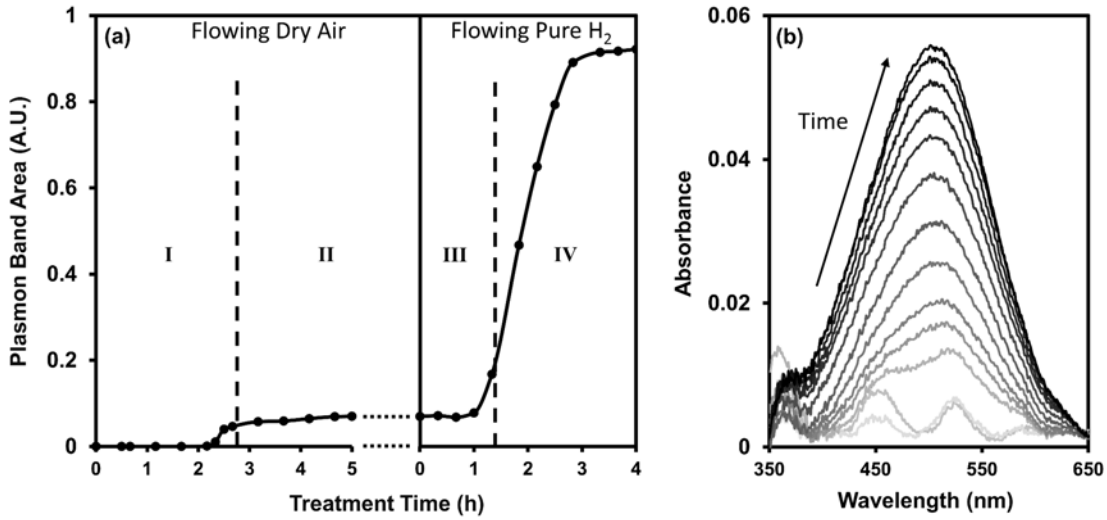

Figure 2.2. (a) Evolution of the 1.1% wt. AuNaLTA LSPR band integrated intensity in flowing air (I and II) or H_2 (III and IV) under (I): 120 K h^{-1} ramp to 623 K, (II): 623 K, (III): 240 K h^{-1} ramp to 623 K, subsequent to cooling to ambient temperature after (II), and (IV): 623 K. (b) Growth of the LSPR band for 1.1% wt. AuNaLTA (following 2 h treatment at 623 K under air flow) in flowing H_2 over the temperature range 543-623 K (240 K h^{-1} ramp to 623 K, 0.17 h between each spectrum) corresponding to hours 1-3 in regions (III) and (IV) in (a). Gas flows were operated at 1.67 cm^3 g^{-1} s^{-1} and 100 kPa with dry air or pure H_2.

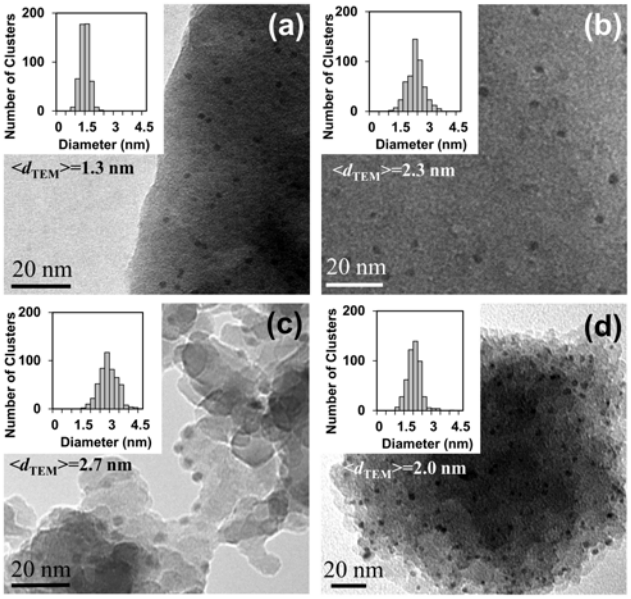

Figure 2.3. TEM micrographs, surface-averaged Au cluster diameters, $\langle d_{TEM} \rangle$ (Eq. 1), and cluster diameter distributions for (a) 1.1% wt. AuNaLTA post-synthetically treated at 573 K, (b) 1.1% wt. AuNaLTA post-synthetically treated at 623 K, (c) 2.2% wt. Au/SiO_2, and (d) 1.9% wt. AuNaMFI.

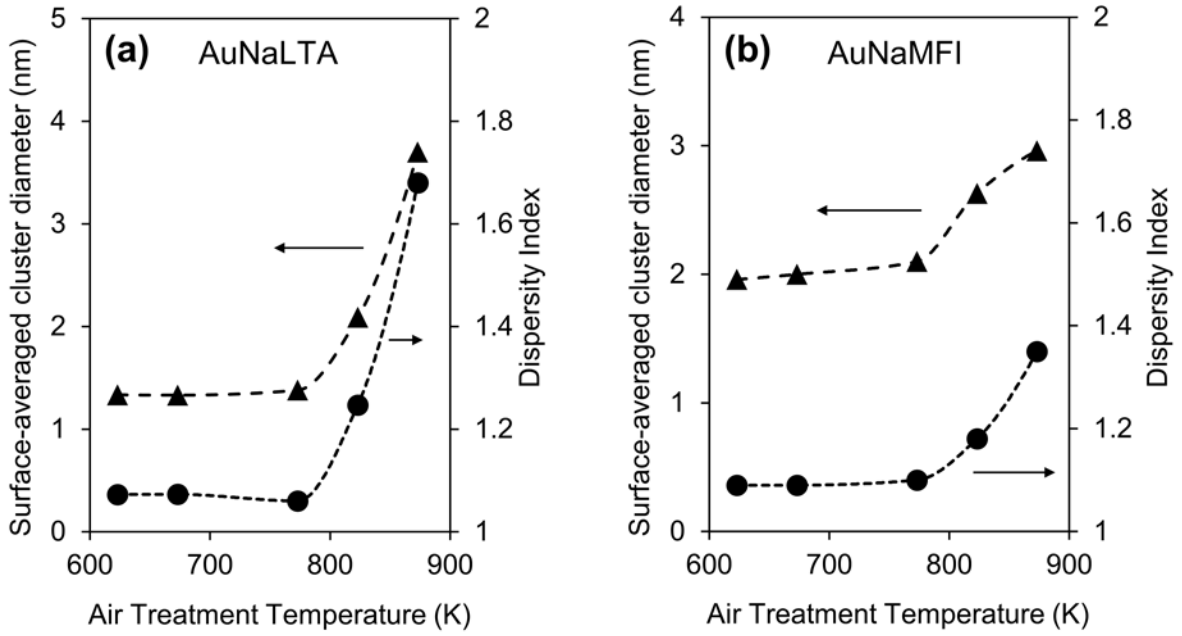

Figure 2.4. Effect of flowing dry air treatment temperature (21 kPa O_2, 79 kPa N_2, 1.67 $cm^3\ g^{-1}\ s^{-1}$, 5 h) on the TEM-derived surface averaged cluster diameter ($\langle d_{TEM} \rangle$, ▲) (Eq. 1), and dispersity index (DI, ●) (Eq. 3) of Au clusters in (a) 1.1% wt. AuNaLTA and (b) 1.9% wt. AuNaMFI.

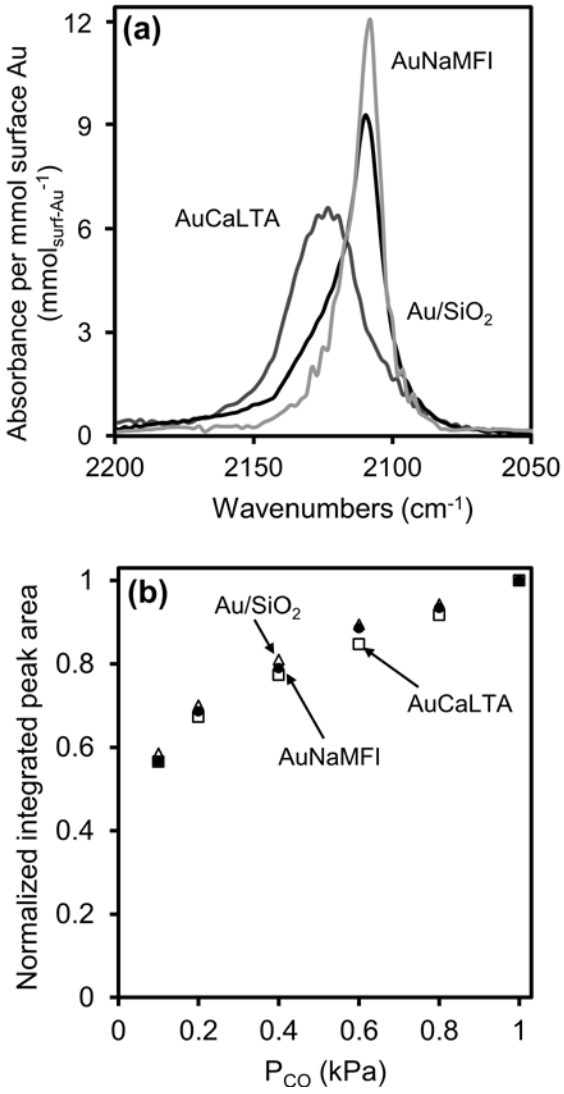

Figure 2.5. (a) Infrared spectra of CO adsorbed on Au clusters in Au/SiO_2 (black), AuCaLTA (gray), and AuNaMFI (light gray) samples at 263 K (1.0 kPa CO, 99.0 kPa He) after flowing H_2 pretreatment (573 K, 20 kPa H_2, 80 kPa He). Spectral intensities are normalized by the moles of exposed surface Au in each sample (estimated with dispersions derived from TEM micrographs and metal loadings measured with ICP-OES analysis). (b) Integrated peak areas for AuCaLTA (□), AuNaMFI (●), and Au/SiO_2 (Δ) measured at 263 K over the range 0.1-1 kPa CO, where areas are normalized by the maximum collected area (at 1 kPa CO) for each respective sample.

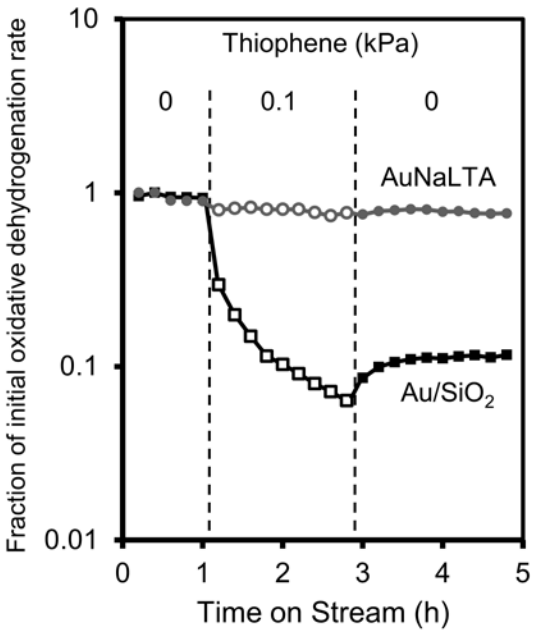

Figure 2.6. Ratio of the initial ethanol oxidative dehydrogenation rate at 393 K under 9 kPa O_2, 4 kPa EtOH, and 0.5 kPa H_2O (rates quantified in terms of s^{-1} $mol_{surf\text{-}Au}^{-1}$) to those exhibited in the presence (0.1 kPa, open markers) and absence (closed markers) of thiophene under continuous reaction for AuNaLTA (●) and Au/SiO_2 (■).

Table 2.1. Metal Loadings, surface averaged particle diameters, and normalized CO-Au IR intensities of Au-zeolite catalysts synthesized with the hydrothermal technique, and a reference Au/SiO_2 sample.

Sample	Metal loading (% wt.)[a]	Au cluster diameter $\langle d_{TEM} \rangle$ (nm)[b]	D^c	DI^d	Ω^e
AuNaLTA	1.1	1.3 ± 0.2	0.89	1.07	0.9 ± 0.1
AuNaLTA	1.1	2.3 ± 0.4	0.51	1.09	1.1 ± 0.1
AuNaLTA	0.5	2.2 ± 0.4	0.53	1.08	1.1 ± 0.1
AuNaMFI	0.2	2.1 ± 0.4	0.55	1.06	0.9 ± 0.1
AuNaMFI	1.9	2.0 ± 0.4	0.58	1.09	1.2 ± 0.1
Au/SiO_2	2.2	2.7 ± 0.5	0.43	1.06	-

[a]Analyzed by inductively coupled plasma optical emission spectroscopy. [b]Surface area weighted mean cluster diameter determined via TEM (Eq. 1). [c]Dispersion estimated from $\langle d_{TEM} \rangle$ (Eq. 2). [d]Dispersity Index computed as the surface averaged cluster diameter divided by the number averaged diameter (Eq. 3). [e]Ratio of sample's integrated CO-Au IR band intensity to that of Au/SiO_2 under 1 kPa CO and 99 kPa He at 263 K, where intensities for each are normalized by the number of surface Au atoms in the sample (as estimated by the metal loading and *D)* (Eq. 5). NaLTA samples were cation exchanged with Ca^{2+} before IR measurements to improve the accessibility of CO to the zeolite interior.

Table 2.2. Catalytic Properties of Au-Encapsulated LTA, MFI, and Au/SiO_2 catalysts in oxidative dehydrogenation (ODH) of alkanols[a]

Sample	Au cluster diameter $\langle d_{TEM} \rangle$ (nm)	Metal loading (% wt.)	Alcohol ODH Turnover Rate (10^{-3} s^{-1} $mol_{surf\text{-}Au}^{-1}$)			
			$r_{ethanol}$ [b]	$r_{isobutanol}$ [b]	χ_{ODH} [c]	ϕ [d]
AuCaLTA	1.3 ± 0.2	1.1	12	0.14	86	57
AuCaLTA	2.3 ± 0.4	1.1	17	0.15	113	76
AuCaLTA	2.2 ± 0.4	0.5	22	0.20	110	73
AuNaLTA	2.3 ± 0.4	1.1	4	0.12	33	22
AuNaMFI	2.0 ± 0.4	1.9	16	9	1.8	1.2
Au/SiO_2	2.7 ± 0.5	2.2	33	22	1.5	-

[a]Oxidative Dehydrogenation: 4 kPa alkanol, 9 kPa O_2, 0.5 kPa H_2O, balance He to 101 kPa at 393 K. [b]Reaction turnover rate defined as number of moles of reactant converted per time normalized by the number of exposed surface metal atoms estimated by TEM. [c]$\chi_{ODH} = r_{ethanol}/r_{isobutanol}$ (Eq. 6). [d]Ratio of the χ_{ODH} value for the sample to that of Au/SiO_2 (Eq. 7).

Table 2.3. Rates of ethanol oxidative dehydrogenation on Au/SiO_2 and AuNaMFI following DBT exposure or pretreatment

	Au-Zeolite Catalyst Ethanol ODH Turnover Rate (10^{-3} s^{-1} $mol_{surf\text{-}Au}^{-1}$)				
Pretreatment	**(1) EtOH[a]**	**(2) EtOH + DBT[b]**	**(3) 673K O_2[c]**	**(4) EtOH→ 673K O_2[d]**	Λ_{DBT}[e]
AuNaMFI	9.4	8.9	16	16	0.95
Au/SiO_2	12	1.3	33	34	0.11

[a]Samples (100mg) agitated in 30 cm^3 of EtOH at ambient temperature for 4 h, treated in ambient air at 343 K for 12 h, then used in ODH reaction (393 K under 9 kPa O_2, 4 kPa EtOH, and 0.5 kPa H_2O). [b]Samples treated analogously with (1), but with dissolved DBT in the EtOH at a 6:1 DBT:Au molar ratio. [c]Fresh samples treated in flowing 20% O_2/He (1.67 cm^3 g^{-1} s^{-1}, 2 h), then used in reaction. [d]Sample (1) was treated in flowing 20% O_2/He (1.67 cm^3 g^{-1} s^{-1}, 2 h) and used again in a second reaction. [e]Ratio of rates from samples (2) and (1) (Eq. 9).

Scheme 2.1 Schematic representation of the synthesis and characterization of Au clusters encapsulated within zeolites

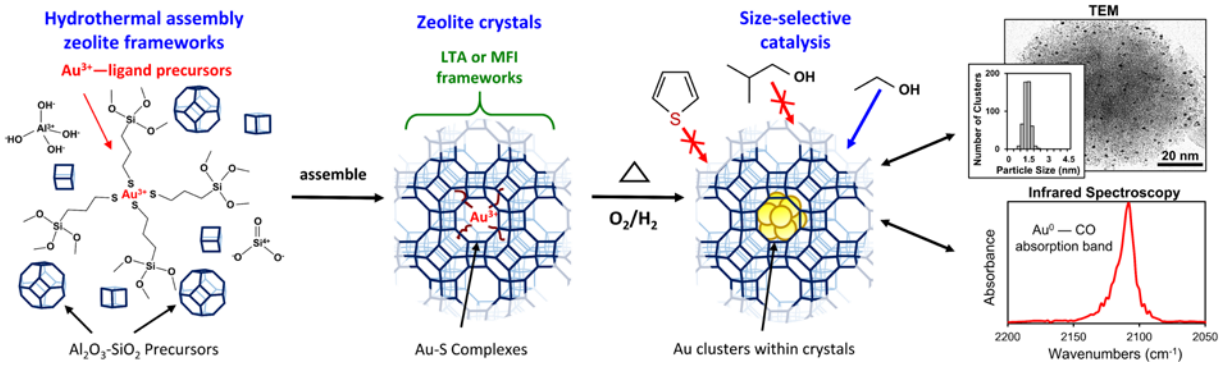

2.7 References

[1] Abad, A.; Corma, A.; García, H. *Chem. Eur. J.* **2008**, *14*, 212.
[2] Mallat, T.; Baiker, A. *Chem. Rev.* **2004**, *104*, 3037.
[3] Hutchings, G. J. *Chem. Commun.* **2008**, 1148.
[4] Shekhar, M.; Wang, J.; Lee, W.-S.; Williams, W. D.; Kim, S. M.; Stach, E. A.; Miller, J. T.; Delgass, W. N.; Ribeiro, F. H. *J. Am. Chem. Soc.* **2012**, *134*, 4700.
[5] Mielby, J.; Abildstrøm, J. O.; Wang, F.; Kasama, T.; Weidenthaler, C.; Kegæs, S. *Angew. Chem. Int. Ed.* **2014**, *53*, 12513.
[6] Veith, G. M.; Lupini, A. R.; Pennycook, S. J.; Mullins, D. R.; Schwartz, V.; Bridges, C. A.; Dudney, N. J. *J. Catal.* **2009**, *262*, 92.
[7] Schmid, G.; Corain, B. *Eur. J. Inorg. Chem.* **2003**, 3081.
[8] Choi, M.; Wu, Z.; Iglesia, E. *J. Am. Chem. Soc.* **2010**, *132*, 9129.
[9] Wu, Z.; Goel, S.; Choi, M.; Iglesia, E. *J. Catal.* **2014**, *311*, 458.
[10] Weisz, P. B.; Frilette, V. J.; Maatman, R.W.; Mower, E. B. *J. Catal.* **1962**, *1*, 307.
[11] Guillemot, D.; Polisset-Thfoin, M.; Fraissard, J. *Catal. Lett.* **1996**, *41*, 143.
[12] Zeng, S.; Ding, S.; Li, S.; Wang, R.; Zhang, Z. *Inorg. Chem. Commun.* **2014**, *47*, 63.
[13] Ojeda, M.; Zhan, B.-Z.; Iglesia, E. *J. Catal.* **2012**, *285*, 92.
[14] Laursen, A. B.; Højholt, K. T.; Lundegaard, L. F.; Simonsen, S. B.; Helveg, S.; Schueth, F.; Paul, M.; Grunwaldt, J. D.; Kegæs, S.; Christensen, C. H.; Egeblad, K. Angew. *Chem. Int. Ed.* **2010**, *49*, 1026.
[15] Højholt, K. T.; Laursen, S. K.; Christensen, C. H. *Top. Catal.* **2011**, *54*, 1026-1033.
[16] Gu, J.; Zhang, Z.; Hu, P.; Ding, L.; Xue, N.; Peng, L.; Guo, X.; Lin, M.; Ding, W. *ACS Catal.* **2015**, *5*, 6893.
[17] Celis, R.; Carmenhermosiän, M.; Cornejo, *J. Environ. Sci. Technol.* **2000**, *34*, 4593.
[18] Billinge, S. J. L.; McKimmy, E. J.; Shatnawi, M.; Kim, H. J.; Petkov, V.; Wermeille, D.; Pinnavaia, T. J. *J. Am. Chem. Soc.* **2005**, *127*, 8492.
[19] Choi, M.; Cho, H. S.; Srivastava, R.; Venkatesan, C.; Choi, D.-H.; Ryoo, R. *Nat. Mater.* **2006**, *5*, 718.
[20] Weitkamp, J.; Ernst, S.; Puppe, L. In *Catalysis and Zeolites: Fundamentals and Applications*; Weitkamp, J., Puppe, L., Eds.; Springer-Verlag: New York, 1999; pp 354-355.
[21] Baerlocher, C.; McCusker, L. B. Database of Zeolite Structures: http://www.iza-structure.org/databases/.
[22] Van de Voorde, B.; Hezinova, M.; Lannoeye, J.; Vandekerkhove, A.; Marszalek, B.; Gil, B.; Beurroies, I.; Nachtiqall, P.; De Vos, D. *Phys. Chem. Chem. Phys.* **2015**, *17*, 10759.
[23] Gevert, B.; Eriksson, L.; Törncrona, A. *J. Porous Mater.* **2011**, *18*, 723.
[24] Zhu, H.; Ma, Z.; Clark, J. C.; Pan, Z.; Overbury, S. H.; Dai, S. *Appl. Catal., A* **2007**, *326*, 89.
[25] Simakova, O. A.; Sobolev, V. I.; Koltunov, K. Y.; Campo, B.; Leino, A.-R.; Kordas, K.; Murzin, D. Y. *Chem. Cat. Chem.* **2010**, *2*, 1535.
[26] Bergeret, G.; Gallezot, P. In *Handbook of Heterogeneous Catalysis;* Ertl, G.; Knozinger, H.; Schuth, F.; Weitkamp, J., Eds.; Wiley-VHC: Weinheim, Germany, 2008; pp 738-765.
[27] Luo, W.; Sankar, M.; Beale, A. M.; He, Q.; Kiely, C. J.; Bruijnincx, P. C. A.; Weckhuysen, B. M. *Nat. Commun.* **2014**, *6*, 1.
[28] Schneider, M.; Duff, D. G.; Mallat, T.; Wildberger, M.; Baiker, A. *J. Catal.* **1994**, *147*, 500.
[29] Kunz, S.; Iglesia, E. *J. Phys. Chem. C* **2014**, *118*, 7468.

[30] Brown, D. H.; McKinlay, G. C.; Smith, W. E. *Inorg. Chim. Acta.* **1979**, *32*, 117.
[31] Peng, S.; McMahon, J. M.; Schatz, G. C.; Gray, S. K.; Sun, Y. *Proc. Natl. Acad. Sci. U.S.A.* **2010**, *107*, 14530.
[32] Mikhlin, Y.; Likhatski, M.; Karacharov, A.; Zaikovski, V.; Krylov, A. *Phys. Chem. Chem. Phys.* **2009**, *11*, 5445.
[33] Tlahuice-Flores, A.; Whetten, R. L.; Jose-Yacaman, M. *J. Phys. Chem. C* **2013**, *117*, 12191.
[34] Lin, X.; Falconer, J. L.; Noble, R. D. *Chem. Mater.* **1998**, *10*, 3716.
[35] Carabineiro, A. A. C.; Nieuwenhuys, B. E.; *Gold Bull*. **2009**, *42*, 288.
[36] Delannoy, L.; Hassan, N. E.; Musi, A.; To, N. N. L.; Krafft, J.-M.; Louis, C. *J. Phys. Chem. B* **2006**, *110*, 22471.
[37] Bore, M. T.; Pham, H. N.; Switzer, E. E.; Ward, T. L.; Fukuoka, A.; Datye, A. K. *J. Phys. Chem. B* **2005**, *109*, 2873.
[38] Terashima, C.; Iwai, Y.; Cho, S.-P.; Ueno, T.; Zettsu, N.; Saito, N.; Takai, O. *Int. J. Electrochem. Sci.* **2013**, *8*, 5407.
[39] Edelstein, A. S.; Cammarata, R. C. *Nanomaterials: Synthesis, Properties and Applications*; IOP Publishing: London, 1996.
[40] Angell, C. L.; Schaffer, P. C. *J. Phys. Chem.* **1966**, *70*, 1413.
[41] Venkov, T.; Fajerwerg, K.; Delannoy, L.; Klimev, H.; Hadjiivanov, K.; Louis, C. *Appl. Catal., A* **2006**, *301*, 106.
[42] Rakić, V.; Dondur, V.; Hercigonja, R. *J. Serb. Chem. Soc.* **2003**, *68*, 409-416.
[43] Guillemot, D.; Borovkov, V. Y.; Kazansky, V. B.; Polisset-Thfoin, M.; Fraissard, J. *J. Chem. Soc., Faraday Trans.* **1997**, *93*, 3587.
[44] Carrasquillo-Flores, R.; Ro, I.; Kumbhalkar, M. D.; Burt, S.; Carrero, C. A.; Alba-Rubio, A. C.; Miller, J. T.; Hermans, I.; Huber, G. W.; Dumesic, J. A. *J. Am. Chem. Soc.* **2015**, *137*, 10317.
[45] Sachtler, W. M. H.; Zhang, Z. *Adv. Catal.* **1993**, *39*, 129.
[46] Karpinski, Z. *Adv. Catal.* **1990**, *37*, 45.
[47] Hartshorn, H.; Pursell, C. J.; Chandler, B. D. *J. Phys. Chem. C* **2009**, *113*, 10718.
[48] Deshlahra, P.; Wolf, E. E.; Schneider, W. F. *J. Phys. Chem. A* **2009**, *113*, 4125.
[49] Zheng, N.; Stucky, G. D.; *J. Am. Chem. Soc*. **2006**, *128*, 14278.
[50] Toulhoat, H.; Raybaud, P.; Kasztelan, S.; Kresse, G.; Hafner, J. *Catal. Today* **1999**, *50*, 629.
[51] Nuzzo, R. G.; Fusco, F. A.; Allara, D. L. *J. Am. Chem. Soc.* **1987**, *109*, 2358.
[52] Bobdok, D.; Besedová, E. *Pet. Coal* **2003**, *45*, 19.
[53] Holz, M. C.; Tölle, K.; Muhler, M. *Catal. Sci. Technol.* **2014**, *4*, 3495.
[54] Mallat, T.; Baiker, A. *Annu. Rev. Chem. Biomol. Eng.* **2012**, *3*, 11.
[55] Chang, C.-R.; Yang, X.-F.; Long, B.; Li, J. *ACS Catal*. **2013**, *3*, 1693.
[56] Angelici, R. J.; *Catal. Sci. Technol.* **2013**, *3*, 279.
[57] Xu, B.; Madix, R. J.; Friend, C. M. *Acc. Chem. Res.* **2014**, *47*, 761.
[58] Guan, Y.; Hensen, E. J. M. *Appl. Catal., A* **2009**, *361*, 49.
[59] Sako, E. O.; Kondoh, H.; Nakai, I.; Nambu, A.; Nakamura, T.; Ohta, T. *Chem. Phys. Lett.* **2005**, *413*, 267.
[60] Meyer, R.; Lemire, C.; Shaikhutdinov, S. K.; Freund, H. J. *Gold Bull.* **2004**, *37*, 72-124.
[61] Kortunov, P.; Vasenkov, S.; Chmelik, C.; Kärger, J.; Ruthven, D. M.; Wloch, *J. Chem. Mater*. **2004**, *16*, 3552.
[62] Fujikata, Y.; Masuda, T.; Ikeda, H.; Hashimoto, K. *Micropor. Mesopor. Mat.* **1998**, *21*, 679.
[63] Teixeira, A. R.; Qi, X.; Chang, C.-C.; Fan, W.; Conner, W. C.; Dauenhauer, P. J. *J. Phys. Chem. C* **2014**, *118*, 22166.

[64] Karwacki, L.; Kox, M. H. F.; Matthijs de Winter, D. A.; Drury, M. R.; Meeldijk, J. D.; Stavitski, E.; Schmidt, W.; Mertens, M.; Cubillas, P.; John, N.; Chan, A.; Kahn, N.; Bare, S. R.; Anderson, M.; Kornatowski, J.; Weckhuysen, B. M. *Nat. Mater.* **2009**, *8*, 959.
[65] Ito, E.; Noh, J.; Hara, M. *Jpn. J. Appl. Phys.* **2003**, *42*, L852.

2.8 Supporting Information

Contents

2.S1. Au encapsulation in NaLTA with bis(ethylenediamine)gold(III) chloride complex

We attempted to encapsulate gold particles within the NaLTA zeolite by using the $Au(en)_2Cl_3$ (en=ethylenediamine) complex, whose synthesis is detailed in Section 2.2.2.3 of the text. The synthetic procedure was analogous to that applied for hydrothermal AuNaLTA synthesis with mercaptosilane ligands (Section 2.2.2.1), except that the entire ligated complex was added to the NaOH solution rather than adding the ligands first and the gold chloride ionic compound second. The ethylenediamine complex did not provide the requisite stability to the gold cations to prevent their reduction during crystallization, as evidenced by the formation of large (>6 nm) Au clusters visible in TEM micrographs (Fig. 2.S1) immediately following crystallization and prior to any further post-synthetic treatments.

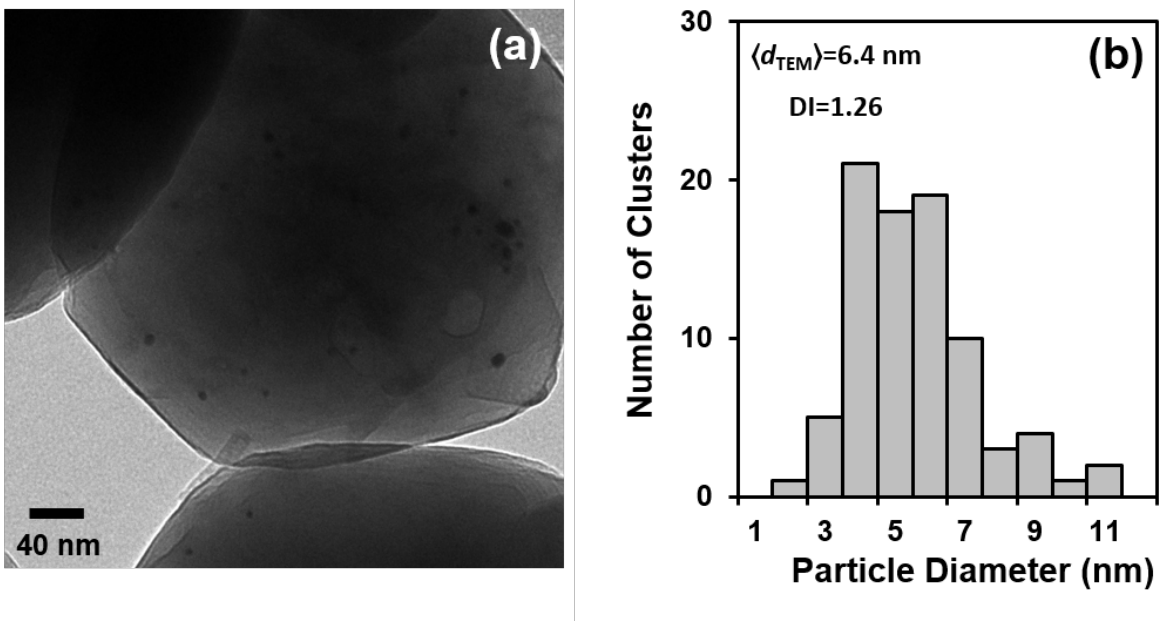

Figure 2.S1. (a) TEM micrograph and (b) Au cluster diameter distribution for AuNaLTA synthesized hydrothermally with an ethylenediamine ligated Au^{3+} complex

2.S2. Plasmon resonance in Au/SiO_2 catalysts treated in air only

Treatment of the as-synthesized Au/SiO_2 catalysts (Section 2.2.3) in flowing dry air only at 623 K (0.033 K s^{-1}) for 2 h results in reduction of the ligated Au^{3+} cations dispersed on the support, as evidenced by the presence of an LSPR band in the treated sample's UV-Vis spectrum (Fig. 2.S2).

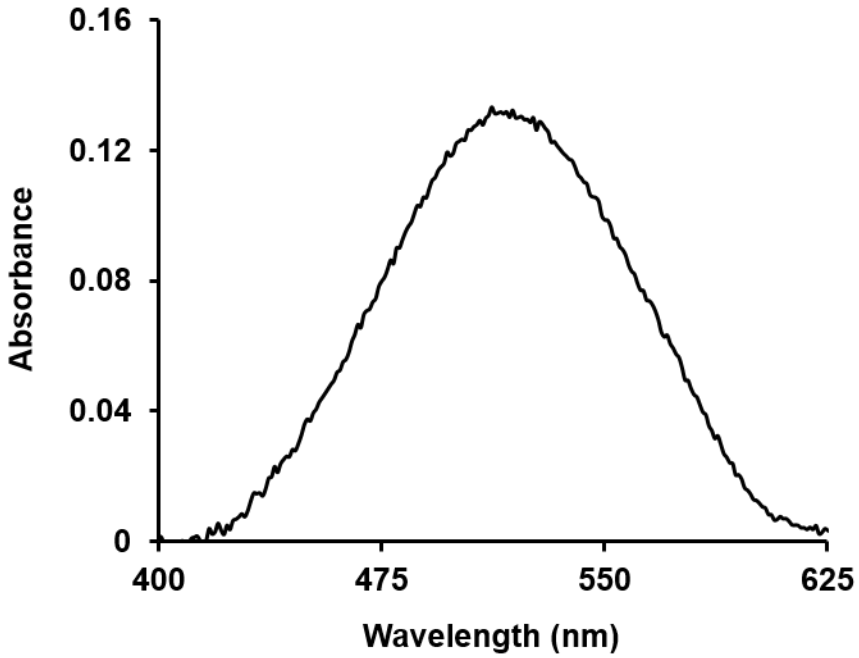

Figure 2.S2. LSPR band exhibited by Au/SiO_2 samples post-synthetically treated in flowing dry air (1.67 $cm^3\ g^{-1}\ s^{-1}$) at 623 K (0.033 K s^{-1}) for 2 h.

2.S3. Evolution of the LSPR band of AuNaLTA during treatment with H_2 alone

Heating AuNaLTA in pure H_2 without preceding treatment in air caused increases in the LSPR band intensity which closely resemble those observed in the AuNaLTA sample that was treated in air at 623 K prior to H_2 treatment (Fig. 2.S3).

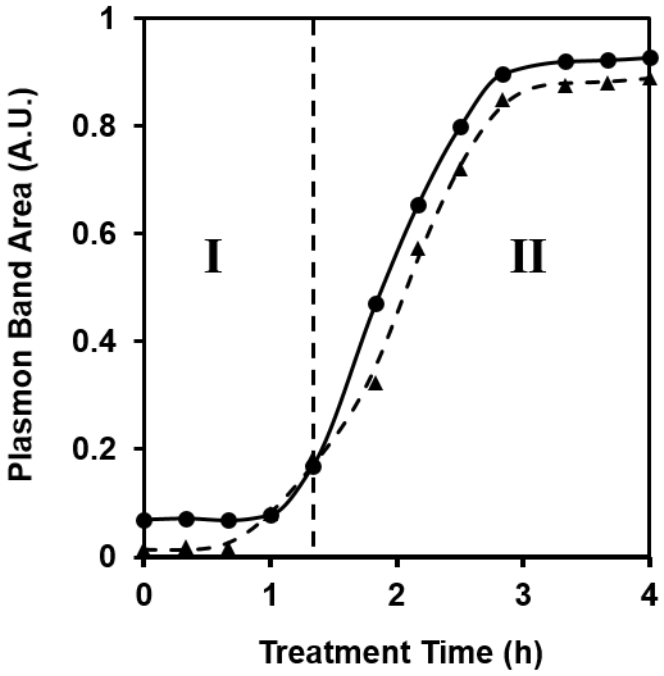

Figure 2.S3. Evolution of the 1.1% wt. AuNaLTA LSPR band integrated intensity in flowing pure H_2 (1.67 cm^3 g^{-1} s^{-1}) under (I): 240 K h^{-1} ramp to 623 K and (II): 623 K. The dashed line represents AuNaLTA treated in H_2 alone without preceding air treatment. The solid line represents AuNaLTA which was treated in flowing dry air (1.67 cm^3 g^{-1} s^{-1}) at 623 K (120 K h^{-1} ramp) for 2 h prior to H_2 treatment.

2.S4. Plasmon resonance in AuNaLTA treated in air only

The as-synthesized 1.1% wt. AuNaLTA exhibited an LSPR band in its UV-Vis spectrum (Fig. S4) following treatment in flowing dry air only at 723 K (1.67 cm^3 g^{-1}; 0.067 K s^{-1}) for 2 h, indicating that sufficiently high temperatures will cause reduction of the embedded Au^{3+} cations in air despite the relative stability provided by the attached mercaptosilane ligands.

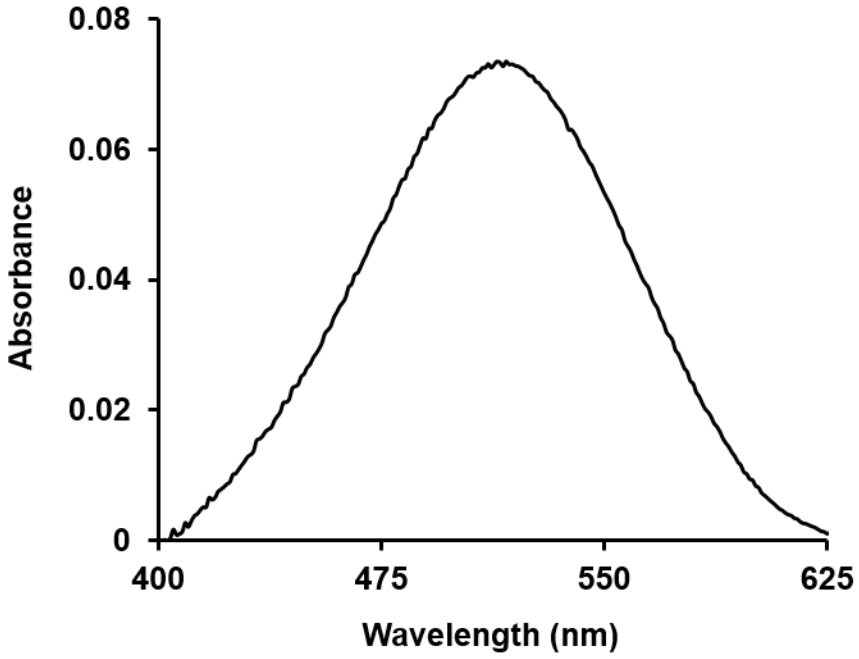

Figure 2.S4. LSPR band exhibited by 1.1% wt. AuNaLTA post-synthetically treated in flowing dry air (1.67 cm^3 g^{-1} s^{-1}) at 723 K (0.033 K s^{-1}) for 2 h.

2.S5. Calculating the fraction of α cages occupied by Au clusters in LTA samples

The fraction of α cages in NaLTA occupied by Au particles (Z) was calculated assuming spherical clusters using

$$Z = \frac{M \times L}{\frac{4/3 \times (d_{TEM}/2)^3 \times \rho}{\frac{M \times (1-L)}{M_{LTA}} \times N_A}} \qquad (S1)$$

where L is the metal loading, M is the weight of the AuNaLTA sample, ρ is the mass density of Au (19.32 g cm^{-3}), N_A is Avogadro's constant, d_{TEM} is the surface-averaged cluster diameter, and M_{LTA} is the molecular weight (17,520 g mol^{-1}) of an ideal LTA lattice ($[Na_{12}^{+}(H_2O)_{27}]_8[Al_{12}Si_{12}O_{46}]_8$) containing one α cage [S1].

2.S6. Au particle size distributions in AuNaMFI following ramped heating in air

Treating AuNaMFI in air with simple ramped heating procedures led to larger Au clusters than those formed by the more sophisticated procedure described in Section 2.2.2.2. Treatment of as-synthesized AuNaMFI (1.9% wt.) in 1.67 cm^3 g^{-1} s^{-1} of flowing dry air from ambient temperature to 723 K (0.033 K s^{-1}) for 3 h led to the formation of relatively large Au particles (3.2 nm; DI 1.12) as measured by TEM micrographs (Fig. 2.S5). Applying an analogous treatment procedure with slower temperature ramping (0.016 K s^{-1}) led to slightly smaller particles with surface-averaged Au cluster diameter of 3.0 nm and DI of 1.09 (Fig. 2.S6).

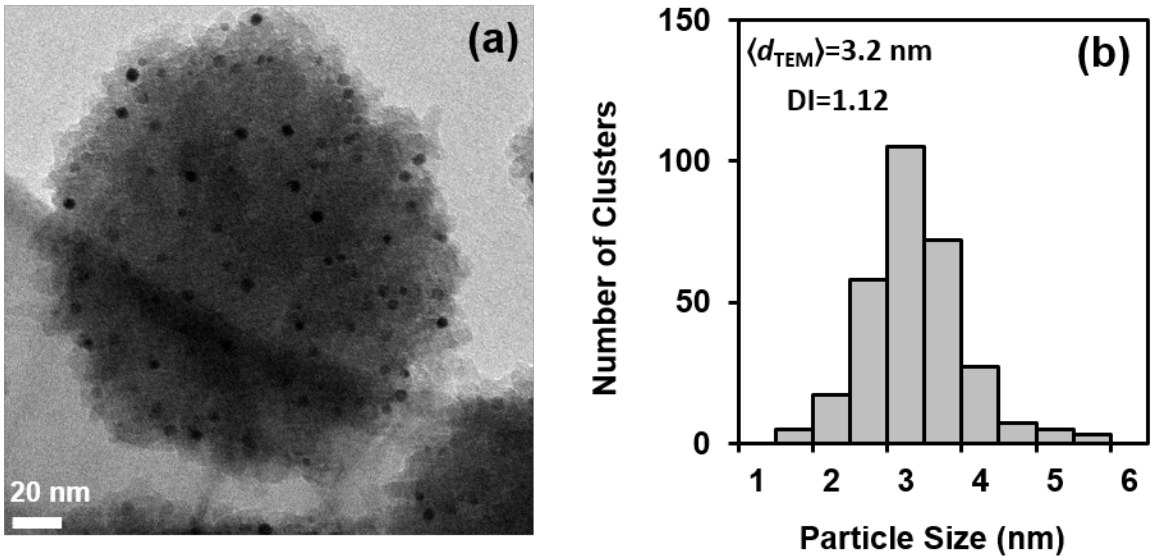

Figure 2.S5. (a) TEM micrograph and (b) Au cluster diameter distribution for AuNaMFI (1.9% wt.) treated in flowing dry air (1.67 cm^3 g^{-1} s^{-1}) at 723 K (0.033 K s^{-1}) for 3 h.

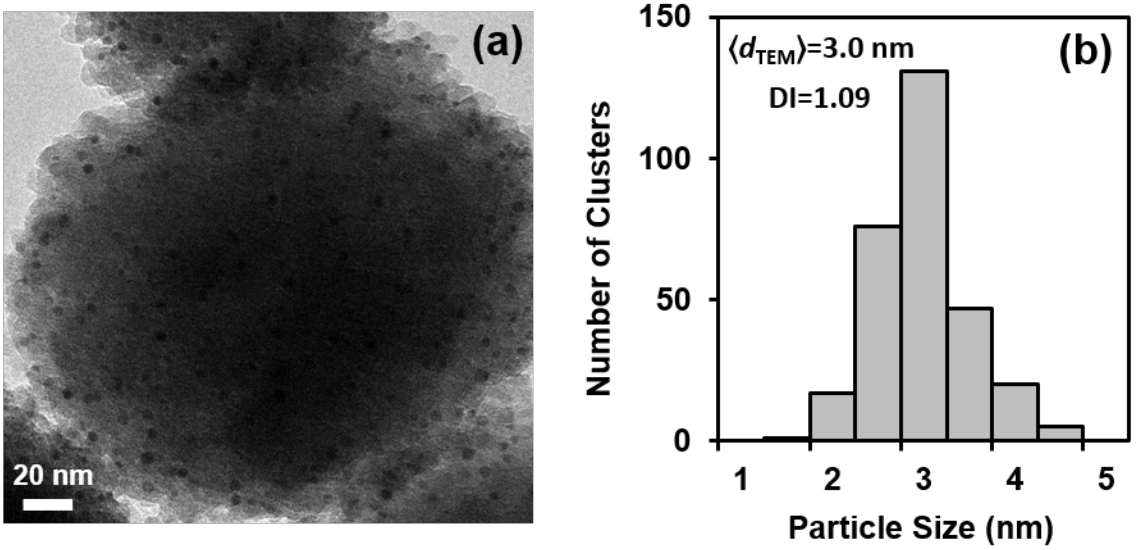

Figure 2.S6. (a) TEM micrograph and (b) Au cluster diameter distribution for AuNaMFI (1.9% wt.) treated in flowing dry air (1.67 cm^3 g^{-1} s^{-1}) at 723 K (0.016 K s^{-1}) for 3 h.

2.S7. X-Ray diffractograms of 6% wt. AuNaLTA and 8% wt. AuNaMFI

The synthesis of 6% wt. AuNaLTA and 8% wt. AuNaMFI using the protocols described in Sections 2.2.2.1 and 2.2.2.2, respectively, resulted in amorphous solid materials rather than the intended zeolite structures (Fig. 2.S7).

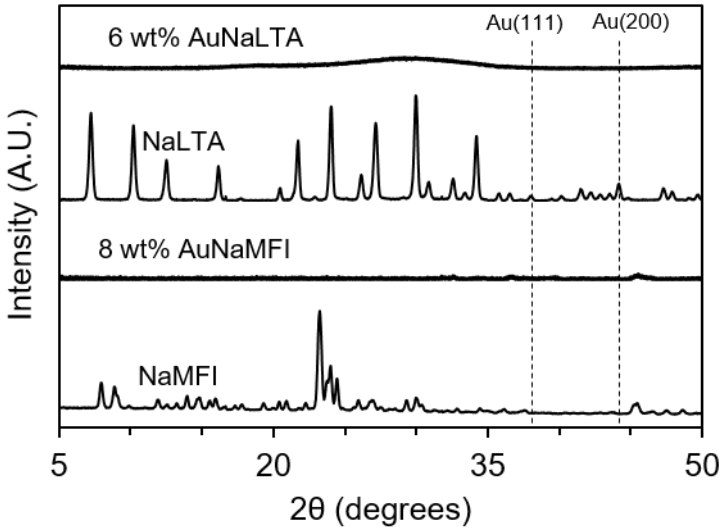

Figure 2.S7. XRD patterns of 6% wt. AuNaLTA, 8% wt. AuNaMFI, and reference AuNaLTA and AuNaMFI samples.

2.S8. Size of Au clusters in AuNaLTA and AuNaMFI following heating in H_2

The temperature range over which Au cluster sintering becomes significant in AuNaLTA and AuNaMFI (>823 K) was the same regardless of whether they were heated in air or pure H_2. Table 2.S1 shows the TEM-derived surface-averaged Au cluster sizes and their DI values in 1.1% wt. AuNaLTA and 1.9% wt. AuNaMFI (synthesized and treated as described in Sections 2.2.2.1 and 2.2.2.2, respectively) following treatment in flowing pure H_2 (1.67 cm^3 g^{-1} s^{-1}, 5 h) at temperatures in the range 673-873 K.

Table 2.S1. Au cluster diameters and dispersity indexes in 1.1% wt. AuNaLTA and 1.9% wt. AuNaMFI following treatment in 1.67 cm^3 g^{-1} s^{-1} of pure flowing H_2 for 5 h at temperatures between 673-873 K

AuNaLTA			AuNaMFI		
Treatment Temperature (K)	Au cluster diameter $\langle d_{TEM} \rangle$ (nm)	DI	Treatment Temperature (K)	Au cluster diameter $\langle d_{TEM} \rangle$ (nm)	DI
673	1.3	1.07	673	2.0	1.06
723	1.3	1.09	723	2.0	1.06
773	1.3	1.10	773	2.1	1.08
823	1.9	1.23	823	2.5	1.18
873	3.3	1.61	873	3.0	1.46

2.S9. CO IR spectra of AuCaLTA and AuNaLTA, and observation of coverage dependent redshift

The Ca^{2+} counterions in the AuCaLTA sample reversibly bind to CO at the temperatures examined in this study, resulting in an intense absorption band at 2177 cm^{-1}. To focus on the CO adsorbed onto Au sites, this contribution to the AuCaLTA spectrum was subtracted using gold-free CaLTA synthesized hydrothermally. Bands associated with gas phase CO were similarly subtracted. IR spectra of CaLTA, AuCaLTA before subtraction, and AuCaLTA after subtraction are shown in Figure 2.S8. Also shown is the IR spectrum of AuNaLTA.

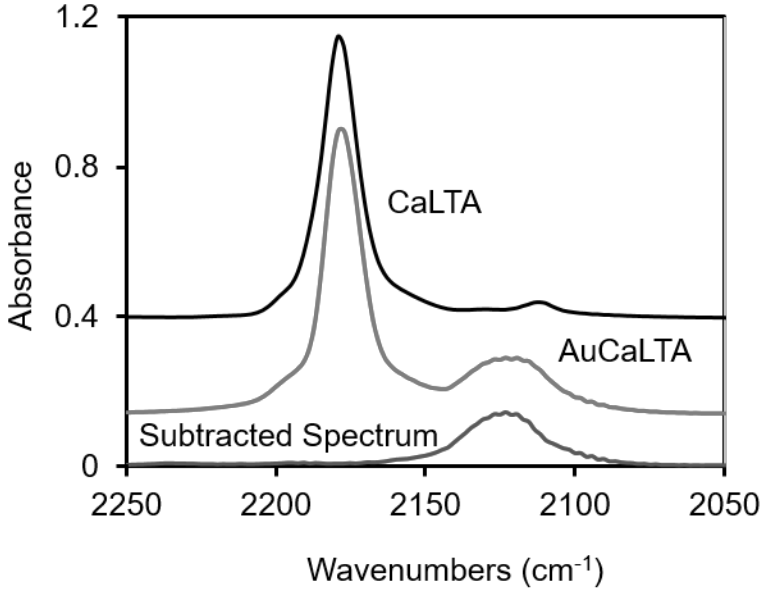

Figure 2.S8. Infrared spectrum of CO adsorbed on Ca^{2+} sites in CaLTA, the spectrum of AuCaLTA prior to subtraction of the Ca^{2+}-CO component, and the subtracted spectrum. Spectra are shown without normalization by the number of surface Au atoms. Spectra were collected at 263 K (1.0 kPa CO, 99.0 kPa He) after flowing H_2 pretreatment of the samples (573 K, 20 kPa H_2, 80 kPa He, 1 h).

AuNaLTA samples were exchanged with Ca^{2+} before measurement of IR spectra to widen the LTA apertures (0.42 nm NaLTA; 0.50 nm CaLTA) and improve the rate of CO diffusion into the zeolite interior. Au-CO bands in AuNaLTA samples collected after 0.25 h of exposure to CO were weak in intensity relative to those collected on AuCaLTA or Au/SiO_2 samples. We attribute this weaker intensity to significantly slower rates of diffusion of guest molecules in NaLTA compared to CaLTA [S2,S3], an effect that dramatically increases the time required for complete CO sorption into the zeolite voids [S2]. Such kinetic limitations in guest diffusion are particularly pronounced at the sub-ambient temperature (263 K) of the IR cell. Ca^{2+}-CO bands in AuCaLTA and Au-CO bands in AuCaLTA and AuNaMFI reached their maximum intensity following 0.25 h of exposure to CO at most, after which the reported spectra were collected.

We also examined the IR spectra of CO adsorbed on Au at a variety of pressures to examine the red shift that occurs as coverage is increased, which allows qualitative understanding of the degree of Au site saturation. Figure S9 shows the IR spectra of CO adsorbed on Au/SiO_2 over 0.1-1 kPa and the associated red shift. The magnitude of the shift was similar for all Au catalyst samples examined.

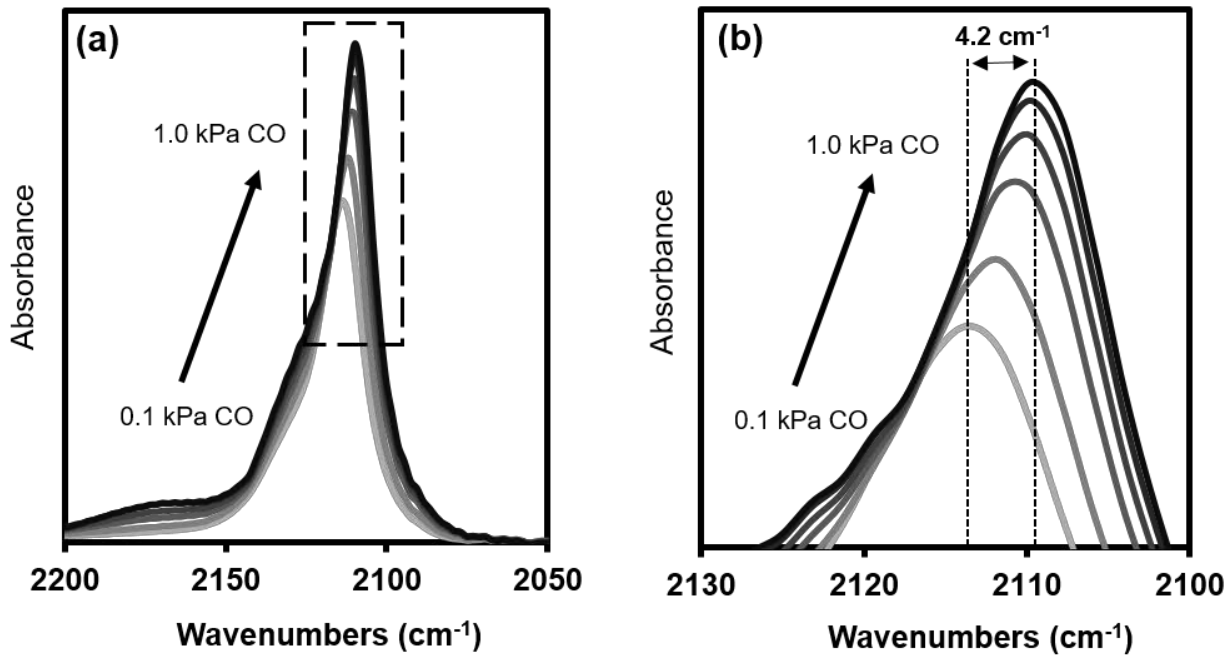

Figure 2.S9. Infrared spectra of CO adsorbed on Au/SiO_2 at 263 K over the range 0.1-1 kPa in balancing He to 100 kPa, and following H_2 pretreatment (573 K, 20 kPa H_2, 80 kPa He). Figure (a) demonstrates the evolution of the entire CO absorption band as the CO pressure is increased while (b) is an inset of (a) which emphasizes the frequency shift.

2.S10. Effect of calcium ion exchanges on the Oxidative Dehydrogenation (ODH) turnover rate on AuCaLTA catalysts

To demonstrate that the AuCaLTA catalysts operate in the diffusion limited regime for the conditions considered here, we measured ethanol ODH turnover rates on AuCaLTA catalysts which were partially exchanged with calcium ions (Fig. 2.S10). We used the number of Ca^{2+} exchange procedures performed on the AuNaLTA catalysts as a proxy for the degree of calcium ion exchange, where one exchange procedure entails a single wash in 1 M $CaCl_2$ and subsequent filtration (as detailed in Section 2.2.2.1). More than 10 exchange procedures did not result in further changes in the measured ODH turnover rate.

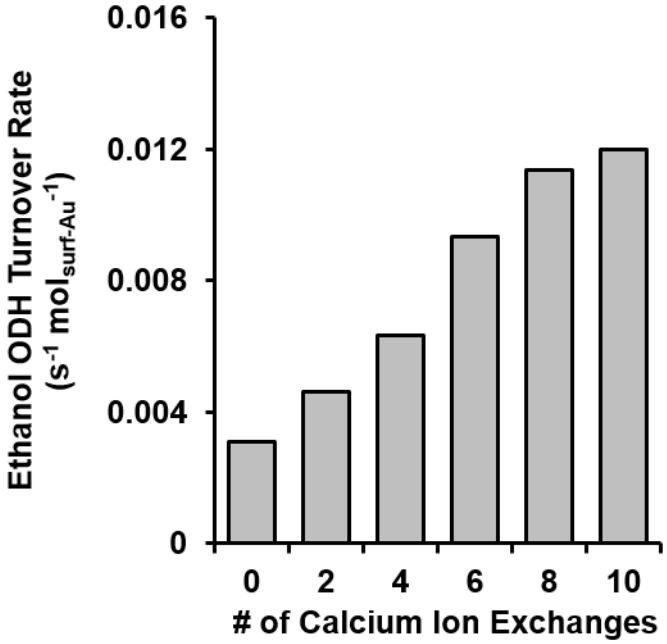

Figure 2.S10. Ethanol ODH (4 kPa ethanol, 9 kPa O_2, 0.5 kPa H_2O, balance He at 393 K) turnover rates on AuNaLTA following a prescribed number of calcium ion exchange procedures, where one exchange involves agitation of the catalyst for 8 hours at ambient temperature in $CaCl_2$ solution (1 g catalyst per 100 cm^3 of 1 M $CaCl_2$) followed by filtration and washing in deionized water (1500 cm^3 g^{-1}).

2.S11. Calculation of the volumetric density of Au surface atoms in AuCaLTA

The volumetric density of surface Au atoms in AuCaLTA ($\rho_{\text{surf-Au}}$) was estimated in units of $1/1000\text{Å}^3$ using

$$\rho_{\text{surf-Au}} = \frac{L \times FD \times M_{LTA} \times D}{192 \times M_{Au}} \qquad (S2)$$

where L is the Au loading of the sample, FD is the framework density of LTA (12.9 $\text{T}/1000\text{Å}^3$, where T=Si, Al) [S4], D is the Au cluster dispersion, M_{Au} is the molecular weight of Au (197 g mol^{-1}), and M_{LTA} is the molecular weight (16,976 g mol^{-1}) of an ideal CaLTA lattice $\left(\left[\text{Ca}_6^{2+}(\text{H}_2\text{O})_{27}\right]_8[\text{Al}_{12}\text{Si}_{12}\text{O}_{46}]_8\right)$ containing one α cage.

References

[S1] Wu, Z.; Goel, S.; Choi, M.; Iglesia, E. *J. Catal.*, **2014**, *311*, 458.
[S2] Onyestyák, G.; Ötvös, Z.; Valyon, J. In *Zeolites and Related Materials: Trends, Targets and Challenges*: Proceedings of the 4th International FEZA Conference, Paris, France, Sept 2-6, 2008; Gédéon, A., Massiani, P., Babonneau, F., Eds.; Elsevier: Amsterdam, 2008.
[S3] Yucel, H.; Ruthven, D.M.; *J. Colloid Interface Sci.*, **1980**, *74*, 186.
[S4] Baerlocher, C.; McCusker, L. B. Database of Zeolite Structures: http://www.iza-structure.org/databases/.

Chapter 3

Synthesis of Stable Monodisperse AuPd, AuPt, and PdPt Bimetallic Clusters Encapsulated within LTA-Zeolites

Abstract

AuPd, AuPt, and PdPt bimetallic clusters uniform in size and composition were prepared using hydrothermal assembly of LTA crystals around cationic precursors stabilized by protecting mercaptosilane ligands. The sulfur moiety in these bifunctional ligands forms adducts that prevent premature reduction or precipitation of metal precursors during crystallization. The silane groups can form bridges with silicate oligomers as they form, thus enforcing homogeneous distributions of precursors throughout crystals and ensuring that subsequent reductive treatments lead to the two elements residing within small and nearly monodisperse clusters. Their confinement within LTA crystals, evident from microscopy and titrations with large poisons, renders them stable against sintering during thermal treatments at high temperatures (820-870 K). Infrared spectra of chemisorbed CO show that bimetallic surfaces are free of synthetic debris after thermal treatments; these spectra also indicate that intracluster segregation occurs upon CO chemisorption, a demonstration of the presence of the two elements within the same clusters. The number and type of atoms coordinated to a given absorber atom, determined from the fine structure in X-ray absorption spectra, are consistent with bimetallic structures of uniform composition. The rates of ethanol oxidative dehydrogenation on these bimetallic clusters were essentially unaffected by exposure to dibenzothiophene, a large poison that suppresses rates on unconfined clusters, indicating that bimetallic clusters are protected within the confines of LTA crystals. These synthetic protocols seem generally applicable to other bimetallic compositions and zeolites, for which the monometallic counterparts have been successfully encapsulated within several microporous frameworks using ligand-stabilized precursors and hydrothermal crystallization methods.

3.1 Introduction

Bimetallic nanoparticles are useful as catalysts because of the unique electronic and structural features conferred by atomic mixing of two or more elements at the nanoscale. Such features, in turn, are consequential for turnover rates and selectivities in reactions as diverse as CO oxidation [1], alkane dehydrogenation [2], and NO_x reduction [3]. These bimetallic synergies also bring ancillary benefits [4]; a second metal can assist the reduction of another one [5], inhibit sintering during thermal treatments [6], or weaken the effects of site blocking by S-atoms or other titrants [7]. These consequences may reflect ligand effects that cause one element to influence the electronic properties of another one [8] or ensemble effects caused by the dilution of monometallic domains [9]. The dissection of such effects into their causative components requires the synthesis of particles uniform in composition and size [9], an elusive objective because of the dearth of effective and general synthetic strategies.

Sequential adsorption and precipitation or co-impregnation of two metal salts onto mesoporous scaffolds [10] does not consistently place the component metals in atomic proximity

[10], a challenge that can be addressed by sequential grafting of organometallic precursors onto supports [10]. Such grafting enforces metal-metal binding through covalent attachments between the first and second precursor deposited. The availability of precursors that prefer mutual interactions over those with the support limits the scope of such protocols, which often lead to the concurrent formation of monometallic clusters of the second precursor used in the sequence [10]. Galvanic displacement and electroless deposition, in contrast, selectively place a second metal into existing clusters of another metal via redox reactions [11]. Compositional uniformity in these methods requires seed clusters uniform in size and strategies to minimize homogeneous nucleation of the second component using solvents as reductants [9]. Colloidal synthesis methods involving the reduction of precursors in the presence of protecting polymers [11] can also form small clusters uniform in size and composition [9,12]; such uniformity, however, is frequently compromised by thermal treatments essential to deprotect the metal surfaces, as required for their catalytic function [9,11].

The nanometer-sized voids provided by crystalline zeolite frameworks can be used as containers for bimetallic clusters [11]. Their confinement within such voids allows the selection of certain reactants and transition states over others based on molecular size and the protection of active surfaces from large titrants and poisons by exploiting zeolite shape selectivity [13,14]. Confinement is often achieved by the exchange of solvated cationic precursors into the anionic zeolite frameworks [4]. Reductive treatments then form monometallic clusters, and the subsequent exchange and reduction of a second metal can form, in some instances, confined bimetallic clusters that are less prone to sintering than their monometallic counterparts [4]. Inhomogeneous cluster compositions, however, are often observed and such exchange methods require zeolite channels that allow the diffusion of the solvated cationic precursors and their charge-balancing double layer [11,15].

Here, we report an alternate route for the synthesis of small bimetallic clusters, uniform in size and composition, within LTA zeolite crystals, a framework with apertures too small to allow precursor exchange. We illustrate this general synthetic strategy for a range of AuPd, AuPt, and PdPt compositions. In doing so, we extend techniques that use protecting ligands to stabilize metal cation precursors against premature precipitation as colloidal metals of oxyhydroxides at the hydrothermal conditions required to crystallize zeolite frameworks [13,14]. Hydrothermal LTA crystallization in the presence of ligated precursors of two different elements leads to the formation of nearly monodisperse bimetallic clusters (1-2 nm); these clusters expose surfaces free of synthetic debris after sequential thermal treatments in O_2 and H_2, without compromising LTA crystallinity. The bimetallic nature of the clusters was shown by X-ray absorption spectroscopy and confirmed by the infrared spectra of chemisorbed CO. The protecting 3-mercaptopropyl-trimethoxysilane ligands prevent precipitation, reduction, and coalescence of the metals before the formation of LTA frameworks. These ligands also form siloxane bridges with silicate oligomers to enforce confinement and uniform placement of precursors throughout zeolite crystals, thus ensuring bimetallic mixing and the nucleation of small confined clusters, even after thermal treatments that remove the ligands and their S-atoms. The retention of these clusters within zeolite crystals was demonstrated from ethanol oxidation rates on samples exposed to dibenzothiophene, which would irreversibly poison any unconfined clusters [13].

3.2 Methods

3.2.1 Reagents

$HAuCl_4 \cdot 3H_2O$ (99.999%, Sigma-Aldrich), $Pd(NH_3)_4(NO_3)_2$ (99.99%, Sigma-Aldrich), $Pd(NH_3)_4Cl_2$ (99.99%, Sigma-Aldrich), H_2PtCl_6 (8% wt. in H_2O, Sigma-Aldrich), 3-mercaptopropyl-trimethoxysilane (95%, Sigma-Aldrich), NaOH (99.99%, Sigma-Aldrich), Ludox AS-30 colloidal silica (30% wt. suspension in H_2O, Sigma-Aldrich), $NaAlO_2$ (53% Al_2O_3, 42.5% Na_2O, Riedel-de Haën), mesoporous SiO_2 (Davisil, grade 646, surface area: 294 m^2 g^{-1}), fumed SiO_2 (Cab-O-Sil, HS-5, 310 m^2 g^{-1}), $CaCl_2 \cdot 2H_2O$ (EMD Millipore), acetone (99.9%, Sigma-Aldrich), ethanol (99.9%, Sigma-Aldrich), ethylenediamine (98%, Sigma-Aldrich), dibenzothiophene (98%, Sigma-Aldrich), air (extra dry; 99.999%, Praxair), H_2 (99.999%, Praxair), He (99.999%, Praxair), Ar (99.999%, Praxair), 25% O_2/He (99.999%, Praxair), and 1.0% CO/He (99.999%, Praxair) were used as received.

3.2.2 Materials Synthesis

3.2.2.1 Synthesis of Au, Pd, Pt and AuPd, AuPt, and PdPt clusters within LTA crystals

Preparation procedures for bimetallic metal-encapsulated Na-LTA zeolites (M_1M_2NaLTA, where M_1 and M_2 are Au, Pd, or Pt) were adapted from hydrothermal synthesis protocols for monometallic systems [13,14]. Similar synthetic protocols were used for monometallic (AuNaLTA, PdNaLTA, PtNaLTA) and bimetallic (Au_nPd_{100-n}NaLTA, Au_nPt_{100-n}NaLTA, Pd_nPt_{100-n}NaLTA; n is the atomic percentage of the first element) samples. For example, $Au_{50}Pd_{50}$NaLTA was prepared by dissolving 3-mercaptopropyl-trimethoxysilane (0.96 g) and NaOH (4.8 g) in deionized H_2O (17.9 MΩ resistance; 18 cm^3) in an open polypropylene bottle (125 cm^3) using magnetic stirring (6.7 Hz; 8 h). Then, aqueous $HAuCl_4 \cdot 3H_2O$ (0.156 g in 9 cm^3 deionized H_2O) and $Pd(NH_3)_4(NO_3)_2$ (0.118 g in 9 cm^3 deionized H_2O) solutions were concurrently added dropwise to the ligand-NaOH solution over 0.5 h while stirring (6.7 Hz). Colloidal silica (10.67 g, Ludox AS-30) was then added, and the polypropylene bottle was capped and heated to 353 K for 0.5 h with continuous agitation (6.7 Hz). The bottle and its contents were then cooled to ambient temperature, and an aqueous solution of $NaAlO_2$ (6.0 g in 18 cm^3 deionized H_2O) was added dropwise while stirring (6.7 Hz, 2 h). This procedure formed a homogeneous synthesis gel with a molar composition of 1.7 SiO_2/1 Al_2O_3/3.2 Na_2O/110 H_2O/0.013 Au/0.013 Pd/0.156 ligand, which was heated to 373 K while stirring (6.7 Hz, 12 h) to form $Au_{50}Pd_{50}$NaLTA.

The solids formed were filtered (Pyrex 3606 fritted funnel, 4-5.5 μm), washed with deionized H_2O until the rinse liquids reached a pH of 7-8, and treated in ambient air within a convection oven at 373 K for 8 h. They were then heated in flowing dry air (1.67 cm^3 g^{-1} s^{-1}) from ambient temperature to 623 K (at 0.033 K s^{-1}) and held for 2 h, cooled to ambient temperature, and then heated to 623 K (at 0.033 K s^{-1}) in flowing H_2 (1.67 cm^3 g^{-1} s^{-1}) and held for 2 h. A final heating procedure in air (1.67 cm^3 g^{-1} s^{-1}) at 723 K (0.033 K s^{-1}) was then conducted for 2 h.

Bimetallic compositions were adjusted by varying the ratio of cationic precursors ($HAuCl_4 \cdot 3H_2O$, $Pd(NH_3)_4(NO_3)_2$, H_2PtCl_6) in the gel, while maintaining the same nominal 1% wt. metal loading as in the monometallic samples. Six moles of 3-mercaptopropyl-trimethoxysilane

were used per mole of metal for all compositions. The metal contents in all samples were measured by inductively coupled plasma optical emission spectroscopy (ICP-OES) using a Perkin Elmer 5300 DV optical emission ICP analyzer.

Metal-NaLTA samples (0.42 nm apertures, [13]) were exchanged with Ca^{2+} ions after O_2 and H_2 treatments to convert them to CaLTA (0.50 nm apertures, [14]) before CO chemisorption and infrared studies (Section 3.2.3.3). Na^+ was exchanged for Ca^{2+} to widen the LTA apertures and allow more rapid diffusion of CO into the interior of the crystallites [14]. The exchange was performed by adding metal-NaLTA samples (1-5 g) to an aqueous solution of $CaCl_2 \cdot 2H_2O$ (1M; 100 cm^3/g zeolite) and stirring (6.7 Hz. 8 h) at ambient temperature. This procedure was repeated ten times to ensure full Ca^{2+} exchange [14]. The solids were finally filtered and washed with deionized water (1500 cm^3 g^{-1}) and treated in a convection oven at 373 K for 12 h before their use in infrared studies.

3.2.2.2 Synthesis of Au, Pd, and Pt clusters on mesoporous SiO_2

Au, Pd, and Pt clusters dispersed on mesoporous SiO_2 were synthesized and used as oxidative dehydrogenation (ODH) catalysts (Section 3.2.3.5, 3.3.5) for comparison with the bimetallic clusters supported by zeolites. Pd/SiO_2 and Pt/SiO_2 catalysts were prepared with incipient wetness impregnation using aqueous solutions of $Pd(NH_3)_4Cl_2$ and H_2PtCl_6, respectively. These silica-supported clusters were treated in ambient air, flowing dry air, and flowing H_2 using the same procedures as the metal-zeolite samples (Section 3.2.2.1).

Au clusters dispersed on SiO_2 (Cab-O-Sil, HS-5, 310 m^2 g^{-1}) were prepared using an $Au(en)_2Cl_3$ (en=ethylenediamine) complex previously shown to lead to small clusters [14,16]. Experimental procedures detailing the synthesis of the $Au(en)_2Cl_3$ complex and Au/SiO_2 can be found in the Supporting Information (SI) (Section 3.S1).

3.2.3 Characterization of zeolite structures and embedded metal clusters

3.2.3.1 Powder X-Ray diffraction

X-Ray diffractograms (XRD) were used to confirm LTA zeolite crystallinity and the absence of large (>10 nm) metal clusters. Diffractograms were measured with a D8 Discover GADDS Powder Diffractometer with Cu-Kα radiation (λ=0.15418 nm, 40 kV, 40 mA) at 2θ values from 5-50° and a scan rate of 0.00625 degrees s^{-1}. The samples were ground into fine powders and placed and leveled on quartz slides for these measurements.

3.2.3.2 Transmission electron microscopy

Transmission electron micrographs (TEM) were collected with a Philips/FEI Technai 12 microscope at 120 kV by dispersing finely ground powders in acetone and then onto holey carbon films supported on 400 mesh copper grids (Ted Pella Inc.). Metal cluster size distributions were measured from >300 particles for each sample, and used to determine surface-averaged cluster diameters $\langle d_{TEM} \rangle$ [13]:

$$\langle d_{\mathrm{TEM}} \rangle = \frac{\sum n_i d_i^3}{\sum n_i d_i^2} \qquad (1)$$

where n_i is the number of clusters with diameter d_i. These size distributions were further used to calculate dispersity index (DI) values, which are given by the ratio of the surface-averaged ($\langle d_{\mathrm{TEM}} \rangle$) to the number-averaged ($\langle d_n \rangle$) diameter [13]:

$$\mathrm{DI} = \frac{\langle d_{\mathrm{TEM}} \rangle}{\langle d_n \rangle} = \frac{\left(\frac{\sum n_i d_i^3}{\sum n_i d_i^2}\right)}{\left(\frac{\sum n_i d_i}{\sum n_i}\right)} \qquad (2)$$

These DI values provide the accepted metric of size uniformity, with values smaller than 1.5 taken as evidence of excellent monodispersity [17]; they are seldom reported, in spite of IUPAC guidance [9], leading us to also report here standard deviations as a less rigorous measure of size uniformity.

Metal dispersions (*D*), defined as the fraction of metal atoms exposed at cluster surfaces, were estimated from $\langle d_{\mathrm{TEM}} \rangle$ [17]:

$$D = 6\frac{\bar{v}_m / \bar{a}_m}{\langle d_{\mathrm{TEM}} \rangle} \qquad (3)$$

where $\bar{v}_m$ is the effective bulk atomic density of the bimetallic samples, estimated as the composition-weighted average of the v_m values for pure Au (16.49×10^{-3} nm^3), Pd (14.70×10^{-3} nm^3), or Pt (15.10×10^{-3} nm^3) [17]. The value of $\bar{a}_m$, the effective area occupied by a metal atom on polycrystalline surfaces, was also calculated as a composition-weighted mean from the pure component values (Au: 8.75×10^{-2} nm^2, Pd: 7.93×10^{-2} nm^2, Pt: 8.07×10^{-2} nm^2) [17].

3.2.3.3 Infrared spectra of chemisorbed CO on metal-LTA zeolites

Infrared (IR) spectra of CO chemisorbed on metal-CaLTA wafers (40 mg cm^{-2}) were used to probe the surface composition of bimetallic clusters. IR spectra were acquired using a Thermo Nicolet 8700 spectrometer equipped with an in situ flow cell. All sample wafers were first heated in flowing 20% H_2/He mixtures (42.0 cm^3 g^{-1} s^{-1}) from ambient temperature to 573 K (0.033 K s^{-1}) for 1 h. Pd_nPt_{100-n}CaLTA samples were then cooled rapidly in He flow (42.0 cm^3 g^{-1} s^{-1}) to 313 K (-0.17 K s^{-1}), and exposed to flowing CO/He (42.0 cm^3 g^{-1} s^{-1}; 1.0 kPa CO) before collecting IR spectra. Au_nPd_{100-n}CaLTA samples were instead cooled to 278 K (-0.17 K s^{-1}) in flowing He (42.0 cm^3 g^{-1} s^{-1}) after the H_2/He treatment at 573 K, before collecting spectra in flowing CO/He (42.0 cm^3 g^{-1} s^{-1}; 1.0 kPa CO). The Au_nPd_{100-n}CaLTA samples were then heated in this flowing CO/He to 353 K (0.033 K s^{-1}) for 0.5 h, and then cooled back to 278 K (-0.17 K s^{-1}) under continuous CO flow for a second spectra to be collected. Au_nPt_{100-n}CaLTA samples were treated analogously to Au_nPd_{100-n}CaLTA, except they were cooled to 263 K instead of 278 K. The AuPd and AuPt bimetallic samples were subjected to this intermittent period of CO exposure and heating with the

intent of inducing changes in the surface compositions of alloyed clusters (Section 3.3.3). Spectral contributions from CO(g) and Ca^{2+}-CO complexes [14] were subtracted from all reported spectra.

3.2.3.4 X-Ray absorption spectroscopy and analysis of the extended X-ray absorption fine structure

X-Ray absorption spectra (XAS) were acquired in transmission mode at the Au-L_3 edge (11,919 eV) [18], the Pd-K edge (24,350 eV) [18], and the Pt-L_3 edge (11,564 eV) [18] using the XDS and XAFS-2 beamlines of the LNLS (Laboratório Nacional do Luz Síncrotron, Campinas, Brazil). Two monochromators were used: a Si(311) crystal for the Pd-K edge and a Si(111) crystal for the Pt-L_3 and Au-L_3 edges. Intensities were measured using three sequential ionization chambers filled with mixtures of N_2 and Ar at ambient temperature and 1 bar of pressure. Photon energies were calibrated using a thin metal film (Au, Pd, or Pt) placed between the second and third ionization chambers. XAS spectra were measured for $Au_{50}Pd_{50}$NaLTA and $Pd_{65}Pt_{35}$NaLTA samples. Spectra were collected at the absorption edge for each metal present in a range between 200 eV before and 1000 eV after each edge. The samples (0.1 g each) were treated in 10% H_2/Ar flow (1.67 $cm^3\ g^{-1}\ s^{-1}$) at 573 K (0.033 K s^{-1}) for 1 h and cooled to ambient temperature under Ar flow (1.67 $cm^3\ g^{-1}\ s^{-1}$). They were then transferred in an Ar blanket to a cell sealed hermetically with Kapton® windows. The samples were stored in this cell for ~10 h, after which the XAS spectra were collected at ambient temperature.

The extended X-Ray absorption fine structure (EXAFS) data were analyzed using the IFEFFIT package (Athena, Artemis) [19]. The coordination numbers (*N*), interatomic distances (*D*), and Debye-Waller factors (σ^2) were obtained from nonlinear regressions of the Fourier transformed data implemented in Artemis [19]. Simulated amplitudes and phase shifts for all single scattering paths were obtained using the FEFF code [20]. These modeled scattering paths were calculated using crystallographic structures of either monometallic lattices (for Au-Au, Pd-Pd, and Pt-Pt paths) or mixed phase lattices (for Pd-Au and Pd-Pt paths) [21-23]. EXAFS data extracted from bimetallic samples were fit simultaneously at both metal edges, ensuring consistency in the *D* and σ^2 values. Single scattering by O and S atoms, with theoretical amplitudes and phases calculated from metal oxide (PdO, PtO) [24,25] or metal sulfide (PdS, PtS, Au_2S_3) [26-28] crystal structures, were also included in the fits to determine if metal oxide or metal sulfide species were present. Passive reduction factors [19] for each metal (Au: 0.95, Pd: 0.83, Pt: 0.96) were obtained from fits to the EXAFS spectra of the metal foils by constraining the average coordination number of the first shell to 12.

3.2.3.5 Catalytic assessment of reactivity and encapsulation

Ethanol oxidative dehydrogenation (ODH) turnover rates were measured on catalyst powders first diluted 10-fold by mass with fumed SiO_2 (Cab-O-Sil, HS-5, 310 $m^2\ g^{-1}$) and then pressed into pellets and sieved to retain 180-250 μm aggregates. These diluted samples were then mixed with 180-250 μm acid-washed quartz granules (1:1 mass) to prevent any temperature gradients caused by exothermic ODH reactions. Catalysts were placed on a porous quartz frit within a quartz tube (10 mm O.D.). Samples were heated in 20% O_2/He (1.67 $cm^3\ g^{-1}\ s^{-1}$) from ambient temperature to 393 K (at 0.033 K s^{-1}) and held at that temperature for rate measurements. Liquid ethanol and deionized water were vaporized into flowing O_2/He streams at 393 K using

liquid syringe pumps (Cole Parmer, 60061 Series). He and O_2 flow rates were adjusted with mass flow controllers (Porter Instrument) to achieve the desired pressures (4 kPa alkanol, 9 kPa O_2, 87.5 kPa He, and 0.5 kPa H_2O). H_2O forms as an ODH product, and can have a co-catalytic effect; it was therefore added to maintain a constant concentration of all species throughout the catalyst bed, thus ensuring differential conditions. Alkanol conversions were kept below 5% and transfer lines were heated to 393 K to avoid condensation.

Turnover rates are defined as the molar ethanol conversion rates per surface metal atom estimated from the dispersion values defined in Equation 3. Product formation was not detectable on NaLTA, fumed silica, or empty reactors. Turnover rates were extrapolated to the start of each experiment. Effluent concentrations were measured by gas chromatography (Shimadzu GC-2014) using a methyl-silicone capillary column (HP-1; 50 m × 0.32 mm, 1.05 μm film thickness) and a flame ionization detector.

Metal-NaLTA samples were exposed ex-situ to dibenzothiophene (DBT), an organosulfur poison that irreversibly titrates noble metal surfaces [29], before their use in ethanol ODH reactions. Ex-situ treatments exposed metal-NaLTA and metal-SiO_2 samples to DBT dissolved in liquid ethanol (300 cm^3 g^{-1}; DBT/metal molar ratio of 6) at ambient temperature for 4 h with magnetic agitation (6.7 Hz). The samples were then filtered and treated in ambient air at 343 K for 12 h, and used in ethanol ODH reactions at 393 K. Control samples were also prepared through an identical procedure but without DBT and used for ethanol ODH.

Ethanol (0.40 nm kinetic diameter, [13]), but not DBT (0.9 nm, [30]), can diffuse through the apertures of NaLTA (0.42 nm, [13]); thus, the extent of deactivation caused by exposure to DBT provides an assessment of the fraction of metal surfaces that are confined within zeolite crystals and therefore protected from any large molecules present in the extracrystalline fluid [13]. A comparison of rates before and after exposure to DBT on metal-NaLTA and metal-SiO_2 samples would then indicate the fraction of the active surfaces present at extracrystalline locations and thus the selectivity of the encapsulation.

3.3 Results and discussion

3.3.1 Metal content and phase purity of metal-LTA samples

LTA-encapsulated metal nanoparticles were synthesized with Au-Pd compositions (Au_nPd_{100-n}NaLTA), Au-Pt (Au_nPt_{100-n}NaLTA), or Pd-Pt (Pd_nPt_{100-n}NaLTA) and a broad range of atomic ratios and a 1% wt. metal content (nominal; based on amounts of reagents used). The measured elemental compositions reported in Table 3.1 confirm the essentially complete incorporation of the metal precursors into the final product. These data indicate that the ability of the ligands to bind to the metal cations through the S-atoms and to the crystallizing framework through covalent siloxane bridges favor metal incorporation into the solids instead of their retention within the supernatant liquid that is removed by filtration after synthesis.

X-Ray diffractograms of all samples (Fig. 3.1) after thermal treatment in O_2 (623 K) and then H_2 (623 K) (Section 3.2.2) detected the intended LTA crystals (>95% crystallinity; from integrated intensities of the three most intense Na-LTA lines). No diffraction lines for metal phases

(Au, Pd, or Pt) were evident after treatment at 823 K and the LTA crystallinity was unaffected by thermal treatments in O_2 or H_2 even at 823 K. These data show that samples are crystalline, thermally stable, and free of large metal crystallites (>10 nm), which would have been evident in the diffractograms even at 1% wt. metal contents.

3.3.2 Assessment of cluster size distributions and thermal stability

Transmission electron micrographs were used to assess the size and infer the location and thermal stability of the metal structures formed during hydrothermal zeolite crystallization and subsequent thermal treatments in O_2 and H_2 (Section 3.2.2). For the respective monometallic systems (Au, Pd, Pt), previous studies have shown that these synthetic protocols lead to highly dispersed clusters free of synthetic debris and preferentially located within LTA or MFI crystals [13,14]. Metal clusters form via ligand removal and reduction of mononuclear cationic species that migrate within LTA crystals and deposit at locations where nuclei first form [13,14]. Their ultimate size depends on the mobility of these species during their reduction, causing higher H_2 treatment temperatures to form larger clusters [14]. These clusters, incipiently formed by treatments in H_2, are stabilized by the local enclosures provided by the zeolite framework and thus maintain their sizes even after subsequent thermal treatments in O_2 or H_2 at even higher temperatures [13,14]. Figure 3.2 shows electron micrographs and size distributions for the monometallic clusters and for select bimetallic clusters in LTA. Table 3.1 reports TEM-derived surface-averaged cluster diameters ($\langle d_{TEM} \rangle$; Eq. 1) and dispersity indices (DI; Eq. 2) for each of the Au_nPd_{100-n}NaLTA, Au_nPt_{100-n}NaLTA, and Pd_nPt_{100-n}NaLTA samples synthesized by the protocols developed in this study. Similar to their monometallic counterparts, the clusters in these bimetallic samples are located predominantly within the zeolite crystallites, as we independently confirm here (Section 3.3.5) by exploiting shape selectivity conferred by confinement.

Surface-averaged diameters for monometallic samples (AuNaLTA: 2.3 nm, PdNaLTA: 1.6 nm, PtNaLTA: 1.3 nm; Table 3.1) vary inversely with the Tammann temperature [31] of each metal (Au: 668 K, Pd: 914 K, Pt: 1022 K), consistent with an inverse link between cohesive energies and the tendency to form the mobile species that mediate cluster growth. Each bimetallic sample gave a surface-averaged cluster size similar to that of the component with the higher Tammann temperature (e.g. $Au_{50}Pd_{50}$NaLTA: 1.5 nm, $Au_{50}Pt_{50}$NaLTA: 1.4 nm, and $Pd_{65}Pt_{35}$NaLTA: 1.3 nm; Table 3.1), indicating that the more mobile metal atoms are scavenged and rendered less mobile by the higher-melting metal. These bimetallic samples showed size distributions that were both unimodal (Fig. 3.2) and monodisperse (DI: 1.05-1.15; Table 3.1). Bimetallic clusters that are heterogeneously distributed in composition would typically show a broad range of cluster sizes because clusters rich in the less stable species tend to form larger agglomerates [31]. The small cluster diameters and monodisperse size distributions (i.e. DI<1.5) of these bimetallic clusters in LTA zeolites, therefore, suggest the predominant presence of nanoparticles of uniform compositions.

The size and compositional uniformity of clusters in Au-containing samples (AuNaLTA, Au_nPd_{100-n}NaLTA, and Au_nPt_{100-n}NaLTA) was also probed via their UV-visible spectra. Monometallic Au clusters and core-shell structures with Au shells show localized surface plasmon resonance (LSPR, [32]) features at 500-600 nm [9], but monometallic Pt and Pd clusters or mixed Au-Pd and Au-Pt clusters do not [9]. Consequently, an LSPR band diagnoses the presence of Au

clusters larger than the minimum size (2 nm diameter) required for detectable plasmon resonance [32]. AuNaLTA and physical mixtures of AuNaLTA with PdNaLTA or PtNaLTA exhibited LSPR bands, but Au_nPd_{100-n}NaLTA and Au_nPt_{100-n}NaLTA did not (Section 3.S2, SI), confirming the absence of monometallic Au clusters >2 nm in diameter in these bimetallic samples.

Previous studies have shown that the confining environment within LTA crystals inhibits agglomeration of Pt and Pd clusters during thermal treatments in air up to 873 K [13]; monometallic Au clusters in LTA and MFI are similarly stabilized by confinement, but start to sinter at slightly lower temperatures (823 K) than Pt or Pd [14]. The thermal stability of Au, Au-Pt and Au-Pd clusters was examined and compared here to determine whether the addition of Pd or Pt could improve the thermal stability of Au clusters. Such stability was probed with thermal treatments in flowing air to temperatures between 623 K and 873 K (at 0.033 K s^{-1}) for 5 h. TEM-derived surface-averaged cluster diameters ($\langle d_{TEM} \rangle$; Eq. 1) for AuNaLTA, $Au_{50}Pd_{50}$NaLTA, and $Au_{50}Pt_{50}$NaLTA are shown in Figure 3.3 as a function of treatment temperature. Cluster diameters (AuNaLTA: 2.3 nm, $Au_{50}Pd_{50}$NaLTA: 1.5 nm, $Au_{50}Pt_{50}$NaLTA: 1.4 nm) were unaffected by thermal treatments up to 773 K. AuNaLTA sintered significantly after treatment at 873 K (3.8 nm), but bimetallic clusters grew only slightly (to 1.8 nm for $Au_{50}Pd_{50}$ and 1.6 nm for $Au_{50}Pt_{50}$) after similar protocols. In the same manner, the dispersity index (DI; Eq. 2) increased significantly for AuNaLTA (1.07 to 1.62) after treatment at 873 K, but much less for bimetallic clusters ($Au_{50}Pd_{50}$NaLTA: 1.09 to 1.23, $Au_{50}Pt_{50}$NaLTA: 1.09 to 1.17), which remained essentially monodisperse (DI<1.5) [17]. We surmise that the presence of Pd or Pt stabilizes Au species, thus decreasing their mobility at these temperatures and leading to greater size stability than in the case of pure Au clusters. These bimetallic effects, combined with the size stability conferred by confinement within microporous crystals [13,14], led to cluster sizes and thermal stabilities unattainable for metal or bimetallic clusters dispersed on mesoporous supports [13,14].

3.3.3 Infrared evidence for bimetallic clusters and for intracluster atomic mobility

Bimetallic clusters are typically described by heuristic constructs based on core-shell arrangements, ordered intermetallic compounds, or randomly mixed elements [33]. Such structures are perturbed through intracluster atomic mobility in response to the binding of molecules [9], to entropy effects that prevail at higher temperatures [34], or to interactions with a support [35]. Such processes require, however, that the two components reside within the same clusters, making changes in surface composition induced by adsorbed species a rigorous indicator of the presence of the two components within the same cluster. Here, we exploit these phenomena by measuring temporal changes in the infrared spectra of chemisorbed CO in order to determine surface compositions and their dynamic response to adsorbate-induced intracluster restructuring.

Infrared spectra of chemisorbed CO were acquired on the monometallic and bimetallic samples prepared as described in Section 3.2.2. The NaLTA hosts (0.42 nm apertures, [14]) were exchanged with Ca^{2+} to form CaLTA (0.50 nm apertures, [14]) before these measurements to allow rapid diffusion of CO at the sub-ambient temperatures required for the slow intracluster atomic diffusion needed to measure a transient response [9,14]. Au_nPd_{100-n}CaLTA and Au_nPt_{100-n}CaLTA bimetallic samples were first treated in H_2 (20 kPa) at 573 K for 1 h and cooled in He flow to sub-ambient temperatures (278 K and 263 K, respectively) before exposure to CO(g) (1 kPa) and infrared measurements (Section 3.2.3.3). This treatment leads to surfaces devoid of adsorbed

species, thus favoring surface enrichment by Au, the component with the lower surface energy [9,36]. Spectra were collected after exposure to CO(g) and samples were then heated to 353 K in 1.0 kPa CO for 0.5 h and cooled back to 278 K or 263 K to acquire additional infrared spectra. The binding energy of CO on Pt (atop: 136 kJ mol^{-1}, [37]) or Pd (atop: 94 kJ mol^{-1}; bridged: 146 kJ mol^{-1}, [37]) is stronger than on Au (atop: 50 kJ mol^{-1}, [38]). Consequently, exposure of bimetallic particles to CO at temperatures that allow intraparticle atomic mobility would cause the return of Pt or Pd to cluster surfaces and to stronger infrared bands than after the initial exposure to CO at these low temperatures. Any differences in the infrared spectra before and after these heating cycles in the presence of CO(g) would indicate the presence of bimetallic clusters in Au_nPd_{100-n}CaLTA and Au_nPt_{100-n}CaLTA. Such hysteresis is expected to be much weaker for Pd_nPt_{100-n}CaLTA samples, because of the similar CO binding energies on Pt and Pd. Bimetallic mixing in Pd_nPt_{100-n}CaLTA was confirmed by combining infrared (Section 3.3.3.3) and EXAFS (Section 3.3.4.2) methods.

3.3.3.1 Infrared spectra of chemisorbed CO on Au_nPt_{100-n}CaLTA

The infrared spectra of CO chemisorbed on 1% wt. (metal) Au_nPt_{100-n}CaLTA (n=0, 33, 50, 67, and 100), measured in the presence of 1.0 kPa CO at 263 K before and after treatment in CO at 353 K, are shown in Figure 3.4. Monometallic Au and Pt samples exhibit absorption bands at 2120 cm^{-1} and 2070 cm^{-1} respectively, corresponding to atop CO species on Au and Pt [14,39]. Bands for bridge-bonded CO on monometallic Pt (1800-1900 cm^{-1}, [40,41]) are too weak for accurate quantitation of their intensity or frequency. Pt-CO bands are evident in each bimetallic sample spectrum both before and after intermittent heating in CO. The intensity of these bands increased monotonically with increasing Pt content, indicative of a concomitant increase in the Pt content of the cluster surfaces. A distinct Au-CO band is visible in the Au-rich bimetallic sample ($Au_{67}Pt_{33}$CaLTA) before and after heating in CO, but becomes weaker and ultimately undetectable at lower Au/Pt ratios. The weakening of this Au-CO band intensity is consistent with the decreasing overall Au content and the preferential adsorption of CO onto more strongly binding Pt atoms at bimetallic surfaces. Heating of Pt-Au bimetallic samples in CO led to hysteresis in their absorbance intensity, while the spectra for monometallic samples were unchanged. The intensity of Pt-CO bands in alloy samples increased after such heating cycles, reflecting the enrichment of Pt-Au particle surfaces with Pt as intracluster atomic mobility increases with increasing temperature. The fractional increase in the Pt-CO band intensity is smaller on samples with greater Pt/Au atomic ratios (20%, 15%, and 9% for Pt/Au=0.5, 1, and 2, respectively), consistent with smaller changes in the fraction of exposed Pt atoms upon CO binding for clusters that are more dilute in Au. We conclude from this infrared evidence that both Pt and Au are present within the same clusters in all Au_nPt_{100-n}CaLTA samples.

3.3.3.2. Infrared spectra of chemisorbed CO on Au_nPd_{100-n}CaLTA

The infrared spectra of chemisorbed CO on 1% wt. Au_nPd_{100-n}CaLTA samples (n=0, 33, 50, 67, and 100) in 1.0 kPa CO at 278 K before and after intervening treatments at 353 K are shown in Figure 3.5. AuCaLTA shows a weak absorption band at 2130 cm^{-1}, corresponding to atop adsorption of CO on Au [14], while PdCaLTA shows much more intense bands at 2090 cm^{-1} and 1930 cm^{-1}, assigned to atop and bridged CO bound on Pd domains, respectively [42]. The weak Au-CO band reflects the prevailing low coverages at these conditions [43,44]. Atop and bridged

Pd-CO bands are evident in all Au_nPd_{100-n}CaLTA spectra, but Au-CO bands cannot be clearly discerned because of their significant overlap with more intense atop Pd-CO bands. Pd-CO band intensities increased with increasing Pd/Au ratios, both before and after heating in CO, indicative of a concomitant increase in the Pd fraction at cluster surfaces. The ratio of the integrated intensities (I) of the bridged and atop Pd-CO bands ($\alpha = I_{bridge}/I_{atop}$) increased monotonically with increasing Pd content (Fig. 3.6). A preference for bridge-bonding, which requires multi-atom Pd ensembles, reflects a decrease in Au content at cluster surfaces. The α values for samples with separate Au and Pd clusters would resemble those on pure Pd and be unaffected by thermal treatments in CO, which favor intracluster surface segregation of Pd atoms only in bimetallic clusters. Figures 3.5 and 3.6 show that the prevalence of bridge-bonded CO increases after exposure to CO at 353 K for Au_nPd_{100-n}CaLTA, but not for PdCaLTA samples. These data thus confirm the CO-induced surface segregation of Pd, which becomes possible only when the two components are present within the same cluster.

The spectra of CO adsorbed on monometallic Pd samples (Figure 3.5) are similar to those reported in the literature, both in terms of their absorption frequencies (atop: 2090 cm^{-1} ; bridged: 1930 cm^{-1}) and the prevalent bridged CO binding (α=2.4) [9,39,40,42]. The presence of adsorbed contaminants on the metal surfaces in PdCaLTA, such as residual sulfur species from the protecting ligands (Section 3.2.2), would have resulted in much less prevalent bridged-bonded CO because of the requirement for multi-atom Pd ensembles and in much lower frequencies as a result of weaker dipole coupling. The presence of titrants on metal surfaces in PtCaLTA would have resulted in lower absorption frequencies than reported on clean Pt surfaces (2123-2054 cm^{-1}, [39,41]) and observed in the present study (2070 cm^{-1}). Sulfur contaminants would preferentially titrate Pt or Pd surface atoms because of the high bond energies of Pt-S (233 kJ mol^{-1}, [45]) and Pd-S (183 kJ mol^{-1}, [45]) relative to Au-S (126 kJ mol^{-1}, [46]). These sulfur species, if present, would have precluded the observed intracluster restructuring (Figs. 3.4, 3.5), because S, with its stronger binding than CO, would have led to Pt or Pd segregation before exposure to CO(g) and thus prevented additional surface enrichment as a result of the temperature cycles. The clean nature of these bimetallic surfaces is consistent with chemisorption and infrared data for Pt, Pd, and Au clusters in LTA treated at similar conditions (air 623 K, H_2 623 K; Section 3.2.2) [13,14]. We conclude that the bimetallic clusters in Au_nPd_{100-n}CaLTA contain accessible surfaces free of synthetic debris.

3.3.3.3 Infrared spectra of chemisorbed CO on Pd_nPt_{100-n}CaLTA

Figure 3.7a shows the infrared spectra of CO chemisorbed on Pd_nPt_{100-n}CaLTA (n=100, 80, 65, 50, 20, and 0) at 313 K and 1.0 kPa CO. On monometallic Pt and Pd samples, these spectra resemble those measured at lower temperatures (Pt-CO: 263 K, Fig. 3.4; Pd: 278 K, Fig. 3.5). PtCaLTA shows an intense band for atop CO binding at 2070 cm^{-1}, while PdCaLTA shows the characteristic Pd bands for atop (2090 cm^{-1}) and bridged (1930 cm^{-1}) CO. The presence of Pt leads to an increase in the intensity of atop CO bands that is monotonic with Pt content in Pd_nPt_{100-n}CaLTA, together with a concomitant decrease in the bridged Pd-CO band intensity. The ratio of the integrated intensities for these bands ($\alpha = I_{bridge}/I_{atop}$) as a function of Pd content is shown in Figure 3.7b. These trends indicate that surfaces become enriched with Pt as the Pt/Pd ratio increases, leading to a decrease in the size of Pd surface ensembles and thus to weaker features for bridge-bonded CO. The value of α declines from 2.8 to 0.1 as the Pd content is diluted from 100

to 50% at., and bridged Pd-CO bands are completely absent for samples with 20% at. Pd. Separate Pt and Pd clusters would have had undiluted Pd ensembles even at very high Pt/Pd ratios, thus giving non-zero α values for all samples containing Pt. These data provide evidence for the prevalence of bimetallic particles in Pd_nPt_{100-n}CaLTA samples.

3.3.4 X-Ray absorption fine structure spectra and the local structure and composition of clusters

The evidence presented up to this point for the presence of highly dispersed bimetallic clusters in Au_nPd_{100-n}NaLTA, Au_nPt_{100-n}NaLTA, and Pd_nPt_{100-n}NaLTA has been based on particle size distributions (Section 3.3.2), thermal stability (Section 3.3.2), and on the infrared spectra of chemisorbed CO (Section 3.3.3). Such data, taken together, are compelling but remain indirect and plausibly circumstantial. The bimetallic clusters are small (1.3-1.7 nm; Table 3.1) and uniform in size (DI 1.05-1.15; Table 3.1), an observation inconsistent with clusters heterogeneous in composition, which would have shown a broad range of cluster sizes (i.e. DI>1.5, [17]) reflecting their different thermal stabilities. The addition of Pd or Pt to Au stabilizes the lower-melting Au clusters against sintering (Fig. 3.3), consistent with heteroatomic metal bonding that is stronger than the like-metal bonding that prevails in monometallic clusters of the less stable metal [31]. The marked hysteresis in the infrared spectra (Section 3.3.3), evident upon heating to induce intracluster rearrangements (AuPt, Section 3.3.3.1; AuPd, Section 3.3.3.2), and the selective decrease in bridge-bonded CO upon addition of Pt to Pd (PdPt, Section 3.3.3.3), are inconsistent with mixtures of predominantly monometallic clusters. None of these techniques, however, provides direct quantitative evidence of the extent to which the two metals have mixed within a given cluster.

Energy dispersive X-ray spectroscopy (EDS) techniques allow detailed particle-by-particle elemental analysis in many scenarios [47], but elemental mapping of the very small clusters in this study would require electron currents or acquisition times that severely damage both metal structures and zeolite crystals [47,48]. As a result, we have used instead X-ray absorption spectroscopy (XAS) to probe the extent of metal mixing in bimetallic samples. In this section, we provide XAS results with a detailed analysis of the extended fine structure (EXAFS) region for $Au_{50}Pd_{50}$NaLTA and $Pd_{65}Pt_{35}$NaLTA samples in order to determine the number and composition of the atoms surrounding each absorber element; these data confirm the small size and the compositional uniformity of the bimetallic samples prepared by the procedures reported here.

The k^3-weighed and Fourier transformed EXAFS data with their respective regressed fits are shown for bimetallic samples and reference foils at the Au-L_3, Pd-K, and Pt-L_3 edges in Figures 3.8, 3.9, and 3.10, respectively. XAS spectra for these samples, including near-edge and post-edge data before data processing, are included in the SI (Figs. 3.S2 and 3.S3). Also included in the SI are the k^2-weighted EXAFS data prior to the application of Fourier transformations (Figs. 3.S4 and S5). The coordination numbers (*N*), interatomic distances (*D*), and Debye-Waller factors (σ^2) obtained from the regression of the EXAFS data using single scattering methods are reported in Table 3.2.

3.3.4.1. EXAFS analysis of $Au_{50}Pd_{50}$NaLTA spectra

Figure 3.8 shows the Fourier transform amplitudes and the corresponding regression fits of the EXAFS oscillations at the Au-L_3 edge for $Au_{50}Pd_{50}$NaLTA and the Au foil. The fits of the Au-L_3 EXAFS for $Au_{50}Pd_{50}$NaLTA confirm that Au absorbers are coordinated with both Au and Pd atoms, with Au-Au and Au-Pd coordination numbers ($N_{Au\text{-}Au}$, $N_{Au\text{-}Pd}$) of 6 ± 1 and 3.2 ± 0.8 at distances of 2.73 ± 0.02 Å and 2.73 ± 0.01 Å, respectively (Table 3.2). The first Au coordination shell thus contains a total of 9 ± 1 atoms after appropriate propagation of uncertainties [49]. This total coordination number is much smaller than the value of 12 characteristic of large Au or AuPd crystals [22], indicating the prevalence of coordinatively unsaturated surface atoms in highly dispersed clusters. The Au-Pd interatomic distance (2.73 Å) derived from the fit is also smaller than that of a bulk $Au_{50}Pd_{50}$ alloy (~2.81 Å) [22], consistent with the demonstrated contraction of metal-metal bonds near cluster surfaces [50]. The total coordination number (9 ± 1) corresponds to 1.3-2.1 nm diameter clusters with an fcc cuboctahedral structure [50-53]; this diameter is in agreement with that measured by TEM (1.6 nm) (Table 3.1).

Next, we compare these results with those extracted from the EXAFS signal at the Pd-K edge to confirm their internal consistency. Fourier transform amplitudes and fits of the EXAFS oscillations at the Pd-K edge for $Au_{50}Pd_{50}$NaLTA and Pd foil are shown in Figure 3.9. Structural parameters derived from these fits (Table 3.2) show that both Au and Pd are coordinated to the Pd absorbers, with a Pd-Pd coordination number of 3.1 ± 0.7 at a distance of 2.69 ± 0.01 Å and a Pd-Au coordination number of 5 ± 1 at a distance of 2.73 ± 0.01 Å. These individual coordination numbers give a total Pd coordination of 8 ± 1. Fits at the Au-L_3 and Pd-K edges did not reveal any metal-S or metal-O coordination, consistent with the exclusive presence of metallic phases. The total coordination numbers for Au and Pd absorbers are similar within the experimental uncertainty, as are the heteroatomic coordination numbers calculated at each metal edge (i.e. $N_{Au\text{-}Pd}$ and $N_{Pd\text{-}Au}$), indicating that the Au and Pd atoms occupy clusters with similarly high dispersion and are in intimate contact within clusters that must therefore contain both elements. The mean atomic coordination between dislike atoms (4 ± 1), computed as the average of $N_{Au\text{-}Pd}$ and $N_{Pd\text{-}Au}$, is approximately half the average total coordination (9 ± 1), indicating that bonds between dislike atoms are equally prevalent as homoatomic bonds. Such similar numbers of homoatomic and heteroatomic bonds are consistent with all clusters reflecting the bulk equimolar amounts of the two elements (Pd/Au=1), with the absence of segregated metal phases, and with essentially uniform distributions of each metal atom within each cluster. Surface enrichment of Au brought forth by pretreatment of the sample (H_2, 353 K; Section 3.3.3) would have resulted in a slight preference for homoatomic bonds; such intracluster segregation was either lost during the intervening period between treatments and XAS spectra acquisition (Section 3.2.3.4) or could not be accurately detected by the single scattering models used here. These parameters derived from the EXAFS, however, are consistent at each metal edge and confirm the small size and intimate metal mixing in $Au_{50}Pd_{50}$NaLTA, as well as the substantial absence of monometallic clusters.

3.3.4.2. EXAFS analysis of $Pd_{65}Pt_{35}$NaLTA spectra

Figure 3.9 shows the Fourier transform amplitudes and fits of the EXAFS signal at the Pd-K edge of $Pd_{65}Pt_{35}$NaLTA; structural parameters derived from these fits are shown in Table 3.2. Pd absorbers were coordinated to both Pd and Pt atoms with coordination numbers of 4.4 ± 0.4

and 4.0 ± 0.3 at distances of 2.74 ± 0.01 and 2.73 ± 0.01 Å, respectively. These coordination shells lead to a total Pd atom coordination of 8.4 ± 0.5, corresponding to 1.1-1.7 nm diameter clusters with an fcc cuboctahedral structure [50-53], in good agreement with the mean cluster size determined from TEM images (1.2 nm, Table 3.2).

Figure 3.10 shows the corresponding Fourier transform amplitudes and fits of the EXAFS at the Pt-L_3 edge of $Pd_{65}Pt_{35}$NaLTA. Structural parameters extracted from the fit (Table 3.2) show that Pt absorbers are coordinated to both Pt and Pd atoms, with Pt-Pt and Pt-Pd coordination numbers ($N_{Pt\text{-}Pt}$, $N_{Pt\text{-}Pd}$) of 5 ± 1 and 4 ± 1 at distances 2.72 ± 0.01 Å and 2.73 ± 0.01 Å, respectively. Pt absorbers thus contain a total of 9 ± 1 atoms in their first coordination shell. This total coordination number is similar to the total coordination derived for Pd atoms (8.4 ± 0.5), indicating that the Pd and Pt atoms occupy clusters with a large and similar fraction of coordinatively unsaturated surface atoms. Pd and Pt absorbers did not show any metal-S or metal-O coordination, consistent with the presence of only metallic phases. PdPt clusters with the bulk composition of $Pd_{65}Pt_{35}$NaLTA (61 Pd: 39 Pt, Table 3.1), a total coordination of 9 ± 1, and random intracluster locations of Pt and Pd would exhibit Pd-Pt and Pt-Pd coordination numbers ($N_{Pd\text{-}Pt}$ and $N_{Pt\text{-}Pd}$) of 4 and 5, respectively, which agree within experimental uncertainty with those derived from EXAFS data; thus, we conclude that clusters are uniform in composition and contain random intracluster distributions of two elements. The prevalence of Pt-rich or Pd-rich clusters would have led to smaller $N_{Pd\text{-}Pt}$ and $N_{Pt\text{-}Pd}$ values than expected for clusters of uniform composition.

3.3.5. Ethanol oxidative dehydrogenation rates and titration of extracrystalline surfaces by large organosulfur poisons as a probe of encapsulation selectivity

Metal cluster confinement within zeolites precludes certain reactants or poisons from accessing intracrystalline clusters; such restricted access also serves to retain large products until they convert to smaller species that can egress by diffusion, while the small intracrystalline voids can stabilize specific transition states. In all cases, these effects are dictated by the size of the voids and their connecting apertures in a given microporous framework [13-15]. Here, we exploit such zeolite shape selective properties by measuring oxidative dehydrogenation (ODH) turnover rates of a small molecule (ethanol, 0.40 nm kinetic diameter, [13]) on samples exposed to a large organosulfur molecule that poisons metal surfaces (dibenzothiophene, DBT; 0.9 nm, [30]) to estimate the extent to which bimetallic clusters reside within zeolite crystals. Organosulfur compounds such as DBT irreversibly adsorb onto Au, Pd, and Pt surfaces, forming unreactive species that block active sites [29]. Consequently, ethanol ODH turnover rates on metal-SiO_2 samples and extracrystalline bimetallic clusters in metal-NaLTA samples would be suppressed by DBT, while clusters protected by the small NaLTA apertures (0.42 nm, [13]) would retain their ODH rates because they cannot be reached by DBT. The rate differences upon contact with DBT then provide a measure of the selectivity of metal encapsulation within intracrystalline domains.

Alkanol ODH reactions form alkanals as primary products; these alkanals can undergo subsequent reactions with alkanols to form hemiacetals or alkoxyalkanols and then dialkoxyalkanes and carboxylic acids through secondary dehydrogenation, oxidation, or condensation reactions [54,55]. These secondary reactions do not affect measured turnover rates, because each product molecule formed involves a single ODH event, in which an alkanal forms via kinetically-relevant β-H abstraction from an adsorbed alkoxide by chemisorbed oxygen

[14,55]. The low conversions prevalent in this study (<5%) minimize secondary reactions and lead to high acetaldehyde selectivities (>95%, C-basis).

Samples were exposed to DBT as described in Section 3.2.3.5 before ODH rate measurements at 393 K. ODH rates were also measured on samples that were not contacted with DBT (denoted as "control samples"), but treated otherwise identically. ODH turnover rates measured on these controls (r_{ODH}) and on samples exposed to DBT ($r_{ODH,\ DBT}$) are used to define a parameter Λ_{DBT}:

$$\Lambda_{DBT,i} = \frac{r_{ODH,\ DBT}}{r_{ODH}} \qquad (4)$$

where i identifies the specific sample (e.g., $Au_{50}Pd_{50}$NaLTA, Pt/SiO_2). The value of $\Lambda_{DBT,i}$ reflects the fraction of the active surfaces that remain active for ODH after DBT exposure. A $\Lambda_{DBT,i}$ value of unity would reflect fully protected clusters, while a value of zero would indicate that all active surfaces can be accessed and fully poisoned by DBT. Metal clusters encapsulated within LTA crystals would be inaccessible to DBT and thus protected from deactivation, while metal clusters outside the zeolite crystals should be accessible and deactivated by DBT. Exposure to DBT thus selectively suppresses the contributions to the ODH rate from extrazeolite clusters. As a result, the value of $\Lambda_{DBT,i}$ is proportional to the fraction of encapsulated clusters in metal-zeolite samples. Values of r_{ODH} and $\Lambda_{DBT,i}$ for Au, Pd, and Pt clusters supported on mesoporous SiO_2 and a representative group of bimetallic samples are shown in Table 3.3.

Ethanol ODH turnover rates were much more weakly suppressed by contact with DBT on metal-NaLTA ($\Lambda_{DBT,i}$ = 0.95-0.98) than on metal-SiO_2 ($\Lambda_{DBT,i}$ = 0.03-0.11) samples (Table 3.3), indicating that (i) DBT effectively titrates unprotected noble metal surfaces; and (ii) most of the metal clusters reside within LTA crystals in metal-NaLTA samples. The small residual ODH activity on SiO_2-supported samples, even after contact with excess DBT (6:1 DBT:metal molar ratio), may reflect steric effects that hinder access to remaining open sites as DBT-derived species reach near-saturation coverages [38]. The remarkable resistance to DBT poisoning in metal-NaLTA samples, evident in their $\Lambda_{DBT,i}$ values near unity (0.95-0.98) (Table 3.3), provides compelling evidence for the near complete encapsulation of these bimetallic clusters, as also found for monometallic clusters encapsulated within LTA and other zeolites using similar hydrothermal synthesis protocols [13,14]. Such resistance may also prove useful in practice when poisons larger than the reactants and products of interest are present in reacting streams.

We therefore conclude that the hydrothermal encapsulation method described here can be more generally applied to prepare bimetallic clusters which are small and uniform in size (Section 3.3.2), highly stable against thermal sintering (Section 3.3.2), homogeneously distributed in composition (Section 3.3.3, 3.3.4), and selectively encapsulated within zeolite crystals (Section 3.3.5).

3.4 Conclusion

A general procedure was developed for the encapsulation of highly dispersed bimetallic clusters (1-2 nm), uniformly distributed in size and composition, within the voids of the LTA

zeolite using a ligand-assisted hydrothermal synthesis technique. Samples with AuPd, AuPt, and PdPt clusters and a variety of metal compositions were synthesized to demonstrate the broad applicability of the technique. Metal encapsulation and alloying is conferred by introducing mercaptosilane-stabilized metal cation precursors into zeolite synthesis gels, which are crystallized hydrothermally to form LTA with metal cations occluded in the pores. The anchoring of these ligated cations to the zeolite framework via siloxane bridges enforces their uniform dispersion throughout the zeolite crystals. Treatment of the crystallized zeolites in O_2 and then H_2 forms bimetallic clusters, which remain narrowly distributed in size following oxidative treatments in excess of 773 K. Such thermal stability results from the confinement of the metal clusters within microporous zeolite voids, which impose thermodynamic barriers that inhibit cluster growth. Encapsulated Au metal further benefits from enhanced thermal sinter-stability through alloying with higher-melting Pd or Pt metal. Metal confinement also exploits the catalytic shape-selective properties of zeolites, which act to protect active metal surfaces from contact by large poison molecules. The present work outlines the synthesis of bimetallic clusters of well-defined size and composition, allowing rigorous studies of alloyed nanoparticle catalysts even at conditions which strongly favor metal agglomeration. Such studies may combine the well-known reactant size selection properties of small-pore zeolites with the synergistic catalysis of bimetallic clusters for tailored applications of these materials. The successful application of this technique to a variety of metal pairs and compositions leads us to predict that it can be analogously applied to any combination of metals (Au, Pd, Pt, Ir, Ag, Rh) and zeolites (LTA, MFI) for which monometallic hydrothermal encapsulation techniques have been developed.

3.5 Acknowledgments

We gratefully acknowledge the generous financial support of the Chevron Energy technology Co, as well as ancillary research support from CONICET (PIP No 1035) and LNLS (Project XAFS1-18861) and an ARCS Foundation Fellowship (for TO). We thank Dr. Reena Zalpuri (Electron Microscope Lab) for support with TEM instrumentation and Dr. Antonio DiPasquale (X-Ray Facility) for assistance with the acquisition of diffraction data.

3.6 Figures, Tables, and Scheme(s)

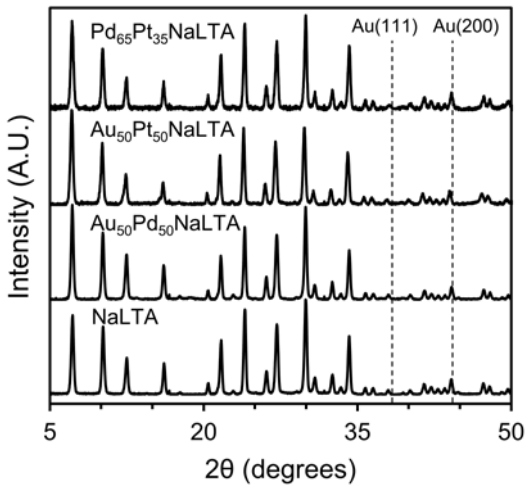

Figure 3.1. XRD patterns of bimetallic metal-zeolite samples (Section 3.2.3.1). Total metal content in each sample is ~1% wt., except for the metal-free NaLTA standard.

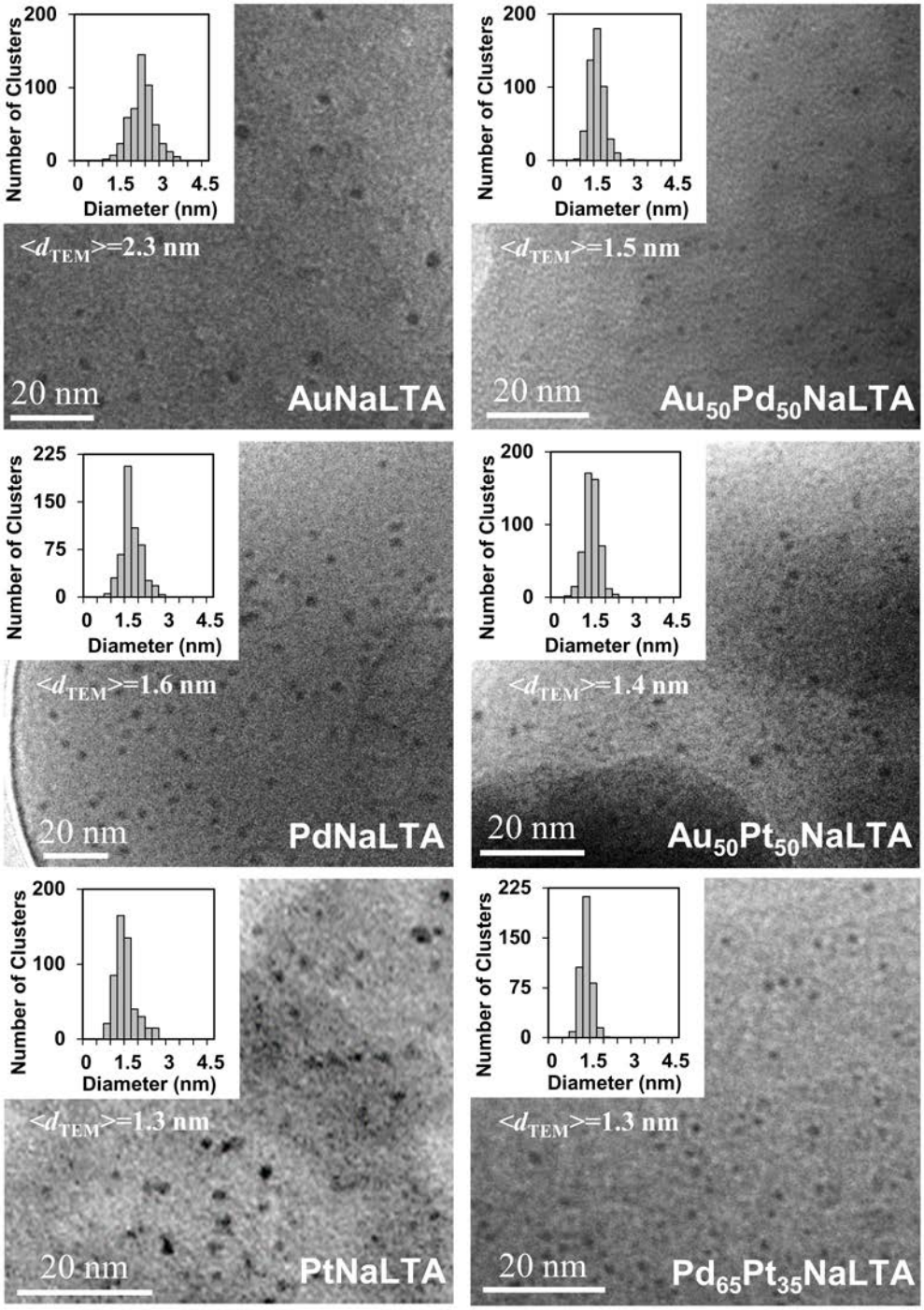

Figure 3.2. Transmission electron micrographs, surface-averaged diameters, $\langle d_{TEM} \rangle$ (Eq. 1), and diameter distributions for monometallic and bimetallic metal-zeolite samples. The metal content in each sample is ~1% wt.

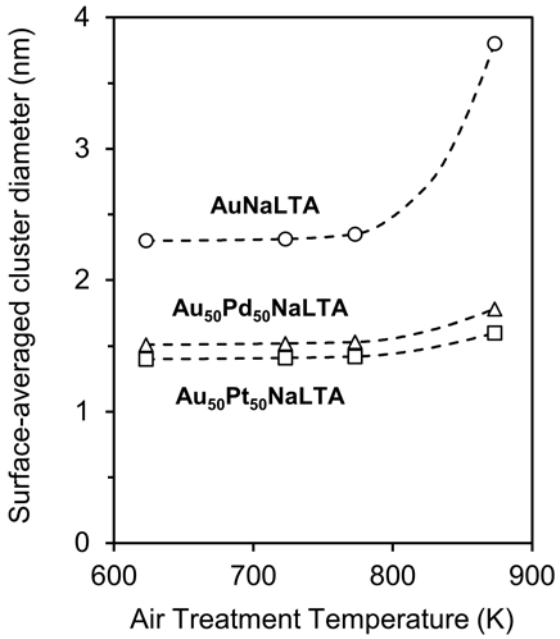

Figure 3.3. Effects of the thermal treatment temperature in flowing dry air (1.67 cm^3 g^{-1} s^{-1}, 0.033 K s^{-1}, 5 h) on the TEM-derived surface-averaged cluster diameter ($\langle d_{TEM} \rangle$, Eq. 1) of metal particles in AuNaLTA (○), $Au_{50}Pd_{50}$NaLTA (△), and $Au_{50}Pt_{50}$NaLTA (□). The total metal content in each sample is ~1% wt.

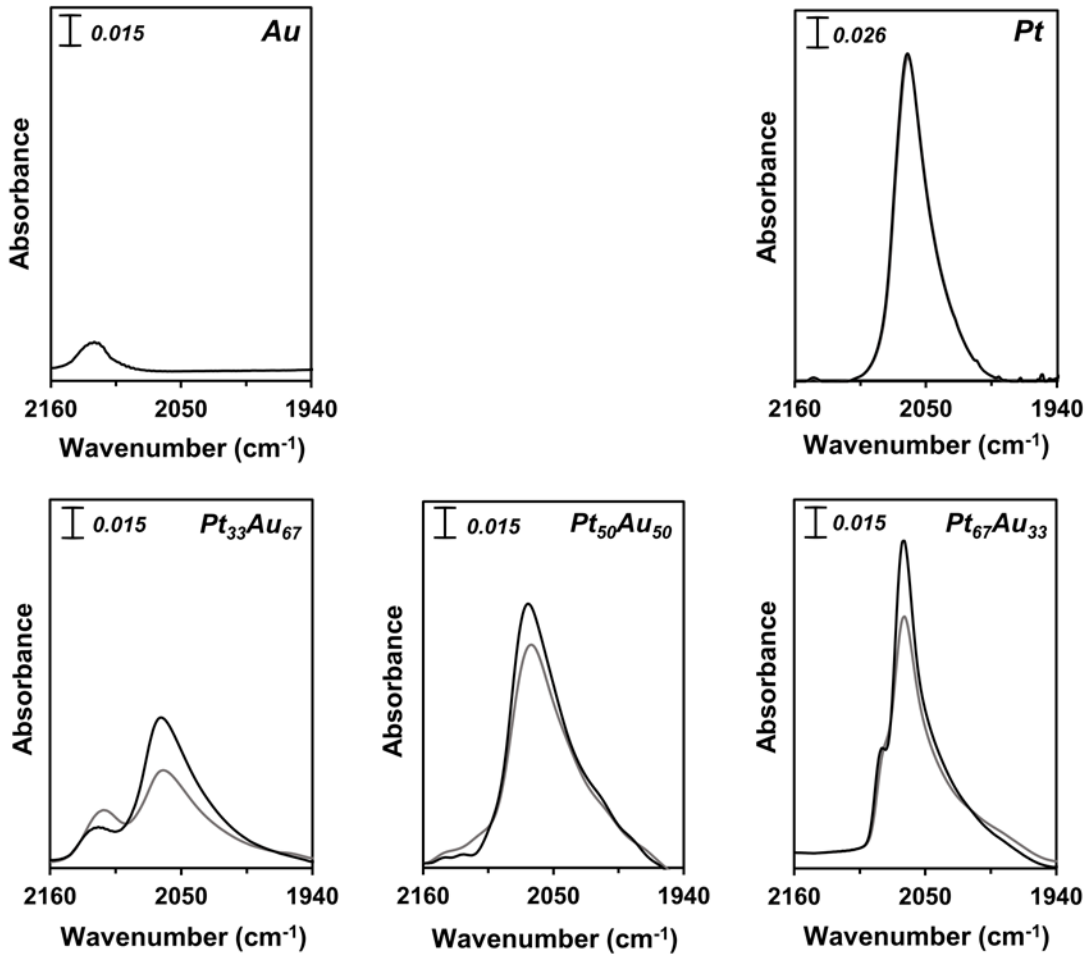

Figure 3.4. Infrared spectra of CO adsorbed on monometallic or bimetallic Au_nPt_{100-n}CaLTA samples (1 kPa CO, 99 kPa He) at 263 K after H_2 treatment (573 K, 20 kPa H_2, 80 kPa He) (gray spectra) and after heating in CO (1 kPa CO, 99 kPa He) up to 353 K (black spectra).

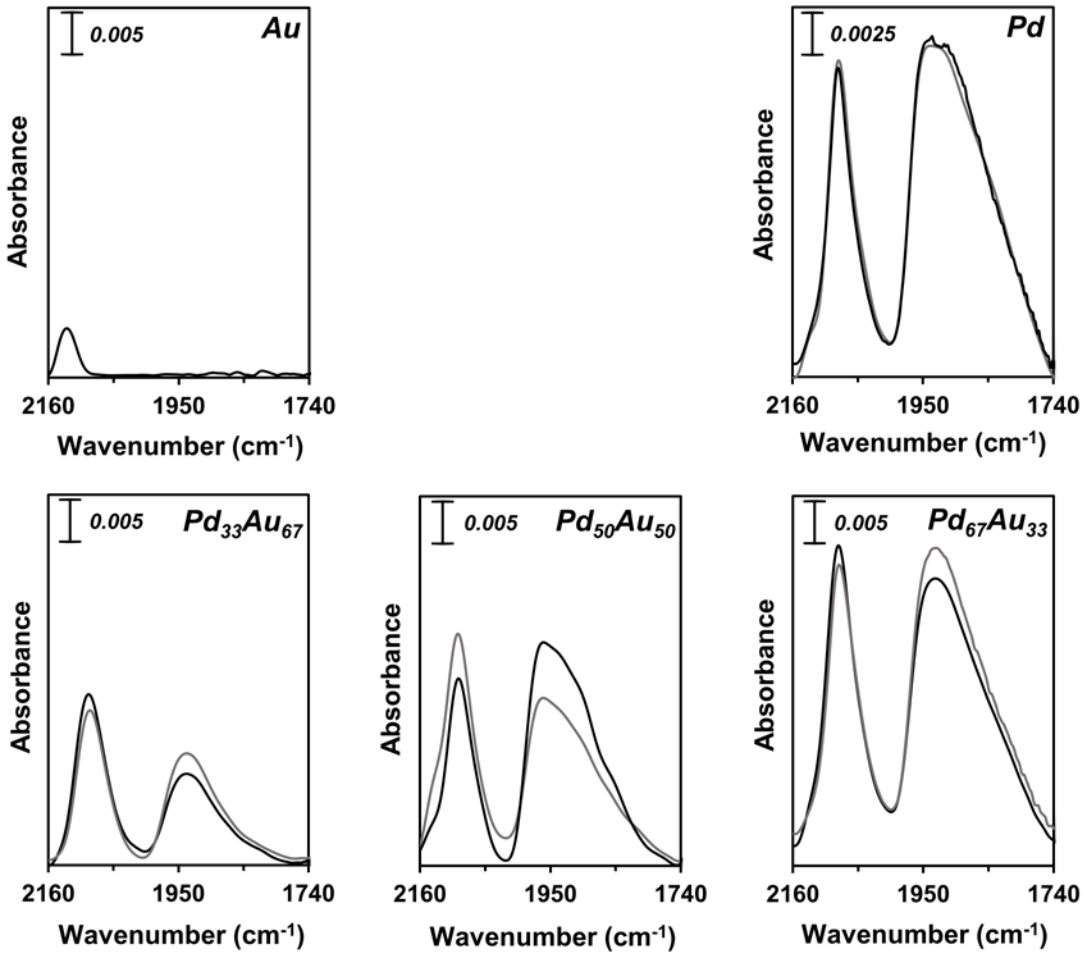

Figure 3.5. Infrared spectra of CO adsorbed on monometallic or bimetallic Au_nPd_{100-n}CaLTA samples (1 kPa CO, 99 kPa He) at 278 K after H_2 treatment (573 K, 20 kPa H_2, 80 kPa He) (gray spectra) and after heating in CO (1 kPa CO, 99 kPa He) up to 353 K (black spectra).

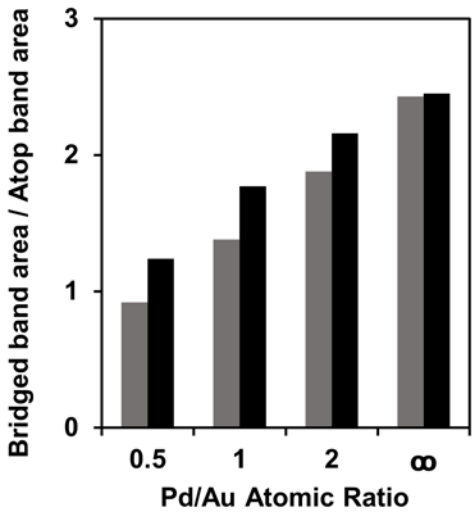

Figure 3.6. Ratios of the integrated intensity of the Pd-CO (bridged) infrared absorption band to that of the Pd-CO atop band as a function of Pd/Au atomic ratio in Au_nPd_{100-n}CaLTA samples. Intensity ratios ($\alpha = I_{bridge}/I_{atop}$) calculated from spectra measured under 1 kPa CO at 278 K after H_2 treatment (573 K, 20 kPa H_2, 80 kPa He) (gray bars) and after heating in CO (1 kPa CO, 99 kPa He) up to 353 K (black bars).

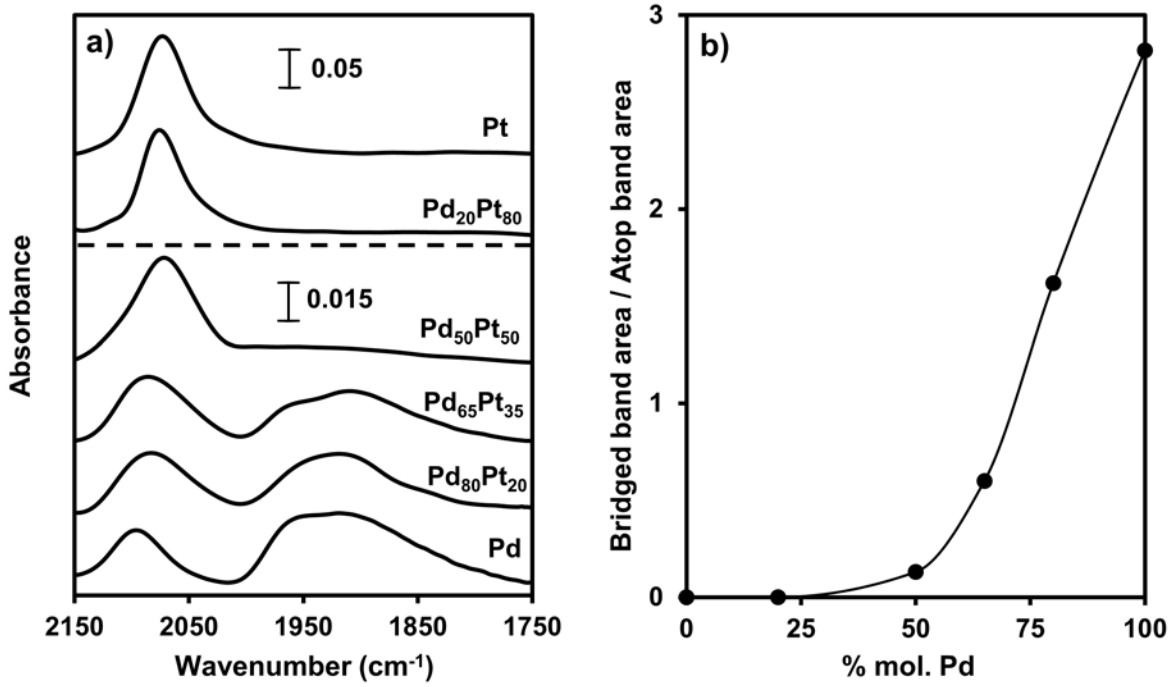

Figure 3.7. a) Infrared spectra of CO adsorbed on monometallic or bimetallic Pd_nPt_{100-n}CaLTA samples (1 kPa CO, 99 kPa He) at 313 K after H_2 treatment (573 K, 20 kPa H_2, 80 kPa He). b) Ratio of the integrated intensity of the Pd-CO (bridged) absorption band (~1900 cm^{-1}) to that of the metal-CO atop band (~2100 cm^{-1}) as a function of Pd content in Pd_nPt_{100-n}CaLTA samples.

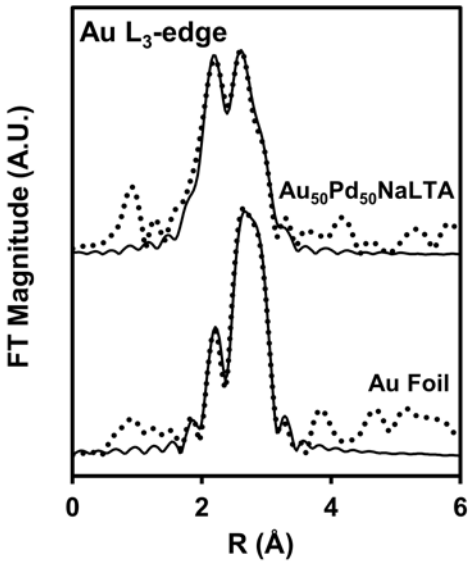

Figure 3.8. Fourier transforms (FT) of the k^3-weighted EXAFS and their corresponding single scattering fits for Au_nPd_{100-n}NaLTA and Au foil measured at the Au-L_3 edge. Dotted lines, experimental data; solid lines, fitted data. X-ray absorption spectra were collected at ambient temperature under 100 kPa Ar following H_2 treatment (573 K, 10 kPa H_2, 90 kPa He).

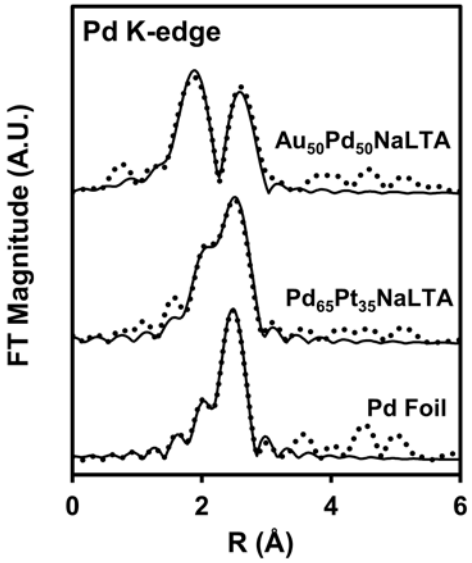

Figure 3.9. Fourier transforms (FT) of the k^3-weighted EXAFS and their corresponding single scattering fits for $Au_{50}Pd_{50}$NaLTA, $Pd_{65}Pt_{35}$NaLTA, and Pd foil measured at the Pd-K edge. Dotted lines, experimental data; solid lines, fitted data. X-ray absorption spectra were collected at ambient temperature under 100 kPa Ar following H_2 treatment (573 K, 10 kPa H_2, 90 kPa He).

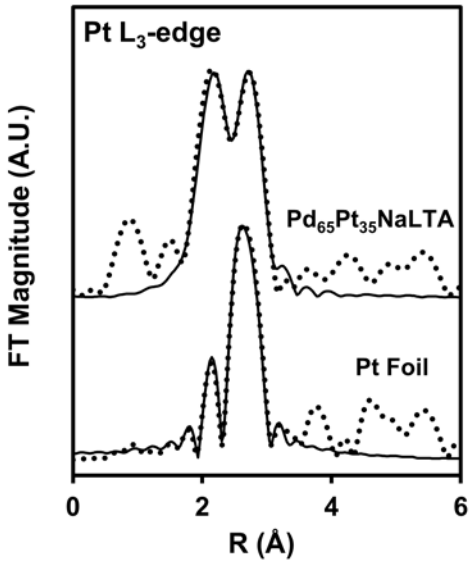

Figure 3.10. Fourier transforms (FT) of the k^3-weighted EXAFS and their corresponding single scattering fits for $Pd_{65}Pt_{35}$NaLTA and Pt foil measured at the Pt-L_3 edge. Dotted lines, experimental data; solid lines, fitted data. X-ray absorption spectra were collected at ambient temperature under 100 kPa Ar following H_2 treatment (573 K, 10 kPa H_2, 90 kPa He).

Table 3.1. Metal Loadings, surface averaged particle diameters, metal compositions, and particle dispersity indices of metal-zeolite and metal-SiO_2 samples

Sample	% wt. Metal[a]	Metal Ratio[a]	$\langle d_{TEM} \rangle$ (nm)[b]	DI[c]
AuNaLTA	1.1	-	2.3 ± 0.4	1.09
PdNaLTA	1.0	-	1.6 ± 0.3	1.10
PtNaLTA	1.1	-	1.3 ± 0.3	1.17
$Au_{67}Pd_{33}$NaLTA	1.0	65 Au: 35 Pd	1.7 ± 0.3	1.09
$Au_{50}Pd_{50}$NaLTA	0.9	54 Au: 46 Pd	1.5 ± 0.3	1.08
$Au_{33}Pd_{67}$NaLTA	0.7	32 Au: 68 Pd	1.5 ± 0.3	1.11
$Au_{67}Pt_{33}$NaLTA	1.1	62 Au: 38 Pt	1.4 ± 0.3	1.15
$Au_{50}Pt_{50}$NaLTA	0.8	52 Au: 48 Pt	1.4 ± 0.3	1.09
$Au_{33}Pt_{67}$NaLTA	1.2	62 Au: 38 Pt	1.3 ± 0.2	1.07
$Pd_{80}Pt_{20}$NaLTA	1.1	80 Pd: 20 Pt	1.4 ± 0.3	1.09
$Pd_{50}Pt_{50}$NaLTA	1.0	56 Pd: 44 Pt	1.5 ± 0.3	1.08
$Pd_{65}Pt_{35}$NaLTA	1.1	61 Pd: 39 Pt	1.3 ± 0.2	1.06
$Pd_{20}Pt_{80}$NaLTA	1.0	24 Pd: 76 Pt	1.3 ± 0.2	1.05
Au/SiO_2	2.2	-	2.7 ± 0.5	1.06
Pd/SiO_2	0.6	-	3.1 ± 0.8	1.18
Pt/SiO_2	0.8	-	2.4 ± 0.7	1.16

[a]Analyzed by inductively coupled plasma optical emission spectroscopy (Section 3.2.2.1). [b]Surface area weighted mean cluster diameter determined via TEM (Section 3.2.3.2). [c]Dispersity Index computed as the surface averaged cluster diameter divided by the number averaged diameter (Section 3.2.3.2).

Table 3.2. Coordination numbers, interatomic distances, and Debye-Waller factors derived from single scattering fits of the EXAFS spectra for the zeolite-encapsulated bimetallic nanoparticles.

Sample	Edge	Scatterer	N^a	D (Å)[b]	σ^2 (Å^2)[c]
$Au_{50}Pd_{50}$NaLTA	Au-L_3	Au	6 (1)	2.73 (2)	0.011 (4)
		Pd	3.2 (8)	2.73 (1)	0.008 (2)
	Pd-K	Au	5 (1)	2.73 (1)	0.008 (2)
		Pd	3.1 (7)	2.69 (1)	0.007 (1)
$Pd_{65}Pt_{35}$NaLTA	Pd-K	Pd	4.4 (4)	2.74 (1)	0.008 (1)
		Pt	4.0 (3)	2.73 (1)	0.008 (1)
	Pt-L_3	Pd	4 (1)	2.73 (1)	0.008 (1)
		Pt	5 (1)	2.72 (1)	0.008 (1)

[a]Average coordination number of absorbing element. [b]Interatomic distance. [c]Debye-Waller factor. Values in parentheses indicate the error in the last digit.

Table 3.3. Rates of ethanol oxidative dehydrogenation on metal-SiO_2 and metal-NaLTA samples

Sample	r_{ODH} (10^{-3} s^{-1} $mol_{surf\text{-}metal}^{-1}$)[a]	Λ_{DBT}[b]
$Au_{50}Pd_{50}$NaLTA	110	0.97
$Au_{50}Pt_{50}$NaLTA	210	0.95
$Pd_{65}Pt_{35}$NaLTA	280	0.98
Au/SiO_2	12	0.11
Pd/SiO_2	320	0.03
Pt/SiO_2	490	0.04

[a]Ethanol ODH turnover rates of samples agitated in EtOH (300 cm^3 g^{-1}) at ambient temperature for 4 h, treated in ambient air at 343 K for 12 h, then used in reaction (393 K under 9 kPa O_2, 4 kPa EtOH, and 0.5 kPa H_2O). [b]$r_{ODH,DBT}/r_{ODH}$ (Eq. 4), where $r_{ODH,\ DBT}$ is the ethanol ODH rate of analogously treated samples but with DBT dissolved in the EtOH at a 6:1 DBT:metal molar ratio. Reaction turnover rate defined as number of moles of reactant converted per time normalized by the number of exposed surface metal atoms estimated by TEM (Eq. 3).

Scheme 3.1 Schematic representation of the synthesis and characterization of bimetallic clusters encapsulated within LTA

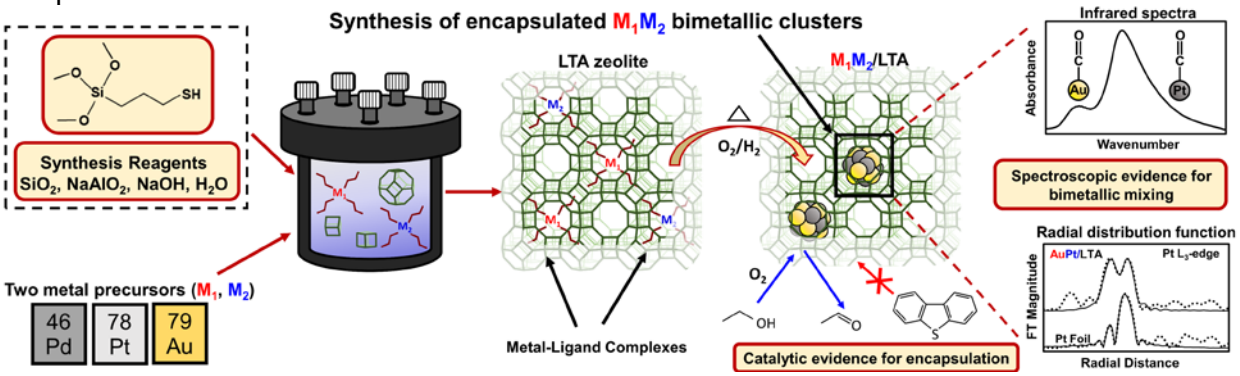

3.7 References

[1] Yu, W. –Y.; Zhang, L.; Mullen, G. M.; Henkelman, G.; Mullins, C. B. *J. Phys. Chem. C* **2015**, *119*, 11754.
[2] Serrano-Ruiz, J. C.; Sepúlveda-Escribano, A.; Rodríguez-Reinoso, F. *J. Catal.*, **2007**, *246*, 158.
[3] Wolf, R. M.; Siera, J.; Vandelft, F.; Nieuwenhuys, B. E. *Faraday Discuss. Chem. Soc.*, **1989**, *87*, 275.
[4] Riahi, G.; Guillemot, D.; Polisset-Thfoin, M.; Khodadadi, A. A.; Fraissard, J. *Catal. Today* **2002**, *72*, 115.
[5] Zhang, Z.; Sachtler, W. M. H.; Suib, S. L. *Catal. Lett.*, **1989**, *2*, 395.
[6] Rades, T.; Pak, C.; Polisset-Thfoin, M.; Ryoo, R.; Fraissard, J. *Catal. Lett.*, **1994**, *29*, 91.
[7] Wada, T.; Kaneda, K.; Murata, S.; Nomura, M. *Catal. Today* **1996**, *31*, 113.
[8] Paál, Z.; Wootsch, A.; Teschner, D.; Lázár, K.; Sajó, I. E.; Győrffy, N.; Weinberg, G.; Knop-Gericke, A.; Schlögl, R. *Appl. Catal., A* **2011**, *391*, 377.
[9] Kunz, S.; Iglesia, E. *J. Phys. Chem. C* **2014**, *118*, 7468.
[10] Alexeev, O. S.; Gates, B. C. *Ind. Eng. Chem. Res.* **2003**, *42*, 1571.
[11] Rebelli, J.; Rodriguez, A. A.; Ma, S.; Williams, C. T.; Monnier, J. R. *Catal. Today* **2011**, *160*, 170.
[12] Alayoglu, S.; Zavalij, P.; Eichhorn, B.; Wang, Q.; Frenkel, A. I.; Chupas, P. *ACS Nano* **2009**, *3*, 3127.
[13] Choi, M.; Wu, Z.; Iglesia, E. *J. Am. Chem. Soc.* **2010**, *132*, 9129.
[14] Otto, T.; Zones, S. I.; Iglesia, E. *J. Catal.* **2016**, *339*, 195.
[15] Weisz, P. B.; Frilette, V. J.; Maatman, R.W.; Mower, E. B. *J. Catal*. **1962**, *1*, 307.
[16] Zhu, H.; Ma, Z.; Clark, J. C.; Pan, Z.; Overbury, S. H.; Dai, S. *Appl. Catal., A* **2007**, *326*, 89.
[17] Bergeret, G.; Gallezot, P. In *Handbook of Heterogeneous Catalysis;* Ertl, G.; Knozinger, H.; Schuth, F.; Weitkamp, J., Eds.; Wiley-VHC: Weinheim, Germany, 2008; pp 738.
[18] Bearden, J. A. *Rev. Mod. Phys.* **1967**, *39*, 78.
[19] Ravel, B.; Newville, M. *J. Synchrotron Rad.* **2005**, *12*, 537.
[20] Zabinsky, S. I.; Rehr, J. J.; Ankudinov, A.; Albers, R. C.; Eller, M. J. *Phys. Rev. B* **1995**, *52*, 2995.
[21] Foiles, S. M.; Baskes, M. I.; Daw, M. S. *Phys. Rev. B* **1986**, *33*, 7983.
[22] Venudhar, Y. C.; Lyengar, L.; Rao, K. V. K. *J. Less-Common Met.* **1978**, *58*, P55.
[23] Raub, E.; Woerwag, G. *Z. Metallk.* **1955**, *46*, 513.
[24] Waser, J.; Levy, H. A.; Peterson, S. W. *Acta Crystallogr.* **1953**, *6*, 661.
[25] Hoekstra, H. R.; Siegel, S.; Gallagher, F. X. *Adv. Chem. Ser.* **1971**, *98*, 39.
[26] Brese, N. E.; Squattrito, P. J.; Ibers, J. A. *Acta Crystallogr., Sect. C: Cryst. Struct. Commun.* **1985**, *41*, 1829.
[27] Bannister, F. A.; Hey, M. H. *Mineral Mag. J. M. Soc.* **1932**, *23*, 188.
[28] Isonaga, T.; Ishikawa, K.; Wakita, S.; Suzuki, Y. *Solid State Ionics* **1995**, *79*, 60.
[29] Sako, E. O.; Kondoh, H.; Nakai, I.; Nambu, A.; Nakamura, T.; Ohta, T. *Chem. Phys. Lett.* **2005**, *413*, 267.
[30] Van de Voorde, B.; Hezinova, M.; Lannoeye, J.; Vandekerkhove, A.; Marszalek, B.; Gil, B.; Beurroies, I.; Nachtiqall, P.; De Vos, D. *Phys. Chem. Chem. Phys.* **2015**, *17*, 10759.
[31] Cao, A.; Lu, R.; Veser, G. *Phys. Chem. Chem. Phys.* **2010**, *12*, 13499.
[32] Peng, S.; McMahon, J. M.; Schatz, G. C.; Gray, S. K.; Sun, Y. *Proc. Natl. Acad. Sci. U.S.A.* **2010**, *107*, 14530.

[33] Sankar, M.; Dimitratos, N.; Miedziak, P. J.; Wells, P. P.; Kiely, C. J.; Hutchings, G. J. *Chem. Soc. Rev.* **2012**, *41*, 8099.
[34] Kaya, S.; Erunal, E.; Shaltaf, R.; Ellialtioğlu, Ş.; Üner, D. *Turk. J. Chem.* **2009**, *33*, 11.
[35] Han, C. W.; Majumdar, P.; Marinero, E. E.; Aguilar-Tapia, A.; Zanella, R.; Greeley, J.; Ortalan, V. *Nano Lett.* **2015**, *15*, 8141.
[36] Miedema, A. R. *Z. Metallk.* **1978**, *69*, 287.
[37] Smith, G. W.; Carter, E. A. *J. Phys. Chem.* **1991**, *95*, 2327.
[38] Meyer, R.; Lemire, C.; Shaikhutdinov, S. K.; Freund, H. –J. *Gold Bull.* **2004**, *37*, 72.
[39] Lu, J.; Low, K. –B.; Lei, Y.; Libera, J. A.; Nicholls, A.; Stair, P. C.; Elam, J. W. *Nat. Comm.* **2014**, *5*, 3264.
[40] Rosseler, O.; Ulhaq-Bouillet, C.; Bonnefont, A.; Pronkin, S.; Savinova, E.; Louvet, A.; Keller, V.; Keller, N. *Appl. Catal., B* **2015**, *166-167*, 381.
[41] Barshad, Y.; Zhou, X.; Gulari, E. *J. Catal.* **1985**, *94*, 128.
[42] Stacchiola, D.; Kaltchev, M.; Wu, G.; Tysoe, W. T. *Surf. Sci.* **2000**, *470*, L32.
[43] Derrouiche, S.; Gravejat, P.; Bianchi, D*J. Am. Chem. Soc.* **2004**, *126*, 13010.
[44] Menegazzo, F.; Manzoli, M.; Chiorino, A.; Boccuzzi, F.; Tabakova, T.; Signoretto, M.; Pinna, F.; Pernicone, N. *J. Catal.* **2006**, *237*, 431.
[45] Toulhoat, H.; Raybaud, P.; Kasztelan, S.; Kresse, G.; Hafner, J. *Catal. Today* **1999**, *50*, 629.
[46] Nuzzo, R. G.; Fusco, F. A.; Allara, D. L. *J. Am. Chem. Soc.* **1987**, *109*, 2358.
[47] Herzing, A. A.; Wantanabe, M.; Edwards, J. K.; Conte, M.; Tang, Z. R.; Hutchings, G. J.; Kiely, C. J. *Faraday Discuss.* **2008**, *138*, 337.
[48] Ugurlu, O.; Haus, J.; Gunawan, A. A.; Thomas, M. G.; Maheshwari, S.; Tsapatsis, M.; Mkhoyan, K. A. *Phys. Rev. B* **2011**, *83*, 113408.
[49] Taylor, J. R. *An Introduction to Error Analysis, The Study of Uncertainties in Physical Measurements*, 2nd ed.; University Science Books: Sausalito, United States, 1997.
[50] Mottet, C.; Tréglia, G. *Surf. Sci.* **1997**, *383*, L719.
[51] Jentys, A. *Phys. Chem. Chem. Phys.* **1999**, *1*, 4059.
[52] Frenkel, A. I.; Hills, C. W.; Nuzzo, R. G. *J. Phys. Chem. B* **2001**, *105*, 12689.
[53] Ramallo-López, J. M.; Requejo, F. G.; Craievich, A. F.; Wei, J. Avalos-Borja, M.; Iglesia, E. *J. Mol. Catal.* **2005**, *228*, 299.
[54] Liu, H.; Iglesia, E. *J. Phys. Chem. B* **2005**, *109*, 2155.
[55] Louis, C.; Tatibout, J. M.; Che, M. *J. Catal.* **1988**, *109*, 354.

3.8 Supporting Information

Contents

3.S1. Synthesis of silica-supported Au clusters

Au clusters dispersed on SiO_2 (Cab-O-Sil, HS-5, 310 m^2 g^{-1}) were prepared using an $Au(en)_2Cl_3$ (en=ethylenediamine) complex previously shown to lead to small clusters [S1]. $Au(en)_2Cl_3$ was prepared by dissolving $HAuCl_4 \cdot 3H_2O$ (1.0 g) in deionized H_2O (10 cm^3) and ethylenediamine (0.40 g) was then added. The solution was agitated by magnetic stirring (6.7 Hz) at ambient temperature for 0.5 h, and ethanol (70 cm^3) was then added to cause precipitation; the slurry was stirred for an additional 0.33 h and the solids were recovered by filtration and treated in ambient stagnant air at 313 K for 12 h.

Au/SiO_2 was prepared by dissolving $Au(en)_2Cl_3$ (0.03 g) in deionized H_2O (50 cm^3) and raising the pH to 10 by adding 1.0 M NaOH; SiO_2 (1.0 g) was added to the solution and 1.0 M NaOH was again used to adjust the pH to 10. The suspension was heated to 338 K while stirring for 2 h, filtered and washed with 1500 cm^3 deionized H_2O, and treated in stagnant ambient air at 343 K for 5 h. These Au/SiO_2 samples were heated from ambient to 423 K (at 0.033 K s^{-1}) in flowing H_2 (1.67 cm^3 g^{-1} s^{-1}) and held for 2 h. The samples were then cooled to ambient temperature, and finally heated to 673 K (at 0.033 K s^{-1}) in flowing dry air (1.67 cm^3 g^{-1} s^{-1}) and held for 2 h. These procedures were previously shown to form active Au clusters free of C and N residues from the ethylenediamine ligands [S1].

3.S2. Evidence for intracluster bimetallic mixing in AuPd and AuPt from UV-visible spectra

UV-visible spectra of treated metal-LTA were acquired using a Varian-Cary 6000i spectrometer with a Harrick scientific diffuse reflectance accessory (DRP-XXX) and a reaction chamber add-on (DRA-2CR). The spectra were collected in He (1 bar) at ambient temperature for Au-containing samples (AuNaLTA, Au_nPd_{100-n}NaLTA, Au_nPt_{100-n}NaLTA; 0.1 g) ground and sieved to retain aggregates <100 μm in diameter. Background spectra were used to isolate the effect of the embedded metals on the spectral absorbance, and were collected on NaLTA samples synthesized and treated as the metal-NaLTA samples but without the addition of metal cation precursors.

The UV-visible spectra of AuNaLTA, Au_nPd_{100-n}NaLTA, and Au_nPt_{100-n}NaLTA samples were used to confirm the absence of monometallic Au clusters in the bimetallic samples. Monometallic Au clusters and core-shell structures with Au shells would show localized surface plasmon resonance (LSPR, [S2,S3]) features at 500-600 nm [S2], but monometallic Pt and Pd clusters or mixed Au-Pd and Au-Pt clusters would not [S2]. Consequently, an LSPR band would diagnose the presence of Au clusters larger than the minimum size (2 nm diameter) required for detectable plasmon resonances [S3]. The UV-visible spectra of AuNaLTA, $Au_{67}Pd_{33}$NaLTA,

$Au_{67}Pt_{33}$NaLTA, and physical mixtures of AuNaLTA with PtNaLTA or PdNaLTA of the same atomic ratio are shown in Figure 3.S1.

AuNaLTA samples and physical mixtures of monometallic AuNaLTA and PdNaLTA or AuNaLTA and PtNaLTA exhibited LSPR absorption bands, consistent with Au clusters larger than 2 nm ($\langle d_{TEM} \rangle$=2.3 nm for AuNaLTA). The LSPR wavelength (~506 nm) is characteristic of Au clusters smaller than 5 nm in diameter [S3], but it does not depend on diameter for smaller clusters [S3]. All samples containing Pt or Pd showed only background absorption in the plasmon region (500-600 nm, [S2]). The absence of plasmon bands in $Au_{67}Pd_{33}$NaLTA and $Au_{67}Pt_{33}$NaLTA shows the absence of Au clusters or Au-rich surfaces, a conclusion also reached for samples with lower Au content (i.e. Au/Pd=0.5,1; Au/Pt=0.5,1). The clusters in $Au_{67}Pd_{33}$NaLTA (1.7 nm) and $Au_{67}Pt_{33}$NaLTA (1.4 nm), however, are smaller than Au clusters exhibiting detectable plasmon resonances. Only 7% and 2% of the clusters in these samples, respectively, are at or above this limit. Monometallic Au clusters, if present in the bimetallic samples, are expected to preferentially comprise these larger nanoparticles because of the relatively low Tammann temperature of Au. It is unclear, however, whether such small concentrations would have been evident in UV-Vis spectra via LSPR absorption. We therefore conclude that the absence of LSPR bands in Au-bimetallic samples is consistent with small cluster sizes and metal alloying, but does not independently confirm this alloying.

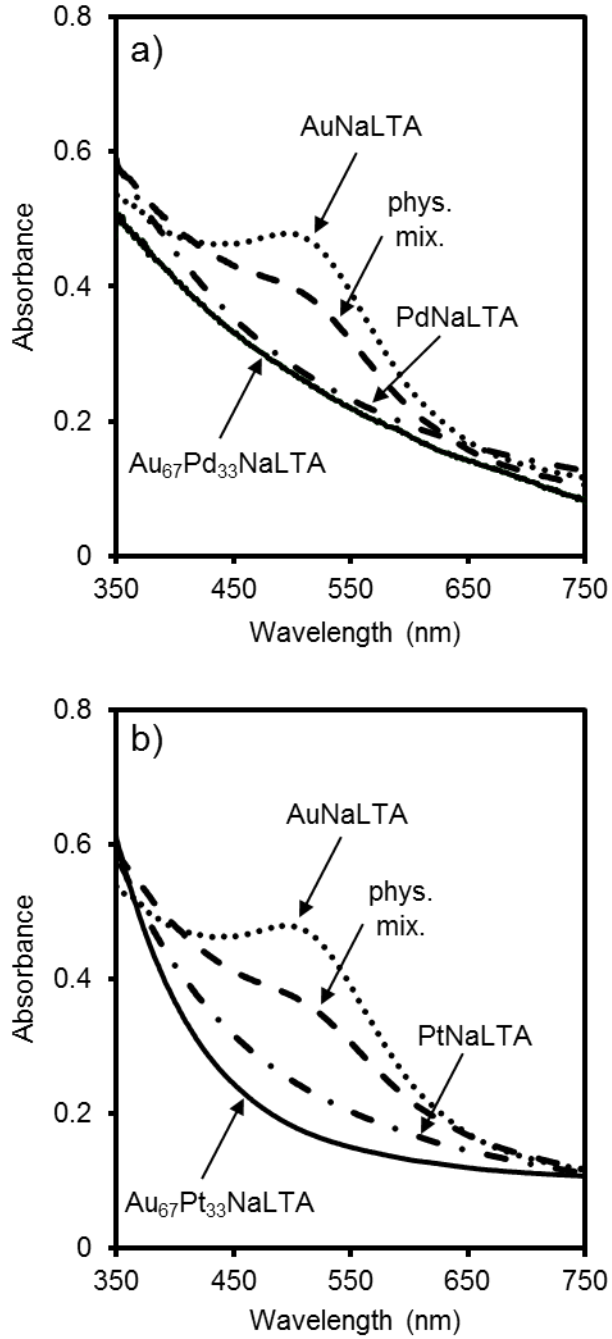

Figure 3.S1. UV-visible absorption spectra of monometallic Au clusters (•••), monometallic Pd (a) or Pt (b) clusters (−•−), a physical mixture of monometallic Au and Pd (a) or Au and Pt (b) clusters (− −), and bimetallic $Au_{67}Pd_{33}$ (a) or $Au_{67}Pt_{33}$ (b) clusters (solid line).

S3. XAS and EXAFS spectra of reference foils and bimetallic samples

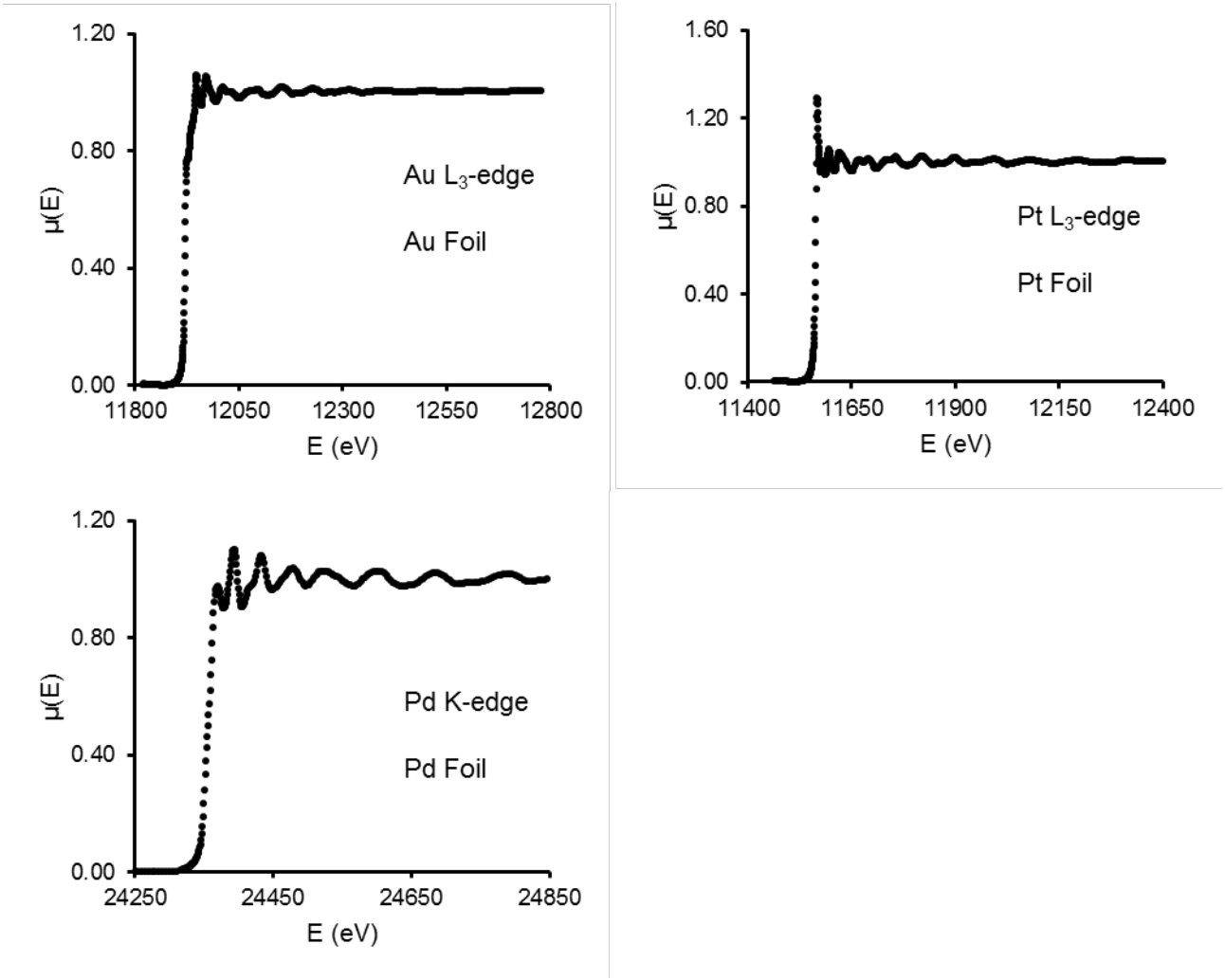

Figure 3.S2. Normalized and background corrected X-ray absorption spectra around the Au-L_3 edge, Pd-K edge, and Pt-L_3 edge of Au, Pd, and Pt foils, respectively.

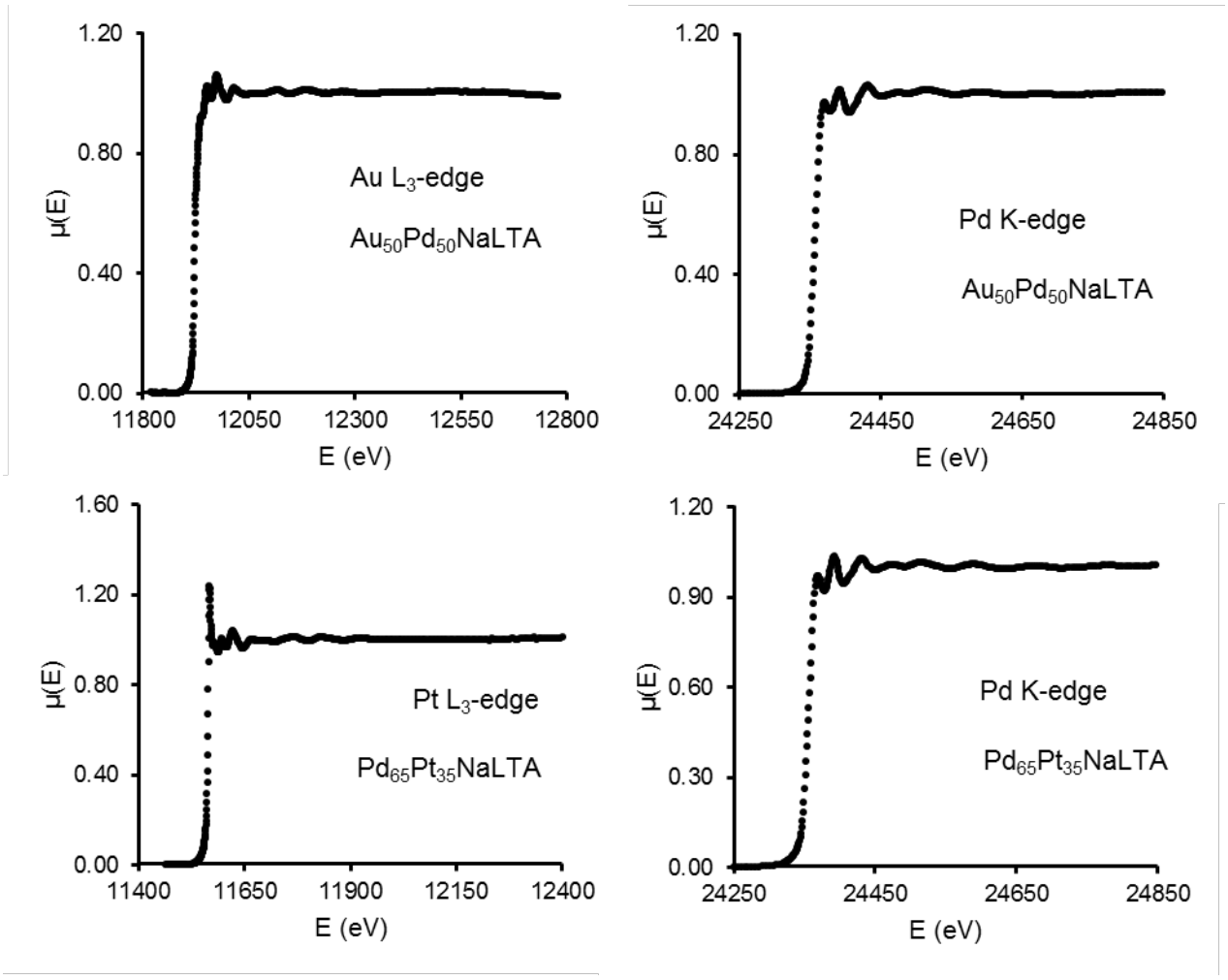

Figure 3.S3. Normalized and background corrected X-ray absorption spectra around the Au-L_3 edge, Pd-K edge, and Pt-L_3 edge of $Au_{50}Pd_{50}$NaLTA and $Pd_{65}Pt_{35}$NaLTA.

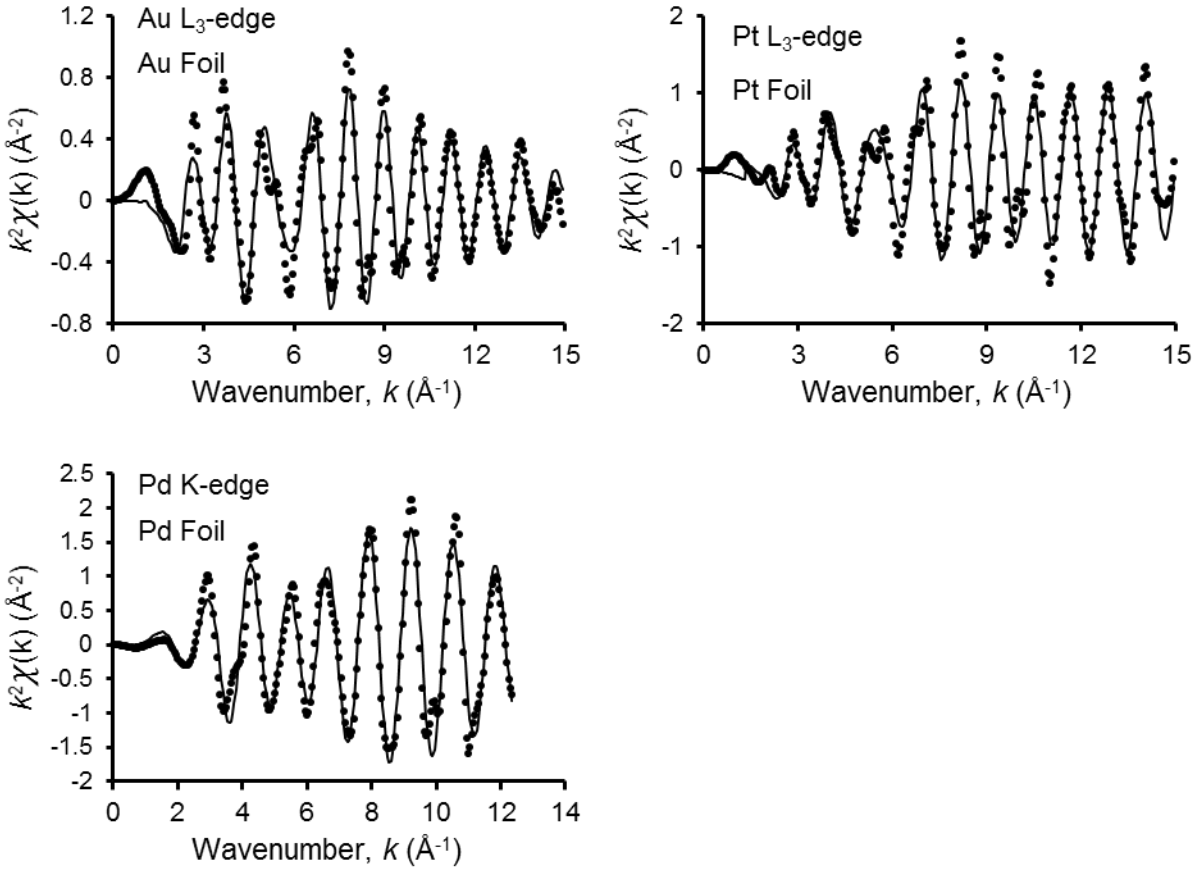

Figure 3.S4. k^2-weighted and background corrected EXAFS data and their corresponding single scattering fits around the Au-L_3 edge, Pd-K edge, and Pt-L_3 edge of Au, Pd, and Pt foils, respectively.

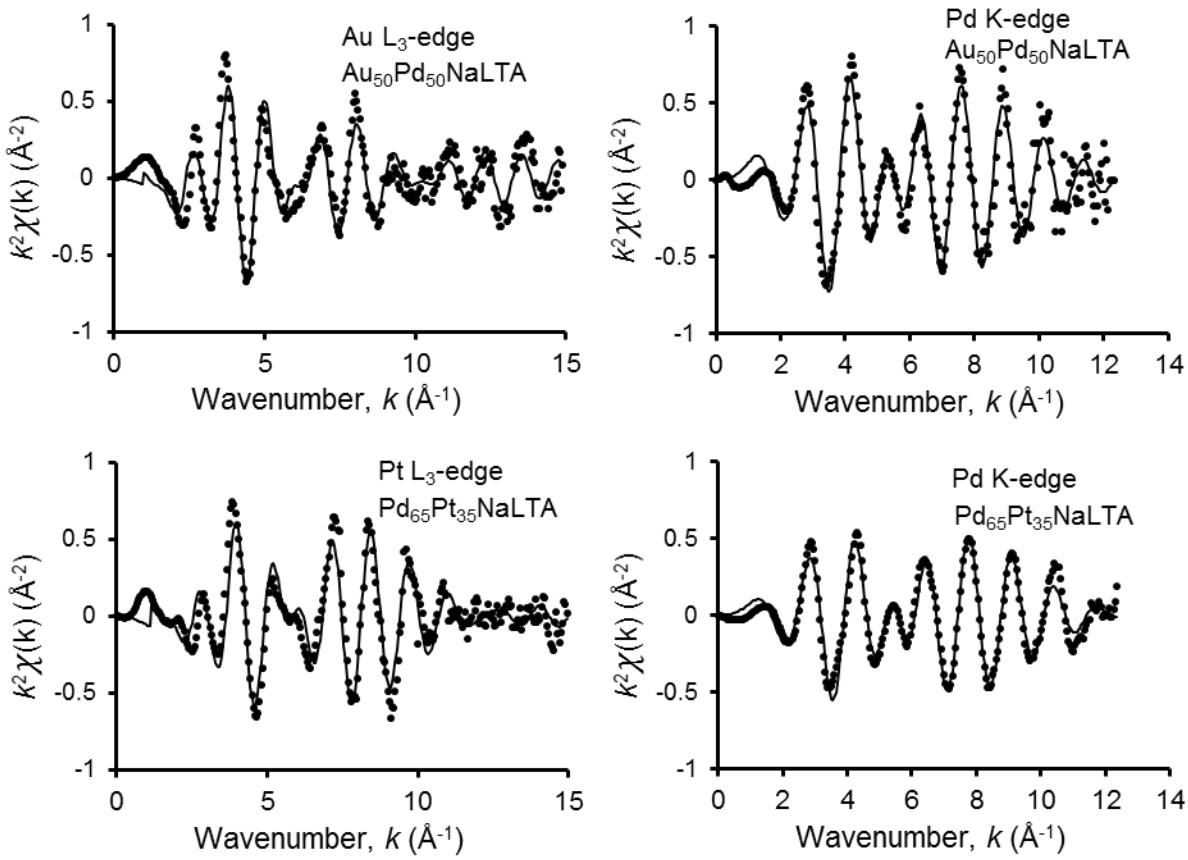

Figure 3.S5. k^2-weighted and background corrected EXAFS data and their corresponding single scattering fits around the Au-L_3 edge, Pd-K edge, and Pt-L_3 edge of $Au_{50}Pd_{50}$NaLTA and $Pd_{65}Pt_{35}$NaLTA.

References

[S1] Zhu, H.; Ma, Z.; Clark, J. C.; Pan, Z.; Overbury, S. H.; Dai, S. *Appl. Catal., A* **2007**, *326*, 89.
[S2] Kunz, S.; Iglesia, E. *J. Phys. Chem. C* **2014**, *118*, 7468.
[S3] Peng, S.; McMahon, J. M.; Schatz, G. C.; Gray, S. K.; Sun, Y. *Proc. Natl. Acad. Sci. U.S.A.* **2010**, *107*, 14530.

Chapter 4

Synthesis of highly dispersed cobalt oxide clusters encapsulated within LTA zeolites

Abstract

Small Co_3O_4 nanoparticles uniformly distributed in size were encapsulated within LTA zeolite crystals in a one-step process through hydrothermal self-assembly of crystalline frameworks around ligated Co^{2+} precursors. The use of bifunctional ligands containing a chelating bidentate amine functionality and an alkoxysilane moiety prevented the precipitation of Co^{2+} species as colloidal hydroxides in the highly alkaline synthesis gels, while also allowing the formation of linkages between precursors and the framework during the nucleation and growth of LTA crystals. Oxidative treatments of ligated compounds occluded within zeolite crystals removed ligand residues and formed small Co_3O_4 nanoparticles visible in transmission electron micrographs. These nanoparticles retained their small size (average diameter 1.5 nm) after oxidative treatment at 620-870 K, a reflection of their stabilization by confinement within zeolite voids. The infrared spectra of adsorbed CO on Co-LTA samples confirmed the absence of Co^{2+} as exchanged cations or aluminosilicates, indicating the presence of Co oxide clusters, with dynamics and stoichiometry of reduction in H_2 corresponding to small Co_3O_4 clusters. Ethanol oxidation rates on Co-LTA samples, exchanged with K^+ or Ca^{2+} cations to vary the diffusive properties of LTA crystals, indicated that more than 97% of the active surfaces on these Co_3O_4 clusters resided within zeolite crystals, where ethanol and O_2 concentrations depend on the diffusive properties of the LTA framework. The Co_3O_4 clusters prepared by these methods, in contrast with Co^{2+} in exchanged or aluminosilicate forms, exhibit reactivity in CO and NO oxidation. Their turnover rates (per exposed Co atom), however, were lower than on bulk Co_3O_4 powders, because of the combined effects of diffusional constraints imposed by the confining framework and the small size of these clusters, which leads to lower intrinsic reactivities as a result of their more difficult reduction during catalytic redox cycles. These clusters would be attractive in catalytic applications requiring stability against sintering during reaction or regeneration, reactant or product shape selectivity, or protection from contact with large molecules that block active surfaces. Such oxide clusters cannot be formed by sequential ion exchange, detachment by reduction to Co^0, and re-oxidation because the extremely high temperatures required for reduction destroy the aluminosilicate frameworks. The synthesis protocols and their mechanistic interpretations described herein represent a conceptual and practical platform for the encapsulation of nanoparticles of base elements within a broad range of confining crystalline environments through one-step hydrothermal self-assembly.

4.1 Introduction

The synthesis of Co oxide nanoparticles and their applications in heterogeneous catalysis are of interest because they are among the most active catalysts in CO oxidation [1], oxidative dehydrogenation [2], oxidative abatement of volatile organic compounds [3], and alcohol oxidation [4]. Co oxides are also precursors to Co metal particles active in Fischer-Tropsch synthesis catalysis [5]. The structure and size of such clusters influence turnover rates and selectivities for many of these reactions [4,5] and rigorous assessments of their effects on reactivity

require the synthesis of clusters that are thermally stable and narrowly distributed in size. Several strategies have been proposed for the synthesis of CoO_x particles; these include incipient wetness impregnation onto mesoporous supports [6,7], sol-gel methods [8], electrochemical deposition of Co^{2+} precursors onto solid substrates [9], and thermal decomposition of organometallic precursors in air [10] or under solvothermal conditions [11]. These methods, with some exceptions [7], typically lead to particles larger than 10 nm and broadly distributed in size [6,10]. Cobalt oxide clusters as small as 4 nm have been prepared through incipient wetness impregnation of cobalt precursors into mesoporous MFI zeolite nanosheets [7]. Such clusters reside within the mesoporous regions of the zeolite sheets and take on the size of the mesopores, which confer improved thermal stability to the cobalt oxide clusters relative to particles dispersed on γ-Al_2O_3. Clusters prepared through this technique, however, cannot retain sizes smaller than the mesopores produced natively by the zeolite synthesis (~4 nm) and do not benefit from the molecular sieving or size-selective effects of the zeolite during catalysis, which reflects their location within fully accessible mesoporous regions [7]. The full extent to which the cobalt particles are stabilized by the mesopores against sintering is also unclear. Highly dispersed CoO_x species make efficient use of Co atoms, but tend to sinter at the temperatures and reactive environments required for their use as catalysts [12].

Synthesis techniques that form metal (Au, Pd, Pt) and alloy (AuPd, AuPt, PdPt) nanoparticles within zeolitic voids of molecular dimensions have been shown previously to circumvent the stability and dispersity hurdles inherent to small metal particles [13-15]. Encapsulation within such voids inhibits the mobility and restricts the size of metal clusters [13], while also providing sieving and shape selective effects that allow preferential access to active sites by certain molecules [16], while stabilizing transition states with preferences that sense their fit within the confining voids [13,14]. When so required for catalytic use, such metal clusters can be converted to their corresponding oxides by thermal treatments in O_2. Most aqueous cations of base metals (e.g. Co^{2+}, Mn^{2+}, Ni^{2+}) [17,18], but not the cationic forms of noble metals (e.g. Pd^{2+}, Pt^{2+}, Au^{3+}) [19], can enter small-pore (8 member-ring (MR) apertures), as well as medium-pore (10 MR) and large-pore (12 MR) zeolites. Encapsulation is viable through post-synthesis aqueous ion exchange when solvated precursors can enter the apertures that connect the voids, but exchanged cations of base metals require reductive treatments at temperatures that often lead to significant sintering of the particles formed and to extracrystalline metal agglomerates [17,18]. Co^{2+} cations attached to LTA framework exchange sites, in particular, require treatments in H_2 above 1000 K to form Co^0 metal particles [17].

Here, we describe an alternate strategy to form Co_3O_4 nanoparticles within LTA zeolite crystals; such clusters are small (1.4-1.6 nm) and nearly monodisperse (dispersity index (DI) [20] 1.03-1.07). These protocols prevent the direct attachment of Co^{2+} cations to framework ion exchange sites through the use of ligands that preclude Co^{2+} species from exchange while promoting the self-assembly of the zeolite around Co precursors during hydrothermal crystallization. Bidentate amine ligands (N-[3-(trimethoxysilyl)propyl]ethylenediamine; TPE) chelate Co^{2+} cations to prevent premature $Co(OH)_2$ precipitation in highly alkaline synthesis gels and form siloxane linkages with LTA nuclei to induce their incorporation as crystallization occurs, without interfering with framework crystallinity at Co contents up to 4% wt. These Co^{2+}-TPE complexes do not form cation-framework linkages that render Co^{2+} species inert towards the formation of CoO_x clusters during subsequent thermal treatments. Ligands are removed by

treatment in O_2 at 623 K, leading to the formation of small and nearly monodispersed Co_3O_4 clusters, resistant to sintering even after O_2 treatment at 870 K.

The temperature and H_2 consumption stoichiometry during reduction confirmed their small size and their Co_3O_4 composition; they reduce at temperatures between those required for the reduction of bulk Co_3O_4 and Co^{2+} exchanged onto LTA. Infrared (IR) spectra did not detect bands for CO bound to exchanged Co^{2+} cations, cobalt silicates, or cobalt aluminates. Ethanol oxidation rates varied as different cations (Na^+, Ca^{2+}, K^+) were exchanged onto LTA crystals to change their intracrystalline diffusivities, consistent with the presence of Co_3O_4 clusters within such crystals. These LTA-encapsulated Co_3O_4 nanoparticles, but not exchanged Co^{2+} cations, were active for CO and NO oxidation, demonstrating their ability to undergo reduction-oxidation cycles and to dissociate molecular oxygen.

These encapsulation strategies, described here for Co-based LTA systems seem generally applicable to other base metals (Cu, Fe, Ni), which form similar stable amine complexes [21] that are essential for stabilization and encapsulation, and to other zeolites (e.g. FAU, EDF, GIS, SOD) that crystallize under hydrothermal conditions similar to those required to form LTA [22].

4.2 Methods

4.2.1 Source and purity of reagents used

$CoCl_2 \cdot 6H_2O$ (99.99%, Sigma-Aldrich), $[Co(NH_3)_6]Cl_3$ (99.99%, Sigma-Aldrich), $Co(NO_3)_2 \cdot 6H_2O$ (>98%, Sigma Aldrich), ethylenediamine (98%, Sigma-Aldrich), N-[3-(trimethoxysilyl)propyl]ethylenediamine (TPE; 98%, Sigma-Aldrich), Ludox AS-30 colloidal silica (30% wt. suspension in H_2O, Sigma-Aldrich), NaOH (99.99%, Sigma-Aldrich), $NaAlO_2$ (53% Al_2O_3, 42.5% Na_2O, Riedel-de Haën), $CaCl_2 \cdot 2H_2O$ (EMD Millipore), KCl (>99.0%, Sigma-Aldrich), Co_3O_4 (99.9%, Sigma-Aldrich), fumed SiO_2 (Davisil Grade 62, Sigma-Aldrich, 300 $m^2 g^{-1}$), acetone (99.9%, Sigma-Aldrich), ethanol (99.9%, Sigma-Aldrich), air (extra dry; 99.999%, Praxair), H_2 (99.999%, Praxair), He (99.999%, Praxair), Ar (99.999%, Praxair), CO_2 (99.999%, Praxair), N_2 (99.999%, Praxair), 4% H_2/Ar (99.999%, Praxair), 1% CO/He (99.999%, Praxair), CO (99.999%, Praxair), 3% NO/He (99.999%, Praxair), and 1% NO_2/He (99.999%, Praxair) were used as received.

4.2.2 Materials Synthesis

4.2.2.1 Synthesis of CoO_x clusters within LTA zeolites and cobalt oxide clusters dispersed on SiO_2

LTA was prepared in its Na form (NaLTA) with encapsulated CoO_x species (CoNaLTA) by adding Co cations protected by amine ligands (ammonia, ethylenediamine, or TPE) to zeolite synthesis gels and subsequent hydrothermal crystallization (373 K, 12 h). Syntheses with ethylenediamine or TPE ligands involved the initial dropwise addition of aqueous $CoCl_2 \cdot 6H_2O$ (0.18-0.91 g in 9 cm^3 deionized H_2O; 17.9 MΩ resistivity) at a rate of 0.2 cm^3 s^{-1} to aqueous ligand solutions (0.09-1.39 cm^3 ethylenediamine or 0.16-1.65 cm^3 TPE dissolved in 9 cm^3 deionized H_2O) while mixing with a magnetic stir bar (6.7 Hz). The amount of ligand used was adjusted for different batches to give ligand/metal molar ratios between 1 and 3. For the case of NH_3 ligands,

$[Co(NH_3)_6]Cl_3$ (0.20-1.00 g) was initially dissolved in 18 cm^3 of deionized H_2O. The aqueous solutions of ligands and metal cations were then transferred into a 125 cm^3 polypropylene bottle and colloidal silica (5.3 g, Ludox AS-30) and NaOH (2.4 g) were sequentially added; the container was sealed and kept at 353 K for 0.5 h with stirring by a magnetic bar (6.7 Hz) and then cooled to ambient temperature. Aqueous $NaAlO_2$ (3.0 g in 9 cm^3 deionized H_2O) was then added, and the contents were magnetically stirred (6.7 Hz) for 2 h at ambient temperature. The resulting homogeneous synthesis gels contained molar ratios of 1.7 SiO_2/1 Al_2O_3/3.2 Na_2O/110 H_2O/0.066-0.33 Co/0.066-0.99 ligand. The bottles containing the gels were sealed and the contents heated to 373 K for 12 h while stirring (6.7 Hz) to form as-synthesized CoNaLTA samples.

The Co content in the synthesis gels was chosen to achieve 1-5% wt. Co in the product solids based on a total yield of ~4.5 g, the approximate yield of NaLTA synthesized without Co using the procedure described here. The solids formed were separated by filtration (Pyrex 3606 fritted funnel, 4-5.5 μm) and washed with deionized water until the rinse liquids reached a pH of 7-8; they were then treated in a convection oven at 373 K for 8 h. The solids were finally heated in flowing dry air (1.67 $cm^3\ g^{-1}\ s^{-1}$) from ambient to 623 K (at 0.033 $K\ s^{-1}$) and held for 3 h. The cobalt content in these samples was measured by inductively-coupled plasma atomic emission spectroscopy (ICP-AES) or estimated from ultraviolet-visible analysis of supernatant liquids after synthesis (Section 4.2.3.3). Elemental analysis of Si, Al, Na, Ca, and K was also conducted to determine Si/Al ratios (Section 4.3.1) and cation contents (Section 4.2.2.2).

Cobalt oxide (Co_3O_4) particles dispersed on mesoporous SiO_2 were prepared and used in CO oxidation and NO oxidation reactions (Section 4.3.3.2) for comparison with LTA-encapsulated Co oxide clusters. Co/SiO_2 was prepared by incipient wetness impregnation of fumed SiO_2 using aqueous $Co(NO_3)_2$ to achieve 30% wt. Co loading. The SiO_2 support was heated in flowing air (1.67 $cm^3\ s^{-1}\ g^{-1}$) at 773 K for 5 h before impregnation; SiO_2 impregnated with $Co(NO_3)_2$ was heated in a convection oven at 400 K for 12 h and then heated again in flowing dry air (1.67 $cm^3\ g^{-1}\ s^{-1}$) to 773 K (at 0.083 $K\ s^{-1}$) and held for 5 h to form Co/SiO_2. This Co/SiO_2 sample was intended for use as a typical supported cobalt oxide catalyst in order to compare its properties with those of the Co-LTA materials considered in this work.

4.2.2.2 Ion-exchange of CoNaLTA samples with Ca^{2+} and K^+

CoNaLTA (0.4 nm apertures) [23] was fully exchanged with Ca^{2+} cations to form CoCaLTA (0.5 nm) [23] or with K^+ cations to form CoKLTA (0.3 nm) [23] in order to adjust the effective pore diameter of the LTA zeolites before using them in spectroscopic (Section 4.3.2.5) or catalytic (Section 4.3.3) experiments. CoNaLTA was also partially exchanged with Ca^{2+} with the intention of replacing half of the exchanged Na^+ ions with Ca^{2+} ions (assuming one Ca^{2+} ion displaces two Na^+ ions) and forming a sample with an effective aperture size between 0.4 and 0.5 nm; such partially exchanged samples are denoted $CoCa_{0.5}Na_{0.5}LTA$. CoCaLTA and CoKLTA were prepared by adding CoNaLTA (1 g) to aqueous $CaCl_2 \cdot 2H_2O$ or KCl solutions (3M; 100 cm^3/g zeolite) and stirring (6.7 Hz) at ambient temperature for 8 h. This exchange process was repeated three times in order to ensure full exchange. $CoCa_{0.5}Na_{0.5}LTA$ samples were prepared by adding CoNaLTA (1.00 g) to an aqueous solution of $CaCl_2 \cdot 2H_2O$ (0.15 M; 9 cm^3/g zeolite) and stirring (6.7 Hz, 24 h) at ambient temperature. The added quantities of CoNaLTA and $CaCl_2 \cdot 2H_2O$ gave a total Na^+/Ca^{2+} ratio of 4 based on the LTA unit cell stoichiometry

($[Na_{12}^{+}(H_2O)_{27}]_8[Al_{12}Si_{12}O_{46}]_8$) [23]. All samples were filtered and washed with deionized water (1500 cm^3 g^{-1}) after these exchange procedures and then heated in flowing dry air (1.67 cm^3 g^{-1} s^{-1}) from ambient temperature to 623 K (at 0.033 K s^{-1}) and held for 3 h.

Elemental analysis of CoNaLTA (3% wt. Co) after exchange with K^+ or Ca^{2+} confirmed the essentially full exchange of these cations into the product CoKLTA (K/Al=0.9) and CoCaLTA (Ca/Al=0.5) samples. The final Na/Ca ratio measured in the $CoCa_{0.5}Na_{0.5}$LTA sample (3% wt. Co; nominal Na/Ca ratio of 2 assuming full Ca^{2+} uptake) was 2.8.

4.2.2.3 Preparation of Co^{2+}-exchanged LTA

Co-LTA samples were prepared by direct ion-exchange of Co^{2+} cations onto NaLTA to provide comparative samples for the CoNaLTA samples prepared by hydrothermal crystallization (Section 4.2.2.1). These samples were compared using spectroscopic (Section 4.3.2.5) and catalytic (Section 4.3.3) data to determine differences in the type of Co species present in each sample and to confirm the absence of exchanged Co^{2+} cations in CoNaLTA. The exchange was carried out to achieve 3% wt. theoretical loading by adding 3 g NaLTA (synthesized as in Section 4.2.2.1 but without ligands or Co precursors) to an aqueous solution of $CoCl_2$•$6H_2O$ (0.36 g in 10 cm^3 H_2O) and stirring (6.7 Hz, 8 h) at ambient temperature. The samples were then filtered, washed, and treated in air as with the CoCaLTA and CoKLTA samples following their ion exchange procedures (Section 4.2.2.2). The essentially full Co^{2+} uptake into LTA (3% wt. Co; Co/Al=0.09) was confirmed by the UV-visible spectra (Section 4.2.3.3) of the supernatant liquids remaining after contact with LTA.

4.2.3 Characterization of frameworks and CoO_x particle size and stoichiometry

4.2.3.1 Powder X-ray diffraction

X-Ray diffractograms (XRD) were used to assess the crystallinity of all samples and to detect any large Co oxide agglomerates (>10 nm) present in CoNaLTA samples. Measurements were carried out using a D8 Discover GADDS Powder Diffractometer with Cu-Kα radiation (λ=0.15418 nm, 40 kV, 40 mA) over a 2θ range of 5-50° at 0.00625 degrees s^{-1} scan rates. Measurements were conducted on finely ground samples spread as a thin level coating onto quartz slides.

4.2.3.2 Transmission electron microscopy

Transmission electron microscopy (TEM) was used to measure the distribution of CoO_x cluster sizes. Micrographs were collected using a Philips/FEI Technai 12 microscope at 120 kV by dispersing ground powders in acetone and then onto holey carbon films supported on 400 mesh copper grids (Ted Pella Inc.). Size distributions were measured from >300 particles for each sample and used to determine surface-averaged cluster diameters $\langle d_{TEM} \rangle$ [24]:

$$\langle d_{\mathrm{TEM}} \rangle = \frac{\sum n_i d_i^3}{\sum n_i d_i^2} \qquad (1)$$

where n_i is the number of clusters with diameter d_i. These size distributions were also used to calculate a dispersity index (DI), defined as the ratio of the surface-averaged ($\langle d_{TEM} \rangle$) to the number-averaged ($\langle d_n \rangle$) mean diameters [24]:

$$\mathrm{DI} = \frac{\langle d_{\mathrm{TEM}} \rangle}{\langle d_n \rangle} = \frac{\left(\frac{\sum n_i d_i^3}{\sum n_i d_i^2}\right)}{\left(\frac{\sum n_i d_i}{\sum n_i}\right)} \qquad (2)$$

DI values provide the accepted metric of size uniformity, with values smaller than 1.5 typically considered to be monodisperse [20].

4.2.3.3 Ultraviolet-visible spectra of aqueous cobalt cation solutions

The ultraviolet-visible (UV-vis) spectra of the supernatant solutions remaining after hydrothermal CoNaLTA syntheses (Section 4.2.2.1) were used to estimate the residual concentrations of ligated Co precursors in solution. UV-vis spectra were measured on liquid aliquots held in quartz cuvettes (10 cm^3, Agilent) using a two-beam spectrophotometer (Varian Cary 400 Bio). Spectra were collected in the 450-650 nm wavelength range at scan rates of 5 nm s^{-1}. Aqueous cationic Co species exhibit strong absorption bands in the visible range (400-700 nm) [25]. Calibration curves relating the integrated intensity of these bands to the cobalt species concentrations were prepared using standard solutions of each ligated complex ($Co(NH_3)_6^{3+}$, Co^{2+}/ethylenediamine, Co^{2+}/TPE; Section 4.2.2.1). Such ligated complexes were dissolved in the supernatant liquid extracted from cobalt-free NaLTA syntheses in order to obtain reliable absorption cross sections. The volumes and Co concentrations of supernatant solutions from CoNaLTA syntheses were then used to calculate the Co uptake into the product solids formed. The accuracy of this technique was confirmed by comparing the calculated metal loadings to those measured directly with ICP analysis for 1% wt. and 3% wt. CoNaLTA samples; the error in the UV-Vis technique, relative to elemental analysis, was < 10%.

4.2.3.4 Temperature programmed oxidation of ligated Co species in Co-LTA zeolites

The formation of combustion products (H_2O, CO_2, N_2, N_2O, NO, NO_2) of ligands was monitored as a function of temperature during treatment of as-synthesized CoNaLTA samples in O_2. These temperature programmed oxidation (TPO) experiments were conducted to identify the stoichiometry of cobalt-ligand attachments and the conditions required for the removal of ligand residues from solid samples. Catalyst samples (0.2 g) were held on a porous quartz frit within a quartz tube (10 mm O.D.) placed in a resistively-heated furnace. Samples were first heated in He (8.3 $cm^3\ g^{-1}\ s^{-1}$) at 373 K for 2 h with the intent to remove physisorbed water and subsequently heated in 10% O_2/He (8.3 $cm^3\ g^{-1}\ s^{-1}$) to 850 K (at 0.167 K s^{-1}). The reactor effluent was analyzed using mass spectroscopy during the latter heating period in O_2; He (4 amu), H_2O (18 amu), N_2 (28 amu), O_2 (32 amu), CO_2 (44 amu), N_2O (44 amu), and NO/NO_2 (30 amu) mass signals were monitored every 10 s (Mini-lab, MKS Instruments, Orion Compact Residual Gas Analyzer; differentially-pumped atmospheric sampling system). Response factors for these species were calculated from calibration experiments using He, O_2, N_2, and CO_2 gases, or by heating in 10%

O_2/He flow known quantities of $Co(NO_3)_2$, which thermally decomposes to form precise quantities of NO_x(g) at ~573 K [26].

4.2.3.5 Temperature programmed reduction of Co species in Co-LTA zeolites

Temperature programmed reduction (TPR) experiments were conducted on CoNaLTA and CoCaLTA samples prepared using hydrothermal methods and ligated Co precursors (Section 4.2.2.1) and on Co-LTA samples prepared by Co^{2+} exchange (Section 4.2.2.3) to determine the Co oxidation state and the reduction onset temperature for each sample. TPR experiments were performed using a Micromeritics AutoChem II 2920 analyzer system equipped with a thermal conductivity detector (TCD) to monitor H_2 consumption. Catalyst samples (0.1 g) were loaded in a quartz U-tube reactor and first heated to 313 K in flowing Ar (0.83 $cm^3\ s^{-1}$) for 0.33 h. The Ar was then replaced with 4% H_2/Ar (0.83 $cm^3\ s^{-1}$) and the samples were heated (at 0.167 K s^{-1}) to 1273 K while the TCD signal in the reactor effluent was continuously monitored. The H_2 response factor for the TCD was determined by treating known amounts of Co_3O_4 to form Co metal while measuring the amount of H_2 consumed.

4.2.3.6 Infrared spectra of adsorbed CO on cobalt-LTA zeolites

The infrared (IR) spectra of CO adsorbed on CoCaLTA and Co^{2+}-exchanged LTA samples were collected in order to detect exchanged Co^{2+}, cobalt silicate, or cobalt aluminate species. The exchange of monovalent Na^+ cations in NaLTA with divalent cations (e.g., Ca^{2+} or Co^{2+}) decreases the total number of cation species in the framework and effectively widens LTA apertures, thus allowing more facile access by CO(g) to intracrystalline voids [13]. The Ca^{2+} exchanged form (CoCaLTA) of the hydrothermally prepared samples was therefore used for these IR experiments. IR spectra were acquired in transmission mode on wafer samples (40 mg cm^{-2}) using a Thermo Nicolet 8700 spectrometer equipped with an in-situ flow cell. Wafers were first heated in flowing He (40 $cm^3\ g^{-1}\ s^{-1}$) from ambient temperature to 473 K (at 0.033 K s^{-1}) and held for 1 h. The samples were then allowed to cool in flowing He to 313 K, and the He was replaced with 1% Co/He (40 $cm^3\ g^{-1}\ s^{-1}$). The wafers were exposed to flowing CO for 0.25 h before spectra were collected. The temperature and CO pressures were chosen in order to minimize coverages by physisorbed species and the adsorption of CO onto Ca^{2+} centers in CoCaLTA [13], which could interfere with the accurate assessment of the bands for CO adsorbed onto exchanged Co^{2+} cations. Contributions to the IR absorption from CO(g), though minimal, were subtracted from the reported spectra.

4.2.3.7 Catalytic assessment of reactivity and encapsulation

Ethanol (EtOH) oxidation turnover rates were measured on CoNaLTA, $CoCa_{0.5}Na_{0.5}$LTA, CoCaLTA, and CoKLTA catalysts that were first diluted (10-fold by mass) with mesoporous SiO_2 and pelleted and sieved to retain 180-250 μm aggregates. Catalyst samples were held on a porous quartz frit within a quartz tube (10 mm O.D.) and treated in 20% O_2/He (1.67 $cm^3\ g^{-1}\ s^{-1}$) at 573 K for 1 h before cooling to reaction temperatures (423-523 K) for rate measurements. Temperatures were controlled using a three-zone resistively-heated furnace; each zone was controlled with a Watlow Series 988 electronic controller. A K-type thermocouple (Omega) attached to the exterior of the quartz tubular reactor was used to measure temperatures. Liquid

EtOH was evaporated into flowing O_2/He streams at 393 K using a liquid syringe pump (Cole Parmer, 60061 Series); mass flow controllers (Porter Instrument) were used to adjust O_2 and He flowrates in order to achieve the desired reactant pressures (4 kPa alkanol, 9 kPa O_2, and 88 kPa He). EtOH conversions were kept below 3% to maintain differential conditions suitable for rate measurements and transfer lines were maintained at ~400 K to avoid condensation of EtOH or its reaction products.

Turnover rates are reported as the molar EtOH conversion rates per surface Co atom. The number of surface Co atoms present in each sample was estimated using the metal loading and cluster dispersion calculated from the surface-averaged nanoparticle diameter (Eq. 2), the bulk atomic density of Co atoms in Co_3O_4 (45 nm^{-3}) [27], and the surface density of fully exposed Co atoms on the (100) surface plane in bulk Co_3O_4 (6.1 nm^{-2}) [27]. Cobalt oxide clusters were assumed to be quasi-spherical. Effluent concentrations were measured using a Shimadzu GC-2014 gas chromatograph equipped with a methyl-silicone capillary column (HP-1; 50 m × 0.32 mm, 1.05 μm film thickness) and a flame ionization detector. Catalyst deactivation was not detected in the time scale of the rate measurements (~1-5 h). Experiments using empty reactors, mesoporous SiO_2, and Co-free LTA with Na^+ (NaLTA), Ca^{2+} (CaLTA), or K^+ (KLTA) counterions did not lead to detectable EtOH conversion levels.

The aperture size available for diffusion of molecules into LTA zeolites varies with the number and ionic radius of the charge-balancing cations exchanged into the framework (e.g. KLTA: 0.3 nm, NaLTA: 0.4 nm, CaLTA: 0.5 nm) [23]. Larger cations (e.g. K+, 0.137 nm) [28] occupy a larger fraction of the intracrystalline space than smaller cations (Na^+, 0.99 nm) [28], thus leading to smaller apertures throughout the LTA framework. Multi-valent cations (Ca^{2+}, 0.100 nm) [28] lead to cation to Al ratios lower than unity and to larger apertures than for monovalent cations. These variations in aperture size lead to more facile diffusion, specifically in this case for EtOH (0.40 nm kinetic diameter) [24] when Ca^{2+} replaces Na^+ or K^+ cations in Co-LTA samples. Rates of EtOH consumption are expected to increase monotonically with effective aperture size if (i) active CoO_x surfaces reside within the zeolite crystallites and (ii) reaction rates are limited by diffusion. A trend of increasing EtOH oxidation rates across samples with monotonically larger apertures would indicate that CoO_x clusters reside predominantly within LTA crystals.

4.2.3.8 Assessment of Co-LTA samples as catalysts for CO and NO oxidation

The reactivity of CoNaLTA, CoCaLTA, Co/SiO_2, and Co^{2+}-exchanged LTA catalysts was examined in CO and NO oxidation reactions. Oxidation rates were measured on catalyst samples (100 mg, 180-250 μm aggregates) diluted with quartz granules (100-900 mg; 180-250 μm aggregates) packed in a stainless steel tubular reactor (6.35 mm ID) for CO oxidation or held on a quartz frit in a quartz tube (10 mm OD) for NO oxidation. Samples were treated in flowing 20% O_2/He (0.83 cm^3 s^{-1}) at 573 K for 1 h, and then brought to the reaction temperature (473-633 K) for rate measurements. Temperatures were measured using a type K thermocouple and adjusted by resistive heating using a temperature controller (Watlow, 96 Series). Gas reactants (CO, NO, NO_2 He, O_2) were metered by electronic flow controllers (Porter Instrument) to achieve the desired reactant pressures and total flowrate for CO oxidation (1 kPa CO, 10 kPa O_2, 90 kPa He, 0.83 cm^3 s^{-1}) or NO oxidation (0.1 kPa NO, 0.3 kPa NO_2, 5 kPa O_2, 96 KPa He, 0.83 cm^3 s^{-1}). Reactant (CO and O_2) and product (CO_2) concentrations for CO oxidation reactions were measured by gas

chromatography (Agilent 6890 GC) using a Porapak Q packed column (80–100 mesh, 1.82 m × 3.18 mm) with a thermal conductivity detector. CO conversions were below 20% in all experiments. For NO oxidation, samples were exposed to reactants at the reaction temperature for 0.5 h before rate measurements. The reactor inlet and outlet NO and NO_2 concentrations were measured using an infrared analyzer (MKS Multi Gas Analyzer 2030, 2 cm^3 cell; 2 cm path length, 353 K). Measured NO conversions were below 20% for all samples. Plug-flow reactor formalisms were used to correct for changes in reactant concentrations along the catalyst beds and report turnover rates at inlet conditions. CO and NO turnover rates are reported as molar CO or NO conversion rates normalized by the number of surface Co atoms.

4.3 Results and Discussion

4.3.1 Effects of synthesis protocols on LTA crystallinity and phase purity and Co retention

CoNaLTA samples were prepared using different ligand species and a range of ligand/Co^{2+} ratios (1, 2, 3, and 6) and Co concentrations (1-5% wt. nominal Co loading) in order to probe the effects of these variables on metal uptakes and LTA crystallinity and, in doing so, to infer the nature of the processes that enforce encapsulation. Ligand species were chosen based on their ability (i) to prevent the precipitation of Co^{2+} cations as colloidal hydroxides at the pH and temperature of LTA synthesis, (ii) to promote the uptake of ligated precursors within LTA crystals, and (iii) to minimize any interference with the crystallization and phase purity of the LTA framework. The results of these studies are summarized in Table 4.1.

Synthesis gels (pH >14) were prepared using $[Co(NH_3)_6]Cl_3$ precursors (i.e. NH_3 ligands) to achieve 1% wt. nominal Co loading; the resulting suspensions changed from orange to black immediately upon heating to 373 K, consistent with the facile detachment of NH_3 ligands and the consequent precipitation of Co oxyhydroxides in such highly alkaline media. CoNaLTA syntheses using ethylenediamine ligands at ligand/Co^{2+} ratios of 3 showed no color changes that would indicate metal precipitation; these precursors led to the formation of crystalline LTA (XRD; Supporting Information (SI) Section 4.S1) without detectable CoO_x diffraction lines in the solid products formed.

The stability of these ligated Co^{2+} complexes during hydrothermal LTA crystallization reflects the chelation effects conferred by the bidentate ethylenediamine moieties. Their incorporation into the solid products (from UV-vis spectra of supernatant liquids; Section 4.S2), however, was not complete (~40% uptake of the Co^{2+} into the product), indicating that LTA crystals can nucleate and grow around ethylenediamine-Co^{2+} complexes, but without the selectivity required for their full retention within the solids formed. Such limitations were addressed by using N-[3-(trimethoxysilyl)propyl]ethylenediamine (TPE) ligands that include a bidentate amine function, but also an alkoxysilane moiety, intended as a strategy for the formation of siloxane bridges that attach the ligated precursors to silicate oligomers during LTA nucleation and growth. CoNaLTA samples synthesized using TPE at ligand/Co^{2+} ratios of 3 and 1% wt. nominal Co contents were crystalline (XRD; Section 4.S1) and free of prematurely precipitated CoO_x agglomerates; these ligands also led to the uptake of >90% of the Co atoms in the synthesis reagents into the crystalline LTA solids. This marked improvement in metal uptakes indicates that

the alkoxysilane moiety in TPE served its intended purpose as a linkage to incipient LTA frameworks without compromising Co^{2+} stability at high pH or the product LTA crystallinity.

The influence of TPE/Co^{2+} ratios (1, 2 and 3) on the stability of ligated Co^{2+} species, Co retention in product solids, and LTA crystallinity was examined for samples with nominal Co loadings of 1% wt. TPE/Co^{2+} ratios of 2 and 3 did not affect the stability of Co^{2+} against precipitation (no detectable precipitation in LTA synthesis gels (Section 4.2.2.1) at 373 K), LTA crystallinity (XRD; Section 4.S1), or Co retention in solids (~90%). Lower ratios (TPE/Co^{2+}=1), however, led to the precipitation of the Co precursors in the synthesis gels at the crystallization temperature (373 K). These data suggest that more than one TPE ligand must coordinate with a Co^{2+} cation to provide the requisite stability, while two TPE ligands are sufficient. Additional ligands may be unable to coordinate at the Co^{2+} center because of steric or electronic consequences brought forth by additional ligand coordination. These data indicate that TPE/Co^{2+} ratios of 2 are sufficient for stability, crystallinity, and Co retention within LTA crystals.

CoNaLTA samples were prepared with a TPE/Co^{2+} ratio of 2 and 1-5% wt. Co (nominal) in the synthesis gels in order to determine how metal loading influences LTA crystallinity and Co retention selectivity. Retention selectivities remained at ~90% for 1-5% Co contents based on UV-vis absorption measurements of supernatant solutions (Section 4.2.3.3). Solids with 1% and 3% Co loading also exhibited sharp diffraction lines for LTA crystals (Figure 4.1). These lines became broader for the sample with 4% Co, while the 5% sample gave a broad background characteristic of amorphous solids, suggesting that ligated precursors, when present at these higher precursor loadings, can disrupt LTA nucleation and growth. The number of Co atoms per LTA α-cage in 1% and 3% wt. CoNaLTA samples (assuming one α-cage in the $([Na_{12}^{+}(H_2O)_{27}]_8[Al_{12}Si_{12}O_{46}]_8)$ lattice [23]) are approximately 3 and 9, respectively. The size of the LTA α-cage (1.1 nm void diameter) [24], however, is of similar diameter as a Co^{2+} cation with two attached TPE ligands (~1 nm, estimated using MolView, v. 2.2, largest dimension) [29], the number of ligands determined in Section 4.3.2.1 from the products evolved during oxidative treatments. Thus, 3-9 Co atoms, each with two attached TPE ligands, cannot reside within each LTA α-cage. Yet, EtOH oxidation reactivity studies (Section 4.3.3.1) indicate that most Co oxide species reside within the intracrystalline LTA voids, as also shown by the small and uniform Co_3O_4 clusters evident in transmission electron micrographs (Section 4.3.2.2) after oxidative treatments, which cannot be predominantly located at the low external surface areas of LTA crystals. Micropore volume and surface area measurements (Section 4.S3) conducted on such oxidatively treated CoNaLTA (0.32 $cm^3\ g^{-1}$; 1030 $m^2\ g^{-1}$) and CoCaLTA (0.27 $cm^3\ g^{-1}$; 880 $m^2\ g^{-1}$) samples (3% wt. Co; CoCaLTA formed from Ca^{2+} ion exchange, Section 4.2.2.2) were similar to metal-free NaLTA (0.34 $cm^3\ g^{-1}$; 1090 $m^2\ g^{-1}$) and CaLTA (0.29 $cm^3\ g^{-1}$; 970 $m^2\ g^{-1}$) samples, further confirming that the zeolite micropore structure remains intact despite the presence of these cobalt oxide particles within the crystallites. Si/Al ratios for crystalline NaLTA and 3% wt. CoNaLTA samples, measured using elemental analysis (Section 4.2.2.1), were 0.98 and 1.02, respectively.

We surmise that the ligated Co^{2+} moieties reside within cavities larger than the α-cages, but still present within LTA crystals, leading to localized disruptions of the crystal lattice without compromising the integrity of the crystallites. When present as small fractions of the crystal volume, nucleation and growth can proceed unaffected, and the subsequent removal of the ligands during oxidative treatments leads to Co_3O_4 clusters and to the healing of the framework in the

surrounding larger voids; such clusters remain protected from the external fluid phase by the diffusional barriers imposed by the many intervening windows between such clusters and the LTA external surfaces. These results provide the required guiding principles for preparing ligated Co species occluded within LTA crystals; these species act as convenient precursors to encapsulated Co_3O_4 clusters, suitable as size-selective catalysts (Sections 4.3.2 and 4.3.3). The selective retention of ligated Co species requires ligands that simultaneously stabilize metal cations in alkaline media and act as nucleation centers for crystallization; the Co loading, however, is inherently limited by the ability of the frameworks to assemble in the presence of high concentrations of ligated complexes that locally disrupt the LTA crystal periodicity. In the next section, we discuss the process by which such ligated Co species can be converted into encapsulated Co_3O_4 clusters.

4.3.2 Characterization of Cobalt-LTA samples

4.3.2.1 Temperature programmed oxidation studies of as-synthesized Cobalt-LTA samples

As-synthesized CoNaLTA samples (discussed in Section 4.3.1; 1% and 3% wt. Co) were treated in O_2 with the intent of removing TPE ligands and forming CoO_x clusters. Such clusters would be expected to form if the ligated complexes precluded the formation of direct Co^{2+}-framework linkages that would render Co^{2+} species inert towards the formation of oxide clusters. The evolution of the products of ligand decomposition and oxidation was monitored by mass spectroscopy as 1% and 3% wt. CoNaLTA samples were heated in 10% O_2/He to 850 K (at 0.167 K s^{-1}; Section 4.2.3.4) in order to determine the Co-ligand stoichiometry and the conditions required for complete removal of the ligands. The TPO profile for 3% wt. CoNaLTA is shown in Figure 4.2 (1% wt. Co sample in SI, Section 4.S4). H_2O, CO_2, N_2, and NO were detected during these treatments; their rates of formation reached a sharp maximum at ~623 K and ligand decomposition was essentially complete by 750 K (Figure 4.2). N/Co and C/Co ratios calculated for 3% wt. CoNaLTA were 3.8±0.4 and 10.5±0.7 (3.9±0.4 and 9.6±0.7 for 1% wt. sample) respectively, consistent with the presence of two TPE ligands per Co atom and with their full removal during thermal treatment. These data were used to select post-synthesis treatments required to decompose ligated precursors (Section 4.2.2.1; treatment in dry air at 623 K, 3 h); decomposition products were not detected upon further treatment of these samples in 10% O_2/He to 850 K, consistent with the prior full removal of all C, N, and H atoms introduced as part of the TPE ligands.

Diffuse reflectance ultraviolet-visible (DR UV-vis) spectra (Section 4.S5) were acquired on as-synthesized CoNaLTA, Co^{2+}-exchanged LTA (Section 4.2.2.3), and oxidatively treated CoNaLTA samples to further demonstrate that oxidative treatment removes the ligands attached to Co^{2+} cations in CoNaLTA, and that such treatment leads to the formation of cobalt oxides. The absorption spectrum of as-synthesized CoNaLTA showed ligand to metal charge transfer and d-d transition bands originating from the ligated Co^{2+} cations in the sample (Section 4.S5). Such bands were absent in oxidatively treated CoNaLTA, consistent with the removal of TPE ligands attached to Co^{2+} cations and the formation of CoO_x species during oxidative treatment (Section 4.S5). Co^{2+}-exchanged LTA showed an intense d-d transition feature characteristic of Co^{2+} cations attached to zeolite exchange sites; similar features were not apparent in the spectra of as-synthesized and oxidatively treated CoNaLTA, consistent with the absence of exchanged Co^{2+} cations in those

samples. These DR UV-vis spectra are therefore consistent with TPO results indicating the removal of TPE ligands from CoNaLTA during oxidative treatment, and further indicate the prevalence of different coordination environments for Co species in as-synthesized CoNaLTA, oxidatively treated CoNaLTA, and Co^{2+}-exchanged LTA samples.

4.3.2.2 Assessment of CoO_x cluster sizes after oxidative treatment of as-synthesized Co-LTA samples

Transmission electron microscopy (TEM) was used to detect the presence of any Co-derived nanoparticles after oxidative treatments and to determine the size of such particles in CoNaLTA and in these samples after Ca^{2+} or K^+ exchange (to form CoCaLTA, $CoCa_{0.5}Na_{0.5}$LTA, or CoKLTA; Section 4.2.2.2). Figure 4.3 shows electron micrographs, cluster size distributions, and dispersity indices (DI; Eq. 2) in these samples. Small clusters were evident in all samples, with surface-averaged diameters (Eq. 1) of ~1.5 nm and narrow size distributions (DI 1.03-1.07). The dispersions of these clusters range from 0.51 (for $\langle d_{TEM} \rangle$=1.6; Eq. 1) to 0.58 (for $\langle d_{TEM} \rangle$=1.4; Eq. 1) (Section 4.2.3.7). Their reduction profiles (Section 4.3.2.4) and infrared spectra (IR; Section 4.3.2.5) indicate that such particles consist of small Co_3O_4 crystallites; they are somewhat larger than the α-cages in LTA (1.1 nm) [24], indicating that they reside within local disruptions of the LTA framework, which do not affect, however, the long-range periodicity of the zeolite crystals (X-ray diffractogram of air-treated CoNaLTA in Section 4.S1). The small and uniform size of these clusters indicates that ligated precursors were uniformly distributed within the gel precursors as LTA crystals formed, leading to a high density of nucleation points during ligand removal. Mean cluster sizes were similar in 1% wt. (1.4 nm) and 3% wt. (1.6 nm) CoNaLTA samples (actual Co contents 0.90% wt. and 2.64% wt. by ICP), as also found for the case of Au clusters within LTA [13]. Such size "limits" may reflect the compensating energies inherent in metal oxide cluster growth to decrease surface energy [30] and in the disruption of the LTA framework required to accommodate clusters larger than the native α-cages in LTA frameworks.

Co-LTA prepared by the direct exchange of Co^{2+} cations (Section 4.2.2.3), in contrast with CoNaLTA prepared by hydrothermal methods (Section 4.2.2.1), did not show any CoO_x agglomerates in micrographs, even after thermal treatments in flowing dry air at 623 K. These data suggest that the TPE ligands coordinated to the Co^{2+} precursors preclude the formation of linkages between Co cations and the zeolite framework; in doing so, these ligands allow the formation of CoO_x clusters after oxidative treatments. Such clusters are suitable as catalysts for redox reactions involving lattice O-atoms, while exchanged Co cations are essentially unreactive as catalysts for such transformations. These conclusions are consistent with the infrared spectra of bound CO shown below in Section 4.3.2.5.

4.3.2.3 Thermal stability of cobalt oxide clusters in LTA

Nanoparticles confined within microporous networks (e.g., Au, Pd, Pt) [13-15,24] show exceptional resistance to coalescence and form larger particles at much higher temperatures than those of similar size dispersed on mesoporous silicates. Such properties reflect kinetic hurdles to migration and thermodynamic effects that balance the lower surface energy of larger crystallites with the required disruptions of the encasing framework.

The thermal stability of CoO_x nanoparticles in CoNaLTA samples was assessed from TEM-derived size distributions (Fig. 4.3) for CoNaLTA samples (1% and 3% wt. Co) treated in flowing dry air (1.87 $cm^3\ s^{-1}\ g^{-1}$) by heating to temperatures between 623 K and 1023 K (at 0.033 $K\ s^{-1}$) and holding for 3 h. Surface-averaged cluster diameters ($\langle d_{TEM} \rangle$; Eq. 1) and dispersity indices (DI; Eq. 2) for 3% wt. CoNaLTA after these treatments are shown in Figure 4.4 (1% wt. sample in SI, Section 4.S6). Thermal treatments up to 873 K did not lead to any detectable changes in $\langle d_{TEM} \rangle$ (1.5 nm for 1%; 1.6 nm for 3%) or DI (1.07 for 1%; 1.06 for 3%) values for both loadings, consistent with the retention of cluster sizes and their monodispersity. Treatment at temperatures of 973 K or greater, however, led an increase in cluster size (to 3.7 and 4.4 nm for 1% and 3% at 1023 K) and dispersity indices (1.34 and 1.40 for 1% and 3% at 1023 K). This increase in cluster size coincides with the thermal decomposition of the LTA structures at 1023 K (XRD; Section 4.S7), suggesting that intact frameworks are essential to stabilizing the highly dispersed cobalt oxide clusters. We will show in Section 4.3.2.5 through IR studies that thermal treatment at 1020 K also causes a significant fraction of the CoO_x nanoparticles to react with the decomposed residues of the framework and form Co aluminosilicates.

The weak effects of metal content on cluster size and stability suggest that the LTA framework, when intact, imposes a limit on the size to which CoO_x clusters can grow. Such limits would favor a high density of nucleation points in high-loading samples and, consequently, small CoO_x clusters of size insensitive to Co content. We surmise that constraints to cluster growth include kinetic limits to metal oxide mobility imposed by the intervening apertures and thermodynamic barriers arising from the energy needed to distort the framework in regions surrounding the particles to allow cluster growth. These considerations and unique stability would require the predominant presence of such clusters within LTA crystallites, which preserve such clusters at conditions that would otherwise lead to their extensive growth. More direct evidence of encapsulation is presented in Section 4.3.3.1 from diffusional effects on the reactivity of these samples for ethanol oxidation.

4.3.2.4 Reducibility of cobalt species in cobalt-LTA samples

The oxidation state and reduction dynamics of Co species in CoNaLTA and Co^{2+}-exchanged LTA were determined using temperature-programmed reduction (TPR) methods involving treatment in 4% H_2/Ar from 313 K to 1273 K (at 0.167 $K\ s^{-1}$) and measurements of H_2 consumption by thermal conductivity (Section 4.2.3.5). The full reduction of zeolite-exchanged Co^{2+} species requires temperatures above 1000 K [17], while bulk Co_3O_4 and CoO reduce at much lower temperatures (473-673 K) [31]. Small CoO_x domains are more resistant to reduction in H_2 than larger crystallites, a trend typically attributed to stabilization of oxides by interactions with the support [5,32,33] or to larger HOMO-LUMO gaps in highly dispersed semiconducting oxides [34]. CoO_x and exchanged Co^{2+} species on silicates (e.g. mesoporous SiO_2, MCM-41) [31,35,36] and aluminates (e.g. Al_2O_3) [37] also form Co-O-Si or Co-O-Al linkages upon thermal treatments in air or H_2 to temperatures above 900 K, because of the formation of Co_2SiO_4 or $Co_2Al_2O_5$ crystallites that require very high temperatures (and significant growth) for their full reduction in H_2 (>900 K) [35,37]. These temperatures approach the stability limits of the LTA structure and most other zeolite frameworks (~1000 K) [38].

Figure 4.5 shows reduction profiles for bulk Co_3O_4, 3% wt. CoNaLTA, 3% wt. CoCaLTA, and Co^{2+}-exchanged LTA (3% wt. Co; Section 4.2.2.3). The onset of bulk Co_3O_4 reduction appeared at ~500 K and showed two features with H_2/Co consumption ratios of 0.33±0.03 and 1.00±0.08, corresponding to the sequential reduction of Co_3O_4 to CoO and then to Co^0 [31]. Co^{2+}-exchanged LTA samples gave a single feature starting at a much higher temperature (~1000 K), consistent with the presence of refractory Co^{2+} cations linked to Si or Al atoms in the framework [17] or Co aluminosilicates [35,37]. The H_2/Co consumption ratio (1.06±0.08) was that expected from the reduction of all Co^{2+} cations exchanged onto LTA. CoNaLTA and CoCaLTA prepared via hydrothermal assembly (Section 4.2.2.1) each gave two reduction features; the first feature (onset at ~800 K) appears at a much higher temperature than in bulk Co_3O_4 (500 K), consistent with the high dispersion of the CoO_x clusters. The second feature (onset at ~1000 K) resembles that for Co^{2+}-exchanged LTA. Such similarities may indicate that some Co species exchanged during hydrothermal synthesis of CoNaLTA or that exposure to these high temperatures lead to LTA structural degradation, loss of confinement, and the consequent formation of Co silicates or aluminates. The absence of the CO IR bands expected for exchanged Co^{2+}, cobalt aluminates, and cobalt silicates in CoCaLTA (Section 4.3.2.5) rules out their formation during synthesis or post-synthesis air treatment at 623 K (Section 4.2.2.1). We will show that the much higher temperatures used during TPR (~1000 K) lead to the degradation of the zeolite and to structural rearrangements that favor the formation of dense mixed oxide structures (Section 4.3.2.5); the reduction of Co cations within such structures account for the H_2 consumption feature centered at ~1100 K.

The total H_2/Co consumption ratios for CoNaLTA and CoCaLTA were slightly larger than unity (1.16±0.09 and 1.14±0.09, respectively), as expected from the presence of Co^{3+} species as Co_3O_4. The presence of Co_3O_4 was also confirmed by CO oxidation rates (Section 4.3.3.2), that depend on the tendency of Co^{3+} to undergo reduction-oxidation cycles [39]. The H_2/Co ratios are lower than expected from pure Co_3O_4 (1.33), indicating that some Co^{2+} species are present as CoO. The Co_3O_4 phase is thermodynamically favored in bulk CoO_x compounds at ambient O_2 pressures below ~1100 K [40]; however, small CoO clusters can persist in oxidizing environments well below this temperature [11], which may reflect hurdles imposed by nucleation barriers or thermodynamics that favor CoO in small clusters because of surface energy considerations. About half of the H_2 is consumed as part of the low-temperature feature (800 K; H_2/Co ratios of 0.66±0.08 and 0.64±0.08 for CoNaLTA and CoCaLTA), suggesting that CoO_x clusters can be partially reduced before their conversion to cobalt aluminosilicates and their ultimate reduction at higher temperatures. These reduction profiles are consistent with the presence of highly dispersed CoO_x clusters in CoNaLTA and CoCaLTA samples after their post-synthesis air treatment at 623 K (Section 4.2.2.1), though the additional presence of some exchanged Co^{2+} cations or Co aluminosilicates cannot be excluded using these data alone. In the next section, evidence is presented to confirm the absence of such Co species using infrared spectroscopy.

4.3.2.5 Identification and assessment of Co species within cobalt-LTA zeolites by infrared spectra of chemisorbed CO

The infrared spectra of CO adsorbed on CoCaLTA, Co_3O_4, and Co^{2+}-exchanged LTA was used to detect the presence of exchanged Co^{2+} and Co aluminosilicates. The CoNaLTA samples (0.4 nm apertures) [23] were first exchanged with Ca^{2+} to form CoCaLTA (0.5 nm apertures) [23], so as to allow CO diffusion at the mild temperatures (~300 K) required for detectable CO

coverages (Section 4.2.2.2) [13]. UV-vis spectra (Section 4.2.3.3) of the supernatant liquids during Ca^{2+} exchange of CoNaLTA did not detect any leached Co^{2+} species. The infrared spectra of CO adsorbed on CoCaLTA (3% wt. Co; $\langle d_{TEM} \rangle$=1.6 nm), Co^{2+}-exchanged LTA (3% wt. Co), and Co_3O_4 at 313 K and 1 kPa CO are shown in Figure 4.6.

The Co^{2+}-exchanged LTA sample shows an intense infrared band at 2180 cm^{-1}, attributed to CO at exchanged Co^{2+} species in zeolites [41,42], while the bulk Co_3O_4 sample did not show comparably intense features in the carbonyl frequency range (1900-2400 cm^{-1}) [41-44]. CoCaLTA also did not show significant bound CO features upon contact with CO(g), indicative of the absence of accessible exchanged Co^{2+} cations, Co silicates, or Co aluminates, which bind CO and would have given intense CO stretches between 2150-2200 cm^{-1} [45-47]. CoCaLTA samples heated in air or H_2 to 1020 K, however, showed absorption bands at 2175 cm^{-1} (Section 4.S7) and significant structural degradation (XRD; Section 4.S7), consistent with LTA decomposition and consequent formation of Co aluminosilicates at these temperatures. The formation of these refractory Co aluminosilicates account for the high temperature reduction feature in TPR (at ~1100 K; Section 4.3.2.4). The absence of significant infrared bands for CO physisorbed on Co_3O_4 [44] or adsorbed on Ca^{2+} cations in CoCaLTA [13,41] reflects the very low CO pressures (1.0 kPa) and modestly high temperatures (313 K) used. These data, taken together with TEM (Section 4.3.2.2) and TPR (Section 4.3.2.4) evidence, show that ligated precursors prevent the formation of exchanged Co^{2+} species or Co aluminosilicates during hydrothermal synthesis of CoNaLTA and lead instead to the formation of CoO_x clusters. These clusters reduce at lower temperatures than exchanged Co^{2+} species bound within inorganic aluminosilicates and are expected to exhibit redox properties more conducive to catalytic turnovers in oxidation reactions than bound isolated cations (Section 4.3.3.2).

4.3.3 Consequences of encapsulation for CoO_x reactivity and diffusional effects on reaction rates as evidence for encapsulation

The size and dispersity of CoO_x clusters in CoNaLTA (Section 4.3.2.2) are consistent with encapsulation within zeolite crystals because of the absence of large structures, their thermal stability, and their unlikely dispersion on the limited external areas of LTA crystals. These CoO_x particles are highly dispersed (1.4-1.6 nm diameter), thermally stable (in 873 K air treatment, 3 h), narrowly distributed in size (DI 1.03-1.07), and uniformly dispersed throughout zeolite crystals (Fig. 4.3). These properties would be atypical for extracrystalline structures, but reflect instead confinement effects that impose thermodynamic and kinetic obstacles to coalescence and sintering [13,14,24]. Their catalytic properties, however, provide the motivation for their synthesis, and the ability of only certain molecules to contact active sites, based on their size and diffusion properties, remain the ultimate arbiter of the selectivity of the synthetic protocols in enforcing encapsulation.

Here, we provide evidence for CoO_x encapsulation from ethanol (EtOH) oxidation reaction rates on Co-LTA samples with varying aperture widths, imposed by the presence of K^+, Na^+, or Ca^{2+} cations (Section 4.2.2.2). Turnover rates that increase as the apertures are made larger to allow more facile access to intracrystalline regions and faster reactant diffusion would then serve as evidence for the presence of active sites within constrained environments, accessible only via such diffusive processes. These effects of cation substitution, when interpreted in terms of appropriate kinetic-transport formalisms, also lead to precise estimates for the encapsulation

selectivity, defined here as the fraction of active CoO_x surface area residing within LTA crystals in each sample.

4.3.3.1 Ethanol oxidation rates on cobalt-LTA catalysts as a probe for deducing encapsulation selectivity

Molecules, whether reactants or poisons, cannot contact active sites and react unless their size allows intracrystalline diffusion in the time scale of catalytic turnover rates. The intracrystalline voids can also preferentially stabilize transition states based on their size and fit within such voids [13,14,19,24]. Here, we exploit the size-selective properties of LTA zeolites by measuring ethanol (EtOH, 0.40 nm kinetic diameter) [24] oxidation rates on CoNaLTA samples exchanged with K^+ or Ca^{2+} cations (to form CoKLTA, CoNaLTA, $CoCa_{0.5}Na_{0.5}$LTA, or CoCaLTA; Section 4.2.2.2) in order to vary their diffusion properties and to estimate the fraction of the CoO_x surface area that resides within zeolite crystallites.

LTA zeolites with these different cations contain apertures of different size (e.g., KLTA: 0.3 nm, NaLTA: 0.4 nm, CaLTA: 0.5 nm; Section 4.2.2.2) because they differ in the number and size of the exchanged species [23]. These apertures determine the approximate size of molecules that can traverse such openings and access intracrystalline active sites [48]; their unequivocal interpretation as a precise pore dimension is precluded by temperature-dependent framework and molecular distortions [48], but the trends of diffusivity with the various cations is clear and well-established [23]. The identity of the exchanged cation would affect EtOH oxidation rates only when CoO_x structures predominantly reside within LTA crystals, because of concomitant effects on EtOH concentration gradients, and specifically, rates would increase as apertures become larger (in the order CoKLTA, CoNaLTA, $CoCa_{0.5}Na_{0.5}$LTA, CoCaLTA).

EtOH oxidation rates were measured at 423-523 K on these samples at 1% and 3% wt. Co loadings (Section 4.2.3.7). Turnover rates are defined here as the molar rate of EtOH conversion per surface Co atom (estimated from the metal loading, $\langle d_{TEM} \rangle$ and the surface area; density of Co atoms in Co_3O_4; Section 4.2.3.7); these rates are shown in Figure 4.7 as a function of reciprocal temperature. Acetaldehyde was the only detectable product for each sample. Rates increased exponentially with temperature (appearing linear on the Arrhenius plot) on all samples. EtOH turnover rates are higher on LTA zeolites with larger apertures at all temperatures, consistent with weaker EtOH concentration gradients as its diffusion becomes more facile. For instance, turnover rates on CoCaLTA were about 40-fold higher than on CoKLTA, indicative of severe constraints in accessing intracrystalline CoO_x active structures in CoKLTA. Turnover rates on $CoCa_{0.5}Na_{0.5}$LTA were intermediate between those on CoNaLTA and CoCaLTA, reflecting the faster diffusion allowed by the partial replacement of two Na^+ for each Ca^{2+}. These results are consistent with previous studies of EtOH oxidation rates on LTA-encapsulated Au clusters, which showed that the narrow LTA apertures lead to diffusional effects on EtOH oxidation rates [13].

The kinetic diameter of ethanol (0.40 nm) [14] is larger than the effective pore diameter of KLTA (0.3 nm) [23], suggesting that turnover rates measured on CoKLTA samples arise predominantly from reaction events occurring on extracrystalline CoO_x surfaces. The kinetic diameter is defined as the effective size of a molecule, taken from its cross section for scattering in gaseous collisions using spherical constructs [49]. Therefore, it neglects distinct orientations,

molecular flexibility, and vibrational motions that determine which molecules can traverse the pore space, thus allowing the possible diffusion of some EtOH even into CoKLTA crystals.

The intrinsic reactivity of CoO_x surfaces depends on cluster size for many oxide-catalyzed reactions [1,3-5]. The reducibility of active Co^{3+} species involved in oxidation reactions [3,50] decreases as the CoO_x clusters become smaller because of more intimate interactions with less reducible supports [5] and higher LUMO energies [34], leading to the ubiquitous lower reactivity of smaller oxide domains. Alkanol oxidation reactions in particular proceed on cobalt oxide surfaces via redox cycles involving the reduction of lattice cobalt cations and their re-oxidation by O_2 [50]. Consequently, alkanols such as methanol [50] and ethanol exhibit higher intrinsic oxidation rates on the more reducible surfaces of large CoO_x particles. Higher Co contents lead to higher active surface areas for clusters of a given size; as a result, they can create stronger concentration gradients within crystallites that restrict diffusion. In our studies, cluster sizes were nearly identical at the two Co loadings used on all samples (Section 4.3.2.2; CoKLTA, CoNaLTA, $CoCa_{0.5}Na_{0.5}$LTA, CoCaLTA; Fig. 4.3); thus, their different EtOH oxidation rates do not reflect cluster size effects on reactivity. Lower Co loadings (1% wt.), however, gave higher turnover rates at all temperatures than samples with higher Co content (3% wt.; Fig. 4.7), indicative of a greater kinetic load in 3% wt. samples that causes more severe reactant depletion within LTA crystallites. These diffusion constraints on reactivity, taken together with the strong effects of the LTA charge balancing cation on measured rates (Fig. 4.7), confirm the predominant presence of CoO_x surfaces within LTA crystals that restrict EtOH access to active sites.

A more quantitative assessment of encapsulation selectivity can be derived by comparing EtOH oxidation rates on the two samples with the most different diffusional access (r_{CoCaLTA} and r_{CoKLTA}). We define the CoO_x encapsulation selectivity (F) as:

$$\mathrm{F} = 1 - \frac{r_{\mathrm{CoKLTA}}}{r_{\mathrm{CoCaLTA}}} \qquad (3)$$

Its value becomes unity for active CoO_x surfaces that reside exclusively within LTA crystals. F increases with the extent of encapsulation, because r_{CoCaLTA} accounts for the combined contributions of external and intracrystalline CoO_x, while r_{CoKLTA} mostly reflects the reactivity of those CoO_x surfaces fully accessible at KLTA external surfaces. F values would precisely account for the fraction of CoO_x surfaces within LTA only in the limiting case where r_{CoKLTA} values solely reflect external CoO_x surfaces and r_{CoCaLTA} values reflect all surfaces, including those within crystals, when all surfaces are accessible to EtOH without diffusional hurdles. As a result, the F values defined as Equation 3 are smaller than, and thus represent a lower limit to, the actual selectivity of encapsulation, because intracrystalline clusters within CoKLTA may contribute to some extent to the measured rates, while concentration gradients are likely to be present even within CoCaLTA.

These lower bounds for encapsulation selectivities are 0.97-0.99 for EtOH oxidation between 423 and 523 K and both 1% and 3% wt. Co samples, indicating that >97% of active CoO_x surfaces reside within the protected environment of LTA crystals. These excellent high encapsulation selectivities are consistent with TEM results (Section 4.3.2.2), which appear to show

CoO_x clusters that are uniformly distributed throughout LTA crystals, much smaller than plausible for unconfined particles at external LTA surfaces, and resistant to coalescence during thermal treatments. The selective encapsulation achieved and demonstrated here serves as the arbiter of success for the synthesis protocols that sought to confine clusters for specific catalytic benefits.

4.3.3.2 Comparison of CO and NO oxidation rates on CoNaLTA, CoCaLTA, Co^{2+}-exchanged LTA, and Co/SiO_2 samples

CO and NO oxidation rates were measured and evaluated to compare the catalytic properties of encapsulated cobalt oxide clusters with exchanged and unconfined Co species. CO oxidation rates, detectable on CoNaLTA (3% wt. Co; $\langle d_{TEM} \rangle$=1.6 nm; DI: 1.06), CoCaLTA (3% wt. Co; $\langle d_{TEM} \rangle$=1.6 nm; DI: 1.06), and Co/SiO_2 (30% wt. Co; $\langle d_{TEM} \rangle$=21.0 nm; DI: 1.65), are shown in Figure 4.8 as a function of temperature (473-543 K) in the form of an Arrhenius plot; CO_2 formation was not detectable on Co^{2+}-exchanged LTA (3% wt. Co).

Measured CO oxidation rates gave linear trends in Figure 4.8, as expected from CO oxidation rates limited by activated diffusion or chemical reactivity. CO oxidation on CoO_x surfaces proceeds via Mars-van Krevelen redox-cycles, limited by the reduction part, in which lattice O-atoms are removed to form vacancies via reaction with CO and the concurrent reduction of Co^{3+} cations [39,51]. Higher turnover rates have been reported on oxide surfaces with higher Co^{3+} concentrations (from X-ray photoelectron spectra, measured before reaction) [39,52]. Co^{2+}-exchanged LTA does not lead to detectable CO oxidation rates, even though infrared spectra show that CO can access intracrystalline Co^{2+} cations (Section 4.3.2.5), a consequence of the stable oxidation state of the prevalent Co^{2+} exchanged cations and consistent with the divalent and unreducible character of such exchanged species evident in reduction studies (Section 4.3.2.4). CoCaLTA, CoNaLTA, and Co/SiO_2 samples, in contrast, catalyze CO oxidation at detectable rates, indicating that Co_3O_4 species able to undergo redox cycles are present in these samples, as also shown by reduction rate data (Section 4.3.2.4).

Turnover rates were two-fold higher on CoCaLTA than on CoNaLTA at all temperatures, in spite of their similar Co content and oxide cluster size (Fig. 4.3), a reflection of the weaker diffusional constraints in CaLTA crystallites. Rates were even higher on Co/SiO_2, for which a given turnover rate (0.002 s^{-1}) required a much lower temperature than on CoCaLTA (490 K vs. 530 K), as a result of the combined effects of residual concentration gradients in CoCaLTA and the larger and more reactive clusters prevalent in Co/SiO_2 (21.0 vs. 1.6 nm).

Similar trends were observed for NO oxidation rates measured as a function of temperature on CoCaLTA, Co^{2+}-exchanged LTA, and Co/SiO_2 samples (Section 4.2.3.8) to determine the temperatures required to reach a given turnover rate. NO oxidation on Co_3O_4 surfaces involves kinetically-relevant O_2 chemisorption on O-vacancies and fast subsequent steps leading to O_2 dissociation and NO-NO_2 interconversion [53]. Turnover rates are much lower on smaller clusters, because of the less reducible nature and lower vacancy coverages characteristic of smaller clusters, which delocalize electrons much less effectively than larger domains [53]. NO conversion rates were not detectable on Co^{2+}-exchanged LTA (<0.05%) over the temperature range 473-633 K, indicative of the substantial absence of Co_3O_4 clusters in these samples and their consequent inability to undergo Co^{3+}/Co^{2+} redox cycles. The temperatures required to reach a given turnover rate (0.002 s^{-1}, 0.003 s^{-1}, 0.004 s^{-1}) were higher on CoCaLTA (600 K, 620 K, 630 K) than Co/SiO_2

(550 K, 560 K, 565 K), an expected consequence of the significantly smaller Co_3O_4 clusters in CoCaLTA (1.6 nm) relative to Co/SiO_2 (21.0 nm), combined with the likely presence of NO and O_2 concentration gradients within CaLTA crystals.

These data show that Co_3O_4 nanoparticles within LTA crystals are less active than larger unconfined particles for CO and NO oxidation, as a consequence of the lower intrinsic reactivity of smaller clusters and of diffusional hurdles imposed by the LTA framework. Such small and stable encapsulated oxides make more efficient use of metal atoms, by exposing larger fractions of them at surfaces, and retain much higher dispersions through unique stabilization conferred by confinement. They also exploit molecular sieving effects that allow the preferential ingress and egress of specific reactant or product molecules, and can protect Co_3O_4 surfaces from deactivation by large poisons, such as sulfur compounds, which would titrate unconfined cobalt oxide clusters [54]. The inert character of exchanged Co^{2+} cations precludes the use of Co^{2+} exchange as a route to active catalysts that exploit the sieving properties of zeolite frameworks.

The synthesis protocols described here lead to Co oxide nanoparticles that are small and stable, as well as uniform in size and in their placement within zeolite crystals (Section 4.3.2). They reside predominantly within the protected environment of LTA frameworks (Section 4.3.3.1) and, in contrast with exchanged cations, catalyze oxidations of EtOH, CO, and NO (Section 4.3.3). The materials prepared make efficient conversion of Co precursors to active species through their selective retention within the crystals formed and by preventing their exchange onto LTA or the formation of Co aluminosilicates (Section 4.3.2.5). In doing so, these methods and the mechanistic inquiries that led to their optimization provide a much more general route for the preparation of zeolite-encapsulated base metal catalysts via hydrothermal assembly than the specific examples at hand may seem to indicate (Section 4.3.1); such examples are meant to provide the basis for the general platform that we proposed through the results presented here.

4.4 Conclusion

A synthesis procedure was developed for the selective encapsulation of cobalt oxide clusters within LTA zeolite crystals using a hydrothermal synthesis protocol with ligated Co^{2+} precursors. The method offers an alternative to more common encapsulation strategies that rely on reductive treatments of ion-exchanged metal cations, which are difficult or impossible to implement for Co because of the poor reducibility of zeolite-exchanged base metal cations. Metal encapsulation is conferred by introducing cobalt coordination complexes into zeolite synthesis gels and subsequently assembling the zeolite framework around such metal complexes. The Co^{2+} cations are stabilized by bifunctional ligands, which include a bidentate amine functionality to stabilize the cation against precipitation in the alkaline gels, and alkoxysilane groups, which can form siloxane bridges with nucleating zeolite precursors to promote metal uptake into the crystallized zeolites. Oxidative treatment of the ligated cobalt species occluded in the zeolite pores removes ligand residues and forms cobalt oxide clusters that are highly dispersed (1.4-1.6 nm), uniformly distributed in size (dispersity index 1.03-1.07), and thermally stable. The high dispersion and sinter-stability of such clusters results from their containment within the zeolite crystals, which impose thermodynamic barriers that limit the size to which the oxide clusters can grow. Temperature programmed reduction and infrared spectroscopy experiments indicate that the synthesis and post-synthetic treatment procedures preclude the formation of exchanged Co^{2+} or Co

aluminosilicates; instead, the cobalt species selectively form Co_3O_4 clusters suitable for use in reactions catalyzed by cobalt oxides. Such clusters overwhelmingly reside within zeolite crystals, as confirmed with ethanol oxidation reactivity studies conducted on LTA samples of variable effective aperture diameters. The encapsulated Co_3O_4 clusters, in contrast with exchanged Co^{2+} cations, are also active for CO and NO oxidation. This work illustrates a synthesis strategy that can be employed to prepare cobalt oxide clusters that are well-defined and small in size and thermally stable, allowing systematic studies of cobalt oxide catalysts under conditions that favor particle sintering. Studies and applications of these materials can further exploit the molecular sieving and transition state selectivity conferred by the microporous voids and cavities of zeolites. We predict that the synthetic route used here can be more broadly applied to other zeolites and base metal species (e.g. Ni, Fe, Cu), for which existing cluster encapsulation techniques are limited or unavailable.

4.5 Acknowledgments

We gratefully acknowledge the Chevron Energy Technology Co for their generous financial support of this research, as well as ancillary support provided for TO by an ARCS foundation fellowship and a National Science Foundation fellowship. We also thank Dr. Reena Zalpuri (Electron Microscope Lab) and Dr. Antonio DiPasquale (X-Ray Facility) for support with TEM and XRD instrumentation, respectively.

4.6 Figures, Tables, and Scheme(s)

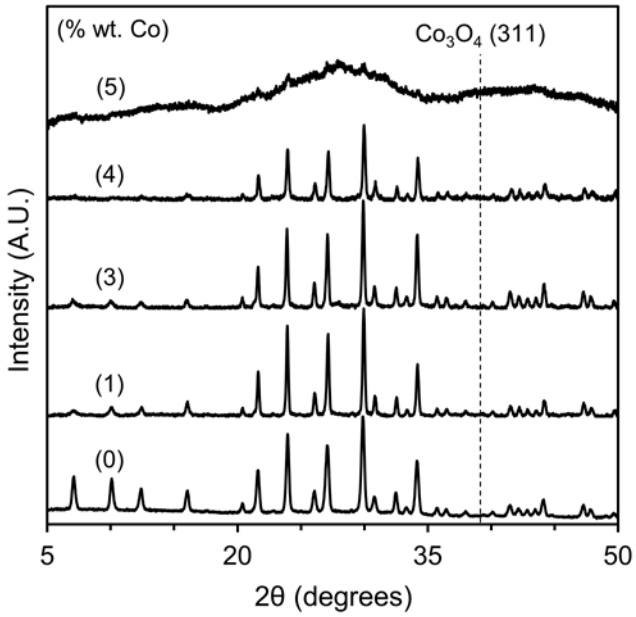

Figure 4.1 X-Ray diffractograms for as-synthesized NaLTA and CoNaLTA samples prepared to achieve 0-5% wt. Co loading in the product solids assuming full metal uptake. Samples prepared with TPE/Co^{2+} ratio of 2.

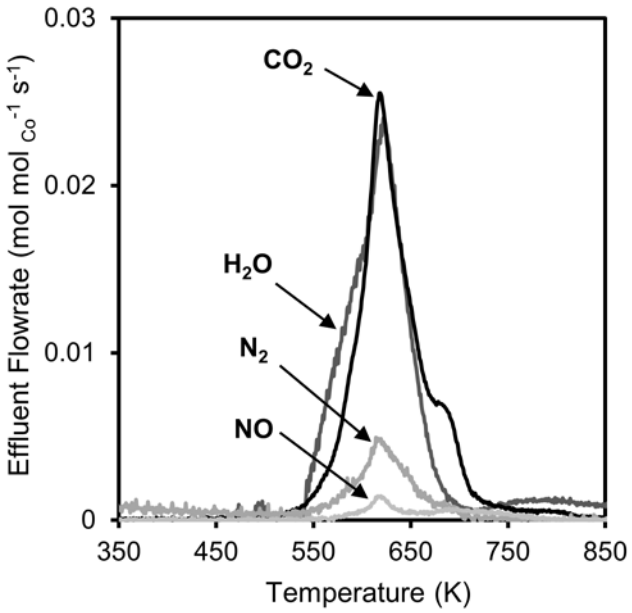

Figure 4.2 Effluent gas flowrates calculated from mass signals for H_2O (18 amu), CO_2 (44 amu), N_2 (28 amu), and NO (30 amu) monitored during the thermal treatment of as-synthesized 3% wt. CoNaLTA with 10% O_2/He (0.83 cm^3 g^{-1} s^{-1}) from 350 K to 850 K (at 0.167 K s^{-1}).

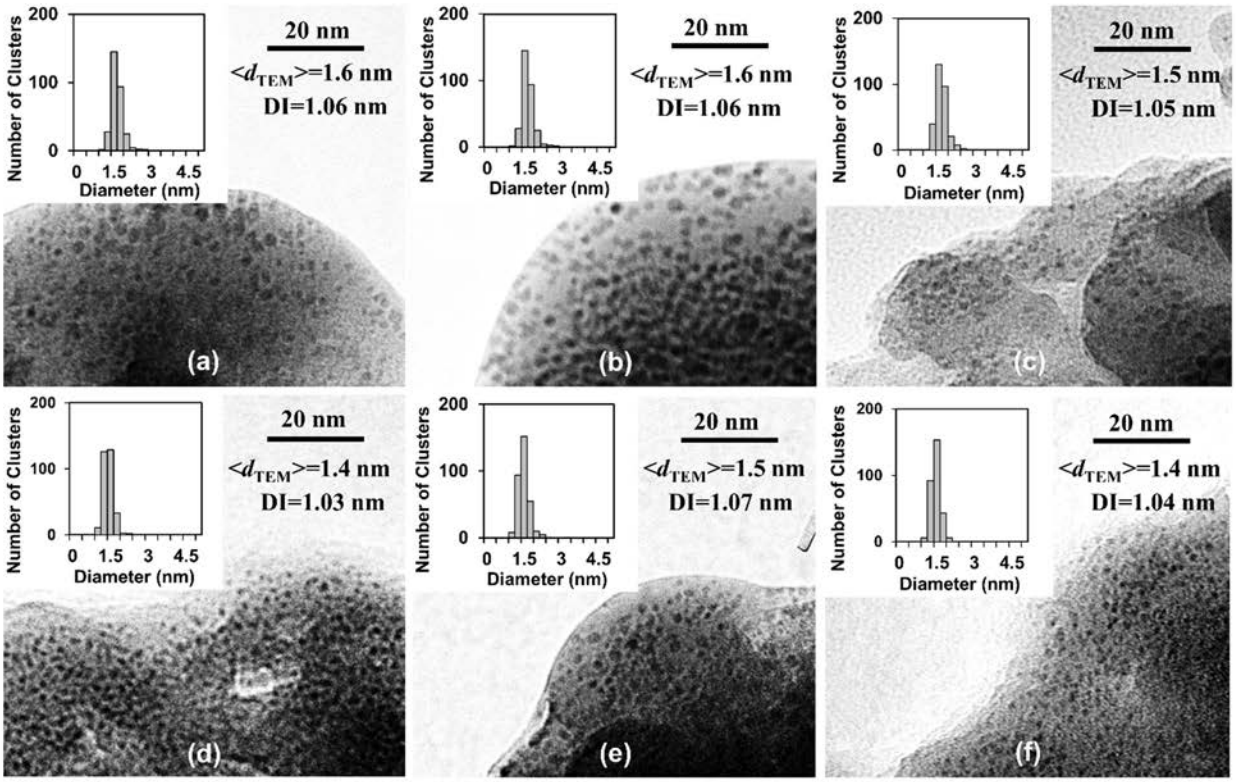

Figure 4.3 Transmission electron micrographs, surface-averaged cluster diameters ($\langle d_{TEM} \rangle$, Eq. 1), particle dispersity indices (DI, Eq. 2), and cluster diameter distributions for (a) CoCaLTA, (b) CoNaLTA, and (c) CoKLTA samples with 3% wt. Co loading and (d) CoCaLTA, (e) CoNaLTA, and (f) CoKLTA samples with 1% wt. Co loading.

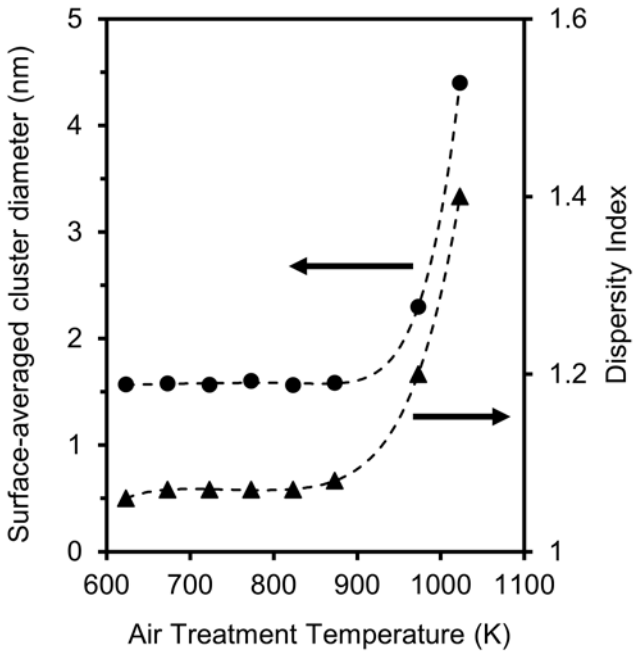

Figure 4.4 Effect of flowing dry air treatment temperature (1.67 cm^3 g^{-1} s^{-1}, 3 h) on the TEM-derived surface-averaged cluster diameter (●; Eq. 1) and Dispersity Index (▲; Eq. 2) of cobalt oxide clusters in CoNaLTA (3% wt. Co loading).

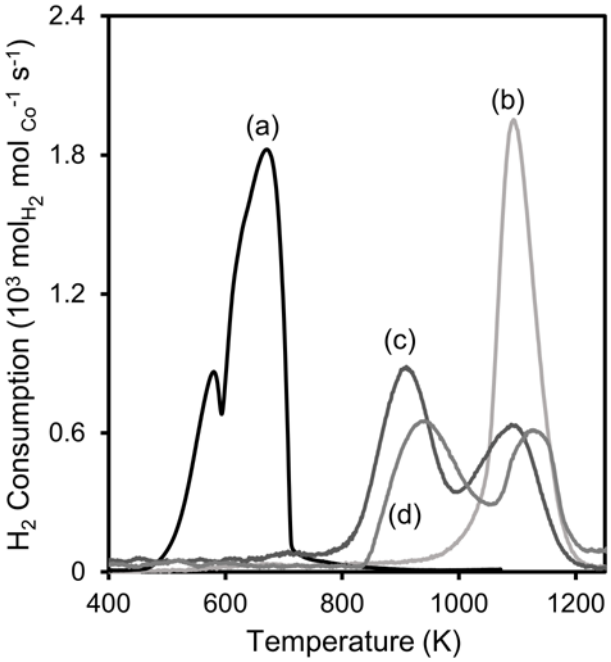

Figure 4.5 Temperature programmed reduction (TPR) profiles of (a) Co_3O_4, (b) 3% wt. Co^{2+}-exchanged LTA, (c) 3% wt. CoNaLTA, and (d) 3% wt. CoCaLTA samples heated in 4% H_2/Ar (8.3 $cm^3\ s^{-1}\ g^{-1}$) from 313 K to 1273 K at 0.167 K s^{-1}.

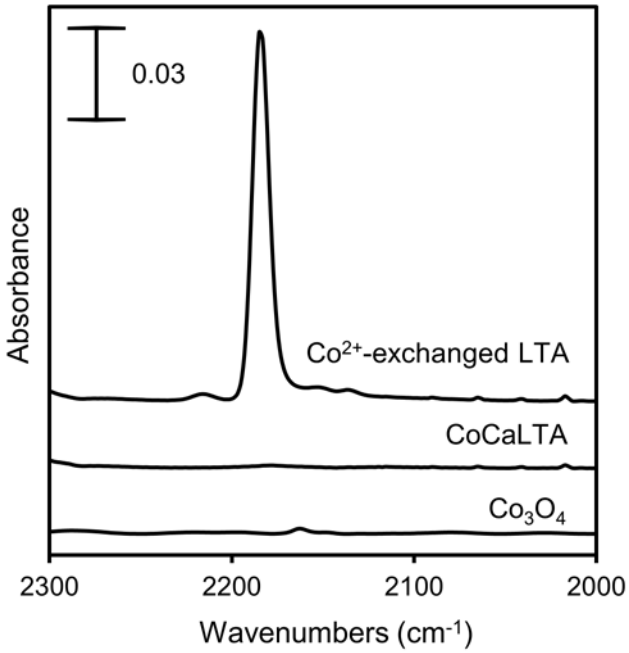

Figure 4.6 Infrared spectra of CO adsorbed on Co_3O_4, CoCaLTA, and Co^{2+}-exchanged LTA samples at 313 K (1.0 kPa CO, 99.0 kPa He) after treatment in flowing He (0.7 cm^3 g^{-1} s^{-1}) at 473 K for 1 h.

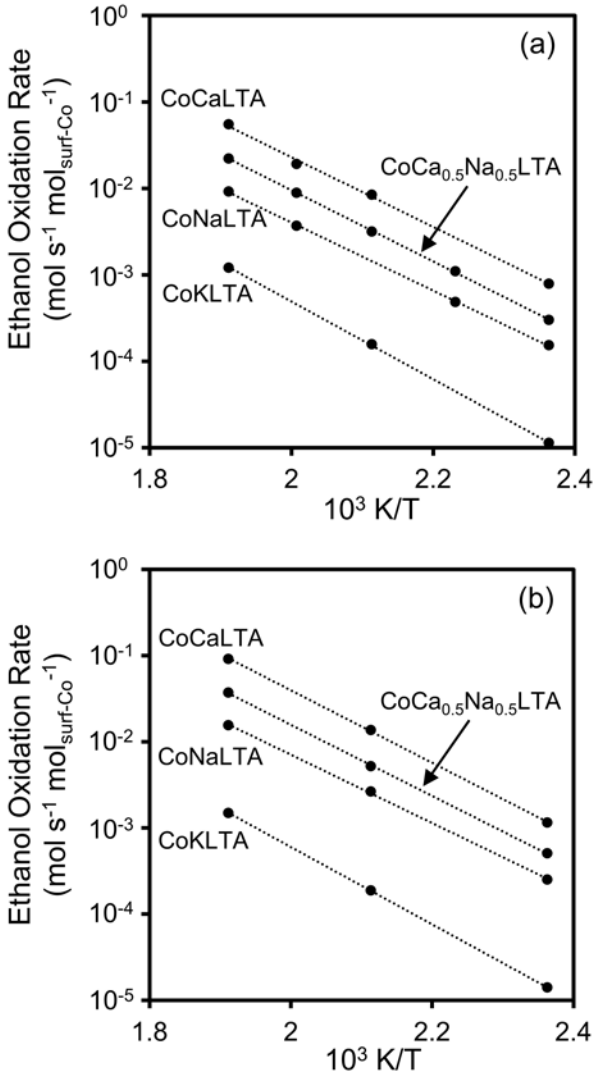

Figure 4.7 Ethanol oxidation turnover rates (per surface Co atom) on CoKLTA, CoNaLTA, $CoCa_{0.5}Na_{0.5}LTA$, and CoCaLTA samples with (a) 3% wt. and (b) 1% wt. Co loading at 423-523 K (9 kPa O_2, 4 kPa ethanol, 88 kPa He). Samples were treated in 20% O_2/He (1.67 $cm^3\ g^{-1}\ s^{-1}$) at 573 K for 1 h before rate measurements.

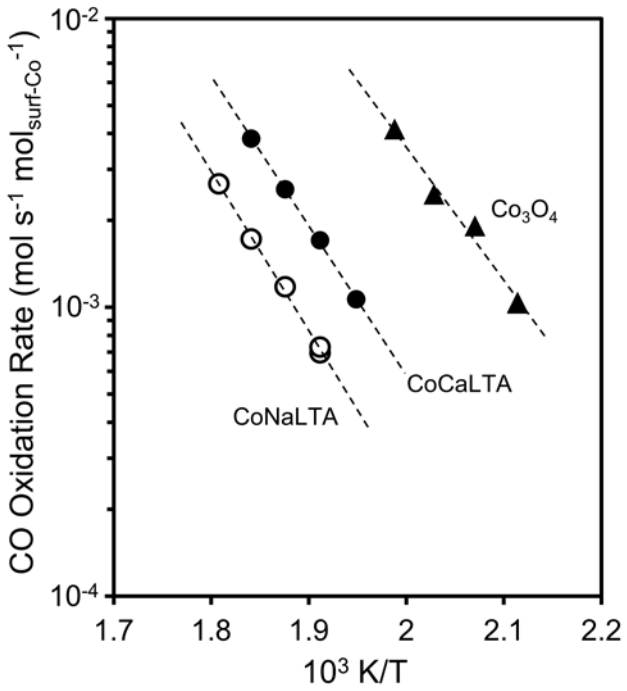

Figure 4.8 CO oxidation turnover rates on CoCaLTA (●; 3% wt. Co; $\langle d_{TEM} \rangle$=1.6 nm), CoNaLTA (○; 3% wt. Co; $\langle d_{TEM} \rangle$=1.6 nm), and Co/SiO_2 (▲; 30% wt. Co; $\langle d_{TEM} \rangle$=21 nm) samples at 473-543 K (1 kPa CO, 10 kPa O_2, 90 kPa He; 8.3 $cm^3\ g^{-1}\ s^{-1}$). Turnover rates are defined as the molar CO conversion rates per surface Co atom. Samples were treated in 20% O_2/He (8.3 $cm^3\ g^{-1}\ s^{-1}$) at 573 K for 1 h before rate measurements.

Table 4.1 Ligand species, ligand/Co ratios, nominal metal loading, metal uptake into solids, stability of ligated cobalt cations in LTA synthesis gels, and crystallinity of synthesized solids for the synthesis of CoNaLTA samples.

Ligand[a]	Nominal metal loading (% wt.)[b]	Ligand/Co ratio[c]	Precursor Stability[d]	% Metal uptake[e]	Crystalline LTA Product?[f]
NH_3	1	6	Unstable	-	-
ethylendiamine	1	3	Stable	40	Yes
TPE	1	1	Unstable	-	-
TPE	1	3	Stable	90	Yes
TPE	1	2	Stable	90	Yes
TPE	2	2	Stable	90	Yes
TPE	3	2	Stable	90	Yes
TPE	4	2	Stable	90	Yes
TPE	5	2	Stable	90	No

[a]Ligand species used to stabilize Co cations in LTA synthesis gels. [b]Metal loading that would be achieved if all of the Co added to the synthesis gel were incorporated into the synthesized solids, assuming a solids yield equivalent to a metal and ligand-free NaLTA synthesis. [c]Molar ratio of ligand/metal added to the synthesis gel. [d]Unstable ligated cobalt precursors precipitate to form black solids in the LTA synthesis gel prior to the completion of crystallization; stable precursors retain their bright coloration and do not precipitate. [e]Actual metal uptake in the isolated solids formed after crystallization, calculated using UV-Vis measurements of Co complex concentrations in supernatant solutions. [f]Determined using XRD.

Scheme 4.1 Schematic representation of the synthesis and characterization of cobalt oxide clusters encapsulated within LTA

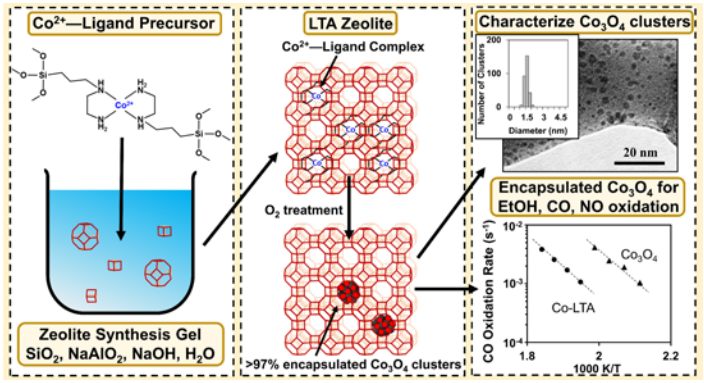

4.7 References

[1] Xie, X.; Shen, W. *Nanoscale* **2009**, *1*, 50.
[2] El Kabouss, K.; Kacimi, M.; Ziyad, M.; Ammar, S.; Ensuque, A.; Piquemal, J. Y.; Bozon-Verduraz, F. *J. Mater. Chem*. **2006**, *16*, 2453.
[3] Wyrwalski, F.; Giraudon, J. M.; Lamonier, J. F. *Catal. Lett*. **2010**, *137*, 141.
[4] Zhu, J.; Kailasam, K.; Fischer, A.; Thomas, A. *ACS Catal*. **2011**, *1*, 342.
[5] Jahangiri, H.; Bennett, J.; Mahjoubi, P.; Wilson, K.; Gu, S. *Catal. Sci. Technol*. **2014**, *4*, 2210.
[6] Eschemann, T. O.; Bitter, J. H.; de Jong, K. P. *Catal. Today* **2014**, *228*, 89.
[7] Kim, J. -C.; Lee, S.; Cho, K.; Na, K.; Lee, C.; Ryoo, R. *ACS Catal*. **2014**, *4*, 3919.
[8] Lakshmi, B. B.; Patrissi, C. J.; Martin, C. R. *Chem. Mater*. **1997**, *9*, 2544.
[9] Meng, Z.; Liu, B.; Zheng, J.; Sheng, Q.; Zhang, H. *Microchim. Acta* **2011**, *175*, 251.
[10] Salavati-Niasari, M.; Khansari, A.; Davar, F. *Inorg. Chim. Acta* **2009**, *362*, 4937.
[11] Ghosh, M.; Sampathkumaran, E. V.; Rao, C. N. R. *Chem. Mater*. **2005**, *17*, 2348.
[12] Ferguson, G. A.; Yin, C.; Kwon, G.; Tyo, E. C.; Lee, S.; Greeley, J. P.; Zapol, P.; Lee, B.; Seifert, S.; Winans, R. E.; Vajda, S.; Curtiss, L. A. *J. Phys. Chem. C* **2012**, *116*, 24027.
[13] Otto, T.; Zones, S. I.; Iglesia, E. *J. Catal*. **2016**, *339*, 195.
[14] Otto, T.; Ramallo-López, J. M.; Giovanetti, L. J.; Requejo, F. G.; Zones, S. I.; Iglesia, E. *J. Catal*. **2016**, *342*, 125.
[15] Wu, Z.; Goel, S.; Choi, M.; Iglesia, E. *J. Catal*. **2014**, *311*, 458.
[16] Rimer, J. D.; Kumar, M.; Li, R.; Lupulescu, A. I.; Oleksiak, M. D. *Catal. Sci. Tech*. **2014**, *4*, 3762.
[17] Asedegbega-Nieto, E.; Díaz, Eva.; Vega, A.; Ordóñez, S. *Catal. Today* **2010**, *157*, 425.
[18] Borqschulte, A.; Callini, E.; Stadie, N.; Arroyo, Y.; Rossell, M. D.; Erni, R.; Geerlings, H.; Züttel, A.; Ferri, D. *Catal. Sci. Technol*. **2015**, *5*, 4613.
[19] Weisz, P. B.; Frilette, V. J.; Maatman, R. W.; Mower, E. B. *J. Catal*. **1962**, *1*, 307.
[20] Bergeret, G.; Gallezot, P. In Handbook of Heterogeneous Catalysis; Ertl, G., Knozinger, H., Schuth, F., Weitkamp, J., Eds.; Wiley-VHC: Weinheim, Germany, 2008; pp 738.
[21] Paoletti, P. *Pure Appl. Chem*. **1984**, *56*, 491.
[22] IZA Synthesis Commission. Synthesis Recipes in the 2nd Edition of Verified Syntheses of Zeolitic Materials. http://www.iza-online.org/synthesis (accessed Feb 22, 2017).
[23] Cheung, O.; Hedin, N. *RSC Adv*. **2014**, *4*, 14480.
[24] Choi, M.; Wu, Z.; Iglesia, E. *J. Am. Chem. Soc*. **2010**, *132*, 9129.
[25] Garcia Rodriguez, A. M.; Garcia de Torres, A.; Cano Pavon, J. M.; Bosch Ojeda, C. *Talanta* **1998**, *47*, 463.
[26] Małecka, B.; Łącz, A.; Drożdż, E.; Małecki, A. J. *Therm. Anal. Calorim*. **2015**, *119*, 1053.
[27] Kotousova, I. S.; Polyakov, S. M. *Kristallografiya* **1972**, *17*, 661.
[28] Shannon, R. D. Revised Effective Ionic Radii and Systematic Studies of Interatomic Distances in Halides and Chalcogenides. *Acta Crystallogr*. **1976**, *A 32*, 751.
[29] Smith, T. J. *J. Mol. Graphics* **1995**, *13*, 122.
[30] Knowles, W. V.; Nutt, M. O.; Wong, M. S. In Catalyst Preparation: Science and Engineering; Regalbuto, J. R., Ed.; CRC Press, Inc.: Boca Raton, FL, 2007; pp 258.
[31] Kogelbauer, A.; Weber, J. C.; Goodwin, J. G., Jr. *Catal. Lett*. **1995**, *34*, 259.
[32] Garces, L. J.; Hincapie, B.; Zerger, R.; Suib, S. L. *Phys. Chem. C* **2015**, *119*, 5484.
[33] Jacobs, G.; Das, T. K.; Zhang, Y.; Li, J.; Racoillet, G.; Davis, B. H. *Appl. Catal. A* **2002**, *233*, 263.

[34] Barton, D. G.; Shtein, M.; Wilson, R. D.; Soled, S. L.; Iglesia, E. *J. Phys. Chem. B* **1999**, *103*, 630.
[35] Okamoto, Y.; Nagata, K.; Adachi, T.; Imanaka, T.; Inamura, K.; Takyu, T. *J. Phys. Chem*. **1991**, *95*, 310.
[36] Lim, S.; Ciuparu, D.; Chen, Y.; Pfefferle, L.; Haller, G. L. *J. Phys. Chem. B* **2004**, *108*, 20095.
[37] Moodley, D.J.; Saib, A.M.; van de Loosdrecht, J.; Welker-Nieuwoudt, C.A.; Sigwebela, B.H.; Niemantsverdriet, J.W. *Catal. Today* **2011**, *171*, 192.
[38] Bhatia, S. Zeolite Catalysis: Principles and Applications; CRC Press, Inc.: Boca Raton, FL, 1990; pp 10.
[39] Iablokov, V.; Barbosa, R.; Pollefeyt, G.; Van Driessche, I.; Chenakin, S.; Kruse, N. *ACS Catal*. **2015**, *5*, 5714.
[40] Dieckmann, R. *Z. Phys. Chem*. **1977**, *107*, 189.
[41] Angell, C. L.; Schaffer, P. C. *J. Phys. Chem*. **1966**, *70*, 1413.
[42] Rakić, V.; Dondur, V.; Hercigonja, R. *J. Serb. Chem. Soc*. **2003**, *68*, 409.
[43] Moskovits, M.; Hülse, J. E. *Surf. Sci*. **1978**, *78*, 397.
[44] Lin, H. K.; Wang, C. B.; Chiu, H. C.; Chien, S. H. *Catal. Lett*. **2003**, *86*, 63.
[45] Khodakov, A. Y.; Lynch, J.; Bazin, D.; Rebours, B.; Zanier, N.; Moisson, B.; Chaumette, P. *J. Catal*. **1997**, *168*, 16.
[46] Busca, G.; Lorenzelli, V.; Escribano, V. S.; Guidetti, R. *J. Catal*. **1991**, *131*, 167.
[47] Subramanian, V.; Zholobenko, V. L.; Cheng, K.; Lancelot, C.; Heyte, S.; Thuriot, J.; Paul, S.; Ordomsky, V. V.; Khodakov, A. Y. *ChemCatChem* **2016**, *8*, 380.
[48] Lobo, R. F. In Handbook of Zeolite Science and Technology; Auerbach, S. M., Carrado, K. A., Dutta, P. K., Eds.; Marcel Dekker, Inc.: New York, New York, USA, 2003; pp 71.
[49] Mehio, N.; Dai, S.; Jiang, D. *J. Phys. Chem. A* **2014**, *118*, 1150.
[50] Natile, M. M.; Glisenti, A. *Chem. Mater*. **2002**, *14*, 3090.
[51] Broqvist, P.; Panas, I.; Persson, H. *J. Catal*. **2002**, *210*, 198.
[52] Xie, Y.; Dong, F.; Heinbuch, S.; Rocca, J. J.; Bernstein, E. R. *Phys. Chem. Chem. Phys*. **2010**, *12*, 947.
[53] Weiss, B. M.; Artioli, N.; Iglesia, E. *ChemCatChem* **2012**, *4*, 1397.
[54] Huang, Y.; Gao, D.; Tong, Z.; Zhang, J.; Luo, H. *J. Nat. Gas Chem*. **2009**, *18*, 421.

4.8 Supporting Information

Contents

4.S1. X-Ray diffraction patterns of as-synthesized and air treated CoNaLTA samples

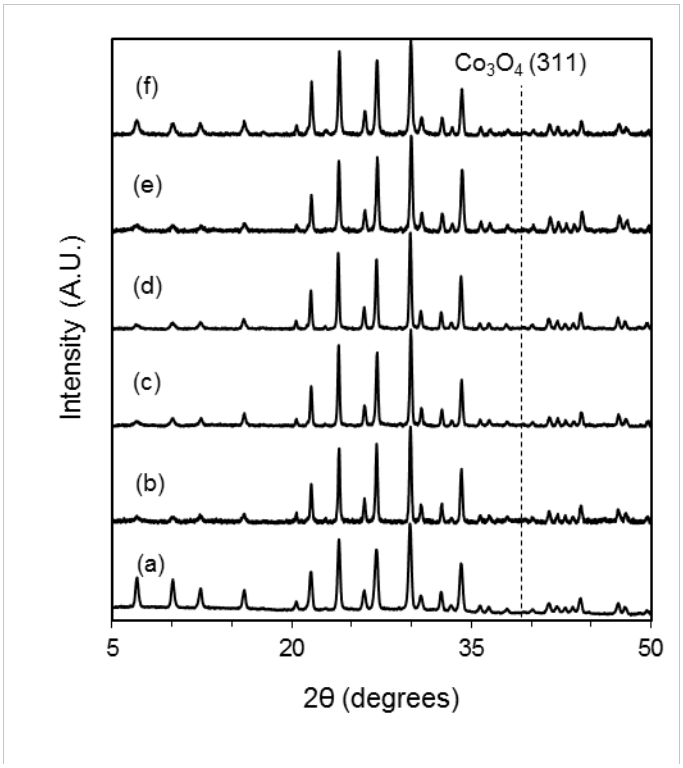

Figure 4.S1. X-ray diffraction patterns of (a) NaLTA standard, (b) as-synthesized CoNaLTA with 1% wt. nominal Co loading prepared with ethylenediamine/Co^{2+} ratio of two, (c) as-synthesized CoNaLTA with 1% wt. nominal Co loading prepared with TPE/Co^{2+} ratio of two, (d) as-synthesized CoNaLTA with 1% wt. nominal Co loading prepared with ethylenediamine/Co^{2+} ratio of three, (e) CoNaLTA with 1% wt. nominal Co loading prepared with TPE/Co^{2+} ratio of two and treated in air (1.67 $cm^3\ g^{-1}\ s^{-1}$) at 623 K for 3 h, and (f) CoNaLTA with 3% wt. nominal Co loading prepared with TPE/Co^{2+} ratio of two and treated in air (1.67 $cm^3\ g^{-1}\ s^{-1}$) at 623 K for 3 h.

4.S2. Ultraviolet-visible spectra of supernatant solutions remaining after CoNaLTA synthesis

Ultraviolet-visible (UV-vis) spectroscopy was used to detect the presence of Co^{2+} species in the supernatant solutions remaining after CoNaLTA syntheses (Section 4.2.3.3, main text). Standard solutions of ligated Co^{2+} compounds were also prepared and examined in order to estimate the concentration of Co^{2+} in such supernatant solutions. Figure 4.S2 shows UV-vis spectra for three such standard solutions (with ethylenediamine/Co^{2+} ratio of three) and for the supernatant liquid of CoNaLTA synthesized with 1% wt. nominal Co loading and an ethylenediamine/Co^{2+} ratio of three.

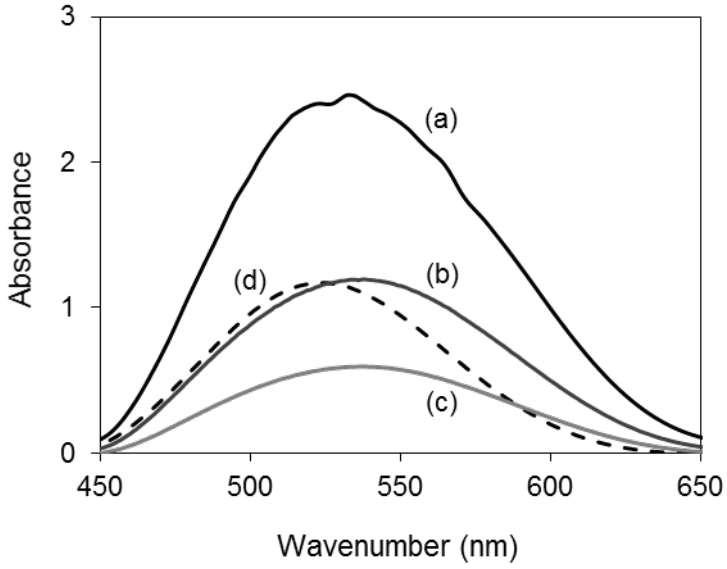

Figure 4.S2. (a)-(c) UV-vis spectra of standard solutions prepared by adding ethylenediamine and Co^{2+} cations (ethylenediamine/Co^{2+} ratio of three) to supernatant solutions extracted from metal-free NaLTA syntheses; metal concentrations correspond to those that would be observed for CoNaLTA syntheses with 3% (a), 2% (b), and 1% wt. (c) theoretical Co loading if none of the metal was incorporated into the formed solids. (d) UV-vis spectra of the supernatant solution remaining after the synthesis of CoNaLTA with 1% wt. theoretical Co loading and an ethylenediamine/Co^{2+} ratio of three.

4.S3. Micropore volume of 3% wt. CoNaLTA and CoCaLTA

CO_2 adsorption measurements were conducted on 3% wt. CoNaLTA and CoCaLTA samples after oxidative treatments at 623 K (main text, Section 4.2.2.1) to determine micropore volumes and surface areas of the host zeolite structures. The CO_2 adsorption measurements (0-800 torr) were performed on a Micromeritics 3Flex Surface Characterization Analyzer at 273 K. Samples were heated to 623 K (at 0.17 K s^{-1}) under vacuum and held for 4 h prior to adsorption measurements. Micropore volumes and surface areas were calculated from CO_2 uptakes using the Dubinin-Astakhov method.[S1] CO_2 uptakes into NaLTA, CaLTA, CoNaLTA, and CoCaLTA samples are shown as a function of CO_2 pressure in Figure S3. CO_2 was used as the adsorbing molecule at 273 K (as opposed to N_2 at 77 K) because the access of N_2 and other species to microporous regions within small-pore zeolites is limited by diffusional constraints at low temperature, leading to uncharacteristically small micropore volumes.[S2]

Micropore volumes and surface areas for metal-free NaLTA (0.34 cm^3 g^{-1}; 1090 m^2 g^{-1}) were similar to those for 3% wt. CoNaLTA (0.32 cm^3 g^{-1}; 1026 m^2 g^{-1}), confirming the absence of significant micropore obstruction by any ligand residues or the encapsulated cobalt oxide particles within CoNaLTA. CaLTA and CoCaLTA micropore volumes (0.29 and 0.27 cm^3 g^{-1}, respectively) and surface areas (970 and 880 m^2 g^{-1}, respectively) were also similar, but slightly lower than those measured for the Na^+-LTA zeolites, reflecting the smaller number of cations in the Ca^{2+}-exchanged framework and thus a lower capacity to adsorb CO_2.[S3]

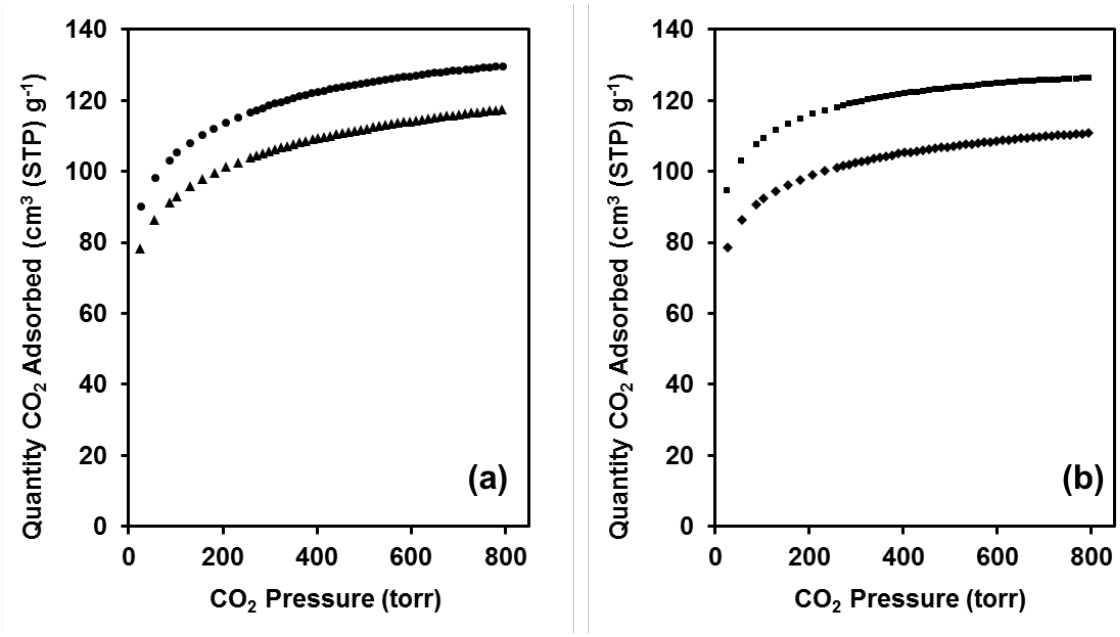

Figure 4.S3. CO_2 adsorption isotherms measured at 273 K for (a) NaLTA (circle) and 3% wt. CoNaLTA (triangle) and (b) CaLTA (square) and 3% wt. CoCaLTA (diamond). Samples were evacuated at 623 K for 4 h prior to adsorption measurements.

4.S4. Temperature programmed oxidation of as-synthesized 1% wt. CoNaLTA

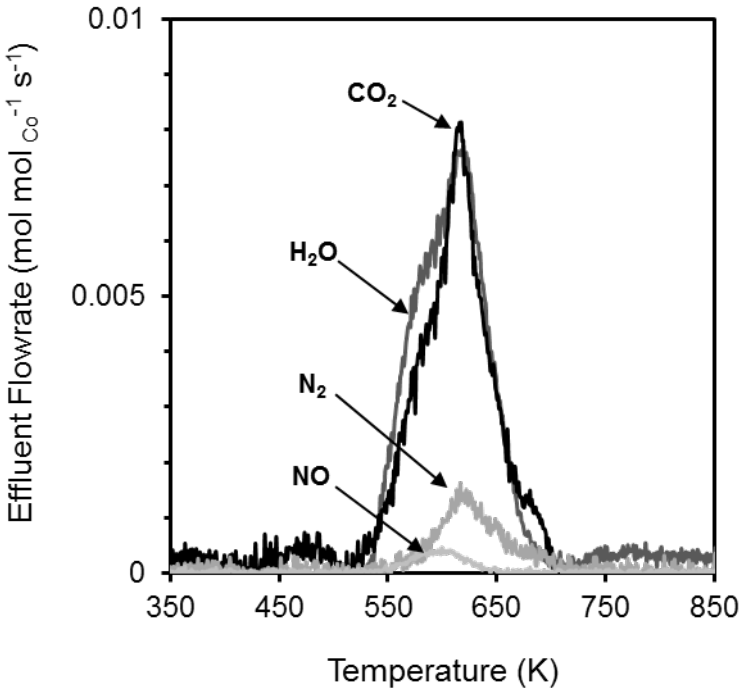

Figure 4.S4. Effluent gas flowrates calculated from mass signals for H_2O (18 amu), CO_2 (44 amu), N_2 (28 amu), and NO (30 amu) monitored during the thermal treatment of as-synthesized 1% wt. CoNaLTA with 10% O_2/He (0.83 $cm^3\ g^{-1}\ s^{-1}$) from 350 K to 850 K (at 0.167 $K\ s^{-1}$).

4.S5. DR-UV-vis analysis of CoNaLTA and Co^{2+}-exchanged LTA samples

Diffuse-reflectance ultraviolet-visible (DR UV-vis) spectra were collected on as-synthesized CoNaLTA, oxidatively treated CoNaLTA (main text, Section 4.2.2.1), and Co^{2+}-exchanged LTA samples, each with 3% wt. Co loading, to demonstrate the full removal of ligands from CoNaLTA by oxidative treatment and to confirm that different Co coordination environments are prevalent in each sample.

DR UV-vis spectra were acquired with a Varian-Cary 6000i spectrometer equipped with a Harrick scientific diffuse reflectance accessory (DRP-XXX) and a reaction chamber add-on (DRA-2CR). A heater underneath the sample cup in the reaction chamber together with a temperature controller (Watlow Series 982) were used to adjust the temperature of the samples. These temperatures were measured using a type K thermocouple (Omega) embedded in the sample holder. The bottom of the sample holder was modified with a stainless steel frit to allow gas flow through the packed powder samples. Samples were heated in He flow (1.67 $cm^3\ g^{-1}\ s^{-1}$) to 373 K (at 0.067 $K\ s^{-1}$) and held for 1 h before cooling to ambient temperature for acquisition of the DR UV-vis spectra. Background spectra (used to isolate the effect of Co species) were collected after identical treatment procedures on metal-free NaLTA samples. Kubelka-Munk (KM) absorbance spectra of the three samples, and a photograph of these samples, are shown in Figure 4.S5.

The Co^{2+}-exchanged LTA sample showed an intense absorbance feature in the visible range centered at ~600 nm, characteristic of zeolite-exchanged and tetrahedrally coordinated Co^{2+},[S4] and accounting for the blue/violet color of the sample. As-synthesized CoNaLTA gave a weak absorption feature in the visible range (~575 nm), likely corresponding to Co^{2+} d-d transitions in the ligated complex,[S5,S6] and leading to the dull pink color of the sample. Also present was an intense, low-wavelength band centered at ~290 nm; the position of this feature suggests that it is a ligand to metal charge transfer band.[S5,S6,S7] Oxidatively treated CoNaLTA was gray in color and showed weak and diffuse background absorption at low wavelengths without any clear bands in the visible range, consistent with the presence of highly dispersed CoO_x particles at <5% wt. Co loading.[S8] Bulk CoO_x species, if present, would have led to broad absorption bands at ~350 and ~650 nm corresponding to $O^{2-} \rightarrow Co^{n+}$ charge transfer and d-d transitions in Co^{n+}, respectively.[S5,S8] The gray color of oxidatively treated CoNaLTA, together with the absence of significant absorption features characteristic of ligated Co^{2+}, zeolite-exchanged Co^{2+}, or bulk CoO_x, is consistent with the removal of ligands from Co^{2+} species and the conversion of such species into highly dispersed cobalt oxide domains during oxidative treatment.

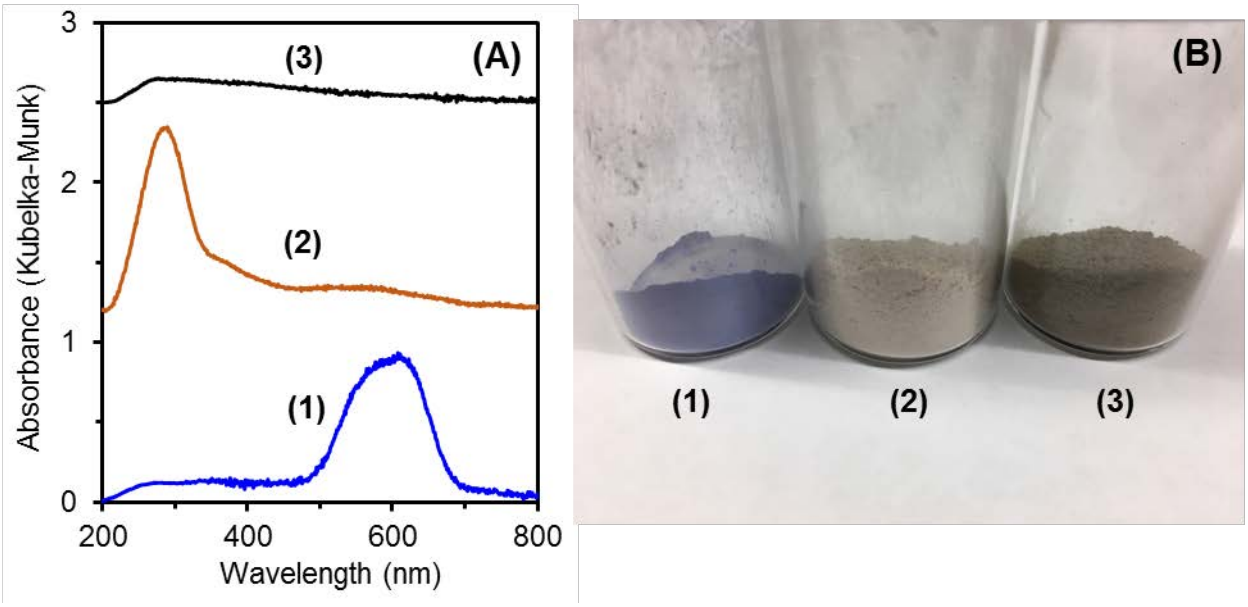

Figure 4.S5. Diffuse-reflectance ultraviolet-visible spectra (A) and photographs (B) of (1) Co^{2+}-exchanged LTA, (2) as-synthesized CoNaLTA, and (3) oxidatively treated CoNaLTA samples, each with 3% wt. Co loading.

4.S6. Thermal stability of cobalt oxide clusters in 1% wt. CoNaLTA

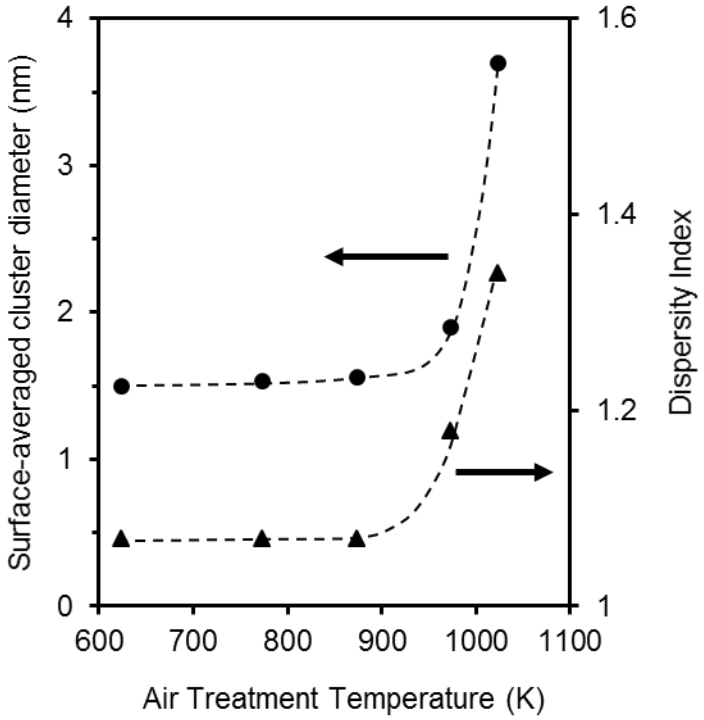

Figure 4.S6. Effect of flowing dry air treatment temperature (1.67 cm^3 g^{-1} s^{-1}, 3 h) on the TEM-derived surface-averaged cluster diameter (●; Eq. 1, main text) and Dispersity Index (▲; Eq. 2, main text) of cobalt oxide clusters in CoNaLTA (1% wt. Co loading).

4.S7. IR spectra of adsorbed CO and XRD patterns of CoCaLTA treated at 1020 K in air or H_2

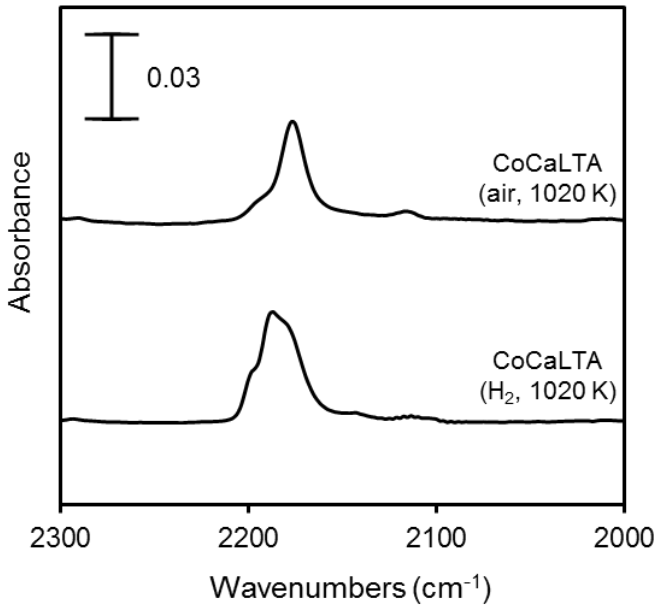

Figure 4.S7. Infrared spectra of CO adsorbed on CoCaLTA (3% wt. Co) samples at 313 K (1.0 kPa CO, 99.0 kPa He) after treatment in 4% H_2/Ar or flowing dry air (8.3 cm^3 s^{-1} g^{-1}) to 1020 K at 0.167 K s^{-1}. Samples were heated from a starting temperature of 313 K and allowed to cool in flowing 4% H_2/Ar or air to ambient temperature immediately after reaching 1020 K. Samples were further treated in flowing He (0.7 cm^3 g^{-1} s^{-1}) at 473 K for 1 h within the infrared cell prior to exposure to CO gas and the collection of absorbance spectra.

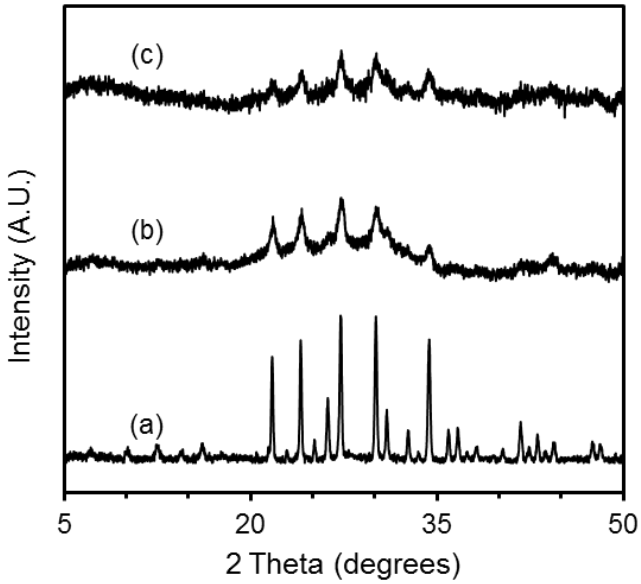

Figure 4.S8. X-ray diffraction patterns of (a) CaLTA standard, (b) CoCaLTA (3% wt. Co) treated in flowing 4% H_2/Ar (8.3 cm^3 s^{-1} g^{-1}) to 1020 K, and (c) CoCaLTA (3% wt. Co) treated in flowing dry air (8.3 cm^3 s^{-1} g^{-1}) to 1020 K. Samples (a) and (b) were heated from a starting temperature of 313 K at a rate of 0.167 K s^{-1} and were allowed to cool in flowing 4% H_2/Ar or air to ambient temperature immediately after reaching 1020 K.

4.S8. References

[S1] Burevski, D. *Colloid Polym. Sci.* **1982**, *260*, 623.
[S2] García-Martinez, J.; Cazorla-Amorós, D.; Linares-Solano, A. *Stud. Surf. Sci. Catal.* **2000**, *128*, 485.
[S3] Choi, S.; Drese, J. H.; Jones, C. W. *ChemSusChem.* **2009**, *2*, 796.
[S4] Palomares, A. E.; Prato, J. G.; Corma, A. *Ind. Eng. Chem. Res.* **2003**, *42*, 1538.
[S5] van de Water, L. G. A.; Bezemer, L. G.; Bergwerff, J. A.; Versluijs-Helder, M.; Weckhuysen, B. M.; de Jong, K. P. *J. Catal.* **2006**, *242*, 287.
[S6] Martins, J. G.; Gameiro, P.; Barros, M. T.; Soares, H. M. V. *J. Chem. Eng. Data* **2010**, *55*, 3410.
[S7] Ahmadi, R. A.; Hasanvand, F.; Bruno, G.; Rudbari, H. A.; Amani, S. *ISRN Inorg. Chem.* **2013**, *2013*, 1.
[S8] Maeda, K.; Ishimaki, K.; Okazaki, M.; Kanazawa, T.; Lu, D.; Nozawa, S.; Kato, H.; Kakihana, M. *Appl. Mater. Interfaces* **2017**, *9*, 6144.

Chapter 5

Synthetic Strategies for the Encapsulation of Nanoparticles of Ni, Co, and Fe Oxides within Crystalline Microporous Aluminosilicates

Abstract

A synthetic strategy is reported here for the selective containment of oxide nanoparticles of base metals within zeolitic voids of molecular dimensions. The technique, though generally applicable, is specifically illustrated to encapsulate Ni, Co, and Fe oxides within LTA, MFI, and FAU zeolites through hydrothermal framework crystallization in the presence of ligand-protected metal cations. Such ligands contain bidentate amine groups that preclude the precipitation of metal precursors in alkaline synthesis gels, and alkoxysilane moieties that form covalent linkages with nucleating zeolite precursors to enforce metal uptake into crystallized solids. These ligands are removed by subsequent oxidative treatments that nucleate oxide nanoparticles without structural degradation of the zeolites. The clusters are small (<2.5 nm) and uniformly distributed in size, reflecting their constrained growth within zeolite crystals. In contrast with exchange strategies for encapsulation, which lead to grafted cations and dense metal aluminosilicates, these methods form oxide nanoparticles, evident from infrared spectra of samples exposed to CO. Oxide nanoparticles undergo more facile redox cycles than grafted cations or dense aluminosilicates, thus rendering oxide domains more effective oxidation catalysts. The dynamics and stoichiometry of nanoparticle reduction in H_2 confirmed the presence of NiO, Co_3O_4, and Fe_2O_3 clusters and their more facile reducibility relative to metal aluminosilicates. Ethanol oxidation rates on these clusters were essentially unaffected by exposure to bulky thiol poisons that titrate metal oxide surfaces, reflecting the selective placement of the oxide nanoparticles within the confines of microporous voids, where they are protected from contact by large molecules. These synthetic strategies and guiding principles circumvent long-standing hurdles in the selective encapsulation of base metals, and provide enabling routes for the synthesis of the many metal-zeolite systems that confront similar hurdles.

5.1 Introduction

Crystalline microporous solids, such as zeotypes, are ubiquitous in water purification [1], molecular separations [2], and catalysis [3,4]. Their applications exploit the molecular sieving and shape-selective properties of zeotypes, which lead to preferential access to intracrystalline regions by specific molecules, based on the size and shape of the connecting apertures and cavities within each porous framework [2,5]. Zeolite catalysts, in particular, benefit from the exclusion of large reactive or poison molecules from intracrystalline active sites [5], from the retention of large products until they fragment and egress more readily as smaller species [6], and from the preferential stabilization of specific transition states within intracrystalline voids [7]. These properties can be combined with the inherent catalytic properties of metal surfaces by encapsulating clusters of metals within zeolite voids and, in doing so, synthesizing size-selective and shape-selective metal catalysts [8-10]. Such clusters benefit from significant resistance to coalescence as a consequence of confinement, thus allowing them to retain their small dimensions

under conditions that would cause their significant coalescence and sintering when dispersed on mesoporous supports [8-11].

Most noble metals, including Pt, Pd, Ir, Re, Rh, Ag, Au [8,11], and their bimetallic mixtures [9,12] have been successfully encapsulated within several zeolites (e.g., CHA [13], LTA [11], MFI [8,14], FAU [12,15]). Ion exchange of metal cations and their subsequent reduction by H_2 enable encapsulation of these metals within large-pore zeolites (12-member ring (MR) apertures or larger; e.g., FAU) [15]. Such methods become unsuitable for small-pore (8 MR) zeolites and, in some cases, for medium-pore (10 MR) zeolites, because of the slow diffusion of solvated aqueous precursors through their narrow apertures [16]. In such instances, encapsulation requires the hydrothermal crystallization of zeolite frameworks around solvated precursors, which must be stabilized by ligands against precipitation or reduction at the pH and temperatures of crystallization [8,11]. Such ligands are subsequently removed by thermal treatments in oxidative or reductive environments to form stable and catalytically-competent encapsulated metal clusters [8,11].

The encapsulation of clusters of base metals (e.g., Ni, Co, and Fe) and their oxides [10] is also of significant interest because of their ubiquitous use as catalysts. NiO, Co_3O_4, and Fe_2O_3 are effective oxidation catalysts for diverse substrates, such as CO [17-19], alcohols [20-22], and methane [23]. These oxides can be reduced to their metallic state in order to render them useful as catalysts for hydrocarbon reforming (Ni) [24], aldehyde hydrogenation (Ni) [25], Fischer-Tropsch synthesis (Co, Fe) [26], and ammonia synthesis (Fe) [27]. Ni^{2+}, Co^{2+}, and Fe^{2+} cations can be exchanged from aqueous media onto most zeolites because they can diffuse (along with their double-layer) in their divalent state even through 8-MR zeolite apertures [28,29]. The conversion of these exchanged cations into metal clusters through post-exchange reductive treatments in H_2 or CO, however, cannot be used in general to form encapsulated base metal clusters because the high temperatures required for their reduction (>1000 K) lead to their agglomeration and to the structural degradation of their crystalline microporous scaffolds [28,30]. In fact, these temperatures lead to the transformation of crystalline aluminosilicates into amorphous mesoporous solids [28] and to the formation of refractory metal aluminosilicates (e.g. $CoAl_2O_4$ [10]) or large metal particles at extracrystalline locations [30].

Several synthetic strategies have sought to circumvent the need for severe thermal treatments in order to avoid damage to the host frameworks. Concentrated sodium borohydride solutions (10 M) cause partial reduction (<50%) of Co^{2+}-exchanged FAU to form small (1.1 nm) encapsulated Co clusters [30]. Encapsulated Co nanoparticles have also been prepared in LTA and FAU zeolites by reducing exchanged Co^{2+} cations with treatment in Cd metal vapor [31]. Small Ni nanoparticles (<5 nm diameter) were encapsulated within FAU by subliming $Ni(C_5H_5)_2$ complexes into zeolite micropores and subsequently decomposing the organic ligands via sequential photolysis with ultraviolet radiation and H_2 treatments [32]. Large (>10 nm) Co_3O_4 particles have been embedded within defective regions in MFI crystals by using Co_3O_4/SiO_2 (instead of SiO_2) as the silica reagent in hydrothermal crystallization [33]. The impregnation of aqueous $Fe(NO_3)_3 \cdot 9H_2O$ solutions onto NaOH-treated MFI (to form mesopores that enhance liquid imbibition) followed by thermal treatments in N_2 formed Fe_2O_3 particles about 20 nm in diameter, but present within mesopores, instead of being contained within the protecting MFI voids [34].

The mixed success and the system-specific nature of these techniques provide the impetus and rationale for the identification of the specific hurdles to achieving the encapsulation of base metal precursors while preventing the formation of refractory exchanged species or bulk compounds, and for the development of the robust general synthetic strategies reported here to circumvent these persistent hurdles. The challenges inherent in the encapsulation of base metals include the selection of stable precursors that can be embedded within zeolites, the difficult reduction of base metal cations when present as exchanged species, the enforcement of the selective placement of the precursors within intracrystalline regions, and the prevention of structural damage to zeolite frameworks during synthesis and subsequent thermal treatments.

This study addresses these hurdles through the hydrothermal assembly of zeolite frameworks around ligated metal precursors that promote metal uptake into zeolite crystals, protect metal precursors from precipitation or agglomeration during synthesis, preclude metal cation attachment to zeolite exchange sites, and preserve the structural integrity of the zeolites during crystallization and thermal treatments. In doing so, general procedures are described here for the successful encapsulation of Ni, Co, and Fe oxide clusters within LTA, MFI, and FAU. These procedures provide guiding principles and specific protocols that can be applied to metal-zeolite systems in general and well beyond the system-specific encapsulation of Co_3O_4 clusters within LTA that we reported previously [10].

Encapsulation is achieved here by adding Ni^{2+}, Co^{2+}, or Fe^{2+} cations protected by chelating ligands (N-[3-(trimethoxysilyl)propyl]ethylenediamine; TPE) into LTA, MFI, or FAU synthesis gels and allowing framework assembly to occur around them. The amine function in these bifunctional ligands chelates and protects metal cations from precipitation in the alkaline synthesis gels. The trimethoxysilyl moiety, in turn, forms siloxane linkages with nucleating zeolite precursors in order to enforce the incorporation of these precursors into the crystallizing frameworks. Oxidative treatments of the crystalline frameworks remove ligand species and form metal oxide particles, visible by transmission electron microscopy, that are small (<2.5 nm) and uniformly distributed in size. The zeolite frameworks retain their crystallinity after oxidative treatment, in spite of local framework disruptions around the particles, because of the relatively low temperatures (673 K) required to detach metal cations from their chelating ligands and to nucleate oxide nanoparticles. The infrared spectra of adsorbed CO showed the absence of exchanged cations or bulk aluminosilicates, consistent with protecting ligands that preclude cation attachment at exchange sites. The stoichiometry and rates of reduction in H_2 of oxide nanoparticles confirmed their compositions (NiO, Co_3O_4, Fe_2O_3) and their facile reduction compared with metal aluminosilicates and exchanged cations. The presence of these species within the protected environment of LTA, MFI, and FAU frameworks was confirmed from catalytic rate measurements on samples with and without exposure to large organosulfur titrants that cannot enter intracrystalline regions.

These synthetic approaches circumvent each of the hurdles inherent in encapsulating base metal oxide particles and their precursors, thus enabling the preparation of diverse metal-zeolite compositions using the same general synthetic strategies. Such procedures, and the bifunctional ligands critical to their success, are thus broadly applicable beyond the specific systems used here to identify and circumvent these hurdles.

5.2 Methods

5.2.1 Source and purity of reagents

$Ni(NO_3)_2•6H_2O$ (99.99%, Sigma-Aldrich), $CoCl_2$ (99.99%, Sigma-Aldrich), $FeCl_2$ (99.99%, Sigma-Aldrich), NiO (99.9%, Sigma-Aldrich), Co_3O_4 (99.9%, Sigma-Aldrich), Fe_2O_3 (99.9%, Sigma-Aldrich), N-[3-(trimethoxysilyl)propyl]ethylenediamine (TPE; 98%, Sigma-Aldrich), 1,4,7,10,13-pentaoxacyclopentadecane (15-C-5; 98%, Sigma-Aldrich), 1,4,7,10-tetraoxa-13-azacyclopentadecane (1-Aza-15-C-5; 97%, Sigma-Aldrich), Ludox AS-30 colloidal silica (30% wt. suspension in H_2O, Sigma-Aldrich), $NaAlO_2$ (53% Al_2O_3, 42.5% Na_2O, Riedel-de Haën), NaOH (99.99%, Sigma-Aldrich), tetraethyl orthosilicate (TEOS; 98%, Sigma-Aldrich), tetrapropylammonium hydroxide (TPAOH; 40% wt. in H_2O, Sigma-Aldrich), $CaCl_2•2H_2O$ (EMD Millipore), NH_4NO_3 (99.99%, Sigma-Aldrich), ethanol (99.9%, Sigma-Aldrich), 2,4,6-trimethylbenzyl mercaptan (TMBM; 98%, Sigma-Aldrich), fumed SiO_2 (Cab-O-Sil M5), acetone (99.9%, Sigma-Aldrich), air (extra dry; 99.999%, Praxair), He (99.999%, Praxair), 20% O_2/He (99.999%, Praxair), N_2 (99.999%, Praxair), 1% CO/He (99.999%, Praxair), Ar (99.999%, Praxair), and 4% H_2/Ar (99.999%, Praxair) were used as received. Deionized H_2O (17.9 Ω cm resistivity) was used in all procedures.

5.2.2 Materials Synthesis

5.2.2.1 Synthesis of Ni, Co, and Fe oxide particles within LTA zeolites

NiO_x, CoO_x, and FeO_x were encapsulated within LTA zeolites (Si/Al = 1) by adding Ni^{2+}, Co^{2+}, or Fe^{2+} cations protected against precipitation by chelating ligands into LTA synthesis gels, subsequently crystallizing these gels under hydrothermal conditions, and treating the crystalline powders in oxidative environments in order to remove the attached ligands and form metal oxide particles. Similar procedures were previously used to encapsulate Co_3O_4 clusters within LTA [10]; the synthetic procedures used here for the encapsulation of NiO_x and FeO_x in LTA were adapted and developed from this previous work in order to address significant synthetic hurdles arising from the tendency of metal cations to precipitate in alkaline solutions and difficulties in selectively converting encapsulated metal precursors into clusters. Such adaptations are intended to allow the encapsulation of metal oxide clusters within LTA through a generalized technique rather than system-specific methods, as were previously applied for the encapsulation of Co_3O_4.

The LTA-encapsulated materials were synthesized by first preparing solutions of the protecting ligand (N-[3-(trimethoxysilyl)propyl]ethylenediamine; TPE; 0.70-1.8 g) dissolved in deionized H_2O (9 cm^3). Separate aqueous solutions of $Ni(NO_3)_2•6H_2O$, $CoCl_2$, or $FeCl_2$ (0.199-1.11 g in 9 cm^3 H_2O) were then added dropwise (~0.2 cm^3 s^{-1}) to the aqueous ligand solutions while stirring with a magnetic bar (6.7 Hz). The amounts of ligand and metal precursor used for each sample were chosen to give a ligand(TPE)/metal(Ni, Co, Fe) molar ratio of 2, because at least two ligands per metal cation are required to protect the metal cations against precipitation in LTA synthesis gels (as shown in Section 5.3.1). These solutions were placed within polypropylene bottles (125 cm^3), and colloidal silica (5.3 g; Ludox AS-30) and NaOH (2.4 g) were sequentially added. The containers were sealed and heated to 353 K for 0.5 h while stirring at 6.7 Hz, and then cooled to ambient temperature. Solutions of $NaAlO_2$ (3 g) dissolved in H_2O (9 cm^3) were added,

and the mixtures were held for 2 h at ambient temperature while stirring (6.7 Hz). These procedures lead to homogeneous LTA precursor synthesis gels (molar ratios 1.7 SiO_2/1.0 Al_2O_3/3.2 Na_2O/110 H_2O/0.098-0.27 metal/0.20-0.52 ligand), which were heated in the sealed bottles to 373 K and held for 12 h while stirring (6.7 Hz) in order to crystallize the intended LTA frameworks (NiLTA, CoLTA, FeLTA). The amount of Ni, Co, or Fe in the gels was chosen to achieve 2-5% wt. metal in the product solids, based on zeolite yields obtained in metal-free LTA syntheses. Synthesis gels were prepared with a range of metal loadings in order to identify the effect of metal content on product LTA crystallinity (determined by X-ray diffraction (XRD), Section 5.2.3.1); metal contents were systematically increased until only amorphous solids were detected in synthesis products (as discussed in Section 5.3.2.1).

The NiLTA, CoLTA, and FeLTA suspensions were filtered and rinsed with deionized H_2O until a pH of 7-8 was reached in the filtrate. The samples were treated in a convection oven at 373 K for 8 h and then heated in flowing dry air (1.67 $cm^3\ g^{-1}\ s^{-1}$) to 623 K (at 0.033 K s^{-1}) and held for 3 h. Treated samples were examined by X-ray diffraction (Section 5.2.3.1), electron microscopy (Section 5.2.3.2), and temperature programmed reduction (Section 5.2.3.4), and used in reactivity (Section 5.2.3.5) studies.

The LTA synthesis procedures form zeolites with Si/Al ratios of unity and Na^+ species as the charge-balancing cations [10]. Na^+ was exchanged by Ca^{2+} before NiLTA, CoLTA, and FeLTA samples were examined by infrared (IR) spectroscopy (Section 5.2.3.3) in order to assess their ability to bind CO at sub-ambient temperatures as a probe of the structure of metal species in the zeolites. The exchange of LTA with Ca^{2+} and other divalent cations (e.g., Co^{2+}) increases rates of intracrystalline CO diffusion, particularly at the near-ambient temperatures used in the IR experiments in order to obtain detectable CO coverages [8,10]. Ca^{2+} exchange was carried out by adding NiLTA, CoLTA, or FeLTA solids (1 g) to 3 M aqueous $CaCl_2$ solutions (100 cm^3/g zeolite) and stirring for 8 h (at 6.7 Hz) at ambient temperature. Samples were then filtered and rinsed with deionized water (1500 $cm^3\ g^{-1}$), and the procedure was repeated thrice. These procedures lead to the essentially full exchange of Na^+ by Ca^{2+}, as confirmed by inductively-coupled plasma atomic emission spectroscopy (ICP-AES) measurements of the Ca and Al contents and Ca/Al ratio (Ca/Al = 0.5 [10]) in Ca^{2+}-exchanged LTA zeolites. The supernatant liquids remaining after Ca^{2+} exchange did not contain detectable Ni, Co, or Fe (ICP-AES), consistent with the absence of metal leaching during Ca exchange. Exchanged samples were treated in flowing dry air (1.67 $cm^3\ g^{-1}\ s^{-1}$) at 623 K (at 0.033 K s^{-1}) for 3 h before IR experiments (Section 5.2.3.3).

5.2.2.2 Synthesis of nickel oxide, cobalt oxide, and iron oxide clusters within MFI zeolites

Hydrothermal synthesis protocols for the preparation of MFI zeolites (Si/Al = 30 [35]) using tetrapropylammonium hydroxide (TPAOH) as an organic structure directing agent (SDA) were modified by incorporating the ligated metal cations described above into synthesis gels to prepare MFI frameworks containing NiO_x, CoO_x, and FeO_x clusters. The crystallization of the gels was followed by oxidative treatments of the product solids to remove the ligands and the SDA species.

NiMFI, CoMFI, and FeMFI samples were prepared using aqueous solutions of TPE (0.56-1.16 g ligand; 5 cm^3 H_2O) and aqueous solutions of $Ni(NO_3)_2$•$6H_2O$, $CoCl_2$, or $FeCl_2$ (0.17-0.72 g

in 5 cm^3 H_2O), which were added dropwise (~0.2 cm^3 s^{-1}) to the aqueous ligand solutions while stirring (6.7 Hz) at ambient temperature. As in metal-LTA synthesis procedures (Section 5.2.2.1), TPE/cation (Ni^{2+}, Co^{2+}, or Fe^{2+}) molar ratios of 2 were used for all cations. TPAOH (40% wt. in H_2O; 8.27 g) and TEOS (17.3 g) were added sequentially to the ligand/cation solutions and stirred (6.7 Hz) for 13 h in sealed polypropylene bottles (125 cm^3) at ambient temperature. Separate solutions consisting of TPAOH (1M in H_2O; 13.18 g), H_2O (0.40 g), and $NaAlO_2$ (0.189 g) were then added to the aged solutions containing TEOS, TPAOH, TPE, and metal cations. These mixtures were sealed within polypropylene bottles and heated at 371 K for 2 h while stirring (6.7 Hz). These procedures led to homogeneous synthesis gels (6.5 TEOS/2.3 TPAOH/0.18 $NaAlO_2$/120 H_2O/0.097-0.20 metal/0.19-0.4 ligand molar ratios), which were transferred into Teflon-lined stainless steel autoclaves (125 cm^3, Parr) and heated at 393 K for 15 h (for NiMFI and CoMFI) or 98 h (for FeMFI); the latter reflects MFI synthesis gels with ligated Fe precursors that require longer synthesis times to form crystalline products (as shown in Section 5.3.2.1). MFI synthesis gels were prepared with different metal contents in order to examine the effects of metal loading on product crystallinity (as discussed in Section 5.3.2.1). Metal contents were increased until amorphous products formed (determined by XRD; Section 5.2.3.1). These experiments led to MFI synthesis gels with metal contents chosen to obtain 2-4% wt. metal loading in MFI solids based on zeolite yields from metal-free MFI syntheses.

NiMFI, CoMFI, and FeMFI suspensions were filtered and rinsed with deionized water until the filtrate pH was 7-8 and then treated at 373 K in ambient air for 8 h. The samples were then heated in flowing dry air (1.67 cm^3 g^{-1} s^{-1}) to 673 K (at 0.01 K s^{-1}) and held for 2 h before their use in X-ray diffraction (Section 5.2.3.1), electron microscopy (Section 5.2.3.2), infrared spectroscopy (Section 5.2.3.3), temperature programmed reduction (Section 5.2.3.4), and reactivity (Section 5.2.3.5) studies.

5.2.2.3 Synthesis of nickel oxide, cobalt oxide, and iron oxide clusters within FAU zeolites

Synthetic techniques for the hydrothermal crystallization of FAU [36] (Si/Al of 2.3) in the absence of an organic SDA were adapted and modified with the addition of base metal cations and protecting ligands to form encapsulated NiO_x, CoO_x, and FeO_x clusters. Hydrothermal assembly of FAU in the presence of ligated metal cations was followed by oxidative treatments to remove ligand species and form oxide clusters.

Synthesis gels were prepared by first dissolving TPE (0.61-1.92 g) and metal precursors ($Ni(NO_3)_2$•$6H_2O$, $CoCl_2$, or $FeCl_2$; 0.18-1.16 g) in deionized H_2O (26.25 cm^3). TPE/cation molar ratios of 2 were used for all cations because two TPE ligands per metal cation are needed to prevent precipitation of the metal in FAU synthesis gels (as shown in Section 5.3.1). $NaAlO_2$ (2.34 g) and NaOH (3.77 g) were added sequentially while stirring (6.7 Hz; 0.25 h). Colloidal silica (28.6 g; Ludox AS-30) was then added to this solution at ambient temperature and stirred (at 6.7 Hz) for 2 h to prepare homogeneous synthesis gels (10 SiO_2/1.0 Al_2O_3/4.3 Na_2O/180 H_2O/0.093-0.29 metal/0.19-0.59 ligand molar ratios). The gels were sealed within 125 cm^3 polypropylene bottles and heated at 373 K for 12 h without stirring to form NiFAU, CoFAU, or FeFAU solids. FAU synthesis gels were prepared with a variety of metal contents in order to identify effects of metal loading on product zeolite crystallinity (as discussed in Section 5.3.2.1). Gels with progressively higher metal contents were prepared until amorphous products were formed by the above

procedures, as determined by XRD (Section 5.2.3.1). The metal content in these gels was chosen to achieve 1-3% wt. metal in products (based on zeolite yields in metal-free syntheses). NiFAU, CoFAU, or FeFAU products were isolated by filtration and rinsed to a filtrate pH of 7-8. These solids were then treated in a convection oven at 373 K for 8 h in ambient air and heated in flowing dry air (1.67 $cm^3\ g^{-1}\ s^{-1}$) to 623 K (at 0.033 $K\ s^{-1}$) and held for 3 h. The treated samples were then used in characterization (Section 5.2.3.1-5.2.3.4) and reactivity (Section 5.2.3.5) studies.

Chelating compounds including crown ethers (1,4,7,10,13-pentaoxacyclopentadecane; 15-C-5) and heterocyclic amines (e.g., 1,4,7,10-tetraoxa-13-azacyclopentadecane; 1-Aza-15-C-5) were examined for their potential dual use as both stabilizing ligands for metal cations and templating agents for FAU assembly. Such species were intended to combine the functionality of the chelating ligand and zeolite templating agent in order to avoid competition for intracrystalline void space by distinct ligand and templating species (Section 5.3.2.1). The ability of these heterocyclic compounds to stabilize metal cations (Ni^{2+}, Co^{2+}, Fe^{2+}) was examined by preparing aqueous solutions with ligand/metal ratios of 1 at concentrations equivalent to those used in the FAU synthesis gels described above. These solutions were then brought to pH 13 using NaOH and heated to the crystallization temperature (373 K) as they were monitored for the formation of solid precipitates.

5.2.2.4 Ion exchange of LTA, MFI, and FAU zeolites with Ni^{2+}, Co^{2+}, or Fe^{2+} cations

LTA, MFI, and FAU zeolites prepared in the absence of ligands or metal cations were post-synthetically exchanged with Ni^{2+}, Co^{2+}, or Fe^{2+} cations in order to provide a comparison with samples prepared by direct hydrothermal synthesis in the presence of ligated cations (Section 5.2.2.1-5.2.2.3). These samples were used in infrared (IR) spectroscopy experiments (Section 5.3.3.1) in order to obtain the spectra for CO bound at exchanged cations and to demonstrate the absence of such species in samples prepared by direct hydrothermal syntheses. The LTA, MFI, and FAU zeolites used for ion exchange with Ni^{2+}, Co^{2+}, or Fe^{2+} were synthesized via hydrothermal synthesis as described in Sections 5.2.2.1-5.2.2.3, but in the absence of TPE ligands or metal precursors.

The exchange of Ni, Co, and Fe cations to replace charge-balancing Na^+ species was carried out on LTA (Si/Al = 1) and FAU (Si/Al = 2.3) by dispersing zeolite powders (3 g) in deionized water (10 cm^3) and adding $Ni(NO_3)_2 \cdot 6H_2O$, $CoCl_2$, or $FeCl_2$ precursors at concentrations required to give 3% wt. metal contents at full uptake, which correspond to metal(Ni, Co, Fe)/Al ratios of 0.09 and 0.12 for LTA and FAU, respectively. A nominal metal content of 3% wt. was chosen for these samples because it resembles the metal loadings in samples formed by direct hydrothermal syntheses with ligated precursors (2-4% wt.; Section 5.3.2). Aqueous mixtures of zeolites and metal cations were placed within polypropylene bottles and stirred (6.7 Hz) at ambient temperature for 12 h. In the case of Fe^{2+}, exchange was performed in a N_2 atmosphere to inhibit the formation of Fe^{3+}. The exchanged zeolites were isolated by filtration, rinsed with deionized H_2O (1500 $cm^3\ g^{-1}$), and treated in ambient air at 373 K for 8 h. Their metal contents (2.5-3.0% wt., ICP-AES) were consistent with nearly full uptake of metal cations.

Exchange protocols for MFI (Si/Al = 30) zeolites were adapted from previous reports [37]; they differ from those used for LTA (Si/Al = 1) and FAU (Si/Al = 2.4) because the exchange of

divalent cations into high-silica zeolites is hindered by the low prevalence of adjacent Al pairs required to dehydrate cation solvation shells and allow their attachment to the framework [38]. The low Al content in MFI (Si/Al = 30; formula $Na_{3.1}[Al_{3.1}Si_{92.9}O_{192}](H_2O)_{16}$ [35]) limits the maximum metal content that can be achieved at full exchange (2.8-2.9% wt. for (Ni,Co,Fe)/Al = 1, assuming the absence of extra-framework alumina) and precludes full exchange when Al next nearest neighbors are required to anchor divalent cations [37]. Cation exchange was encouraged by the use of above-ambient temperatures and longer exchange times than for LTA and FAU. The H-form instead of the Na-form of MFI was also used to prevent the localized precipitation of $Co(OH)_2$ in zeolite channels during exchange, which can occur when the exchange is conducted at elevated temperature (353 K) over an extended period of time [39].

Metal-free MFI samples were first exchanged with NH_4^+ cations by suspending MFI powders (2.5 g) in aqueous 0.5 M NH_4NO_3 (50 cm^3) and stirring (6.7 Hz) at 353 K for 10 h. The solids were recovered by filtration and rinsed with deionized H_2O (1500 $cm^3\ g^{-1}$); this procedure was repeated two more times. H-MFI was then treated in ambient air at 373 K for 12 h, and then in flowing dry air (1.67 $cm^3\ g^{-1}\ s^{-1}$) at 773 K for 20 h. This process leads to the nearly complete exchange of Na^+ for H^+ (<0.1% wt. residual Na) [37]. H-MFI solids were then suspended in 0.05 M $Ni(NO_3)_2 \cdot 6H_2O$, $CoCl_2$, or $FeCl_2$ solutions (250 $cm^3\ g^{-1}$) and stirred (6.7 Hz) at 353 K for 16 h in ambient air (Co^{2+}, Ni^{2+}) or a N_2 atmosphere (Fe^{2+}). The solids were recovered by filtration, rinsed with deionized water (1500 $cm^3\ g^{-1}$), and treated in ambient air at 373 K for 8 h. ICP-AES analysis indicated partial exchange was achieved (cation/Al = 0.04, 0.03, and 0.02 corresponding to 0.12% wt., 0.09% wt., and 0.06% wt. for Ni^{2+}, Co^{2+}, and Fe^{2+}). These low metal contents reflect the small fraction of Al sites present as Al-Al next nearest neighbors in Si-rich zeolites [38]. These metal contents, however, are sufficient to allow exchanged metal species to be probed by infrared spectroscopy (Section 5.3.3.1) and temperature-programed reduction (Section 5.3.3.2).

5.2.3 Characterization of zeolite structures and of the size, stoichiometry, and encapsulation selectivity of metal oxide clusters

5.2.3.1 X-Ray diffraction

X-Ray diffraction (XRD) was used to determine the structure and crystallinity of the metal-zeolite samples and to detect the presence of any large metal oxide crystallites (>10 nm). Diffractograms were measured using a D8 Discover GADDS Powder Diffractometer with Cu-Kα radiation (λ = 0.15418 nm, 40 kV, 40 mA) over a 2θ range of 5-50° (0.00625 degrees s^{-1}) on ground powders dispersed uniformly onto quartz slides. The crystallinities of metal-zeolite samples were determined quantitatively from the integrated intensities of the three most intense Bragg lines present in the diffractograms, using metal-free LTA, MFI, and FAU as standards (Section 5.2.2).

5.2.3.2 Transmission electron microscopy

Size distributions of metal oxide nanoparticles were measured by transmission electron microscopy (TEM). A Philips/FEI Tecnai 12 microscope operating at 120 kV was used to obtain micrographs on samples prepared by dispersing ground powders in acetone and then onto holey carbon films mounted on 400 mesh copper grids (Ted Pella Inc.). Particle size distributions were

based on measurements of >300 particles for each sample; these distributions were used to calculate surface-averaged particle diameters $\langle d_{\mathrm{TEM}} \rangle$ [40]:

$$\langle d_{\mathrm{TEM}} \rangle = \frac{\sum n_i d_i^3}{\sum n_i d_i^2} \qquad (1)$$

where n_i is the number of clusters with diameter d_i. The dispersion of these particles (*D*), defined as the fraction of metal (Ni, Co, Fe) atoms present at the surface of the metal oxide clusters, was determined using [40]:

$$D = 6\frac{v_m / a_m}{\langle d_{\mathrm{TEM}} \rangle} \qquad (2)$$

where v_m is the atomic volume of Ni atoms in bulk NiO (0.0183 nm^3 [41]), Co atoms in bulk Co_3O_4 (0.0222 nm^3 [42]), or Fe atoms in bulk Fe_2O_3 (0.0256 nm^3 [43]); and a_m is the area per fully exposed atom on the (001) plane of NiO (0.0877 nm^2 [41]), the (100) plane of Co_3O_4 (0.164 nm^2 [42]), and on the (0001) plane of Fe_2O_3 (0.0841 nm^2 [43]).

Particle size distributions were also used to determine dispersity indices (DI) for each sample; these values are defined as the surface-averaged particle diameter ($\langle d_{\mathrm{TEM}} \rangle$) divided by the arithmetic mean diameter ($\langle d_{\mathrm{n}} \rangle$) [40]:

$$\mathrm{DI} = \frac{\langle d_{\mathrm{TEM}} \rangle}{\langle d_n \rangle} = \frac{\left(\frac{\sum n_i d_i^3}{\sum n_i d_i^2}\right)}{\left(\frac{\sum n_i d_i}{\sum n_i}\right)} \qquad (3)$$

The DI constitutes a rigorous metric for particle size uniformity; sets of particles with DI values smaller than 1.5 are typically considered to be narrowly distributed in size [40].

5.2.3.3 Infrared spectra of adsorbed CO on samples prepared by direct hydrothermal synthesis and post-synthetic exchange

Metal-zeolite samples prepared by direct hydrothermal synthesis (Section 5.2.2.1-5.2.2.3) and post-synthesis exchange (Section 5.2.2.4) were exposed to CO, and their infrared (IR) spectra were collected in order to detect the presence of exchanged metal cations or metal aluminosilicate compounds. NiLTA, CoLTA, and FeLTA samples prepared via hydrothermal synthesis were used in their Ca^{2+}-exchanged form because substitution of monovalent Na^+ with divalent cations (e.g., Ca^{2+}, Co^{2+}) allows more facile access by CO into intracrystalline regions (Section 5.2.2.1). Spectra were measured using sample wafers (40 mg cm^{-2}) and a Thermo Nicolet 8700 spectrometer equipped with an in-situ flow cell. Samples were heated (at 0.033 K s^{-1}) in flowing N_2 (40 cm^3 g^{-1} s^{-1}) to 523 K and held for 1 h before exposure to CO. They were then cooled to 273 K and exposed to flowing 1% CO/He (40 cm^3 g^{-1} s^{-1}) for 0.25 h before measuring spectra. The spectral contributions from CO(g), CO bound at Ca^{2+} or Na^+ cations [44], and CO physisorbed onto the

aluminosilicate framework were subtracted using the corresponding spectra for metal-free LTA, MFI, and FAU. Low CO pressures (1.0 kPa) were used in order to minimize CO adsorption onto Ca^{2+} and Na^{+} charge-balancing cations [44] and on surfaces of oxide crystallites [45-47], which would interfere with the accurate detection of CO bands on metal aluminosilicates or exchanged Ni^{2+}, Co^{2+}, and Fe^{2+} cations.

5.2.3.4 Rate and stoichiometry of reduction for samples prepared by direct hydrothermal synthesis and post-synthetic ion exchange

The reduction stoichiometries and rates for each sample were measured using temperature-programmed reduction (TPR) methods and a Micromeritics AutoChem II 2920 analyzer system equipped with a thermal conductivity detector (TCD) in order to measure H_2 concentrations in the outlet stream. Samples (0.02-0.50 g) were placed within U-shaped quartz tubes and heated to 313 K in flowing Ar (0.83 $cm^3\ s^{-1}$) for 0.33 h, and then exposed to flowing 4% H_2/Ar (0.83 $cm^3\ s^{-1}$) and heated to 1273 K at 0.167 K s^{-1}. The TCD response was calibrated using the stoichiometric reduction of bulk Co_3O_4 and used to calculate H_2 consumption rates as a function of extent of reduction and temperature.

5.2.3.5 Encapsulation selectivities from ethanol oxidative dehydrogenation rates with and without titration of external particles

Ethanol (EtOH) oxidative dehydrogenation (ODH) rates before and after selective titration of extracrystalline oxide surfaces were measured on all metal-zeolite samples in order to determine the extent of encapsulation of metal oxide nanoparticles within zeolite voids. Metal-zeolite samples were exposed to a bulky organosulfur titrant (2,4,6-trimethylbenzyl mercaptan; TMBM) that cannot readily diffuse through the zeolite apertures. EtOH ODH rates on these samples, on untitrated samples, and on the respective bulk oxides (NiO, Co_3O_4, Fe_2O_3) were compared to determine the fraction of the oxide surface areas residing within the protected environment of the zeolite voids (Section 5.3.4).

Metal-zeolite and bulk oxide samples were exposed to TMBM before ethanol ODH reactions by suspending the powder samples (0.1 g) in 0.2 M solutions of TMBM in EtOH (15 cm^3). The suspensions were stirred (6.7 Hz) at ambient temperature for 2 h (Ni, Co) or 16 h (Fe). Longer exposure times were found to be required in order to titrate bulk Fe oxide surfaces (Section 5.3.4). Solids were isolated by filtration and treated in ambient air at 373 K for 8 h. These procedures were used, but without TMBM in the liquid EtOH solution, in order to prepare the untitrated control samples used as comparisons.

The titrated and control samples were diluted (10-fold by mass) with SiO_2 and pelleted and sieved to retain aggregates 180-250 μm in size in order to avoid any temperature gradients from exothermic oxidation reactions. These aggregates were placed within fritted quartz tubes (8 mm I.D.) and heated to 393 K in flowing 20% O_2/He (1.67 $cm^3\ g^{-1}\ s^{-1}$). Temperature was controlled using a three-zone resistively-heated furnace equipped with Watlow Series 988 electronic controllers and measured with a type-K thermocouple (Omega, Inc.) attached to the outer tube surface. Liquid EtOH was introduced into an O_2/He stream using a syringe pump (Cole Parmer; 60061 Series) through a port held at 393 K. Gas flow rates were metered using Porter Instrument

mass flow controllers set to achieve the desired EtOH, O_2, and He pressures (4 kPa EtOH, 9 kPa O_2, 87 kPa He). EtOH conversions were kept below 3% and all transfer lines were heated to 393 K to prevent condensation of reactants or products.

Turnover rates for EtOH ODH are reported here based on the number of surface atoms determined from metal contents and dispersions for metal-zeolite samples (Eq. 2) and from BET surface areas and atom surface densities for bulk oxides (Supporting Information (SI), Section 5.S1). Effluent concentrations of EtOH and acetaldehyde, the only product detected, were measured by flame ionization after chromatographic separation (phenylmethyl-silicone capillary column; HP-5; 50 m × 0.32 mm, 1.05 μm film thickness; Shimadzu GC-2014). Deactivation was not detected in the time scale of these experiments (~8 h). Empty reactors, mesoporous silica, and metal-free LTA, MFI, and FAU did not lead to detectable amounts of any EtOH oxidation products.

5.3 Results and Discussion

5.3.1 Assessing the stability of ligated metal precursors in zeolite synthesis gels

The stability of coordination complexes formed from Ni^{2+}, Co^{2+}, and Fe^{2+} cations and ligands (N-[3-(trimethoxysilyl)propyl]ethylenediamine; TPE) was examined by treating these complexes at the pH and temperature required for the crystallization of each zeolite framework in order to detect colloidal precipitation. Scheme 5.1 shows the schematic structure of TPE; also shown in Scheme 5.1 are other heterocyclic chelating complexes used (or proposed for use) in this work as bifunctional stabilizing ligands and organic structure directing agents, specifically for the synthesis of metal-FAU samples (Section 5.3.2.1). TPE was chosen as the stabilizing ligand because of its bidentate amine functionality, which is known to chelate metal cations [48,49], and is thus able to confer resistance to precipitation of cations as hydroxides in alkaline solutions [10]. Temperatures (373-393 K), pH levels (13-14), and concentrations of solvated cations (0.03-0.09 M) used for the stability tests were chosen to reflect those required to crystallize LTA, MFI, and FAU (Section 5.2.2). Solutions with TPE/cation ratios of unity formed solid precipitates, even at temperatures lower than required to form LTA and FAU (373 K; Section 5.2.2.1, 5.2.2.3) for all cations, consistent with the displacement of the ligands by OH^- and the formation of oxyhydroxides. Ni^{2+}, Co^{2+}, and Fe^{2+} solutions prepared with TPE/cation ratios of 2, in contrast, did not precipitate even after 100 h at the conditions required to form LTA, MFI, or FAU (373-393 K; Section 5.2.2.1-5.2.2.3). These data show that TPE ligands stabilize Ni^{2+}, Co^{2+}, and Fe^{2+} cations at molar ratios of 2 or higher. Monodentate amine ligands, such as NH_3, were unable to prevent precipitation of Co cations even at NH_3/Co ratios of 6 at LTA synthesis conditions [10]. The stability against precipitation of metal precursors conferred by TPE ligands requires the chelating action that is provided by the bidentate amine moiety. The use of these TPE ligands therefore overcomes one of the principal hurdles in the encapsulation of base metals by preventing the formation of oxyhydroxides at the temperature and pH conditions required for framework nucleation and growth. The ability of the TPE ligands to stabilize all three cationic species (Ni^{2+}, Co^{2+}, Fe^{2+}) at the conditions of hydrothermal synthesis demonstrates the versatility of these ligand species and their general applicability, in spite of the differing tendencies of these three cations to precipitate in alkaline solutions.

5.3.2 Synthesis of crystalline zeolite frameworks and their stability during thermal treatment protocols

5.3.2.1 Effects of the ligand and metal contents of synthesis gels on the crystallinity of zeolites prepared by hydrothermal synthesis

The presence of ligated cations in zeolite synthesis gels can inhibit or even prevent crystallization when such species are present at sufficiently high concentrations and occupy volumes larger that the framework voids [8,10]. The alkoxysilane moiety in TPE enforces the uptake of ligated precursors within the void structure by forming siloxane bridges with the framework as nuclei form and grow [8-10]. Such siloxane linkages and the bulky nature of these coordination complexes, however, can locally disrupt zeolite crystal periodicity [8,10]. The size of Ni^{2+}, Co^{2+}, and Fe^{2+} cations with two attached TPE ligands (~1.1 nm, ~1.0 nm, and 1.1 nm, respectively; estimated by MolView, v. 2.2, largest dimension [50]) is similar or slightly larger than the α-cage diameters in LTA (1.1 nm [51]) and FAU (1.1 nm [51]) or the channel intersections in MFI (0.64 nm [51]), indicating that the framework structures must distort locally when these complexes are occluded within intracrystalline voids. This imposes limits on the volumetric density of ligated precursors that can be placed within frameworks without preventing their nucleation and, consequently, on the loading of metal cations (and ultimately of metal and oxide particles) that can be encapsulated via direct hydrothermal syntheses.

Metal-zeolite samples with 2-5% wt. metal content in their synthesis gels were prepared in order to determine the highest metal loadings that could be attained without compromising framework crystallinity. The results, including the metal and ligand contents in synthesis gels and the crystallinity of the solids formed, are summarized in Table 5.1. Our previous studies showed CoLTA samples could be prepared with up to 4% wt. Co, but higher loadings prevented LTA crystallization [10]. X-Ray diffractograms of NiLTA and FeLTA prepared with 4% wt. and 3% wt. metal loading, respectively, gave sharp Bragg lines indicative of crystalline LTA structures (Section 5.S2, SI). NiLTA and FeLTA samples synthesized with 5% wt. and 4% wt. nominal metal contents, however, gave diffuse backgrounds without detectable diffraction lines, consistent with the prevalence of amorphous solids (XRD; Section 5.S2, SI).

Similar effects of higher loadings were evident for MFI and FAU frameworks. NiMFI, CoMFI, and FeMFI with 3%, 3%, and 2% metal contents in the synthesis gels gave the diffraction patterns of crystalline MFI, while higher loadings (4%, 4%, and 3%) gave amorphous samples (Section 5.S3, SI). Metal-FAU samples (NiFAU, CoFAU, and FeFAU) were crystalline for nominal metal contents as high as 2% wt., but were amorphous when prepared with 3% wt. nominal loadings (Section 5.S4, SI). The ratios of TPE ligands to T atoms (T = Si, Al) present in LTA, MFI, and FAU synthesis gels leading to the highest metal contents that allowed framework crystallization were 0.07-0.09, 0.03-0.04, and 0.03, respectively. These ratios were similar for gels containing Ni or Co cations (LTA: 0.09, MFI: 0.04, FAU: 0.03) and slightly lower for LTA and MFI gels containing Fe cations (LTA: 0.07, MFI: 0.03, FAU: 0.03), showing that the addition of Fe, instead of Ni or Co, to the synthesis gels places more stringent limits on the maximum attainable loadings. The TPE/T-atom ratios present in synthesis gels at these maximum attainable loadings show that crystalline zeolites can form even when up to 9% of T-atoms are derived from the alkoxysilane moieties in the TPE ligands, demonstrating that zeolite self-assembly processes

are quite tolerant of the disruptions imposed by the TPE ligands. These data establish upper limits to attainable metal loadings and confirm that ligated metal precursors can disrupt zeolite crystallization when present at sufficiently high concentrations.

The mechanistic basis of these specific limits for each given framework and metal remain speculative. These limits may reflect the fraction of the silicates/aluminates in gels that form linkages with the TPE siloxy groups (present at TPE/cation ratios of 2). These linkages serve to anchor metal precursors to aluminosilicate oligomers during zeolite crystal growth [8-10], but also appear to disrupt framework assembly by displacing the cations (Na^+, TPA^+) that template the crystallization of a given framework, while also possibly forming these framework attachments at positions ill-suited for ultimate nucleation and growth. Such disruptions may be caused by steric effects from the ligand alkyl chain, which interfere with crystal growth by preventing the attachment of aluminosilicate oligomers or by distorting their orderly attachment to pre-existing framework nuclei. The maximum ligand contents (and thus metal contents) that allow crystallization for LTA, MFI, and FAU synthesis gels (TPE/T-atom ratios: 0.09, 0.04, 0.03) differ among these frameworks; they do not systematically correlate with framework density (LTA: 14.2, MFI: 18.4, FAU: 13.3; units: T-atom $(1000Å^3)^{-1}$) [51], with the largest void size (LTA: 1.1 nm, MFI: 0.64 nm, FAU: 1.1 nm) [51], with the molar ratios of templating cations (Na^+ for LTA, FAU; TPA^+ for MFI) to metal cations (LTA: 30, MFI: 16, FAU: 44) in the synthesis gels, with Si/Al ratios (LTA: 1.0, MFI: 30, FAU: 2.4), or with the mean crystal diameter (from TEM; LTA: ~600 nm, MFI: ~200 nm, FAU: ~800 nm).

Ligated Fe precursors appear to impose more significant hurdles to crystallization than Ni or Co precursors, as evident from the lower metal contents attainable for Fe-containing samples (Table 5.1). FeMFI synthesis gels (1.5% wt. nominal loading) held at hydrothermal synthesis conditions for 15 h formed viscous liquids without detectable solids, while NiMFI and CoMFI synthesis gels with 1.5% wt. metal formed crystalline solids after 15 h (Figure 5.1). Longer crystallization times (98 h; Section 5.2.2.2) ultimately led to the formation of MFI crystals in FeMFI gels (Figure 5.1). These more significant hurdles imposed by ligated Fe precursors at similar molar contents in gels may reflect the different binding orientations of TPE ligands to Fe cations, which could impose greater local disruptions to the assembly of aluminosilicate oligomers. Fe^{2+} cations may also oxidize to form ligated Fe^{3+} species in synthesis gels, which could cause greater perturbations in zeolite crystallization than divalent cations by abstracting a larger number of H_2O molecules from the hydrothermal synthesis mixtures into their solvation shells.

At a specific pH and temperature, Fe^{3+} cations can be inserted into zeotype frameworks [52,53] through the formation of Si-O-Fe linkages [53]. The formation of such linkages in Fe-zeolite synthesis gels would require the oxidation of ligated Fe^{2+} cations to Fe^{3+} and the displacement of the attached TPE ligands. Ligand detachment would allow the formation of the Si-O-Fe linkages required to adopt the tetrahedral coordination of framework T-sites, which would have been evident from the rapid precipitation of ligated precursors during stability tests (Section 5.3.1), because ligand detachment in the absence of Si or Al sources would have led to the formation of Fe-O-Fe linkages and to the nucleation of colloidal oxyhydroxides. Indeed, ligated Ni, Co, and Fe precursors form oxide clusters instead of framework heteroatoms after oxidative treatments, as shown by the infrared (Section 5.3.3.1), reduction (Section 5.3.3.2), and reactivity (Section 5.3.4) data below.

The 1,4,7,10,13-pentaoxacyclopentadecane (15-C-5 crown ether; Scheme 5.1) ligand was examined as an alternative to TPE ligands for cation stabilization during the synthesis of FAU, which had the lowest attainable metal content of the three zeolite frameworks prepared from TPE-stabilized cations (2% wt.; Table 5.1). 15-C-5 forms chelate complexes with divalent first-row transition metal cations such as Ni^{2+}, Co^{2+}, and Fe^{2+} [54], and also acts as an organic structure-directing agent for FAU (OSDA) [55]. 15-C-5 is incorporated into FAU crystals during the framework assembly process [55]; however, unlike TPE, 15-C-5 does not form siloxane linkages with zeolite precursors and therefore does not disrupt crystal periodicity. As a result, the use of 15-C-5 as a chelating agent for metal cations could provide a route to forming crystalline zeolites with higher metal loading than can be achieved with TPE ligands. Solutions with (15-C-5)/cation ratios of unity, however, led to fast precipitation of metal precursors at a pH of 13, indicative of the displacement of the chelating crown ethers by OH^-. We conclude that the interactions between cations and the O-atoms in 15-C-5 are much weaker than the coordinative attachments formed between cations and the two amine groups in TPE [54]. The use of 1,4,7,10-tetraoxa-13-azacyclopentadecane crown ethers (1-Aza-15-C-5; Scheme 5.1), which contain a secondary amine instead of one of the O-atoms as part of the heterocycle, also led to fast precipitation at ambient temperature and a pH of 13. Identical experiments conducted with ligand/cation ratios of 2 also led to precipitation using either 15-C-5 or 1-Aza-15-C-5 ligands.

Metal cation interactions with amine groups are generally stronger than with O-atoms within crown ethers [54], but interactions with a single amine group are insufficient to prevent ligand displacement by OH^- at the pH required for hydrothermal syntheses. We surmise that 15-C-5 cyclic species with more than one amine moiety, such as 1,4,10-trioxa-7,13-diaza-cyclopentadecane and 1,7-dioxa-4,10,13-triaza-cyclopentadecane (Scheme 5.1), may provide the requisite stability at the conditions of hydrothermal syntheses. The use of such heterocyclic amines as chelating agents for metal cations could also serve to provide organic templates for FAU synthesis, as in the case of 15-C-5. The dual nature of these heterocyclic amines, as templates and protecting ligands, would also avoid the exclusion of the template, required for framework crystallization, from intracrystalline voids by the competing presence of a separate ligated cation complex. Such ligand-template species would open new routes to confine metal and oxide nanoparticles within FAU or other zeolites that use crown ethers as templates at metal loadings even higher than those attainable by the synthesis protocols reported here. The search for molecules that act as templates for other structures, but which also stabilize metal cations, would make these synthetic strategies applicable in general for broader classes of zeolites and nanoparticle compositions and with fewer inherent limits on attainable metal contents.

These results, taken together, demonstrate the ubiquitous hurdles that interfere with the concurrent need to stabilize metal precursors with ligands that also encourage their inclusion within the void structure, but which do not disrupt the nucleation and growth of the microporous frameworks. They also provide the guidance and protocols required to circumvent them, to the extent allowed by the nature of the ligands that prevent the precipitation of precursors at the pH and temperature needed for hydrothermal crystallization. Ligated precursors in synthesis gels, when present in excess of a critical concentration, disrupt the formation of periodic framework structures and limit the attainable metal contents. Consequently, these critical concentrations in the synthesis must be determined, by experimentation at the current time, in order to ensure

successful encapsulation. Specific metal precursors, such as Fe^{2+} cations, can impose nucleation barriers that can be addressed by longer synthesis times. Structure-directing molecules with functional groups that prevent precursor precipitation would avoid the inherent compromises between metal content and framework crystallinity. Such species would serve the dual function to template framework assembly and to chelate metal precursors, thus eliminating disruptions to framework assembly caused by covalent linkages between ligands and framework precursors and by the displacement of templating agents by ligands from within zeolite voids. In the next section, we describe protocols and practices intended to preserve zeolite crystallinity during the post-synthetic treatments required to convert ligand-protected metal precursors occluded within zeolites into nanoparticles.

5.3.2.2 Zeolite crystallinity and oxide formation after ligand removal via thermal treatments

Post-synthetic treatments are required to remove ligands and transform ligated precursors into metal or oxide particles; such treatments can disrupt framework structures when high temperatures are required. The reduction of zeolite-exchanged base metal cations to metal nanoparticles, for instance, requires treatments in H_2 above 1000 K [28], which destroy aluminosilicate frameworks and form large metal crystallites within the amorphous aluminosilicates that form [28,30]. The chelating TPE ligands used here were chosen with the intent of preventing, through preferential coordination and steric hindrance, direct linkages between metal cations and framework T-sites, thus allowing the conversion of these precursors into oxide clusters at temperatures lower than those required to reduce exchanged cations. Temperature-programmed oxidation studies on CoLTA showed that TPE ligands can be removed by oxidative treatments at 623 K, without affecting the host framework or leading to the grafting of Co^{2+} cations onto LTA exchange sites [10].

The metal-zeolite samples prepared here by direct hydrothermal synthesis using TPE-ligated metal precursors were treated in oxidative environments (21% O_2) at 623-673 K (Section 5.2.2.1-5.2.2.3) in an attempt to remove the organic ligands (TPE) and the MFI OSDA (TPAOH; Section 5.2.2.2). The structural integrity of zeolite frameworks and the presence of nanoparticles in the treated samples were determined by XRD (Section 5.2.3.1) and TEM (Section 5.2.3.2), respectively.

The X-ray diffractograms for samples prepared by direct hydrothermal syntheses (NiLTA, CoLTA, FeLTA, NiMFI, CoMFI, FeMFI, NiFAU, CoFAU, FeFAU) and then treated in air at 623-673 K (Section 5.2.2) are shown in Figure 5.1, together with those for metal-free LTA, MFI, and FAU. LTA, MFI, and FAU (Figure 5.1) were prepared with 3% wt., 1.5% wt., and 1.5% wt. nominal metal contents, respectively. All samples gave diffraction lines that were sharp and indicative of the exclusive presence of the intended framework. Diffraction features for bulk metal oxides were not detected (e.g., (111) reflection in NiO, $2\theta = 37^{O}$; (311) in Co_3O_4 $2\theta = 39^{O}$; (311) in Fe_2O_3, $2\theta = 36^{O}$).

Ni, Co, and Fe contents in the recovered solids were only slightly below those in the synthesis gels (10-20%; Table 5.2), indicative of the predominant incorporation of the metal precursors into the solids formed and of the ability of alkoxysilane moieties in TPE ligands to promote encapsulation through the formation of siloxane linkages to the nucleating frameworks

[8-10]. The remaining ligated precursors were retained within supernatant solutions, which were separated from the solids by filtration (Section 5.2.2).

The size distributions of oxide nanoparticles after oxidative treatments were measured by transmission electron microscopy (TEM). Surface-averaged particle diameters ($\langle d_{TEM} \rangle$; Eq. 1), fractional dispersions (D; Eq. 2), and dispersity indices (DI; Eq. 3) (Section 5.2.2) are shown in Table 5.2 for all samples. TEM data for NiLTA, FeMFI, and CoFAU samples are shown in Figure 5.2 and for all other samples (CoLTA, FeLTA, NiMFI, CoMFI, NiFAU, FeFAU) in the SI (Section 5.S5).

Nanoparticles are evident in all zeolite samples, indicative of the removal of the chelating TPE ligands by oxidative treatments and of the nucleation and growth of small nanoparticles (1.5-2.3 nm) uniformly distributed in size (DI<1.11) during (or after) ligand removal (Table 5.2). Their mean diameters are slightly larger than the α-cages in LTA (1.1 nm [51]) and FAU (1.1 nm [51]) or than the channel intersections in MFI (0.64 nm [51]), indicative of particle growth that locally disrupts the crystalline frameworks, with the consequent energetic cost of such disruptions likely responsible for limiting particle growth. These framework disruptions cannot be detected in diffractograms (Fig. 5.1), because the fraction of the crystal volume occupied by oxide particles is less than 1.5% in all samples (calculated from framework densities [51], the number of particles, and the bulk densities of NiO, Co_3O_4, Fe_2O_3). Micropore volume measurements conducted using CO_2 adsorption (Section 5.S6, SI) on metal-LTA (0.32 $cm^3\ g^{-1}$), metal-MFI (0.16-0.17 $cm^3\ g^{-1}$), and metal-FAU (0.34-0.36 $cm^3\ g^{-1}$) samples were similar to their metal-free counterparts (LTA: 0.34 $cm^3\ g^{-1}$, MFI: 0.19 $cm^3\ g^{-1}$, FAU: 0.38 $cm^3\ g^{-1}$), further confirming that the micropore structures of these zeolites remain largely intact despite the presence of metal oxide nanoparticles within the crystallites. We surmise that the absence of framework disruptions in numbers sufficient to detect their presence by XRD or CO_2 adsorption reflects (i) TPE/T-atom ratios in the synthesis gels (LTA: 0.066-0.071, MFI: 0.021-0.022, FAU: 0.022-0.023) that are well below the critical values that significantly disrupt the assembly of crystalline frameworks (LTA: 0.093-0.11, MFI: 0.044-0.055, FAU: 0.043-0.046; Table 5.1), (ii) the relatively small fraction of crystal volume occupied by the nanoparticles ultimately formed (<1.5%), and (iii) partial healing of the framework defects upon oxidative removal of the occluded TPE ligands. Such infrequent disruptions do not compromise the framework integrity or the protection of intracrystalline nanoparticles against sintering or contact with large molecules present in the extracrystalline fluid phase.

Mean diameters were similar for all metals in each given zeolite (e.g., NiLTA: 1.5 ± 0.2 nm, CoLTA: 1.6 ± 0.3 nm, FeLTA: 1.9 ± 0.3 nm); they were smallest in LTA and largest in FAU for a given metal, in spite of the higher metal contents achieved in LTA (2.5-2.7% wt.) than in MFI (1.2-1.3% wt. nominal) or FAU (1.2-1.4% wt.). These trends in size parallel the respective sizes of the apertures in each host framework (LTA: 0.41 nm apertures; 8-MR [51]; 1.5-1.9 nm oxides; MFI: 0.55 nm apertures; 10-MR [51]; 1.7-1.9 nm oxides; FAU: 0.74 nm apertures; 12-MR [51]; 2.2-2.3 nm oxides). These sizes are likely set by kinetic or thermodynamic hurdles to coalescence or sintering, imposed by the confining framework, which must be locally disrupted to allow the growth of nanoparticles [8-10]. The inverse correlation between cluster size and zeolite aperture size may reflect larger energy penalties incurred to rupture smaller apertures.

These data show that oxidative treatments convert ligated precursors into nanoparticles without significant framework disruptions and that TPE ligands prevent the attachment of Ni^{2+}, Co^{2+}, and Fe^{2+} at exchange sites, a process that would have prevented the formation of oxide nanoparticles. Such size and structural stability reflects: (i) the modest temperatures required for ligand removal, (ii) the low density of the oxide nanoparticles that cause the local disruptions, and (iii) the energetic penalties associated with framework disruptions required for nanoparticle growth. The next section confirms that exchanged cations are not detectable by infrared spectra of adsorbed CO and that their reduction rates are consistent with the properties of the oxide nanoparticles that are evident from TEM (Fig. 5.2), instead of exchanged cations.

5.3.3 Binding properties and stoichiometry of encapsulated oxide nanoparticles

5.3.3.1 Infrared spectra of adsorbed CO and evidence for the absence of exchanged metal cations and metal aluminosilicates

Metal oxide particles are generally more effective catalysts [17-23] than isolated exchanged cations [10], because they undergo more facile redox cycles than isolated exchanged cations; these exchanged species are more difficult to reduce [28,30] and exhibit larger HOMO-LUMO gaps than oxide particles [10,56]. The infrared spectra of adsorbed CO show distinct bands for CO coordinated to exchanged cations [57-59] and metal-aluminosilicate compounds [60-62], but much weaker features for CO interacting with oxide nanoparticle surfaces [45-47].

Infrared spectra of CO adsorbed on metal-zeolite samples (273 K; 1 kPa CO) are shown in Figure 5.3 for materials prepared by direct hydrothermal synthesis and subsequent oxidative treatments (623-673 K; Section 5.2.2). The spectra of CO adsorbed onto LTA, MFI, and FAU exchanged with Ni^{2+}, Co^{2+}, or Fe^{2+} (Section 5.2.2.4) are also shown in Figure 5.3. NiLTA, CoLTA, and FeLTA samples were exchanged with Ca^{2+} cations in order to allow the more facile diffusion of CO throughout LTA frameworks (Section 5.2.2.1).

LTA, MFI, and FAU zeolites exchanged with Ni^{2+}, Co^{2+}, and Fe^{2+} showed intense bands at 2200-2160 cm^{-1}, consistent with carbonyl stretches for CO bound at Ni, Co, and Fe cations [57-59]. Any contributions from CO adsorbed on Na^{+} or Ca^{2+} cations were subtracted from these spectra using CO adsorption spectra collected on metal-free LTA, MFI, and FAU (Section 5.2.3.3). CO absorption bands were much less intense in (metal-exchanged) MFI than for LTA and FAU because of the lower metal contents (LTA, FAU: 2.5-3.0% wt.; MFI: 0.12-0.06% wt.), a consequence, at least in part, of the small number of exchange sites at high Si/Al framework ratios (Section 5.2.2.4).

Metal-zeolite samples prepared by direct hydrothermal synthesis methods (Section 5.2.2) did not show detectable infrared bands corresponding to CO coordination at exchanged Ni, Co, or Fe cations (2200-2160 cm^{-1} [57-59]) or at surfaces of metal aluminosilicates (e.g. Ni aluminate, Co silicate, Fe silicate; 2205-2170 cm^{-1} [60-62]). The absence of such features indicates that cations are predominantly present as oxide nanoparticles instead of exchanged species or metal aluminosilicate surfaces. The rates of oxide reduction (Section 5.3.3.2) and of ethanol oxidation on these oxides (Section 5.3.4) described below confirm the prevalence of oxide nanoparticles in these samples.

Metal-zeolite samples prepared by direct hydrothermal synthesis did not show detectable bands for CO physisorbed on oxide surfaces (NiO, Co_3O_4, Fe_2O_3) because their weak binding leads to very low surface coverages at 1 kPa CO [45-47]. Such low CO pressures were specifically chosen in order to minimize the concurrent physisorption of CO at Na^+ and Ca^{2+} cations [44], which would interfere with infrared features for CO adsorbed onto exchanged Ni^{2+}, Co^{2+}, or Fe^{2+} cations. These results, taken together with TEM data (Fig. 5.2; Section 5.3.2.2), show that the ligated precursors confined within all frameworks decompose during oxidative treatments, through the removal of ligands and the formation of oxide nanoparticles; the effects of titration with large organosulfur compounds on ethanol oxidation rates (Section 5.3.4) show that such nanoparticles reside predominantly within the protected confines of the zeolite voids.

5.3.3.2 Reduction properties and the stoichiometry of oxide nanoparticles in metal-zeolite samples

The dynamics of reduction, the extent of reduction, and the oxidation states of Ni, Co, and Fe species present in metal-zeolite samples were determined using temperature-programmed reduction (TPR) methods by heating samples from 313 to 1273 K at 0.167 K s^{-1} in flowing 4% H_2/Ar and measuring the amounts of H_2 consumed (Section 5.2.3.4). The reduction profiles of metal-zeolite samples and of bulk NiO, Co_3O_4, and Fe_2O_3 are shown in Figure 5.4. Small oxide domains are more difficult to reduce than larger crystallites because of their more intimate interactions with insulating supports [63] and their larger HOMO-LUMO gaps [56]. Ni, Co, and Fe oxide domains can also form metal aluminates or silicates (e.g., $NiAl_2O_4$, Co_2SiO_4, Fe_2SiO_4 [60-62]) at high temperatures (~800 K or greater) through reactions with aluminosilicates, including in their crystalline zeolite forms [10]. These bulk compounds resist reduction even above 900 K; they can form during TPR before the full reduction of the oxide domains and before or during the incipient thermal degradation of the zeolite frameworks [10,64]. Consequently, these TPR features (Fig. 5.4) may arise from the reduction of the oxide nanoparticles evident in micrographs (Fig. 5.2; Section 5.3.2.2) or from the reduction of metal aluminosilicates that may form in-situ before the full reduction of the oxide nanoparticles.

The reduction of bulk NiO (Fig. 5.4a) starts at ~530 K and shows the H_2/Ni consumption ratio expected for the reduction of all Ni^{2+} cations to Ni^0 (1.03 vs. 1.0). Ni^{2+} reduces to Ni^0 in a in a single two-electron reduction event, and the two reduction features for bulk NiO in Figure 5.5a reflect bimodal size distributions of NiO crystallites, which lead to concomitant effects of oxide domain size on reduction properties [65]. NiFAU and NiMFI reduce with a single H_2 consumption feature at onset reduction temperatures of 670 K and 690 K, and with H_2/Ni consumption ratios of 1.05 and 1.06, respectively. These data are consistent with the stoichiometry of NiO and with small nanoparticles (1.9-2.3 nm; Table 5.2) that reduce at higher temperatures than larger bulk NiO crystallites (410 nm; SI, Section 5.S1). NiLTA gave three visible reduction features centered at 730 K (H_2/Ni = 0.17), 930 K (H_2/Ni = 0.66), and 1120 K (H_2/Ni = 0.13), with the onset of reduction at 675 K. The total H_2/Ni consumption ratio (0.96) is consistent with the reduction of all Ni^{2+} species in this sample. The two high-temperature features together account for the majority of the reduced Ni (~82%), and are likely to arise from Ni silicates, which reduce in this temperature range (900-1200 K [66]). Such species, if present after oxidative treatments, would have been evident from their CO infrared bands (Section 5.3.3.1) given their prevalence in TPR profiles, suggesting that metal aluminosilicates form via reactions between NiO nanoparticles and the LTA

frameworks as the latter incipiently degrade before the reduction of NiO is complete. The low-temperature feature (730 K) in NiLTA is typical of small (<8 nm) NiO crystallites supported on silicates [67] and is likely to arise from reduction of NiO nanoparticles before they form Ni aluminosilicates.

The reduction profiles of bulk Co_3O_4 and of CoFAU, CoMFI, and CoLTA samples are shown in Figure 5.4b. Bulk Co_3O_4 reduction becomes detectable at ~500 K and consists of two features (580 K, H_2/Co = 0.33; 680 K, H_2/Co = 1.0), corresponding to the sequential reduction of Co_3O_4 to CoO and then of CoO to Co^0 and consistent with the complete reduction of Co_3O_4 aggregates (H_2/Co = 1.33) [68]. The total H_2/Co consumption ratios for CoFAU, CoMFI, and CoLTA (1.28, 1.21, and 1.16, respectively) are consistent with full reduction of nanoparticles predominantly consisting of Co_3O_4 (H_2/Co = 1.33), but with some particles containing a deficit of Co^{3+} cations. Each sample shows two reduction features (I: 600 K, 710 K, and 920 K; II: 990 K, 1000 K, and 1100 K; CoFAU, CoMFI, and CoLTA). The high temperature reduction processes occur at temperatures (>900 K) typical of the reduction of bulk Co_2SiO_4 or $Co_2Al_2O_5$ [69,70], which appear to form before all the Co oxide nanoparticles reduce to Co^0, as in the case of Ni-zeolite samples. Infrared spectra indeed show that treatment of CoLTA at 1020 K in H_2 or O_2 leads to the appearance of CO infrared bands corresponding to these Co aluminosilicates, which occurs after samples are treated at the same temperatures that cause the disappearance of LTA diffraction lines [10].

The first reduction feature in Co-zeolite samples (H_2/Co ratios of 0.35, 0.41, and 0.66 for CoFAU, CoMFI, and CoLTA) is assigned here to the partial reduction of the Co_3O_4 nanoparticles evident in electron micrographs (Fig. 5.2; Section 5.3.2.2) to Co metal or CoO. The onset of such reduction features occurs at higher temperatures for CoMFI and CoLTA (660 K, 800 K, respectively) than for bulk Co_3O_4 (~500 K), consistent with their much smaller particle diameters (1.7, 1.6 nm, Table 5.2 vs. 28 nm, Section 5.S1). The onset of reduction in CoFAU, however, occurs at 530 K, a temperature similar to those required for the incipient reduction of bulk Co_3O_4 (~500 K). The low intensity of this feature (H_2/Co = 0.35) relative to the total H_2 consumed (H_2/Co = 1.28) and its low temperature suggest that it reflects the presence of a few larger Co_3O_4 particles, too few in number to be detectable by TEM (Section 5.3.2.2) or XRD (Section 5.3.2.2). Below, reactivity studies and titrations with organosulfur species show that such extrazeolitic clusters constitute a small fraction (<6%) of the total Co oxide surface area in this sample (Section 5.3.4). The onset of the second reduction feature in CoFAU (H_2/Co = 0.93) occurs at temperatures (~800 K) similar to those required to reduce the Co_3O_4 nanoparticles in LTA, suggesting that it arises, at least in part, from the reduction of the nanoparticles visible in the electron micrographs of these samples (Fig. 5.2). This feature is broad and bimodal and extends into the temperature range (810-1150 K) reported for the reduction of Co in aluminosilicates (>900 K) [69,70], indicative of the partial conversion of Co_3O_4 clusters into Co_2SiO_4 or $Co_2Al_2O_5$ before their complete reduction to Co metal.

The reduction profiles of bulk Fe_2O_3 and of FeFAU, FeMFI, and FeLTA samples derived from direct hydrothermal syntheses are shown in Figure 5.5c. Fe_2O_3 reduces in three distinct stages, evident at 630 K (H_2/Fe = 0.17), 700-940 K (H_2/Fe = 0.33), and 900-1200 K (H_2/Fe = 1.0), which correspond to the respective reductions of Fe_2O_3, Fe_3O_4, and FeO [71]. FeFAU and FeLTA each showed two reduction features (I: 730 K and 680 K; II: 1130 K and 1160 K; FeFAU and

FeLTA) and gave total H_2/Fe consumption ratios (1.42, 1.43) consistent with the predominant presence of iron(III) oxide (Fe_2O_3; H_2/Fe = 1.5) in these samples after oxidative removal of the ligands from Fe precursors. The high-temperature reduction features in these two samples are attributed to Fe aluminate or silicate species [72,73], which, as in the case of Ni and Co zeolite samples, form via FeO_x reactions with the aluminosilicate frameworks. The first H_2 consumption feature for FeFAU (730 K; H_2/Fe = 0.61) and FeLTA (680 K; H_2/Fe = 0.60) occurs in a temperature range (670-830 K) characteristic of Fe^{3+} to Fe^{2+} reduction in highly-dispersed Fe_2O_3 and Fe_3O_4 on silica [74]. The onset temperatures of reduction for these peaks (~580 K and ~565 K for FeFAU and FeLTA, respectively) are slightly above those required to reduce bulk Fe_2O_3 (~510 K), as expected from the less reducible nature of small oxide domains. The H_2/Fe ratios for these low-temperature features in the reduction profiles of FeFAU (H_2/Fe = 0.61) and FeLTA (H_2/Fe = 0.60) are similar to those expected from the reduction of Fe^{3+} in Fe_2O_3 to Fe^{2+} ($Fe_2O_3 \rightarrow FeO$; H_2/Fe = 0.5), indicating that Fe aluminosilicate species, which are responsible for the second reduction feature (FeFAU: 1130 K, H_2/Fe = 0.81; FeLTA: 1160, H_2/Fe = 0.83), are derived from FeO nanoparticles formed via Fe^{3+} reduction in Fe_2O_3.

FeMFI reduced in two stages (675 K (H_2/Fe = 0.29); 875 K (H_2/Fe = 0.64)). The onset temperature for the first feature (~550 K) is slightly higher than for bulk Fe_2O_3 (~510 K), as expected from the small Fe_2O_3 domains present within FeMFI. These two H_2 consumption features appear to reflect, as is the case for bulk Fe_2O_3, the sequential reduction of trivalent Fe via the conversion of Fe_2O_3 to Fe_3O_4 and then Fe_3O_4 to FeO, respectively. H_2/Fe ratios of these reduction features, however, were greater than would be expected for the exclusive reduction of trivalent Fe within Fe_2O_3 (H_2/Fe = 0.5) via a two-step process (I: $Fe_3O_4 \rightarrow Fe_2O_3$, H_2/Fe = 0.17; II: $Fe_2O_3 \rightarrow$ FeO, H_2/Fe = 0.33), indicating that a portion of the H_2 consumed accounts for the reduction of divalent FeO in tandem with the reduction of Fe_2O_3 and Fe_3O_4. The total H_2/Fe consumption ratio (0.93) is significantly lower than that expected for the total reduction of Fe_2O_3 (1.5) to Fe^0, consistent with the presence of unreactive Fe silicates [73] or aluminates [72] that form during thermal treatment in H_2 and which could not be reduced even at 1270 K.

These data, taken together with results from TEM (Section 5.3.2.2) and infrared spectra (Section 5.3.3.1), indicate the predominant presence of well-dispersed base metal oxides within zeolite void structures and with the stoichiometry of NiO, Co_3O_4, and Fe_2O_3. Their small sizes are evident from their resistance to reduction in comparison with bulk oxides and are generally consistent with TEM-derived size distributions. Their reduction temperatures can lead to the incorporation of cations into aluminosilicate compounds, within which such cations become even more resistant to reduction. The mean diameters of the oxide domains (1.5-2.3 nm) are slightly larger than the void diameters of LTA (1.1 nm [51]), MFI (0.64 nm [51]), and FAU (1.1 nm [51]); the resulting framework disruptions may lead to local defects near the oxide domains, which would favor the formation of metal aluminosilicates. Such metal aluminosilicates may form in tandem with, and as a result of, the incipient structural collapse of the crystalline frameworks, which occurs at temperatures [LTA (~1000 K) [75], MFI (~1300 K) [76], or FAU (~1160 K) [77]] slightly above those required to form these refractory compounds, as previously proposed for Co oxides within LTA [10]. In the next section, we demonstrate that the oxide nanoparticles evident from TEM data are redox active and that they reside within regions inaccessible to large organosulfur titrants, as expected from their predominant presence within zeolite crystals.

5.3.4 Encapsulation selectivities from ethanol oxidation rates with and without titration of extracrystalline oxide surfaces by large organosulfur compounds

Nanoparticles encapsulated within microporous zeolites benefit from the molecular sieving and size-selective effects conferred by the small apertures within the host void structures. Such effects include the protection of nanoparticle active surfaces from contact with large reactant or poison molecules [8], the resistance against coalescence with adjacent particles [9], and the stabilization of specific transition states by the confining framework [7]. These effects are dictated, in all cases, by the size of the voids and of their connecting apertures within a given zeolite and by the corresponding dimensions of the molecules, intermediates, and transition states involved [8].

The size-selective properties of zeolites are exploited here in assessing the selectivity of metal encapsulation through measurements of ethanol (EtOH) oxidation rates on samples exposed to a bulky organosulfur titrant (2,4,6-trimethylbenzyl mercaptan; TMBM). Thiols such as dodecanethiol and TMBM form thiolates via reactions with Ni, Co, or Fe oxide surfaces [78]; these bound species block active surfaces and thus suppress the rates of catalytic reactions. EtOH (0.40 nm kinetic diameter [79]) diffuses readily through the apertures in LTA (0.41 nm [51]), MFI (0.55 nm [51]), and FAU (0.74 nm [51]), but TMBM (kinetic diameter >0.86 nm [80]) is essentially excluded from intracrystalline regions. As a result, EtOH oxidation turnover rates on bulk oxides (NiO, Co_3O_4, Fe_2O_3) and on oxide domains at external zeolite crystal surfaces would be suppressed by exposure to TMBM, but turnovers occurring on domains present within LTA, MFI, and FAU crystals would remain active. The effects of TMBM exposure on ethanol oxidation rates thus reflect the fraction of the oxide surfaces that reside within the protected environment of zeolite crystals.

EtOH oxidation rates were measured on bulk NiO, Co_3O_4, Fe_2O_3, and metal-zeolite samples at 393 K before and after ex-situ exposure to TMBM using the procedures described in Section 5.2.3.5. An inhibition factor (λ) is defined here as the ratio of the rates measured on samples with exposure ($r_{i,j,s}$) and without exposure ($r_{i,j}$) to TMBM titrants:

$$\lambda_{i,j} = \frac{r_{i,j,s}}{r_{i,j}} \qquad (4)$$

where the subscript i denotes the metal (Ni, Co, Fe) and j either the bulk metal oxide (b) or the specific zeolite framework (LTA, MFI, or FAU). The magnitude of $\lambda_{i,b}$ for bulk oxides reflects the residual reactivity and in turn the fraction of active surface area that remains untitrated by TMBM, with $\lambda_{i,b}$ values of zero indicative of full suppression of rates and unity an indication of surfaces that do not interact with TMBM strongly enough to prevent ethanol oxidation turnovers.

On bulk NiO, Co_3O_4, and Fe_2O_3, the prevalence of mesopores allows EtOH and TMBM to access catalytic surfaces without diffusional hindrance. Consequently, their $\lambda_{i,b}$ values reflect the accessibility and reactivity of such surfaces after interactions with TMBM. The apertures in zeolites, by contrast, protect intracrystalline oxide domains from contact with TMBM titrants, but allow EtOH and O_2 reactants to access intracrystalline regions. In such samples, only the oxide domains present at the external surfaces of zeolite crystals are titrated by TMBM. Their $\lambda_{i,j}$ values therefore reflect the fraction of the catalytic surface area that resides within the protected confines

of zeolite crystals ($F_{i,j}$). These $\lambda_{i,j}$ values, however, are not strictly proportional to $F_{i,j}$ because bulk oxides (and thus clusters present outside zeolite crystals) may retain some reactivity even after extended contact with TMBM. These effects require that we account for the residual reactivity of the titrated oxide surfaces after exposure to TMBM in order to determine $F_{i,j}$:

$$F_{i,j} = \lambda_{i,j} - \lambda_{i,b}\frac{\left(1-\lambda_{i,j}\right)}{\left(1-\lambda_{i,b}\right)} \qquad (5)$$

Equation 5 corrects $\lambda_{i,j}$ in order to accurately reflect $F_{i,j}$ values by subtracting contributions to $\lambda_{i,j}$ derived from residual rates on TMBM-titrated surfaces (the second term in Eq. 5). In addition, extrazeolitic oxide surfaces are exposed to the reactant concentrations prevalent in the extracrystalline gas phase (4 kPa EtOH, 9 kPa O_2; Section 5.2.3.5), but concentration gradients within zeolite crystals would lead to lower oxidation turnover rates on encapsulated oxide surfaces than on those at external surfaces or bulk oxides. These diffusional effects lead to $\lambda_{i,j}$ (and $F_{i,j}$) values that underestimate the actual encapsulation selectivity. These $F_{i,j}$ values also ignore the slow but finite diffusion rates of TMBM through FAU apertures, which would titrate some intracrystalline oxide surfaces and cause $F_{i,j}$ values to be lower than the actual encapsulation selectivity. Consequently, these $F_{i,j}$ values represent a conservative lower limit for the preference of oxide nanoparticles to reside within intracrystalline locations as a result of the synthetic protocols reported in this study.

The $\lambda_{i,j}$ and $F_{i,j}$ values derived from EtOH oxidation rates before and after titration of unprotected surfaces are shown in Table 5.3. EtOH oxidation turnover rates for each given metal increased monotonically with the size of the framework aperture (LTA: 0.41 nm, MFI: 0.55 nm, FAU: 0.74 nm [51]) for untitrated samples, consistent with diffusional constraints that cause intracrystalline concentration gradients and lower reaction rates. The presence of such diffusional constraints provides independent de facto evidence that these oxide nanoparticles reside predominantly within zeolite crystals. Turnover rates on bulk oxides were higher than on metal-zeolite samples, because of the lack of diffusional constraints and the higher redox surface reactivity typical of larger oxide domains [10,56]. Co_3O_4 (28 nm aggregates, Section 5.S1) gave the highest turnover rate (0.68 mmol s^{-1}) among the three bulk oxides (NiO: 0.25 mmol s^{-1}, 410 nm; Fe_2O_3: 0.12 mmol s^{-1}, 76 nm), reflecting the greater intrinsic redox activity of the Co cations within Co oxide relative to Ni and Fe oxides. Co^{2+} cations exchanged within LTA, MFI, and FAU zeolites (Section 5.2.2.4), however, did not oxidize EtOH at detectable rates (<0.00001 mmol s^{-1}) as the bulk (0.68 mmol s^{-1}) or zeolite-encapsulated Co oxides (0.0062-0.10 mmol s^{-1}; Table 5.3) did, a consequence of exchanged Co^{2+} cations that are much less reducible than bulk oxides or oxide nanoparticles (TPR data in Section 5.S7, SI).

Encapsulation selectivities were >0.93 for all metal-zeolite samples (except FeFAU; $F_{Fe,FAU}$ = 0.12), indicating that the oxide nanoparticles evident in electron micrographs (Section 5.3.2.2) reside predominantly within zeolite crystallites. The FeFAU data reflects the gradual diffusion of TMBM within FAU over the time required to titrate Fe oxide surfaces. Fe_2O_3, FeLTA, FeMFI, and FeFAU were exposed to TMBM for longer times (16 h; Section 5.2.3.5) than the Ni or Co samples (2 h), because longer times were required to significantly suppress of rates on bulk Fe_2O_3 ($\lambda_{Fe,b}$ = 0.67). Rates were more strongly suppressed by TMBM titration on NiO ($\lambda_{Ni,b}$ = 0.12)

and Co_3O_4 ($\lambda_{Co,b}$ = 0.12), even after shorter exposure times (2 h), and were essentially constant with longer TMBM exposure times (16 h; $\lambda_{Ni,b}$ = 0.10; $\lambda_{Co,b}$ = 0.08). Treatment of NiFAU and CoFAU with TMBM for 16 h, however, leads to more severe suppression of rates ($\lambda_{Ni,b}$ = 0.47; $\lambda_{Co,b}$ = 0.52) than 2 h treatment ($\lambda_{Ni,b}$ = 0.93; $\lambda_{Co,b}$ = 0.95). These effects of TMBM exposure times on NiFAU and CoFAU (but not for their LTA or MFI counterparts) indicate that TMBM gradually enters large-pore zeolites and titrates intracrystalline oxide surfaces. As a result, the value of $F_{Fe,FAU}$ reported in Table 5.3 (0.12), which required longer exposures because of the kinetic hurdles for TMBM binding on Fe oxides, does not accurately reflect its encapsulation selectivity. Its true encapsulation selectivity is likely to resemble that shown by all other samples, for which $F_{i,j}$ values more accurately reflect such selectivities.

These results, taken together, show how synthetic hurdles that impede the selective encapsulation of base metals within microporous voids can be systematically addressed and overcome through general strategies that lead to encapsulation for a broad range of zeolite frameworks. Encapsulation of NiO, Co_3O_4, and Fe_2O_3 clusters was achieved in LTA, MFI, and FAU frameworks, materials that differ substantially in their Si/Al ratios (1.0, 30, 2.3), aperture sizes (8-MR, 0.41 nm; 10-MR, 0.55 nm; 12-MR, 0.74 nm), and in the conditions required for their crystallization (Section 5.2.2). For all metal species and frameworks, bifunctional TPE ligands successfully stabilize metal precursors against precipitation in synthesis gels, enforce their uptake into zeolite crystals, and are removed by oxidative treatments without damage to the host framework. These synthesis procedures and post-synthetic oxidative treatments lead to the aggregation of small and nearly monodisperse oxide nanoparticles that reside predominantly within zeolite crystals and which do not form redox-inactive metal aluminosilicates or exchanged cations. These high encapsulation selectivities are the result of the chelating properties of the bidentate amine moiety in TPE ligands, which prevent cation precipitation during synthesis and the attachment of metal cations to zeolite exchange sites; they also reflect the role of the ligand alkoxysilane moieties, which bind ligated precursors to nucleating zeolite structures through the formation of covalent siloxane linkages. The broad success of these protocols bodes well for their extension to other zeolite frameworks and metal species, and to the preparation of multimetallic clusters by combining ligated precursors of two or more metals.

5.4 Conclusions

Ni, Co, and Fe oxide nanoparticles were selectively encapsulated within LTA, MFI, and FAU zeolites using a generalized synthetic procedure. Encapsulation was achieved in all cases through the analogous incorporation of metal cation precursors (Ni^{2+}, Co^{2+}, Fe^{2+}) protected by chelating ligands (N-[3-(trimethoxysilyl)propyl]ethylenediamine) into zeolite synthesis gels, which were allowed to crystallize under hydrothermal conditions to form zeolites with occluded ligated metal species. The ligands preclude premature precipitation of the metal cation precursors as bulk oxide or hydroxide aggregates under the alkaline conditions required for framework assembly, and form covalent linkages with nucleating zeolites to promote metal uptake into the crystallized frameworks. Treatment of these frameworks under oxidative conditions leads to the formation of highly dispersed (< 2.5 nm) metal oxide nanoparticles that are homogeneous in size. Characterization of these materials with infrared spectroscopy indicated the absence of base metal species in the form of exchanged cations or metal aluminosilicates, consistent with the selective formation of metal oxide nanoparticles during oxidative treatment. The reducibility of the base

metal species in H_2 and the stoichiometry of their reduction were consistent with the presence of small NiO, Co_3O_4, or Fe_2O_3 clusters. The overwhelming majority of active metal oxide surfaces (>92%) were protected from contact by large organosulfur poison molecules that selectively or exclusively titrate extrazeolitic metal oxide clusters, confirming that the nanoparticles formed by the synthesis technique predominantly reside within zeolite crystals. This work presents a generalized synthesis technique for encapsulating base metal oxides within zeolites, and demonstrates the efficacy of the technique through its successful application to a variety of metal species (Ni, Co, Fe) and zeolite frameworks (LTA, MFI, FAU). The synthetic approach shown here also illustrates guiding principles and strategies that can be applied to prepare an even wider variety of zeolite-encapsulated base metal clusters. Such materials have potential catalytic applications that seek to combine the catalytic chemistries of metal oxide surfaces with the molecular size and shape selectivity, transition state selectivity, and thermal stability conferred by encapsulation within zeolites.

5.5 Acknowledgments

We gratefully acknowledge the Chevron Energy Technology Co for their generous financial support of this research, as well as ancillary support provided for TO by an ARCS foundation fellowship and a National Science Foundation fellowship.

5.6 Figures, Tables, and Scheme(s)

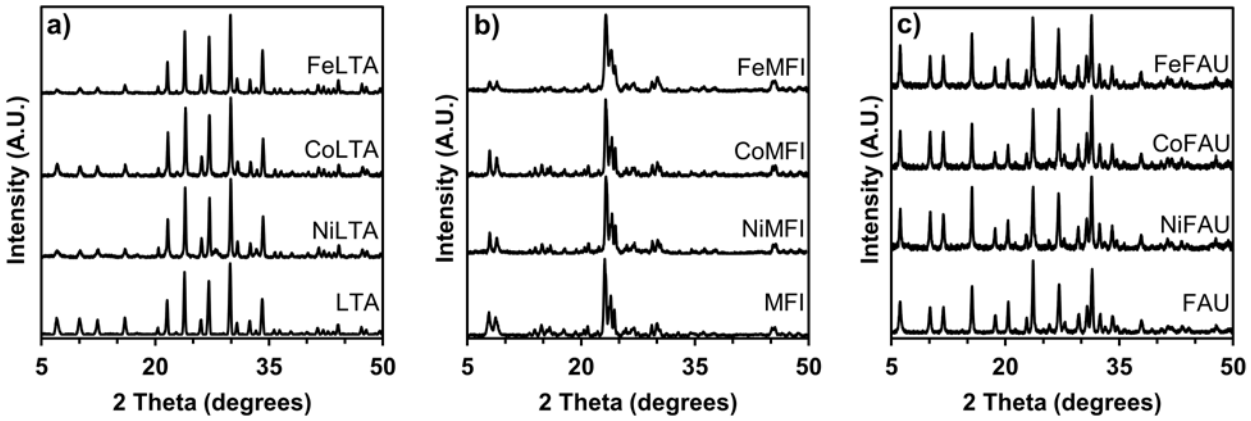

Figure 5.1. X-Ray diffractograms of a) metal-LTA, b) metal-MFI, and c) metal-FAU samples prepared via hydrothermal assembly in the presence of ligated metal precursors and comparative metal-free samples prepared using the procedures in Section 5.2.2. Diffractograms were collected on samples following their post-synthetic oxidative treatment in flowing dry air (1.67 $cm^3\ g^{-1}\ s^{-1}$; 0.033 K s^{-1}; 623 K; 2 h).

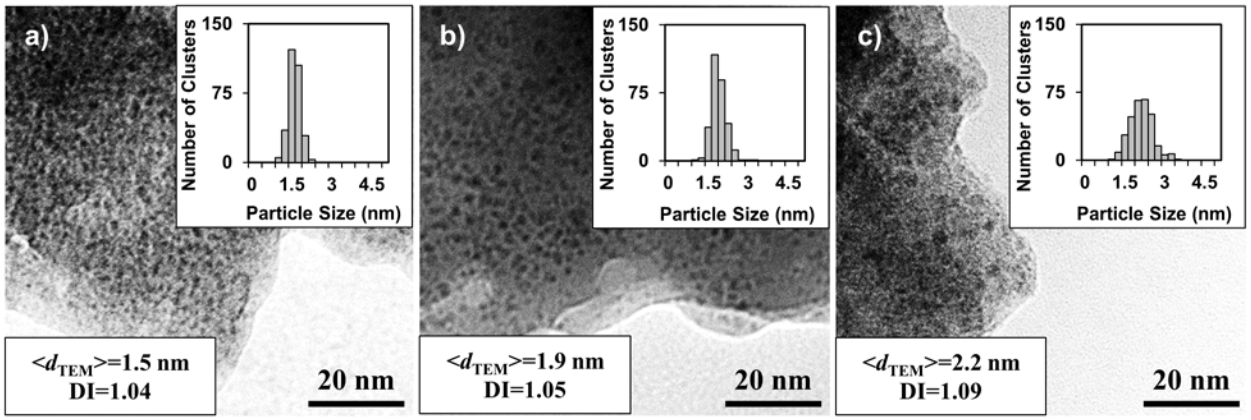

Figure 5.2. Electron micrographs, surface-averaged cluster diameters ($\langle d_{TEM} \rangle$, Eq. 1), particle dispersity indices (DI, Eq. 3), and cluster diameter distributions for (a) NiLTA, (b) FeMFI, and (c) CoFAU samples.

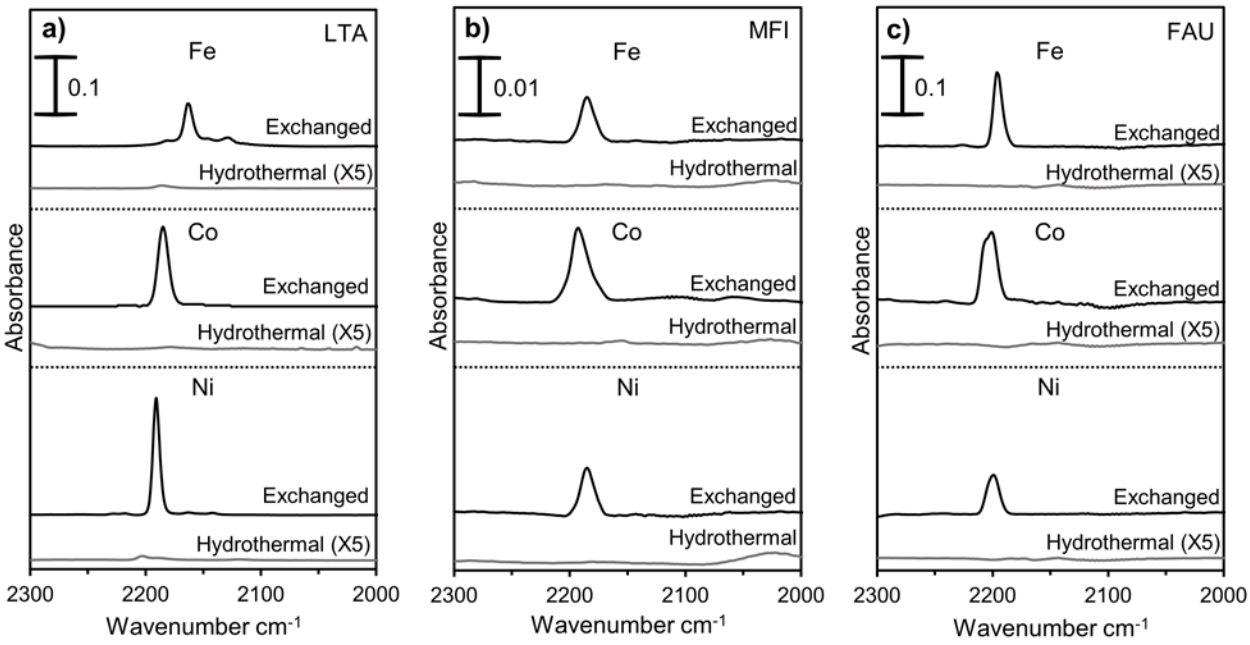

Figure 5.3. Infrared difference spectra of CO adsorbed on a) metal-LTA, b) metal-MFI, and c) metal-FAU samples prepared via ion-exchange of metal cations (Ni^{2+}, Co^{2+}, Fe^{2+}; black lines; "exchanged") or by hydrothermal assembly in the presence of ligated metal precursors (gray lines; "hydrothermal"). Spectra were collected on these samples at 273 K (1.0 kPa CO, 99 kPa He) after pretreatment (Section 5.2.3.3). Spectral contributions of CO(g), CO physisorbed in the frameworks, or CO adsorbed on Na^{+} or Ca^{2+} were subtracted (Section 5.2.3.3).

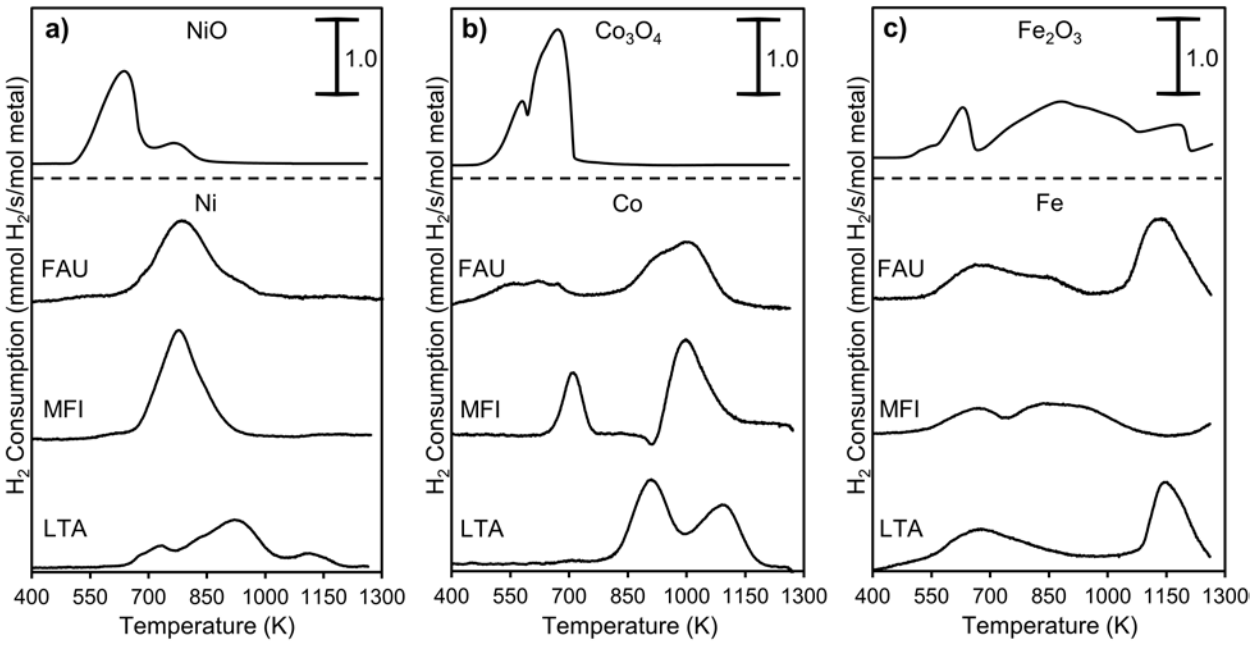

Figure 5.4. Temperature programmed reduction profiles of bulk a) Ni, b) Co, and c) Fe oxides and of a) Ni-zeolite, b) Co-zeolite, and c) Fe-zeolite samples prepared via hydrothermal assembly in the presence of ligated metal precursors. Samples were heated in 4% H_2/Ar (8.3 cm^3 s^{-1} g^{-1}) from 313 K to 1273 K at 0.167 K s^{-1}.

Table 5.1. Metal species, targeted framework, nominal metal loading, ligand content, and crystallinity of synthesized solids for the synthesis of metal-zeolite samples.

Metal	Zeolite Synthesis Gel	Nominal metal loading (% wt.)[a]	TPE/T-atom[b]	% Crystallinity[c]
Ni	LTA	4	0.089	98
	LTA	5	0.11	0
	MFI	3	0.042	97
	MFI	4	0.055	3
	FAU	2	0.030	99
	FAU	3	0.043	16
Co	LTA	4	0.088	96
	LTA	5	0.11	3
	MFI	3	0.042	96
	MFI	4	0.055	5
	FAU	2	0.030	99
	FAU	3	0.043	1
Fe	LTA	3	0.071	95
	LTA	4	0.093	0
	MFI	2	0.030	95
	MFI	3	0.044	7
	FAU	2	0.032	98
	FAU	3	0.046	2

[a]Metal loading that would result if all metal added to the synthesis gel were incorporated into the synthesized solids, assuming solid yields equivalent to metal and ligand-free LTA, MFI, or FAU syntheses.
[b]Molar ratio of TPE ligands to the total number of T atoms (T = Si, Al) in the synthesis gel.
[c]Determined by XRD. Diffractograms shown in supporting information, Sections 5.S2 (LTA), 5.S3 (MFI), and 5.S4 (FAU). Calculated from integrated intensities of the three most intense Bragg lines using metal-free LTA, MFI, and FAU as standards (Section 5.2.3.1).

Table 5.2. Metal loadings, particle diameters, particle dispersions, and particle dispersity indices of metal-zeolite samples.

Sample	Metal loading (% wt.)[a]	Particle diameter $\langle d_{TEM} \rangle$ (nm)[b]	Fractional dispersion (D)[c]	Dispersity index (DI)[d]
NiLTA	2.7 (3.0)	1.5 ± 0.2	0.81	1.04
NiMFI	1.3 (1.5)	1.9 ± 0.3	0.66	1.06
NiFAU	1.4 (1.5)	2.3 ± 0.4	0.55	1.10
CoLTA	2.6 (3.0)	1.6 ± 0.3	0.51	1.06
CoMFI	1.3 (1.5)	1.7 ± 0.2	0.47	1.03
CoFAU	1.4 (1.5)	2.2 ± 0.4	0.37	1.09
FeLTA	2.5 (3.0)	1.9 ± 0.3	0.74	1.07
FeMFI	1.2 (1.5)	1.9 ± 0.3	0.74	1.05
FeFAU	1.2 (1.5)	2.2 ± 0.4	0.62	1.09

[a]Measured for crystallized samples after oxidative treatment using inductively coupled plasma optical emission spectroscopy. Nominal metal loading in synthesis gels shown in parentheses.
[b]Surface-averaged cluster diameter determined by TEM (Eq. 1).
[c]Particle dispersion estimated using $\langle d_{TEM} \rangle$ (Eq. 2).
[d]Particle dispersity index calculated as the surface-averaged cluster diameter divided by the arithmetic mean diameter (Eq. 3).

Table 5.3. Ethanol oxidation turnover rates and encapsulation selectivities of metal-zeolite and bulk metal oxide samples.

Sample	r (10^{-3} s^{-1} $mol_{surf\text{-}metal}^{-1}$)[a]	Inhibition Factor (λ)[b]	Encapsulation Selectivity (F)[c]
NiLTA	0.0030	0.99	0.99
NiMFI	0.030	0.96	0.96
NiFAU	0.046	0.93	0.93
CoLTA	0.0062	0.98	0.97
CoMFI	0.061	0.96	0.96
CoFAU	0.10	0.95	0.94
FeLTA	0.0071	0.99	0.97
FeMFI	0.025	0.98	0.93
FeFAU	0.033	0.71	0.12
NiO	0.25	0.12	0
Co_3O_4	0.68	0.12	0
Fe_2O_3	0.12	0.67	0

[a]EtOH oxidation turnover rates of samples suspended in liquid EtOH (300 cm^3 g^{-1}) at ambient temperature for 2 h (for Ni, Co samples) or 16 h (for Fe samples) and then used in reaction (9 kPa O_2, 4 kPa EtOH) at 393 K. Turnover rates are defined as the moles of EtOH converted per unit time normalized by the number of exposed metal surface atoms estimated from particle dispersions or BET surface areas (Section 5.2.3.5).
[b]r_S/r (Eq. 4), where r_S are EtOH oxidation rates measured on similarly treated samples but with TMBM dissolved in the EtOH to achieve a 0.2 M solution.
[c]Encapsulation selectivity, defined as the fraction of active metal oxide surface area encapsulated within zeolite crystallites, as estimated from λ values (Eq. 5).

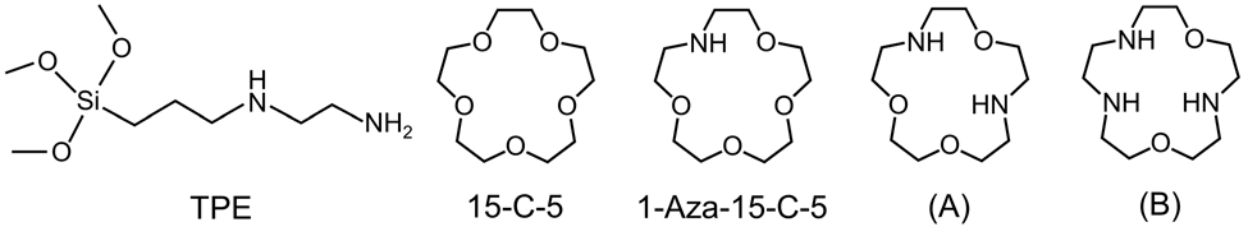

Scheme 5.1 Chelating agents and ligands mentioned and/or used in this work: N-[3-(trimethoxysilyl)propyl]ethylenediamine (TPE); 1,4,7,10,13-pentaoxacyclopentadecane (15-C-5); 1,4,7,10-tetraoxa-13-azacyclopentadecane (1-Aza-15-C-5); 1,4,10-trioxa-7,13-diaza-cyclopentadecane (A)**;** 1,7-dioxa-4,10,13-triaza-cyclopentadecane (B)

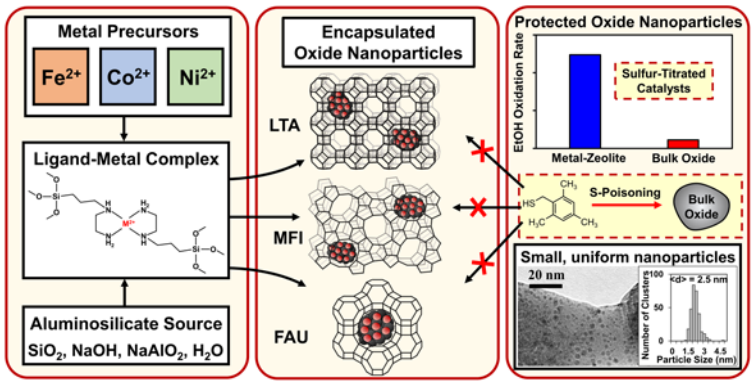

Scheme 5.2 Schematic representation of the synthesis and characterization of base metal oxide clusters encapsulated within zeolites

5.7 References

[1] Pabalan, R. T.; Bertetti, F. P. *Rev. Mineral. Geochem*. **2001**, *45*, 453.
[2] Noack, M.; Caro, J. *Microporous Mesoporous Mater*. **2008**, *115*, 215.
[3] Weckhuysen, B. M.; Yu, J. *Chem. Soc. Rev*. **2015**, *44*, 7022.
[4] Ennaert, T.; Van Aelst, J.; Dijkmans, J.; De Clercq, R.; Schutyser, W.; Dusselier, M.; Verboekend, D.; Sels, B. F. *Chem. Soc. Rev*. **2016**, *45*, 584.
[5] Rimer, J. D.; Kumar, M.; Li, R.; Lupulescu, A. I.; Oleksiak, M.D. *Catal. Sci. Technol*. **2014**, *4*, 3762.
[6] Deimund, M. A.; Harrison, L.; Lunn, J. D.; Liu, Y.; Malek, A.; Shayib, R.; Davis, M. E. *ACS Catal*. **2016**, *6*, 542.
[7] Song, B.; Lo, A.-Y.; Wang, J. *Mol. Catal*. **2017**, *437*, 47.
[8] Otto, T.; Zones, S. I.; Iglesia, E. *J. Catal*. **2016**, *339*, 195.
[9] Otto, T.; Ramallo-López, J. M.; Giovanetti, L. J.; Requejo, F. G.; Zones, S. I.; Iglesia, E. *J. Catal*. **2016**, *342*, 125.
[10] Otto, T.; Zones, S. I.; Hong, Y.; Iglesia, E. *J. Catal*. **2017**, *356*, 173.
[11] Wu, Z.; Goel, S.; Choi, M.; Iglesia, E. *J. Catal*. **2014**, *311*, 458.
[12] Cho, S. J.; Ryoo, R. *J. Phys. Chem. B* **2001**, *105*, 1293.
[13] Moliner, M; Gabay, J. E.; Kliewer, C. E.; Carr, R. T.; Guzman, J.; Casty, G. L.; Serna, P.; Corma, A. *J. Am. Chem. Soc*. **2016**, *138*, 15743.
[14] Højholt, K. T.; Laursen, A. B.; Kegnæs, S.; Christensen, C. H. *Top. Catal*. **2011**, *54*, 1026.
[15] Sebastian, V.; Irusta, S.; Mallada, R.; Santamaría, J. *Appl. Catal., A* **2009**, *366*, 242.
[16] Djakovitch, L.; Koehler, K. *J. Am. Chem. Soc*. **2001**, *123*, 5990.
[17] Foster, J. J.; Masel, R. I. *Ind. Eng. Chem. Prod. Res. Dev*. **1986**, *25*, 563.
[18] Iablokov, V.; Barbosa, R.; Pollefeyt, G.; Van Driessche, I.; Chenakin, S.; Kruse, N. *ACS Catal*. **2015**, *5*, 5714.
[19] Kandalam, A. K.; Chatterjee, B.; Khanna, S. N.; Rao, B. K.; Jena, P.; Reddy, B. V. *Surf. Sci*. **2007**, *601*, 4873.
[20] Shamsipur, M.; Najafi, M.; Milani Hosseini, M.-R. *J. Appl. Electrochem*. **2013**, *43*, 1027.
[21] Zhu, J.; Kailasam, K.; Fischer, A.; Thomas, A. *ACS Catal*. **2011**, *1*, 342.
[22] González-Arellano, C.; Campelo, J. M.; Macquarrie, D. J.; Marinas, J. M.; Romero, A. A.; Luque, R. *ChemSusChem* **2008**, *1*, 746.
[23] Bhavsar, S.; Veser, G. *Energy Fuels* **2013**, *27*, 2073.
[24] Sehested, J. *Catal. Today* 2006, *111*, 103.
[25] Adkins, H.; Cramer, H. I. *J. Am. Chem. Soc*. **1930**, *52*, 4349.
[26] Schulz, H. *Stud. Surf. Sci. Catal*. **2007**, *163*, 177.
[27] Wilk, B.; Pelka, R.; Arabczyk, W. *J. Phys. Chem. C* **2017**, *121*, 8548.
[28] Asedegbega-Nieto, E.; Díaz, E.; Vega, A.; Ordóñez, S. *Catal. Today* **2010**, *157*, 425.
[29] Borqschulte, A.; Callini, E.; Stadie, N.; Arroyo, Y.; Rossell, M. D.; Erni, R.; Geerlings, H.; Züttel, A.; Ferri, D. *Catal. Sci. Technol*. **2015**, *5*, 4613.
[30] Wang, Y.; Wu, H.; Zhang, Q.; Tang, Q. *Microporous Mesoporous Mater*. **2005**, *86*, 38.
[31] Fraenkel, D.; Gates, B. C. *J. Am. Chem. Soc*. **1980**, *102*, 2478.

[32] Inokawa, H.; Maeda, M.; Nishimoto, S.; Kameshima, Y.; Miyake, M.; Ichikawa, T.; Kojima, Y.; Miyaoka, H. *Int. J. Hydrogen Energy* **2013**, *38*, 13579.
[33] Liu, J.; Wang, D.; Chen, J.-F.; Zhang, Y. *Int. J. Hydrogen Energy* **2016**, *41*, 21965.
[34] Luo, L.; Dai, C.; Zhang, A.; Wang, J.; Liu, M.; Song, C.; Guo, X. *RSC Adv.* **2015**, *5*, 29509.
[35] Gevert, B.; Eriksson, L.; Törncrona, A. *J. Porous Mater*. **2011**, *18*, 723.
[36] Liu, Z.; Shi, C.; Wu, D.; He, S.; Ren, B. *J. Nanotechnol*. **2016**, *2016*, 1.
[37] Li, W.; Yu, S. Y.; Meitzner, G. D.; Iglesia, E. *J. Phys. Chem. B* **2001**, *105*, 1176.
[38] R.P. Townsend, E.N. Coker, in: H. van Bekkum, E.M. Flanigen, P.A. Jacobs, J.C. Jansen (Eds.), Studies in Surface Science and Catalysis, second ed., Elsevier Science B.V., Amsterdam, 2001, pp. 512.
[39] de Correa, C. M.; Villa, A. L.; Zapata, M. *Catal. Lett*. **1996**, *38*, 27.
[40] G. Bergeret, P. Gallezot, in: G. Ertl, H. Knozinger, F. Schuth, J. Weitkamp (Eds.), Handbook of Heterogeneous Catalysis, second ed., Wiley-VHC, Weinheim, 2008, pp. 738-765.
[41] Leineweber, A.; Jacobs, H.; Hull, S. *Inorg. Chem*. **2001**, *40*, 5818.
[42] Kotousova, I. S.; Polyakov, S. M. *Kristallografiya* **1972**, *17*, 661.
[43] Dzade, N.; Roldan Martinez, A.; de Leeuw, N. *Minerals* **2014**, *4*, 89.
[44] Montanari, T.; Salla, I.; Busca, G. *Microporous Mesoporous Mater*. **2008**, *109*, 216.
[45] Platero, E. E.; Scarano, D.; Spoto, G.; Zecchina, A. *Faraday Discuss. Chem. Soc*. 1985, 80, 183.
[46] Lin, H.-K.; Wang, C.-B.; Chiu, H.-C.; Chien, S.-H. *Catal. Lett*. **2003**, *86*, 63.
[47] Zecchina, A.; Scarano, D.; Reller, A. *J. Chem. Soc., Faraday Trans. 1* **1988**, *84*, 2327.
[48] Ul-Haque, M.; Caughlan, C. N.; Emerson, K. *Inorg. Chem*. **1970**, *9*, 2421.
[49] Cooke, K.; Olenev, A. V.; Kovnir, K. *Acta Cryst*. **2013**, *E69*, m332.
[50] Smith, T. J.; *J. Mol. Graphics* **1995**, *13*, 122.
[51] C.M. Baerlocher, Database of Zeolite Structures. http://www.iza-structure.org/databases/, 2017 (accessed February 2018).
[52] Miyake, K.; Hirota, Y.; Ono, K.; Uchida, Y.; Miyamoto, M.; Nishiyama, N. *New J. Chem.* **2017**, *41*, 2235.
[53] Ratnasamy, P.; Kumar, R. *Catal. Today* 1991, 9, 329.
[54] J.W. Steed, J.L. Atwood, Supramolecular Chemistry, second ed., Wiley, Chichester, 2009, pp. 106-219.
[55] Chatelain, T.; Patarin, J.; Soulard, M.; Guth, J. L.; Schulz, P. *Zeolites* **1995**, *15*, 90.
[56] Barton, D. G.; Shtein, M.; Wilson, R. D.; Soled, S. L.; Iglesia, E. *J. Phys. Chem. B* **1999**, *103*, 630.
[57] Angell, C. L.; Schaffer, P. C. *J. Phys. Chem.* 1996, 70, 1413.
[58] Rakić, V.; Dondur, V.; Hercigonja, R. *J. Serb. Chem. Soc*. 2003, 68, 409.
[59] Kim, J.; Jentys, A.; Maier, S. M.; Lercher, J. A. *J. Phys. Chem. C* 2013, 117, 986.
[60] Areán, C. O.; Mentruit, M. P.; López López, A. J.; Parra, J. B. *Colloids Surf. A* 2001, 180, 253.
[61] Subramanian, V.; Zholobenko, V. L.; Cheng, K.; Lancelot, C.; Heyte, S.; Thuriot, J.; Paul, S.; Ordomsky, V. V.; Khodakov, A. Y. *ChemCatChem* **2016**, *8*, 380.
[62] Wielers, A. F. H.; Kock, A. J. H. M.; Hop, C. E. C. A.; Geus, J. W.; van Der Kraan, A. M.; *J. Catal*. **1989**, *117*, 1.

[63] Kim, J.-C.; Lee, S.; Cho, K.; Na, K.; Lee, C.; Ryoo, R. *ACS Catal*. **2014**, *4*, 3919.
[64] Zieliński, J. *J. Chem. Soc., Faraday Trans*. 1997, 93, 3577.
[65] Sá, J.; Kayser, Y.; Milne, C. J.; Fernandes, D. L. A.; Szlachetko, J. *Phys. Chem. Chem. Phys*. 2014, 16, 7692.
[66] Zhao, Z.; Lakshminarayanan, N.; Swartz, S. L.; Arkenberg, G. B.; Felix, L. G.; Slimane, R. B.; Choi, C. C.; Ozkan, U. S. *Appl. Catal., A* **2015**, *489*, 42.
[67] Solsona, B.; Concepción, P.; López Nieto, J. M.; Dejoz, A.; Cecilia, J. A.; Agouram, S.; Soriano, M. D.; Torres, V.; Jiménez-Jiménez, J.; Castellón, E. R. *Catal. Sci. Technol*. 2016, 6, 3419.
[68] Kogelbauer, A.; Weber, J. C.; Goodwin Jr., J. G. *Catal. Lett*. **1995**, *34*, 259.
[69] Okamoto, Y.; Nagata, K.; Adachi, T.; Imanaka, T.; Inamura, K.; Takyu, T. *J. Phys. Chem*. 1991, 95, 310.
[70] Moodley, D. J.; Saib, A. M.; van de Loosdrecht, J.; Welker-Nieuwoudt, C. A.; Sigwebela, B. H.; Niemantsverdriet, J. W. *Catal. Today* **2011**, *171*, 192.
[71] Liu, Z.; Su, H.; Chen, B.; Li, J.; Woo, S. I. *Chem. Eng. J*. **2016**, *299*, 255.
[72] Acomb, J. C.; Wu, C.; Williams, P. T. *Appl. Catal., B* **2016**, *180*, 497.
[73] Zhang, C.-H.; Wan, H.-J.; Yang, Y.; Xiang, H.-W.; Li, Y.-W. Catal. Commun. 2006, 7, 733.
[74] Messi, C.; Carniti, P.; Gervasini, A.; *J. Therm. Anal. Calorim*. **2008**, *91*, 93.
[75] S. Bhatia, Zeolite Catalysis: Principles and Applications, CRC Press, Inc., Boca Raton, 1990, pp. 10.
[76] Tallon, J. L.; Buckley, R. G.; *J. Phys. Chem*. 1987, 91, 1469.
[77] Ambs, W. J.; Flank, W. H.; *J. Catal*. **1969**, *14*, 118.
[78] Hoertz, P. G.; Niskala, J. R.; Dai, P.; Black, H. T.; You, W.; *J. Am. Chem. Soc*. **2008**, *130*, 9763.
[79] Van Mao, R. L.; Nguyen, T. M.; Mclaughlin, G. P. *Appl. Catal*. **1989**, *48*, 265.
[80] Tukur, N. M.; Al-Khattaf, S. *Energy Fuels* **2007**, *21*, 2499.

5.8 Supporting Information

Contents

5.S1. N_2 adsorption isotherms for bulk NiO, Co_3O_4, and Fe_2O_3 samples

N_2 adsorption isotherms were measured on bulk NiO, Co_3O_4, and Fe_2O_3 samples to determine their surface areas. These surface areas were used, in turn, to estimate the number of surface metal atoms present in these samples (main text, Section 5.2.3.5). The N_2 adsorption measurements were conducted at 77 K (0-800 torr) using a Micromeritics 3Flex Surface Characterization Analyzer. The metal oxides were heated to 623 K (at 0.17 K s^{-1}) under vacuum for 4 h before the adsorption measurements. Metal oxide surface areas were calculated from the quantities of N_2 adsorbed using Brunauer-Emmett-Teller (BET) analysis. The N_2 adsorption and desorption isotherms are shown as a function of the saturation vapor pressure of N_2 for NiO, Co_3O_4, and Fe_2O_3 in Figure 5.S1. The calculated BET surfaces areas were 2.20 ± 0.05 m^2 g^{-1}, 35.3 ± 0.2 m^2 g^{-1}, and 15.0 ± 0.1 m^2 g^{-1} for NiO, Co_3O_4, and Fe_2O_3, respectively.

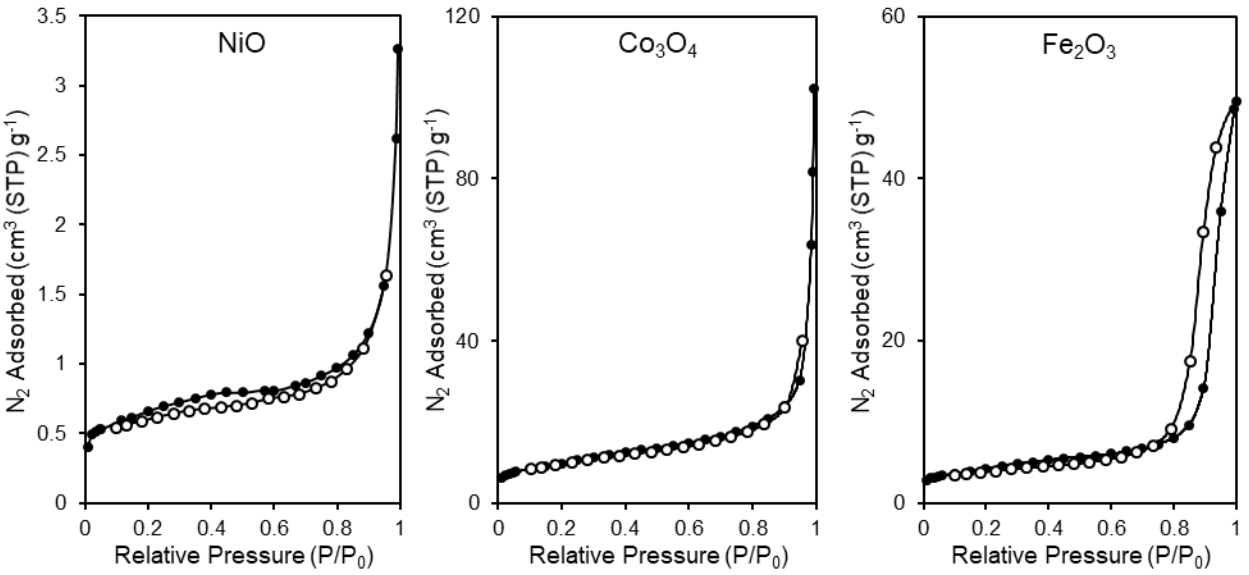

Figure 5.S1. N_2 adsorption and desorption isotherms measured at 77 K for bulk NiO, Co_3O_4, and Fe_2O_3 samples. Filled circles denote adsorption isotherms and open circles are desorption isotherms. Samples were heated under vacuum for 4 h at 623 K prior to adsorption measurements.

The average aggregate sizes in NiO, Co_3O_4, and Fe_2O_3 samples were estimated using BET surface areas and bulk metal oxide densities by assuming that the aggregates are quasi-spherical in shape. The calculated average aggregate diameters in NiO, Co_3O_4, and Fe_2O_3 are 410 nm, 28 nm, and 76 nm, respectively.

5.S2. X-Ray diffraction patterns of metal-LTA samples with 3%, 4%, or 5% wt. theoretical loading

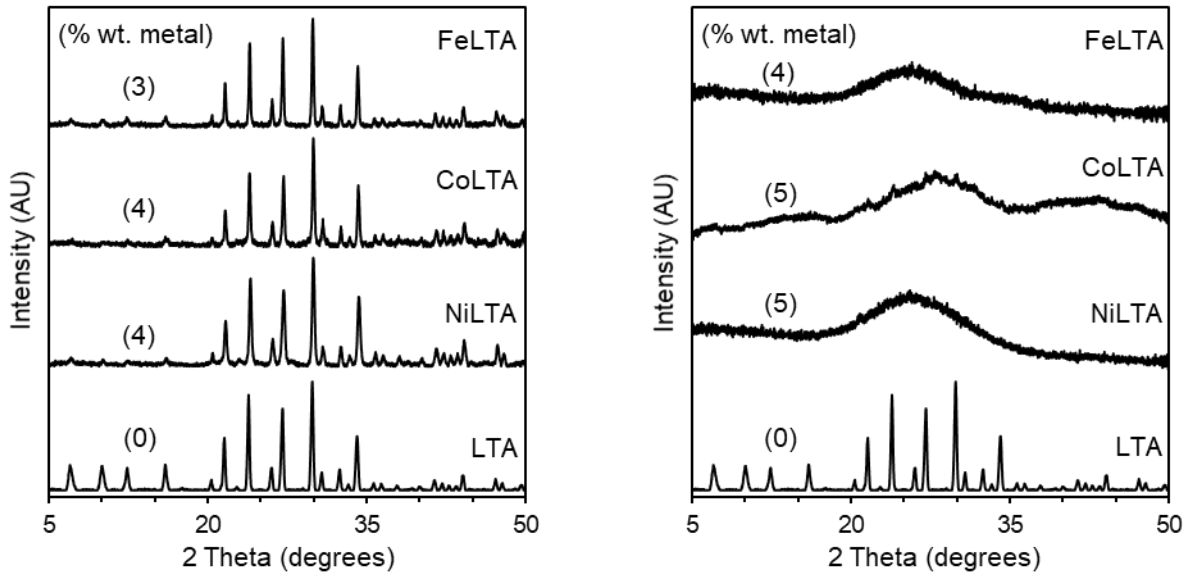

Figure 5.S2. X-Ray diffraction patterns of metal-LTA samples prepared with 3%, 4%, and 5% wt. nominal metal loading.

5.S3. X-Ray diffraction patterns of metal-MFI samples with 2%, 3%, or 4% wt. theoretical loading

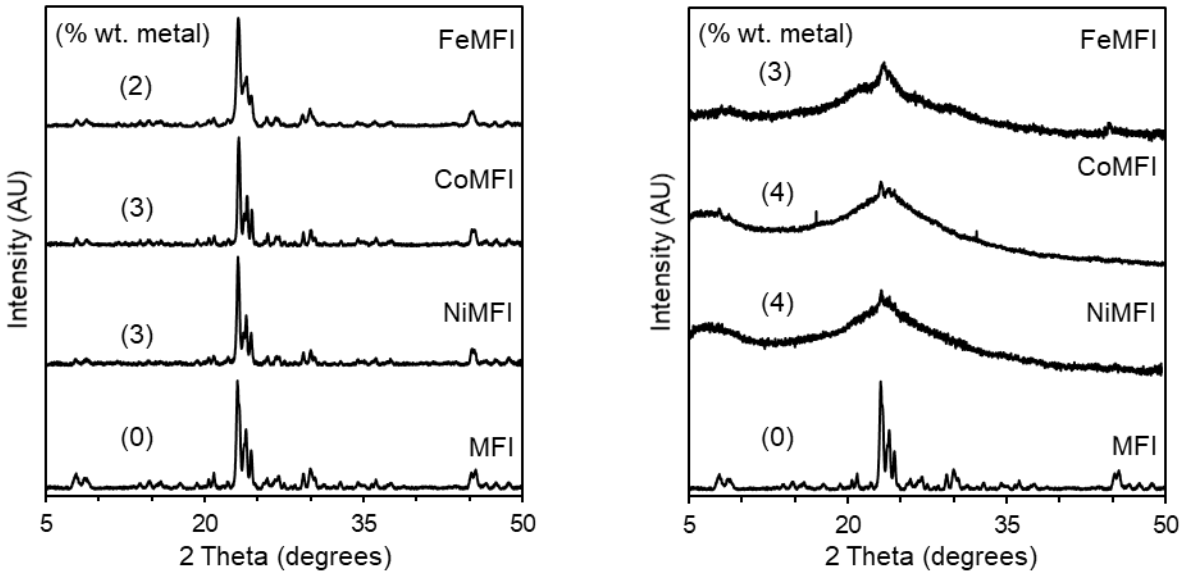

Figure 5.S3. X-Ray diffraction patterns of metal-MFI samples prepared with 2%, 3%, and 4% wt. nominal metal loading.

5.S4. X-Ray diffraction patterns of metal-FAU samples with 2% or 3% wt. theoretical loading

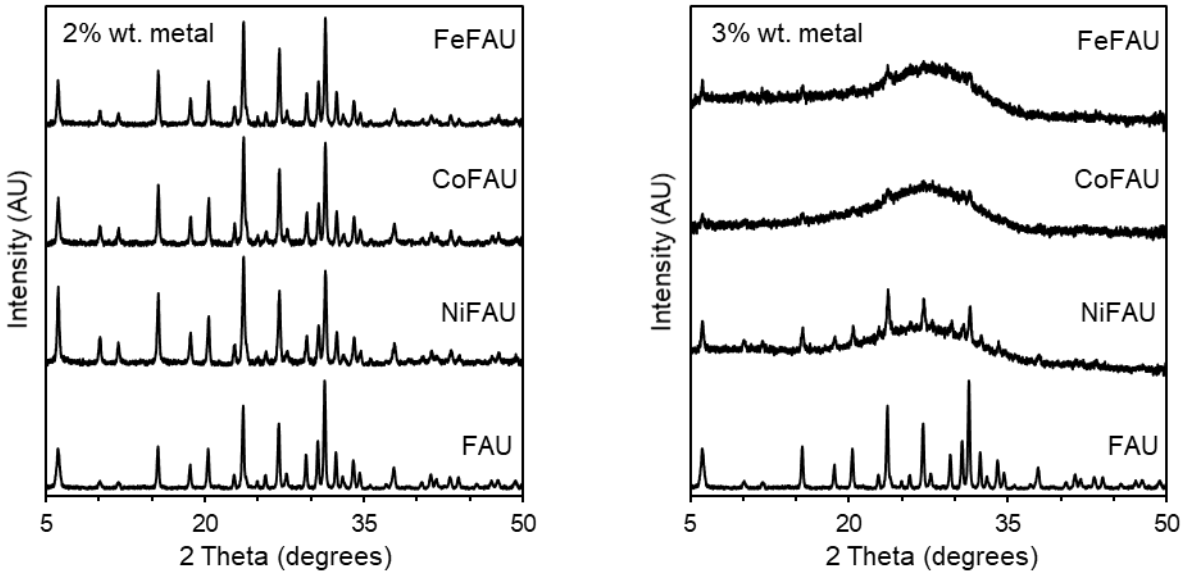

Figure 5.S4. X-Ray diffraction patterns of metal-FAU samples prepared with 2% or 3% wt. nominal metal loading.

5.S5. Electron micrographs and particle size distributions for CoLTA, FeLTA, NiMFI, CoMFI, NiFAU, and FeFAU samples

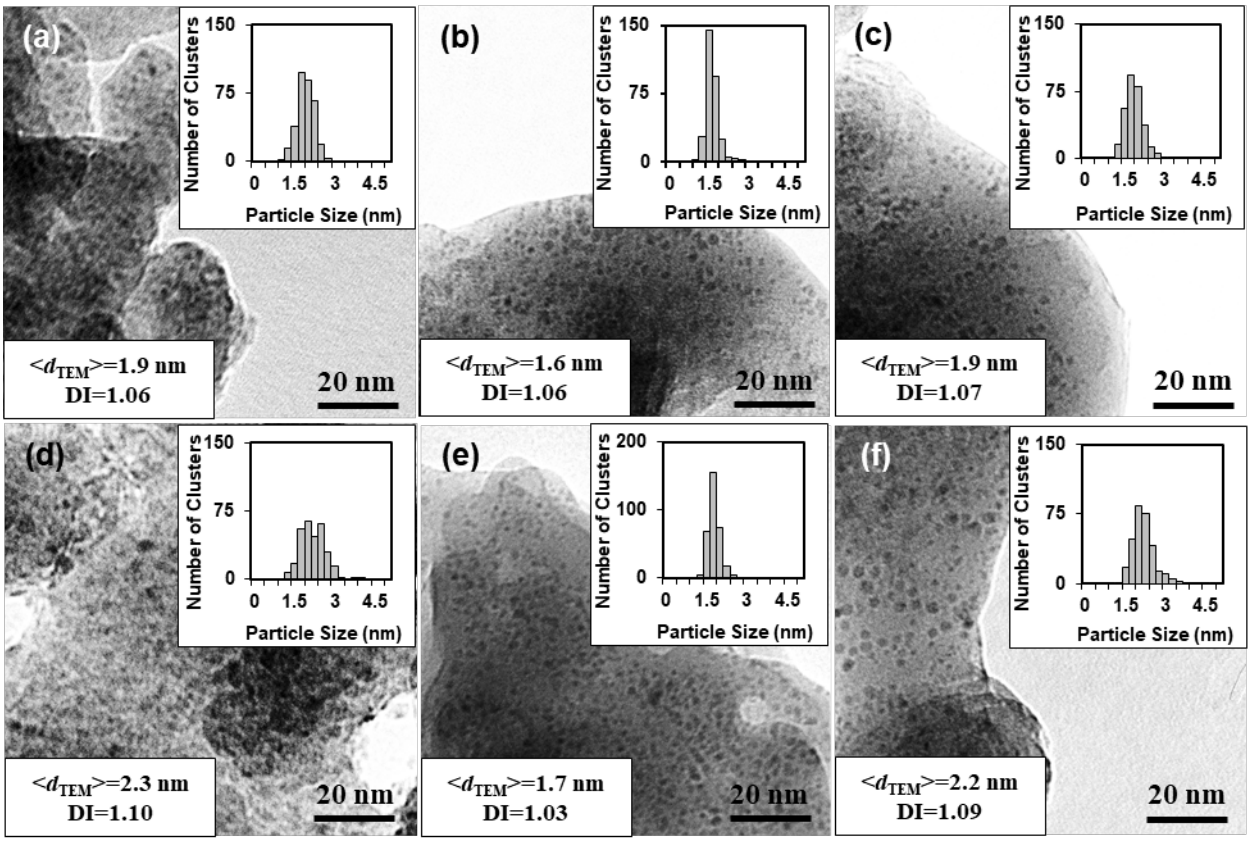

Figure 5.S5. Electron micrographs, particle size distributions, surface-averaged cluster diameters ($d_{TEM}\rangle$, Eq. 1), and particle dispersity indices (DI, Eq. 3) of (a) NiMFI, (b) CoLTA, (c) FeLTA, (d) NiFAU, (e) CoMFI, and (f) FeFAU.

5.S6. Micropore volumes of metal-free, metal-zeolite, and metal ion-exchanged zeolite samples

Adsorption isotherms of CO_2 were measured for metal-zeolite samples (main text, Table 5.2) prepared by direct hydrothermal synthesis (main text, Section 5.2.2.1-5.2.2.3) to determine micropore volumes of the crystalline zeolites. Analogous measurements were also conducted on LTA, MFI, and FAU zeolites synthesized without metal (Section 5.2.2.1-5.2.2.3) and zeolites ion-exchanged with Ni^{2+}, Co^{2+}, or Fe^{2+} (Section 5.2.2.4) to provide a basis for comparison with the hydrothermally synthesized metal-zeolite samples. All samples were heated to 623 K (at 0.17 K s^{-1}) and held for 4 h while under vacuum before their use in CO_2 adsorption experiments. CO_2 uptakes were measured over a pressure range of 0-800 torr at 273 K using a Micromeritics 3Flex Surface Characterization Analyzer. CO_2 uptakes were used to calculate micropore volumes using the Dubinin-Astakhov method [S1]. Figure 5.S6 shows calculated micropore volumes and CO_2 uptakes as a function of CO_2 pressure for metal-free, metal ion-exchanged, and hydrothermally crystallized metal-zeolite samples. CO_2 was used as the probe species (at 273 K) for these micropore volume measurements instead of N_2 at 77 K because the diffusion of N_2 into microporous solids is severely restrained at cryogenic temperatures, leading to inaccurate micropore volumes [S2].

Micropore volumes for the metal-free zeolites (LTA: 0.34 cm^3 g^{-1}, MFI: 0.19 cm^3 g^{-1}, FAU: 0.38 cm^3 g^{-1}) were similar to those of the metal-zeolite samples prepared by direct hydrothermal synthesis (metal-LTA: 0.32 cm^3 g^{-1}, metal-MFI: 0.16-0.17 cm^3 g^{-1}, metal-FAU: 0.34-0.36 cm^3 g^{-1}), consistent with the absence of substantial micropore obstructions by organic residues and a relatively low prevalence of framework defects resulting from the occlusion of oxide nanoparticles within the zeolite crystals. Micropore volumes of metal (M) ion-exchanged samples (M^{2+}-LTA: 0.28 cm^3 g^{-1}, M^{2+}-MFI: 0.17-0.18 cm^3 g^{-1}, M^{2+}-FAU: 0.34 cm^3 g^{-1}) were similar to or slightly lower than the metal-free LTA (Na^+ counterion), MFI (H^+ counterion), and FAU (Na^+ counterion), reflecting the smaller number of cations in metal-exchanged frameworks and thus their lower capacity to adsorb CO_2 [S3]. The high Si/Al ratio of the MFI framework (30), and the concomitant low density of charge-balancing cations, accounts for the minimal impact of the exchanged counterions on the micropore volumes of MFI samples. The micropore volumes measured here by CO_2 adsorption are similar to theoretical maximum micropore volumes accessible by CO_2, as calculated from LTA (0.37 cm^3 g^{-1}), MFI (0.19 cm^3 g^{-1}), and FAU (0.40 cm^3 g^{-1}) framework structures [S4], consistent with the integrity of the microporous structures of zeolites used in this work.

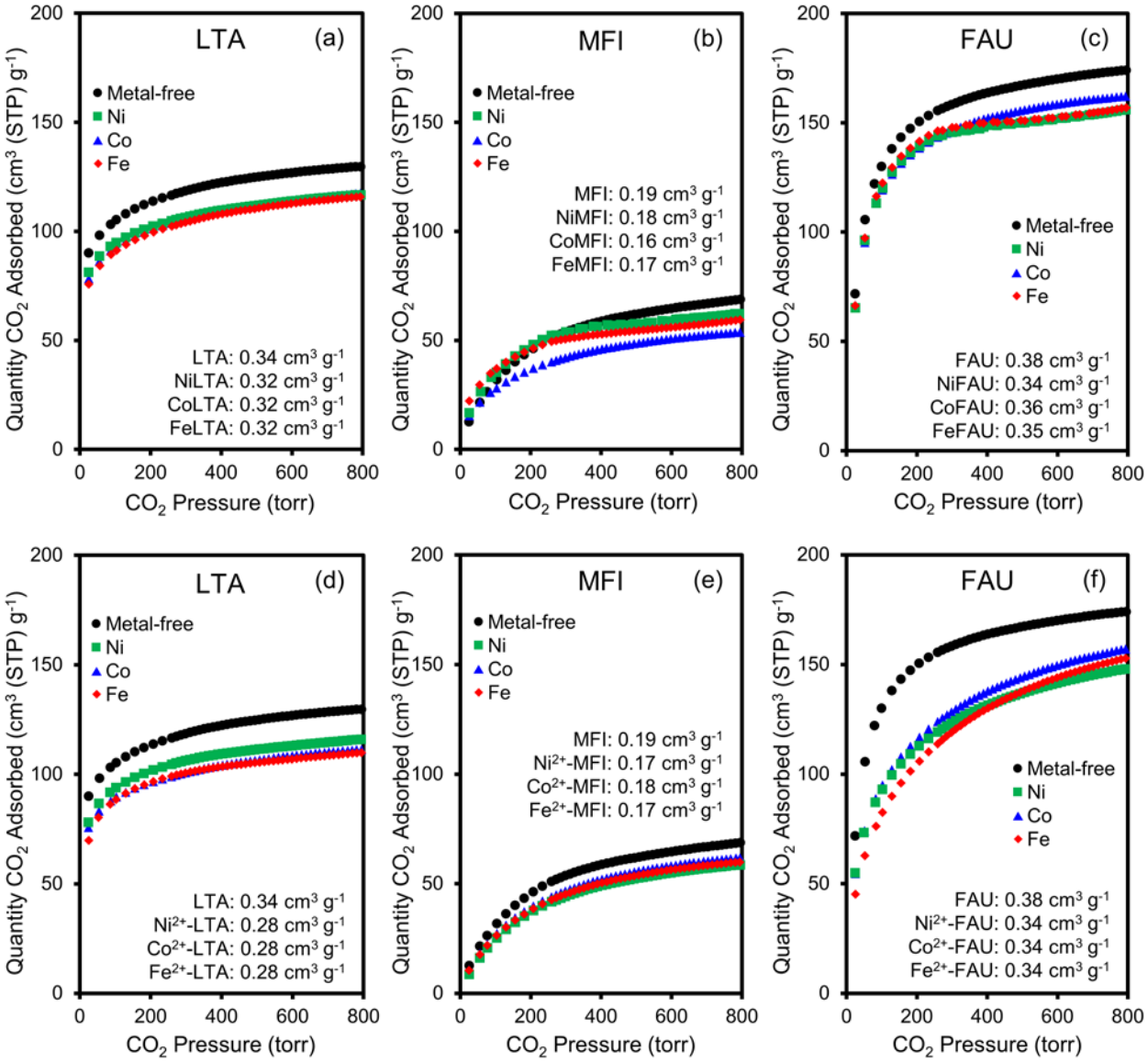

Figure 5.S6. CO_2 adsorption isotherms at 273 K and calculated micropore volumes for (a) metal-LTA samples prepared by direct hydrothermal synthesis, (b) metal-MFI samples prepared by direct hydrothermal synthesis, (c) metal-FAU samples prepared by direct hydrothermal synthesis, (d) metal-LTA samples prepared by ion-exchange, (e) metal-MFI samples prepared by ion-exchange, (f) metal-FAU samples prepared by ion exchange.

5.S7. Temperature programmed reduction profiles of metal-zeolite samples prepared by ion exchange

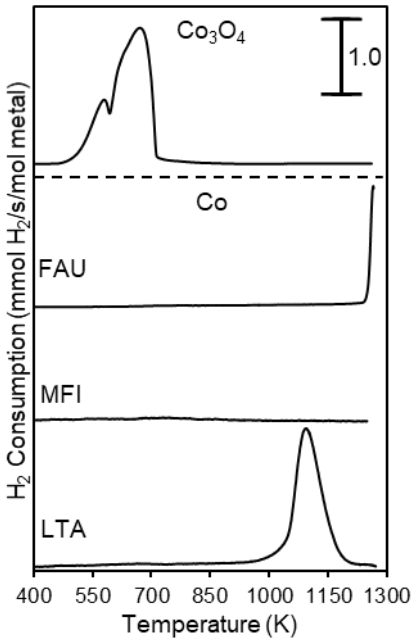

Figure 5.S7. Temperature programmed reduction profiles of bulk Co oxide and of Co-zeolite samples prepared via ion exchange with Co^{2+}. Samples were heated in 4% H_2/Ar (8.3 cm^3 s^{-1} g^{-1}) from 313 K to 1273 K at 0.167 K s^{-1}.

5.S8. References

[S1] Burevski, D. *Colloid Polym. Sci*. **1982**, *260*, 623.
[S2] M. Thommes, K.A. Cychosz, A.V. Neimark, in: J.M.D. Tascón (Ed.), Novel Carbon Adsorbents, first ed., Elsevier, Amsterdam, 2012, pp. 112.
[S3] Choi, S.; Drese, J. H.; Jones, C. W. *ChemSusChem* **2009**, *2*, 796.
[S4] First, E. L.; Gounaris, C. E.; Wei, J.; Floudas, C. A. Phys. Chem. Chem. Phys. **2011**, *13*, 17339.

Chapter 6

Synthesis of Au Nanoparticles Encapsulated within the TS-1 Zeotype Framework

Abstract

A synthetic procedure has been developed for the selective encapsulation of Au nanoparticles (3.6-3.8 nm in diameter) within TS-1 zeotype frameworks. The synthetic technique, though demonstrated specifically here to prepare Au within TS-1, follows generally applicable procedures that can be analogously used on other metal species or high-silica zeotype frameworks. Encapsulation was achieved via hydrothermal crystallization of TS-1 synthesis gels in the presence of ligated Au cations, which results in the assembly of TS-1 frameworks around Au coordination complexes. TS-1 was successfully crystallized at much milder conditions than previously reported in order to prevent the decomposition (or reaction with alkanols formed during hydrolysis of Ti or Si precursors) of Au-ligand complexes in the synthesis gels without adversely affecting Ti incorporation into the framework or sample crystallinity. The changes made to the established synthesis procedures for TS-1 include much lower crystallization temperatures (393 K vs. 448 K) compensated by longer crystallization times (120 vs 48 h) and the addition of TS-1 seed crystals. Post-synthetic oxidative treatments were developed in order to remove ligand species and organic structure-directing agents from the crystallized Au/TS-1 solids while minimizing the generation of local exotherms; these procedures led to the formation of small Au nanoparticles selectively embedded within microporous TS-1 crystals, as demonstrated by their protection from bulky organosulfur titrants during ethanol oxidation reactions. The Au/TS-1 systems have potential applications as effective alkene epoxidation catalysts that utilize H_2O_2 or OOH oxidants generated in-situ, because the close atomic proximity between Au and Ti domains conferred by encapsulation would facilitate the transfer of highly reactive peroxy intermediates formed on Au surfaces to Ti active sites, where epoxidation occurs.

6.1 Introduction

Au nanoparticles have attracted considerable attention because of their catalytic diversity and high reactivity in CO oxidation, alkanol oxidation, and diene hydrogenation [1-3]. Highly dispersed (<5 nm) Au nanoparticles dispersed on amorphous or crystalline oxides containing Ti atoms (e.g., TiO_2 and titanium-containing silicalite-1 (TS-1)) can also catalyze alkene epoxidation using O_2 as the oxidant [3-6]. Au/Ti-oxide catalysts for propylene epoxidation are of specific practical interest because of the use of propylene oxide (PO) as a precursor in the synthesis of polyether polyols, propylene glycol, and several other products [7]. Propylene epoxidation occurs on Au/Ti-oxide compounds in the presence of H_2/O_2 mixtures that are proposed to form H_2O_2 on Au surfaces, which then binds to Ti centers present within molecular distances as hydroperoxy (*OOH) [7,8] or hydrogen peroxide (*HOOH) species [9]. These peroxides then react with propylene to form propylene oxide via mechanisms also involved when H_2O_2 is used as the co-reactant [3]. Hydroperoxy species have also been proposed to form on Au surfaces from H_2O/O_2 mixtures [10-12]. With both reactant mixtures, epoxidation rates and selectivities depend sensitively on the proximity of the Au and Ti sites [8-12] because of the required transfer of highly-reactive intermediates from Au to Ti domains. Such intimacy requirements have led to significant

efforts to develop protocols for the synthesis of solids with proximate Au and Ti domains. These methods typically focus on placing well-dispersed Au on or within TS-1 crystals, which provide isolated Ti centers with the tetrahedral coordination shown to be most effective for alkene-H_2O_2 reactions [8,11,12].

Au nanoparticles 2-4 nm in diameter can be deposited onto TS-1 via deposition-precipitation (DP) methods using Na_2CO_3 [13-15], K_2CO_3 [16], or Cs_2CO_3 [16] as the reagents to precipitate $HAuCl_4$ precursors. These procedures lead to some of the most active and selective Au/TS-1 catalysts for propylene epoxidation with both H_2/O_2 and H_2O/O_2 [11,13-16], even though the Au function resides primarily at the external surfaces of TS-1 crystals. Density functional theory (DFT) [17] calculations indicate that propylene epoxidation with H_2/O_2 is most favorable on Ti sites within atomic contact of small (<1 nm) Au nanoparticles [17]. Propylene epoxidation rates are substantial on catalysts prepared by the deposition of Au nanoparticles on silicalite-coated TS-1 crystals, suggesting that a small fraction of highly dispersed (<1 nm) Au clusters formed via DP and residing deep within TS-1 crystals, rather than on external surfaces, may account for much of the observed epoxidation activity on Au/TS-1 [15,18]. DP methods that form Au nanoparticles with the required small diameters (<5 nm [19]) are limited to low Au loadings (<0.35% wt. [11]) and only precipitate ~5% of the Au^{3+} species present in the aqueous solutions that are used to disperse TS-1 crystals [11]. Solid grinding methods [20] can be used to form small (<2 nm) Au clusters at external TS-1 surfaces with the near-complete deposition of the Au precursors mixed with TS-1 crystals, but at very low Au contents (<0.30% wt.). AuPd particles (~2 nm) can be dispersed within mesopores in hierarchical TS-1 samples (prepared by crystallization of protozeolitic precursors) via post-synthetic impregnation and thermal treatment of Au^{3+} and Pd^{2+} precursors [21]. Benzyl alcohol oxidation rates with H_2/O_2 mixtures (to generate H_2O_2 in-situ) on these AuPd samples were higher than on larger AuPd particles formed by deposition-precipitation on hierarchical TS-1 crystals [21]. These methods represent the current state-of-the-art in the synthesis of H_2O_2 or OOH-generating Au functions within short distances (but larger than atomic and molecular dimensions) of Ti centers within TS-1.

The present study reports a synthetic strategy for the direct encapsulation of Au nanoparticles within TS-1 crystals during hydrothermal synthesis. These protocols place the Au and Ti functions within short distances for a system that cannot be prepared by the post-synthetic exchange of solvated Au^{3+} precursors followed by thermal treatment [22]. TS-1 lacks cation exchange sites and its 10 member-ring (10-MR) apertures impede the diffusion of aqueous Au^{3+} into intracrystalline regions [23]. The protocols used here involve hydrothermal assembly of TS-1 zeotype frameworks around ligand-protected Au^{3+} cations to form coordination complexes occluded within TS-1 voids. Subsequent thermal treatments remove ligand species and lead to the formation of small and stable nanoparticles selectively contained within intracrystalline voids. These methods represent an extension of protocols developed for a variety of metals and zeotypes (e.g., LTA, MFI, FAU, GIS, ANA, SOD, CHA; [24-28]) to Au nanoparticles within TS-1 and SIL structures that lack exchange sites.

These encapsulation methods are particularly challenging for Au cations, because of their propensity to reduce and prematurely form large Au^0 colloids [23], and for TS-1 because the temperatures required for TS-1 crystallization (443-448 K; [29,30]) are higher than those for aluminosilicates used previously to demonstrate encapsulation protocols (e.g., LTA, MFI; 373-

393 K; [23,24]). Such high temperatures promote the deprotection of ligated precursors and their premature precipitation or reduction during the assembly of zeotype frameworks [23,31,32]. The challenges of high synthesis temperatures and the facile reduction of Au^{3+} relative to other noble metal cations [33], especially when alkanols formed by the hydrolysis of Si and Ti alkoxides act as chemical reductants [23], have prevented the synthesis of Au nanoparticles selectively dispersed within TS-1 until now.

These synthetic hurdles were surmounted by (i) using 3-mercaptopropyl-trimethoxysilane (MPS) ligands that simultaneously protect Au^{3+} cations and enforce metal incorporation into proto-zeolitic species via their alkoxysilane moieties, (ii) fully removing alkanol reductants formed by alkoxide hydrolysis, and (iii) crystallizing synthesis gels at moderate temperatures that preclude the premature reduction of Au^{3+} cations without compromising framework crystallization. The successful syntheses exploited TS-1 crystallization temperatures that are lower than those used in previous reports (393 K vs. 443-448 K; [29,30]) balanced by longer times (120 h vs. 48 h) and the addition of seed crystals. These procedures led to the formation of Au/TS-1 with high crystallinity, high yields, and Ti centers within the framework at Au contents of 0.2-0.9% wt. Post-synthetic oxidative and reductive treatments successfully removed the ligands and organic templates and led to formation of 3.6-3.8 nm Au nanoparticles uniform in size and residing within TS-1 voids, as indicated by their size selectivity during catalytic reactions. The formation of small and uniform Au nanoparticles required the gradual removal of organic ligand and template species, which generate local exotherms during oxidative treatments that can promote the sintering of Au nanoparticles during critical periods of particle nucleation. Treatment procedures that minimize the impact of such exotherms were identified by systematically varying the rate and duration of thermal treatment procedures and examining the sizes of Au nanoparticles formed. The size uniformity and surface cleanliness of the confined Au particles were confirmed by transmission electron microscopy (TEM) and infrared (IR) spectra of chemisorbed CO, respectively. Micropore volumes, UV-visible and infrared spectra, and X-ray diffractograms (XRD) we consistent with crystalline structures containing Ti in their framework. Au particles were predominantly present within TS-1 voids (>96% of exposed Au surfaces) as shown from ethanol oxidative dehydrogenation (ODH) rates on Au/TS-1 before and after exposure to dibenzothiophene (DBT), which poisons Au surfaces but cannot enter TS-1 voids. These materials have potential applications as effective catalysts for the epoxidation of alkenes with H_2/O_2 or H_2O/O_2, because the close atomic proximity between confined Au particles and surrounding framework Ti atoms is likely to facilitate the critical transfer of highly reactive H_2O_2 or OOH species generated on Au surfaces to the Ti domains where epoxidation occurs.

6.2 Methods

6.2.1 Source and purity of reagents used

Distilled and deionized H_2O (17.9 Ω cm resistivity) was used in all procedures. $HAuCl_4 \cdot 3H_2O$ (99.99%, Sigma-Aldrich), 40% wt. tetrapropylammonium hydroxide (TPAOH) in H_2O (99% purity; Sigma-Aldrich), tetraethyl orthosilicate (TEOS; 98%, Sigma-Aldrich), tetraethyl orthotitanate (TEOT; 98%, Sigma-Aldrich), 3-mercaptopropyl-trimethoxysilane (95%, Sigma-Aldrich), ethanol (99.9%, Sigma-Aldrich), dibenzothiophene (DBT; 98%, Sigma-Aldrich), fumed SiO_2 (Cab-O-Sil M5), $BaSO_4$ (>99%, Sigma-Aldrich), air (extra dry; 99.999%, Praxair), H_2

(99.999%, Praxair), 1% CO/He (99.999%, Praxair), and He (99.999%, Praxair) were used as received.

6.2.2 Synthesis of TS-1 frameworks with ligated Au precursors in product crystals

The synthesis of Au/TS-1 was carried out using a modified version of the International Zeolite Association (IZA) recommended procedure [29] for TS-1 ($Ti_{1.3}Si_{94.7}O_{192}$) by introducing Au^{3+} cations (from $HAuCl_4$) protected by 3-mercaptopropyl-trimethoxysilane (MPS) ligands into TS-1 synthesis gels. The modifications were substantial and included not only the presence of the ligated Au^{3+} species but also much longer times, lower temperatures, the full removal of alkanol reductants formed by the hydrolysis of Si and Ti precursors, and the use of seed crystals to promote crystallization at the milder conditions required to avoid the reduction of Au cations. These modified procedures lead to the successful crystallization of TS-1 frameworks at a temperature (393 K) much lower than previously reported (448 K; [29]).

The Au/TS-1 synthesis gels were prepared by combining tetraethyl orthosilicate (TEOS; 19.2 g) and tetraethyl orthotitanate (TEOT; 0.354 g) in a sealed polypropylene bottle and heating at 308 K for 0.5 h under magnetic stirring (6.7 Hz). This TEOS/TEOT mixture was cooled to 273 K in an ice bath and added dropwise (0.02 cm^3 s^{-1}) to 20 g of 40% wt. aqueous tetrapropyl ammonium hydroxide (TPAOH) also kept at 273 K and magnetically stirred at 6.7 Hz. The resulting mixture was heated to 358 K for 4 h while stirring (6.7 Hz) in an open polypropylene bottle to allow partial evaporation of the liquid to occur. This step removes some water and most of the ethanol formed upon hydrolysis of TEOS and TEOT. Ethanol decreases the solubility of silicate precursors during crystallization [29]; most importantly in this case, it also acts as a reductant for Au cations at synthesis temperatures [23]. One-half of the evaporated volume (after heating at 358 K for 4 h) was replaced with an aqueous solution of the MPS ligand (0.077-0.387 g in ~12 cm^3 H_2O). This mixture was homogenized at ambient temperature by stirring (6.7 Hz) and the remaining volume removed by evaporation (~12 cm^3) was replaced by dropwise addition of an aqueous solution of $HAuCl_4 \cdot 3H_2O$ (0.02-0.11 g), followed by heating to 358 K for 4 h while stirring (6.7 Hz) in an open bottle. Deionized H_2O was periodically added to the solution during this second evaporation process in order to maintain a constant volume. These procedures lead to homogeneous Au/TS-1 synthesis gels with molar ratios of 1 TiO_2/70 SiO_2/1980 H_2O/30 TPAOH/0.30-1.49 ligand/0.043-0.213 Au.

Batches of Au/TS-1 synthesis gels were crystallized within Teflon-lined stainless steel autoclaves by heating them (while rotating at 17 Hz) at temperatures between 393 and 448 K for periods between 48 and 120 h. Au/TS-1 solids were isolated by centrifugation (Sorvall RC-6 plus, 133 Hz) and repeatedly washed with deionized water until the suspending liquids in centrifuge tubes (~50 cm^3 g^{-1}) reached a pH of 7-8; isolated and washed samples were treated for 8 h at 373 K in ambient air. The different crystallization times and temperatures were examined in order to identify synthesis conditions that led to the formation of crystalline TS-1 without premature reduction of Au cations and the formation of colloidal Au. In some tests, TS-1 seeds (0.548 g) were added to Au/TS-1 synthesis gels before heating and crystallization. The seed crystals were prepared using the above procedures with crystallization at 448 K for 48 h, but without ligands or Au precursors. The amount of seed crystals added (0.548 g) corresponds to 10% wt. of the solids yield resulting from the complete crystallization of the starting gel at 448 K for 48 h and in the

absence of added Au^{3+} or MPS. The Au content in most tests was chosen to form Au/TS-1 with ~1% wt. Au. Samples were also synthesized with lower Au loading to achieve 0.2% wt. nominal Au content. Procedures that lead to the assembly of crystalline TS-1 without the premature reduction of Au^{3+} species were devised based on synthesis experiments conducted at a variety of conditions (Section 6.3.1), and entail the crystallization of Au/TS-1 synthesis gels in the presence of 10% wt. seed crystals at 393 K for 120 h. The temperature used (393 K) is about 50 K lower than in standard TS-1 synthesis protocols, and prevented the reduction and decomposition of ligated Au precursors or the premature formation of Au colloids that cannot be encapsulated within TS-1 crystals because of their size.

6.2.3 Post-synthetic treatment of as-synthesized Au/TS-1

Post-synthetic thermal treatments were applied with the intention of removing organic templates and ligands from as-synthesized Au/TS-1 and forming small Au nanoparticles. The oxidative removal of organic templates from zeotype crystals typically leads to local exotherms that can sinter occluded Au species [23], thus requiring staged thermal treatments to moderate the extent of removal over time [23]. The size and surface cleanliness (Section 6.2.4) of the Au particles formed after a specific thermal treatment protocol were examined in order to establish procedures that allowed the removal of synthetic residues without compromising the size, surface cleanliness, or encapsulation selectivity of the Au nanoparticles. These systematic studies led to a procedure in which Au/TS-1 was sequentially heated in flowing air (1.67 $cm^3\ g^{-1}\ s^{-1}$) to 448 K, then 498 K, and finally 548 K (each at 0.017 K s^{-1}) and held for 2 h at each temperature. The sample was then cooled to ambient temperature and the thermal ramping procedure was repeated, but with each step at higher temperature than during the first treatment (573 K, 623 K, and 673 K). In the final air treatment step, the Au/TS-1 was heated again from room temperature to 723 K and then 773 K, and again held at each temperature for 2 h. A final treatment in H_2 (1.67 $cm^3\ g^{-1}\ s^{-1}$) was carried out by heating the Au/TS-1 from ambient temperature to 723 K (at 0.017 K s^{-1}) and holding for 2 h. A diagram of the thermal treatment procedure in air is shown in Section 6.S1 of the Supporting Information (SI).

6.2.4 Characterization of TS-1 frameworks and Au nanoparticle size and surface cleanliness

X-Ray diffraction (XRD) was used to determine TS-1 crystallinity using a D8 Discover GADDS Powder Diffractometer with Cu-Kα radiation (λ=0.15418 nm, 40 kV, 40 mA; 2θ = 5-50°; 0.00625 degree s^{-1} scan rate) and finely ground solids dispersed onto quartz slides. The pattern for metal-free TS-1 (prepared via the IZA method [29]; Section 6.2.2) was used as a standard to determine the crystallinity of Au/TS-1 samples from the integrated intensities of the three most intense diffraction lines.

Transmission electron microscopy (TEM) was used to measure the size of Au nanoparticles in Au/TS-1 samples. Samples were prepared for TEM analysis by grinding them into powder, dispersing them in acetone, and then depositing them onto holey carbon films mounted on 400 mesh copper grids (Ted Pella Inc.). A Philips/FEI Technai 12 microscope operating at 120 kV was used to collect the electron micrographs. Au particle sizes were measured based on the micrograph images and then used to calculate surface-averaged diameters ($\langle d_{TEM} \rangle$) [25]:

$$\langle d_{\mathrm{TEM}} \rangle = \frac{\sum n_i d_i^3}{\sum n_i d_i^2} \qquad (1)$$

where n_i is the number of particles with diameter d_i. The Au dispersion (defined as the fraction of Au atoms that reside at particle surfaces; *D*) was estimated from $\langle d_{\mathrm{TEM}} \rangle$ values [34]:

$$D = 6 \frac{v_m / a_m}{\langle d_{\mathrm{TEM}} \rangle} \qquad (2)$$

where a_m is the area occupied by an Au atom (8.75×10^{-2} nm^2) on a polycrystalline Au surface and v_m is the bulk atomic volume of Au (16.49×10^{-3} nm^3) [35]. Au particle diameters were also used to calculate number-averaged diameters ($\langle d_n \rangle$) and dispersity indices (DI) [25]:

$$\mathrm{DI} = \frac{\langle d_{\mathrm{TEM}} \rangle}{\langle d_n \rangle} = \frac{\left(\frac{\sum n_i d_i^3}{\sum n_i d_i^2} \right)}{\left(\frac{\sum n_i d_i}{\sum n_i} \right)} \qquad (3)$$

These DI values represent the accepted IUPAC metric of size uniformity, with samples having values smaller than 1.5 considered as essentially monodisperse [34].

The micropore volume of TS-1 and Au/TS-1 samples was measured via CO_2 adsorption measurements (0-107 kPa) at 273 K. Measurements were conducted using a Micromeritics 3Flex Surface Characterization Analyzer, and micropore volumes were calculated from CO_2 uptakes with the Dubinin-Astakhov method [36]. Samples were heated at a rate of 0.17 K s^{-1} to 623 K under vacuum and held for a period of 4 h before CO_2 uptake measurements. CO_2 was used as the adsorbing molecule at 273 K rather than N_2 at 77 K because the diffusion of N_2 into the microporous regions of zeotypes is limited at low temperatures, which can cause underestimation of micropore volumes [37].

UV-visible spectra were used to probe the Ti species present in TS-1 and Au/TS-1 samples and to detect plasmon resonance bands, characteristic of Au particles larger than 2 nm in diameter. Spectra were acquired on powders (<100 μm diameter) using a Varian-Cary 6000i spectrometer and a Harrick scientific diffuse reflectance accessory (DRP-XXX) with a reaction chamber (DRA-2CR). Powders were held on a steel fritted disc that allowed flow though the samples. A temperature controller (Watlow Series 982) connected to a heating element and thermocouple (type K) embedded in the sample holder was used to maintain the sample temperature. The samples were treated within the cell in flowing He (1.67 cm^3 g^{-1} s^{-1}) at 623 K for 1 h to remove adsorbed water, and spectra were measured (200-800 nm) after cooling samples to ambient temperature in flowing He. Silicalite-1, synthesized as described in Section 6.2.2, but without the addition of Au, ligands, or Ti, or $BaSO_4$ were used to provide the background spectra required to convert reflectance data into pseudo-absorption intensities using the Kubelka-Munk formalism.

IR spectra were used to measure the extent of incorporation of Ti into the framework for TS-1 and Au/TS-1 samples and to determine the cleanliness of Au surfaces from the intensity and frequency of the bands for chemisorbed CO. Transmission IR spectra were acquired with a Thermo Nicolet 8700 spectrometer on samples consisting of wafers prepared from finely ground samples

(40 mg cm^{-2}). The wafers were held in a controlled atmosphere cell and heated to 523 K at a rate of 0.033 K s^{-1} in flowing He (40 cm^3 g^{-1} s^{-1}) and held for 1 h; they were then cooled to 263 K or ambient temperature before spectra were acquired (400-2200 cm^{-1}). IR measurements at ambient temperature were used to examine vibrations resulting from the presence of framework Ti species and were conducted under a He atmosphere. The IR experiments carried out at sub-ambient temperature were used to determine the cleanliness of Au nanoparticles. Cooling of the samples to 263 K was followed by replacement of the flowing He with 0.1-1.0% CO/He (40 cm^3 g^{-1} s^{-1}) for a period of 0.25 h prior to the collection of absorption spectra. Absorption features derived from CO(g) were subtracted from all collected spectra.

6.2.5 Catalytic assessment of the reactivity and selectivity of encapsulation of Au nanoparticles

The encapsulation selectivity of Au particles within TS-1 was estimated by measuring ethanol (EtOH) oxidative dehydrogenation (ODH) rates on Au/TS-1 and Au/SiO_2 (prepared by deposition-precipitation, as described elsewhere [23]) before and after exposure to dibenzothiophene (DBT). DBT (0.9 nm kinetic diameter [38]) binds irreversibly to Au surfaces [23], but cannot access the small voids (0.55 nm for MFI [39]) in 10-MR zeotypes, such as TS-1. These titration procedures can be used to calculate the fraction of Au surface area in each sample that resides within the protected environment of TS-1 voids by examining the decrease in rate upon DBT titration.

Au/TS-1 and Au/SiO_2 were exposed to DBT prior to rate measurements by agitating (with a magnetic bar at 6.7 Hz) the solid powders at ambient temperature in liquid EtOH (300 cm^3 g^{-1}) containing dissolved DBT at a DBT:Au molar ratio of 6:1. Samples were exposed to the DBT solutions for a period of 4 h, which allows sufficient time for DBT to attach to accessible extracrystalline Au surfaces but not to substantially diffuse into 10-MR MFI apertures [23]. The treated samples were isolated by filtration, heated in ambient air at 343 K for 12 h, diluted 10-fold (by mass) with SiO_2, pelleted into 180-250 μm aggregates, and used in EtOH ODH reactions without further pretreatment (to minimize DBT desorption or decomposition). EtOH ODH rates were also measured on samples treated similarly but without DBT in the EtOH media.

These aggregates were packed onto a porous quartz disk held within a quartz tube (10 mm OD) and heated to 393 K using a resistively-heated tube furnace, a temperature controller (Watlow, 96 Series), and a type K thermocouple. The flowrate and composition of the inlet stream (9 kPa O_2, 4 kPa EtOH, 0.5 kPa H_2O, 87.5 kPa He) were metered using gas flow controllers (for He, O_2; Porter Instrument) or a liquid syringe pump (for H_2O, EtOH; Cole Parmer, 60061 Series); reactant lines were kept at 343 K to vaporize EtOH and prevent its condensation. The concentrations of EtOH and acetaldehyde (the only detected product) were measured using gas chromatography (Shimadzu GC-2014) with a methyl-silicone capillary column (HP-5; 50 m × 0.32 mm, 1.05 μm film thickness) and a flame ionization detector. EtOH turnover rates are normalized here by the number of surface Au atoms present in each sample (estimated from Au content and size distributions; Eq. 2). Reported EtOH turnover rates represent their values at <5% conversions during the initial stages of each experiment.

6.3 Results and Discussion

6.3.1 Effects of crystallization conditions on the stability of ligated Au precursors, solid product yield, and TS-1 phase purity

Au/TS-1 synthesis gels (prepared as described in Section 6.2.2) were crystallized at temperatures between 393 and 448 K for periods of time between 48 and 120 h. The solids recovered were characterized by XRD and TEM to confirm (i) the TS-1 crystallinity and (ii) the absence of large Au metal colloids, which were examined as a first evaluation of the success of the synthesis protocols and of the effective protection of the ligated Au^{3+} cations. X-Ray diffractograms of as-synthesized TS-1 and Au/TS-1 (1% wt. nominal Au loading) crystallized using the IZA procedures (448 K; 48 h; Section 6.2.2; [29]) are shown in Figure 6.1. Au/TS-1 gels held at 448 K for 48 h led to crystalline TS-1 (96%; Table 6.1), but also to the premature reduction and extensive agglomeration of Au-derived species into large Au metal crystallites (5-50 nm) evident in electron micrographs (Figure 6.2). At these conditions (448 K; 48 h), the presence of Au^{3+} and MPS species in the synthesis gel did not substantially interfere with the assembly of titanosilicate oligomers as TS-1, likely because of the presence of Au^{3+}-MPS coordination compounds as minority species (T-atom:MPS molar ratio of 48:1, where T = Si, Ti for MPS:Au molar ratio of 6:1 in this sample). Au/TS-1 gels crystallized at a slightly lower temperature (438 K) for 48 h also showed sharp TS-1 diffraction lines (Figure 6.1) and large Au particles (Figure 6.2). Even lower temperatures (423 K, 48 h) caused the premature deprotected of ligated Au precursors (Figure 6.2), and these milder conditions also led to less crystalline solids than the TS-1 standard (73%; Table 6.1) and to the formation of an amorphous phase, as evident from a slight broad background feature in diffractograms (Figure 6.1). The apparently mild effect of added Au^{3+} coordination complexes on the product crystallinity of Au/TS-1 gels prepared at 438-448 K suggests the formation of amorphous phases in Au/TS-1 crystallized at 423 K results largely from the lower temperature used, which was intended, but failed, to preclude the premature deprotection of Au^{3+} species. The high temperatures typically required (>443 K) to crystallize Ti-containing zeotypes reflects, in part, the inhibitory effect of Ti precursors, even at very low Ti/Si ratios, on crystallization rates of the silicate framework [40].

Au/TS-1 synthesis gels were crystallized at lower temperatures (393-413 K) and for longer periods of time (up to 120 h) than in previously established procedures (448 K; 48 h) in an effort to (i) prevent deprotection of ligated Au^{3+} precursors and (ii) compensate for the effects of low temperatures on TS-1 crystallinity with longer crystallization times. Figure 6.3 shows the diffractograms of as-synthesized Au/TS-1 crystallized at 413 K for 48, 72, 96, and 120 h. The phase purity of TS-1 frameworks increased monotonically from 73% to 92% with longer synthesis times (48 h to 120 h), confirming that the intended compensation in fact occurred. Hydrothermal synthesis of Au/TS-1 even at 413 K, however, led to the formation of large Au metal agglomerates, as evident from electron micrographs (Figure 6.2; Table 6.1).

Au/TS-1 samples prepared by hydrothermal crystallization at 393 K for 120 h showed no detectable Au particles in micrographs (Figure 6.2), suggesting that MPS ligands are able to protect Au^{3+} cations at this temperature. The high crystallinity of this sample (93%; Table 6.1) indicates that TS-1 frameworks can be formed at much lower temperatures than prescribed in accepted synthesis protocols (448 K). The TS-1 solids yield in this Au/TS-1 sample was smaller (65%;

Table 6.1) than in the TS-1 standard (448 K, 48 h), indicating that a substantial fraction of Si and Ti precursors are removed with the supernatant liquids upon filtration (Section 6.2.2). The addition of as-synthesized TS-1 seeds (10% wt. based on expected solids yield for TS-1 standard; Section 6.2.2; synthesized for 48 h at 448 K) to the Au/TS-1 synthesis gel before crystallization for 120 h at 393 K led to a substantial improvement in solids yield (85%; Table 6.1), even after accounting for the added seeds. Seed crystals may provide silicate and titanate oligomers that aid crystal growth through their addition to growing proto-zeolitic moieties or by spalling during hydrothermal treatments to form small fragments that act as nuclei for crystal growth [41].

The application of analogous synthesis procedures (Section 6.2.2) and crystallization conditions (393 K for 120 h with 10% wt. seeds) to an Au/TS-1 synthesis gel with 0.2% wt. nominal Au loading similarly led to the formation of crystalline frameworks (96%; Figure 6.1) with high yield (89%) and the absence of any prematurely formed Au particles visible in electron micrographs (Section 6.S2, SI). The similar framework crystallinities and product yields of the 0.2% wt. and 1.0% wt. Au/TS-1 samples (crystallinity: 96%, 94%; yield with 10% wt. seeds: 89%, 85%; for 0.2% and 1.0% wt. nominal Au loading, respectively) indicate that the specific crystallization conditions chosen for Au/TS-1 synthesis gels, rather than the amount of Au^{3+}-MPS complexes and the number of siloxane linkages formed between such complexes and titanosilicate precursors, have a controlling effect on the assembly of TS-1 crystals over the range of metal contents examined. The relatively small impact of the added metal-ligand complexes can be attributed to their sparse presence in the TS-1 synthesis gels (T-atom:MPS molar ratio of 48:1 and 240:1 for 1.0 and 0.2% wt. Au loading samples, respectively). In the next section, additional characterization data are shown for these samples following post-synthetic oxidative and reductive treatments (Section 6.2.3).

6.3.2 Characterization of Au/TS-1 samples after thermal treatments

The preparation of Au/TS-1 samples for use as catalysts requires post-synthetic treatments that remove occluded ligand and organic structure-directing agent (OSDA) species and lead to the formation of small Au particles. The oxidative removal of OSDA compounds is exothermic and prone to create high local temperatures that promote Au particle growth [23]. A thermal treatment protocol that preserves small monodisperse Au particles while fully removing synthetic residues was developed through a systematic analysis of the effects of thermal ramping procedures and treatment gases on the size and surface cleanliness of Au clusters and framework micropore volumes. A detailed description of the sequential oxidative and reductive treatments developed and used for Au/TS-1 (0.2-1.0% wt. nominal Au loading; crystallized with 10% wt. TS-1 seeds at 393 K for 120 h) is included in Section 6.2.3 and shown diagrammatically Section 6.S1 (SI).

6.3.2.1 Assessment of framework crystallinity, micropore volume, and Au nanoparticle size after post-synthetic treatment of Au/TS-1

Diffractograms of treated Au/TS-1 samples (Figure 6.4) show that TS-1 frameworks are highly crystalline after post-synthetic treatments (96% and 93% for Au/TS-1 with 0.2% wt. and 1.0% wt. nominal Au loading, respectively), as they were before such treatments (96% and 94%). The Au contents of Au/TS-1 samples (0.2% wt. and 0.9% wt. for 0.2% and 1.0 % wt. nominal Au loading, respectively; measured by inductively coupled plasma optical emission spectroscopy;

ICP-OES) are consistent with the nearly quantitative incorporation of all Au precursors in the gels into the solids formed, which would have led to Au contents of 0.2-1.1% wt. These high Au uptake efficiencies likely reflect the preferential formation of siloxane linkages between MPS ligands and zeotype precursors, which favor the embedding of the ligated precursors within crystals as they form [23,26]. Post-synthetic treatment of Au/TS-1 with 0.9% wt. Au led to the formation of relatively small Au particles ($\langle d_{TEM} \rangle$=3.8 nm; Eq. 1; Figure 6.5) uniformly distributed in size (DI=1.11; Eq. 3). Such clusters are substantially greater in diameter than the largest voids present in the TS-1 framework (channel intersections; 0.64 nm [39]). We show in Section 6.3.2.4 that such nanoparticles, despite their large size relative to channel intersections, are protected from contact by bulky organosulfur titrants that cannot enter narrow framework apertures (0.55 nm [39]), and therefore overwhelming reside within TS-1 crystals. The small sizes of the Au nanoparticles likely result from the uniform dispersion of the ligated Au precursors throughout TS-1 crystals during synthesis, which mitigates nanoparticle growth upon ligand removal [23,26]. The crystallization and post-synthetic treatment of Au/TS-1 with lower Au content (0.2% wt. Au, nominal and measured) led to Au nanoparticles near identical in size ($\langle d_{TEM} \rangle$=3.6 nm; DI=1.12; Figure 6.5); these limiting sizes seem to reflect the need to locally rupture TS-1 frameworks, which imposes a thermodynamic barrier to growth as particles reach a size for which their decrease in surface energy can no longer compensate for the required framework disruptions. Such thermodynamic barriers also account for the thermal stability of Au nanoparticles in Au/TS-1, which are relatively small and monodisperse in size despite the use of high temperature treatments in air (773 K) and H_2 (723 K) in post-synthetic treatment procedures (Section 6.2.3). The disruptions required to accommodate 3.6-3.8 nm Au particles within TS-1 voids (0.64 nm) do not measurably influence framework crystallinity (Figure 6.4), because such particles occupy less than <0.3% of the microporous void volume of TS-1 (for 0.9% wt. Au/TS-1).

The complete removal of the organic template and the ligands by these thermal treatments (Section 6.2.3) was confirmed from micropore volumes measured by CO_2 uptakes at 273 K (1-107 kPa; Section 6.S3, SI) and elemental sulfur analysis (ICP-OES). The micropore volume of Au/TS-1 with 0.9% wt. Au (0.17 $cm^3\ g^{-1}$; Section 6.S3, SI) matched that of the metal-free TS-1 standard treated in air at 823 K for 4 h (0.16 $cm^3\ g^{-1}$; Section 6.S3, SI) and the volume reported for a silicalite-1 standard (0.20 $cm^3\ g^{-1}$; [37]). Sulfur was undetectable by ICP-OES in treated Au/TS-1 (<1 ppm), indicative of the full removal of the ligands by these thermal treatments.

6.3.2.2 Interrogation of Au surfaces with IR spectroscopy of adsorbed CO

The infrared spectra of chemisorbed CO is used here to confirm the absence of S-containing ligands and the cleanliness of exposed Au surfaces. CO is used as the titrant of Au surface atoms, instead of O_2 or H_2, because the latter dissociate very slowly at the low temperatures required for monolayer coverages [42]. Figure 6.6 shows infrared spectra for chemisorbed CO (at 263 K, 1 kPa CO) on Au/TS-1 ($\langle d_{TEM} \rangle$=3.8 nm; 0.9% wt. Au; DI 1.11) and Au/SiO_2 ($\langle d_{TEM} \rangle$=2.7 nm; 2.2% wt.; DI 1.06; prepared by deposition-precipitation). The intensities of the CO infrared bands are normalized by the number of surface Au atoms in each sample. Previous studies have shown that the deposition-precipitation method used to prepare Au/SiO_2 forms Au surfaces free of synthetic debris, and that Au surfaces are at or near saturation coverage with CO at the conditions of the IR measurement (263 K, 1 kPa CO; [23]).

Au/TS-1 and Au/SiO_2 show absorption bands (at ~2110 cm^{-1}) for the carbonyl stretch vibrations of CO bound on Au^0 surfaces [43]. The number of exposed and accessible Au atoms present in these two samples can be quantitatively compared by calculating a quantity Ω, defined as:

$$\Omega = \frac{\tilde{I}_{\mathrm{Au/TS-1}}}{\tilde{I}_{\mathrm{Au/SiO_2}}} \qquad (4)$$

where $\tilde{I}_{\mathrm{Au/TS-1}}$ and $\tilde{I}_{\mathrm{Au/SiO_2}}$ are the integrated Au-CO band intensities (normalized by the number of surface Au atoms) for Au/TS-1 and Au/SiO_2, respectively, at each CO pressure. The value of $\tilde{I}_{\mathrm{Au/SiO_2}}$ is used as a reference because Au surfaces in Au/SiO_2 are known to be accessible and free of contaminants [23]. As a result, a Ω value at or near unity would be an indication that the Au surfaces in Au/TS-1 are also accessible and free of synthetic debris derived from the protective MPS ligands or other species. The calculated values of Ω (0.84-0.97) are near unity at all pressures (0.1-1.0 kPa CO), indicating that the post-synthetic thermal treatments applied to Au/TS-1 (Section 6.2.3) are effective at removing organic moieties from the Au metal surfaces that ultimately form. These results therefore indicate that the Au nanoparticles in Au/TS-1, visible in election micrographs (Figure 6.6), are accessible and free of surface contamination.

6.3.2.3 Characterization of Ti species using infrared and UV-visible spectra

Isolated tetrahedral Ti atoms in the TS-1 framework are considered the most active and desirable structures for alkene epoxidation [8,11,12]. The predominant presence of Ti species within Au/TS-1 samples as tetrahedrally coordinated atoms integrated into the framework would indicate that the synthetic and post-synthetic treatment procedures (Section 6.2.2-6.2.3) used to prepare such samples do not adversely affect Ti incorporation relative to established TS-1 synthesis protocols [29]. In this section, we present the characterization of Ti species present in post-synthetically treated Au/TS-1 using IR and UV-vis spectroscopy.

The presence of tetrahedrally coordinated Ti-centers in TS-1 frameworks was confirmed from IR framework vibrations at 960 cm^{-1} and 800 cm^{-1} [44]. The feature at 960 cm^{-1} is thought to correspond to Si-O vibrations associated with Si atoms near framework Ti [44], and is indicative of the successful incorporation of Ti into the framework. The intensity of this band relative to the reference absorption band at 800 cm^{-1} (characteristic of the MFI framework [44]) provides an indication of the Ti content of TS-1. The ratios of absorption band intensities at 960 cm^{-1} and 800 cm^{-1} are expected to be similar for the standard TS-1 sample (crystallized at 448 K for 48 h; Si/Ti = 78, measured by ICP-OES) and the Au/TS-1 samples (for 0.2% wt. Au sample: Si/Ti = 74; 0.9% wt. Au sample: Si/Ti = 76) if Ti incorporation into the frameworks of Au/TS-1 samples is minimally impacted by the relatively low synthesis temperature (393 K), protracted crystallization time (120 h), seed crystals, and ligated Au^{3+} complexes used in the synthesis procedure (Section 6.2.2). IR spectra of the TS-1 standard and Au/TS-1 samples are shown in Figure 6.7. The ratio of adsorption bands at 960 cm^{-1} and 800 cm^{-1} was only slightly greater for TS-1 (1.17) than Au/TS-1 (1.08 and 1.06 for 0.2% wt. and 0.9% wt. Au samples, respectively), consistent with the predominant uptake of Ti into Au/TS-1. The calculated absorption band ratios (TS-1: 1.17; Au/TS-1: 1.06-1.08) are roughly consistent with values reported in the literature for TS-1 frameworks with low Ti content (absorption band ratio of 1.50 for Si/Ti ratio of 53.5) [44].

UV-vis spectra were acquired on post-synthetically treated TS-1 and Au/TS-1 in order to probe the coordination environment of Ti species in these samples. TS-1 and Au/TS-1 were treated in He (1.67 cm^3 g^{-1} s^{-1}) at 623 K for 1 h within the UV-vis cell prior to spectral acquisition at ambient temperature in a He atmosphere (Section 6.2.4). The thermal treatment in He was applied to the samples in order to remove water, which can potentially interact with tetrahedrally coordinated (framework) Ti in order to form complexes that absorb light within the range (250-300 nm; [7]) that is also typical of Ti species present in an amorphous oxide (~270 nm; [45]). H_2O_2 or hydroperoxy species generated on Au surfaces, which can form in the presence of H_2O and O_2 alone [10], may also interact with nearby framework Ti sites to form Ti-OOH complexes that give a broad absorption band at a frequency (~340 nm; [7]) that is similar to that of anatase TiO_2 (320 nm; [45]). As a result, it is important to remove water in order to decrease ambiguity in the interpretation of the UV-vis spectra of TS-1 and Au/TS-1; such spectra are shown in Figure 6.8.

The spectra of the TS-1 standard and Au/TS-1 (0.2% wt. Au) background-corrected with the spectrum of silicalite-1 (synthesized identically to TS-1 but without the addition of Ti precursors) both showed a sharp absorption band at 220-230 nm corresponding to tetrahedrally coordinated framework Ti species [15]. The absence of significant absorbance between 270-330 nm in the spectrum of TS-1 reflects the substantive absence of any extra-framework Ti species [18,45]. The spectrum of Au/TS-1 with 0.2% wt. Au gave a second absorption feature of moderate intensity at ~520 nm reflecting the localized surface plasmon resonance of Au nanoparticles [46]. The spectrum of Au/TS-1 (with silicalite-1 or $BaSO_4$ as the background) with higher loading (0.9% wt. Au) is dominated by an intense plasmon absorption band at ~520 nm and accompanying background absorbance between 250-600 nm that obscures any low-intensity peaks corresponding to Ti species within the relevant wavelength range (220-330 nm). The prominence of these absorbance features can be attributed to the relatively high Au content of the sample (0.9% wt.) in tandem with the possible interaction of Au surface plasmons with adjacent species (e.g., Si, Ti, or impurities) that are weak absorbers of ~250-600 nm light, which can greatly enhance the rate of extinction of such absorbers [47] and thus lead to more intense background features in the spectrum. Absorption bands resulting from Ti species in Au/TS-1 with 0.9% wt. Au loading were isolated by using the absorbance spectrum of an Au/silicalite-1 sample (synthesized and post-synthetically treated with identical procedures and Au loading as Au/TS-1, but without the addition of Ti precursors; Section 6.2.2) to background-correct the spectrum for Au/TS-1. The application of this reference spectrum to Au/TS-1 removes most of the background and plasmon resonance absorption and leads to the clear emergence of an absorption feature at 220-230 nm corresponding to framework Ti.

The Au/TS-1 samples with 0.2% and 0.9% wt. Au loading each showed a weak absorption feature near ~270 nm, indicating the presence of a small fraction of amorphous Ti [45]. Such amorphous species may correspond to Ti defect sites within the TS-1 framework, which could form as a result of interruptions in the framework periodicity imposed by the attachment of MPS ligands to nucleating titanosilicates, or from the generation of local framework defects by the agglomeration and growth of Au nanoparticles during post-synthetic treatment. The prevalence of these defect or extra-framework Ti species, however, is small relative to tetrahedrally coordinated Ti incorporated into TS-1, as indicated by the relative magnitude of the bands at ~225 and 270 nm and independently corroborated by IR experiments (Figure 6.7).

6.3.2.4 Estimation of the encapsulation selectivity of Au nanoparticles within TS-1 by titration of extracrystalline Au surfaces with dibenzothiophene

Metal nanoparticles confined within microporous zeotypes are protected from contact by certain reactant and poison molecules that are too large to enter narrow framework apertures [22-27]. The microporous framework windows and cavities can also stabilize transition states and enhance the selectivity of specific reactions by retaining large products until they can transform into species small enough to traverse the zeotype pores. These shape-selective effects are mediated by the dimensions and morphology of the apertures and cavities of a specific zeotype material [22-27]. Such effects are utilized in this work to estimate the selectivity of Au encapsulation within TS-1 by measuring the oxidative dehydrogenation (ODH) rate of ethanol (EtOH; 0.40 nm kinetic diameter [23]) on Au/TS-1 and Au/SiO_2 catalysts deliberately poisoned with a bulky organosulfur molecule (dibenzothiophene; DBT; 0.9 nm kinetic diameter [23]). DBT strongly attaches to and deactivates Au surfaces which it can access [23]; as a result, EtOH turnover rates on exposed Au nanoparticles supported on mesoporous SiO_2 or external TS-1 crystal surfaces should substantially decrease upon treatment with DBT, while Au surfaces shielded by TS-1 framework apertures (0.55 nm [39]) should be protected from contact with DBT and retain their ODH activity. Changes in the ODH rates on Au/TS-1 and Au/SiO_2 conferred by exposure to DBT can therefore be evaluated to estimate the fraction of Au surfaces present within Au/TS-1 that reside within intracrystalline microporous regions.

EtOH ODH rates (Section 6.2.5.1) were measured for DBT-treated samples ($r_{ODH,DBT}$) and control samples (r_{ODH}) and used to calculate inhibition factors (λ), defined as:

$$\lambda_{DBT,i} = \frac{r_{ODH,DBT}}{r_{ODH}} \qquad (5)$$

where i denotes the specific sample (Au/TS-1, Au/SiO_2). The value $\lambda_{DBT,Au/SiO2}$ is equivalent to the fraction of DBT-accessible Au surfaces that are fully deactivated by ex-situ exposure to DBT, because Au surfaces in Au/SiO_2 are not confined within zeotype crystals and should be fully accessible to DBT. DBT is expected to have limited or no access to Au surfaces residing within TS-1 crystallites because the size of DBT (0.9 nm kinetic diameter [38]) relative to the aperture size of TS-1 (0.55 nm [39]) sterically precludes facile diffusion of DBT within narrow microporous channels. A fraction of even DBT-accessible Au surfaces in Au/SiO_2 and Au/TS-1 are expected to remain active after DBT treatment because steric repulsion by bulky DBT molecules on Au surfaces prevents full monolayer coverage of Au atoms by the DBT titrants [23]. This phenomenon would result in extra-crystalline Au nanoparticles in Au/TS-1 samples retaining a fraction of their activity for EtOH ODH even after DBT treatment, leading to $\lambda_{DBT,Au/TS-1}$ values that do not precisely reflect the fraction of encapsulated Au surfaces. This partial deactivation of accessible Au surfaces by DBT can be corrected to arrive at a more accurate estimate for the encapsulation selectivity of Au nanoparticles within Au/TS-1 (F), which is defined as:

$$F = \lambda_{DBT,Au/TS-1} - \lambda_{DBT,Au/SiO2}\frac{\left(1-\lambda_{DBT,Au/TS-1}\right)}{\left(1-\lambda_{DBT,Au/SiO2}\right)} \qquad (6)$$

The second collection of terms in Equation 6 corrects for the residual EtOH ODH activity on extracrystalline Au surfaces that remains after exposure to DBT, thereby precluding ODH turnover events occurring on non-encapsulated surfaces from counting as turnover events on encapsulated Au surfaces, which would have the effect of inflating the encapsulation selectivity. EtOH ODH rates, inhibition factors, and the Au encapsulation selectivity for Au/TS-1 (0.9% wt. Au) are shown in Table 6.2.

The calculated encapsulation selectivity for Au/TS-1 with 0.9% wt. Au (0.96; Table 6.2) confirms that the overwhelming majority of Au nanoparticles were successfully encapsulated. The values of $\lambda_{DBT,Au/TS-1}$ and F (0.96) were identical at a precision of two significant figures because the correction applied to the inhibition factor by Equation 6 had a minimal impact. This minimal impact can be attributed to the relatively small activity on unprotected Au surfaces that persists (~11%) after treatment with DBT. The EtOH ODH rate on Au/TS-1 (10×10^{-3} s^{-1}) was slightly lower than on Au/SiO_2 (12×10^{-3} s^{-1}), which likely reflects slight diffusional limitations on the rate in Au/TS-1. Such diffusional constraints would lead Equation 6 to underestimate the true encapsulation selectivity, because rates on the small fraction of extracrystalline Au nanoparticles reflect their inherent activity at the reactant concentrations present in the surrounding fluid phase (9 kPa O_2, 4 kPa EtOH). Encapsulated Au nanoparticles, by contrast, would be exposed to lower reactant concentrations, and thus give lower turnover rates, because of the presence of reactant concentration gradients imposed by diffusional barriers.

These data, taken together with the spectroscopic and other characterization techniques presented in Sections 6.3.2.1-6.3.2.3, suggest that the synthetic strategy outlined in Section 6.3.1 was successful at preparing Au nanoparticles confined within TS-1 crystallites. TEM (Figure 6.5) and IR (Figure 6.6) results indicate that Au nanoparticles are small, uniformly dispersed, and free of synthetic debris following post-synthetic treatments. Such nanoparticles, despite being larger (3.8 nm) than the TS-1 channel intersections (0.55 nm [39]), reside predominantly (>96%) within zeotype crystallites, as indicated by their significant shape-selectivty during catalysis. The relatively low crystallization temperature (393 K), prolonged crystallization time (120 h), and seed crystals (10% wt.) required to assemble Au/TS-1 without decomposing Au-MPS precursors did not result in significant adverse effects on framework crystallinity (Figure 6.4; XRD), micropore volume (Section 6.S3, SI), or Ti incorporation (IR, Figure 6.7) relative to TS-1 crystallized at established conditions (448 K; 48 h).

The Au/TS-1 systems prepared in this work have potential applications as alternatives to existing Au/Ti-oxide catalysts for propylene epoxidation reactions, which could benefit from the close proximity between Au and Ti domains present in Au/TS-1. The Au/TS-1 catalysts could similarly be applied for the epoxidation of other substrates able to enter the pores of the TS-1 framework, including butylene and cyclohexene. Such epoxidation reactions could be carried out with either H_2/O_2 or H_2O/O_2 gas-phase mixtures to take advantage of the ability of the small encapsulated Au nanoparticles to generate hydroperoxo or H_2O_2 species in-situ. The synthesis approach devised to encapsulate Au nanoparticles within TS-1 while avoiding premature decomposition of ligated precursors could analogously be applied to other high-Si frameworks such as silicalite-1 or ZSM-48 which, like TS-1, are generally crystallized at elevated temperatures (443-448 K; [44,48]) that promote the decomposition of metal coordination compounds. A variety of metal cation species that can attach to the thiol moieties of MPS (e.g., Pt^{2+}, Pd^{2+}, Ag^{+}, Ir^{4+}) could

be added in lieu of the Au^{3+} species used in the synthesis procedure described in this work in order to prepare encapsulated nanoparticles of these metals within TS-1 or other zeotypes. Two different metal cation precursors could also be added to the synthesis gel in order to form encapsulated bimetallic nanoparticles within TS-1. AuPd bimetallic nanoparticles encapsulated within TS-1 would be of particular interest for use as epoxidation catalysts, because such metal mixtures have been found to be more effective for H_2O_2 formation than their monometallic Au or Pd counterparts and, more generally, are amongst the most active catalysts examined to date for the direct synthesis of H_2O_2 [21,49].

6.4 Conclusion

Au nanoparticles, small and monodisperse in size, were encapsulated within TS-1 frameworks via the hydrothermal assembly of TS-1 synthesis gels containing MPS-protected Au^{3+} cations. Significant modifications to established crystallization procedures for TS-1 were required in order to prevent the premature decomposition of Au^{3+} coordination compounds within the synthesis gels without adversely affecting the crystallinity of the TS-1 frameworks formed. Such modifications included the use of a lower crystallization temperature, a longer crystallization time, and the incorporation of TS-1 seed crystals into the synthesis gels. The application of these modified procedures leads to the assembly of crystalline TS-1 with ligated Au^{3+} species occluded in TS-1 micropores; subsequent thermal treatments involving gradual heating in an oxidative environment result in the formation of clean Au nanoparticles selectively encapsulated within TS-1 crystallites. The synthetic procedures outlined in this work provide guiding principles for the encapsulation of metal species within high-Si zeotype frameworks, which typically require high crystallization temperatures that strongly promote the premature decomposition of ligated metal precursors incorporated into synthesis gels. The specific Au/TS-1 system prepared here, or modified versions thereof, also has potential applications as a propylene epoxidation catalyst that improves upon existing catalysts by decreasing the average distance between Au and Ti domains required for propylene epoxidation.

6.5 Figures and Tables

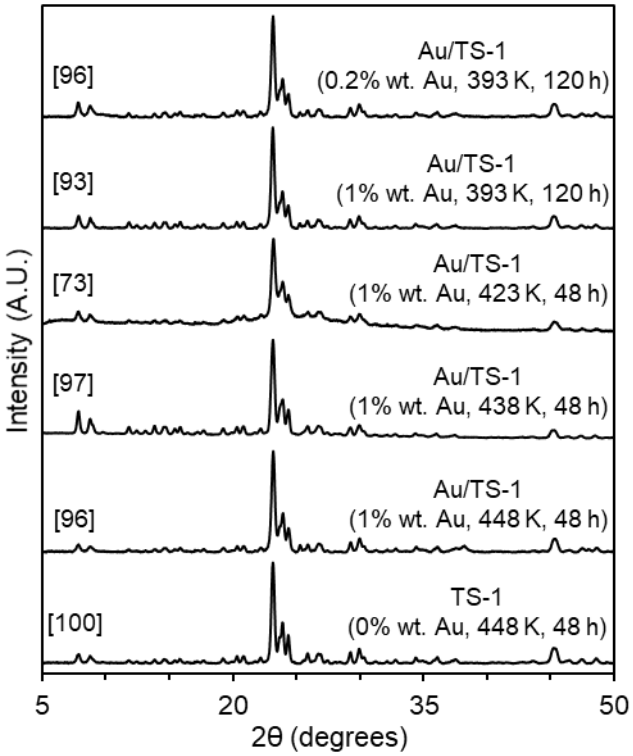

Figure 6.1 X-Ray diffractograms of as-synthesized TS-1 crystallized at 448 K for 48 h, and Au/TS-1 (0.2-1% wt. nominal Au loading) crystallized at 448 K for 48 h, 438 K for 48 h, 423 K for 48 h, and 393 K for 120 h. The Au/TS-1 sample with 0.2% wt. Au loading was crystallized in the presence of 10% wt. TS-1 seed crystals. Framework crystallinities (%) relative to the TS-1 standard are shown in brackets.

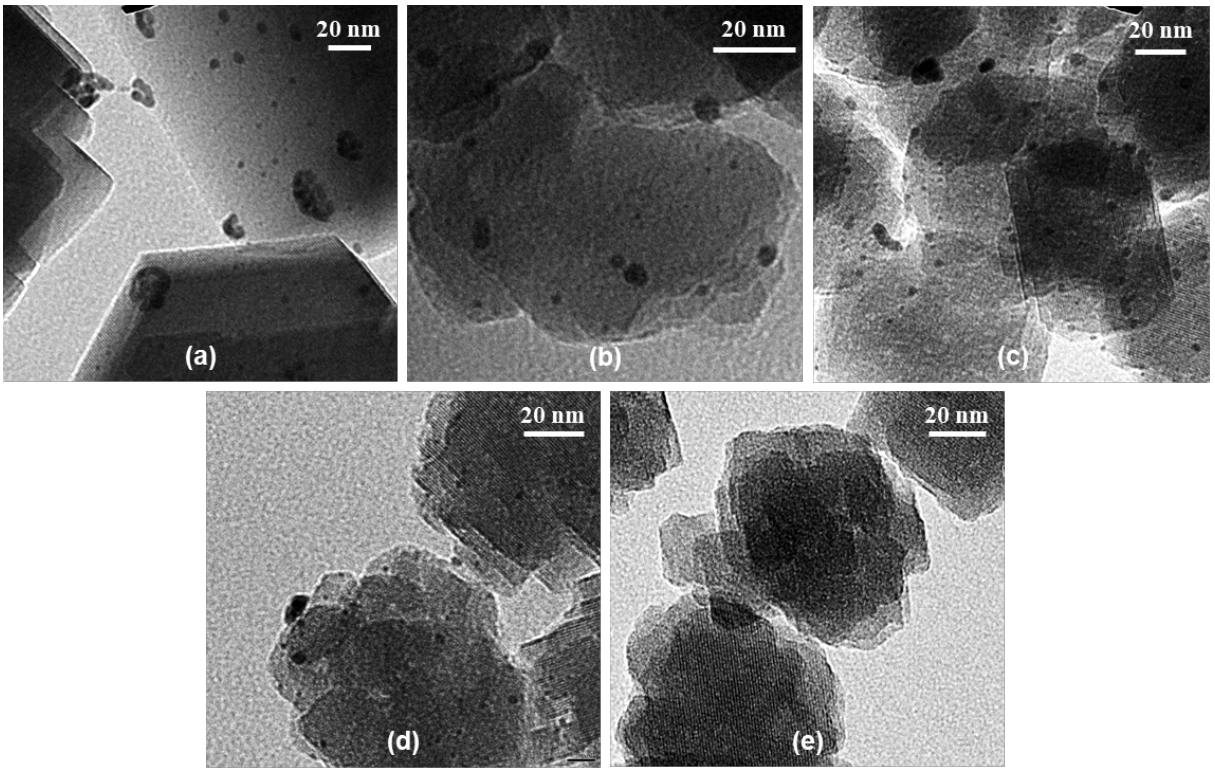

Figure 6.2 Transmission electron micrographs of as-synthesized Au/TS-1 crystallized with 1% wt. nominal Au loading and without seed crystals at (a) 448 K for 48 h, (b) 438 K for 48 h, (c) 423 K for 48 h, (d) 413 K for 120 h, and (e) 393 K for 120 h.

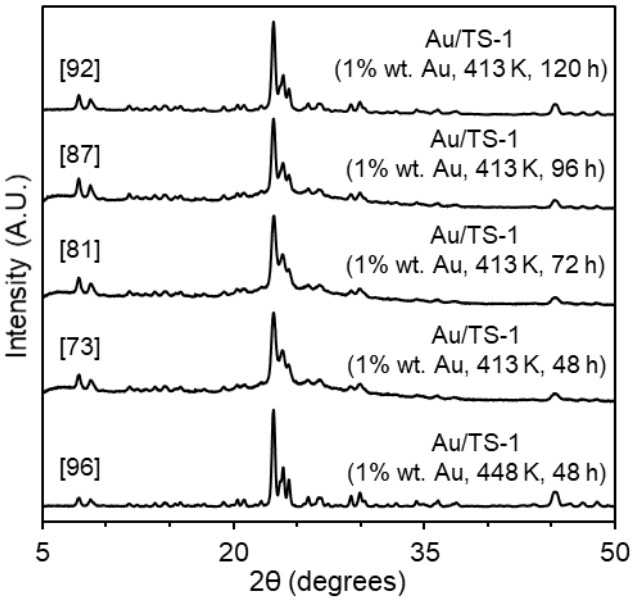

Figure 6.3 X-Ray diffractograms of as-synthesized Au/TS-1 (1% wt. nominal Au loading) crystallized without seed crystals at 448 K for 48 h, and at 413 K for 48 h, 72 h, 96 h, and 120 h. TS-1 framework crystallinities (%) relative to an Au-free TS-1 standard are shown in brackets.

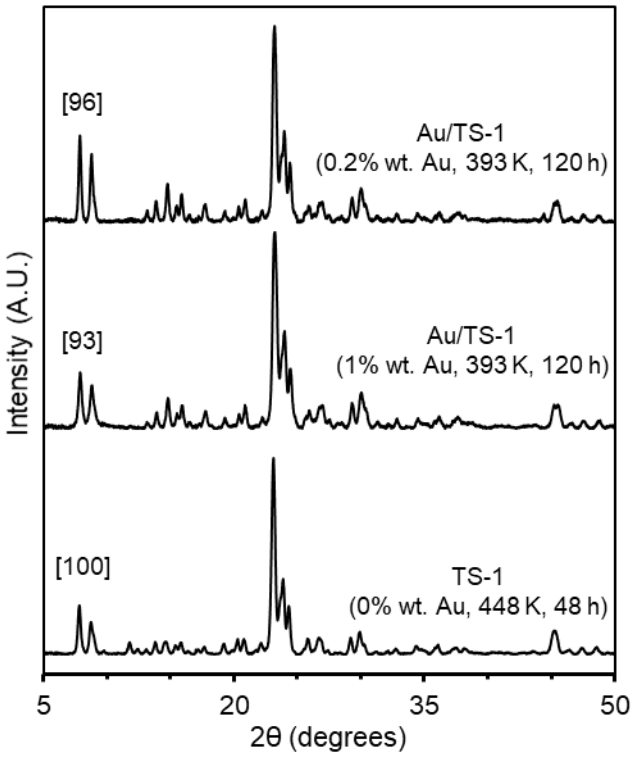

Figure 6.4 X-Ray diffractograms of TS-1 crystallized at 448 K for 48 h and post-synthetically treated in flowing dry air (1.67 cm^3 g^{-1} s^{-1}) at 823 K for 4 h, and Au/TS-1 crystallized at 393 K for 120 h in the presence of 10% wt. seed crystals with 0.2-1% wt. nominal Au loading, and post-synthetically treated in air and H_2 with staged thermal ramping procedures (Section 6.2.3). TS-1 framework crystallinities (%) relative to the TS-1 standard are shown in brackets.

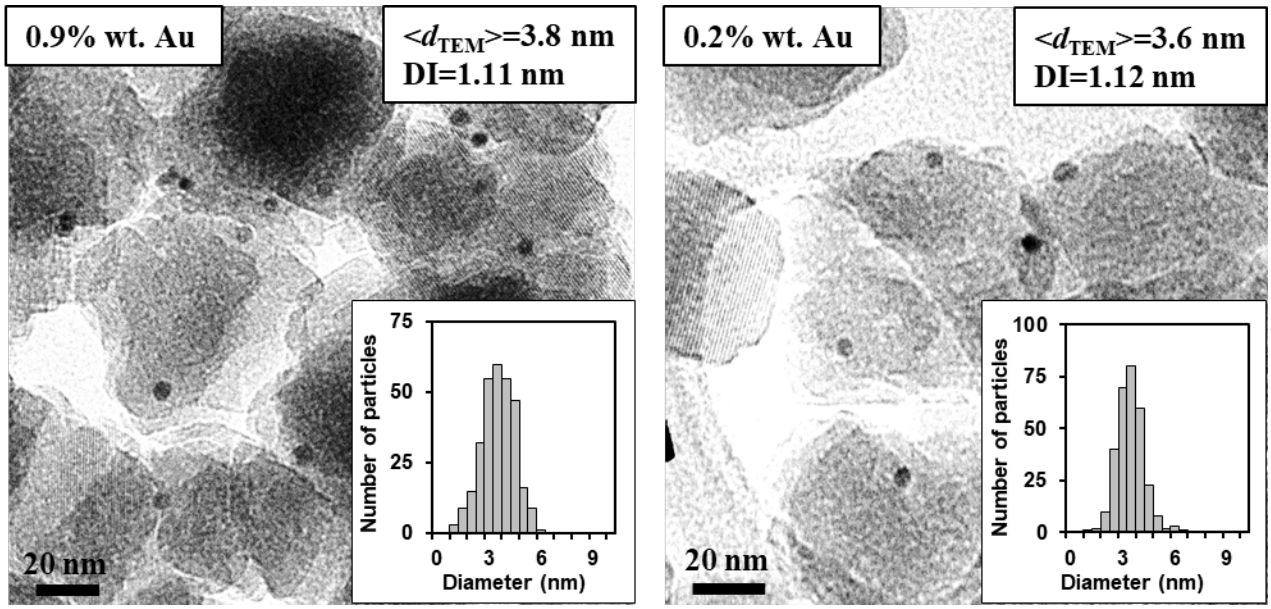

Figure 6.5 Transmission electron micrographs, surface-averaged nanoparticle diameters ($\langle d_{TEM} \rangle$, Eq. 1), particle dispersity indexes (DI, Eq. 3), and nanoparticle diameter distributions for post-synthetically treated Au/TS-1 (0.2-1.0% wt. nominal Au loading) crystallized at 393 K for 120 h with 10% wt. seed crystals.

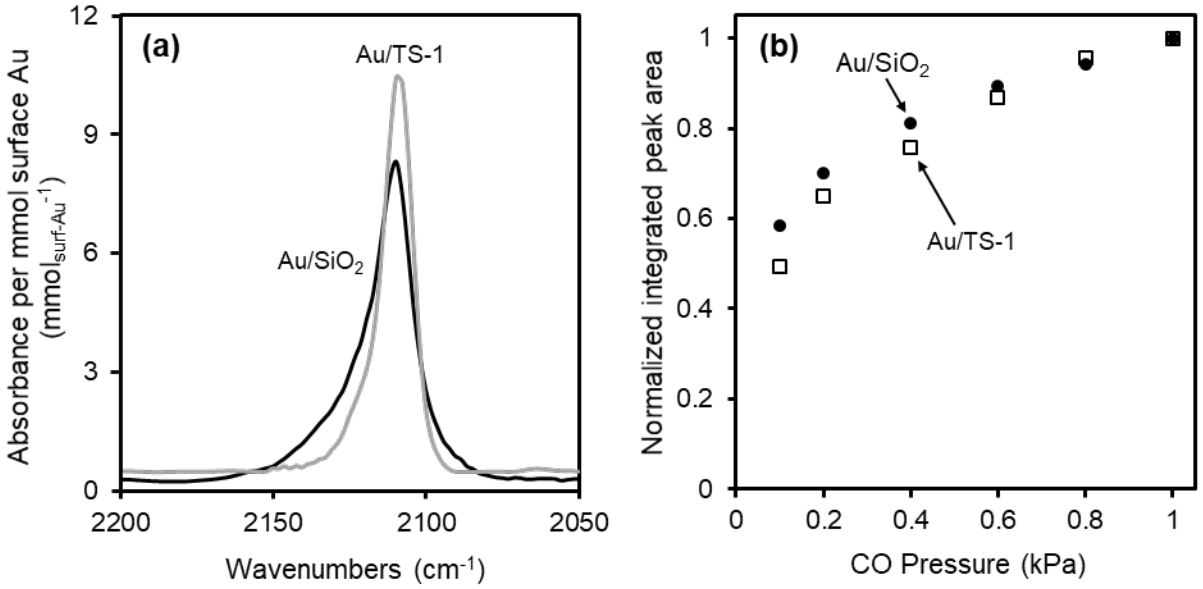

Figure 6.6 (a) Infrared spectra of CO adsorbed on Au nanoparticles in Au/SiO_2 (black) and Au/TS-1 (0.9% wt. Au, gray) samples at 263 K (1.0 kPa CO, 99.0 kPa He) after flowing He pretreatment (473 K, 1 h). Intensities are normalized by the moles of surface Au atoms in each sample. (b) Integrated absorption band area of Au/SiO_2 (●) and Au/TS-1 (0.9% wt. Au, □) at 0.1-1.0 kPa CO and 263 K. Absorption band areas are normalized by the maximum area (collected at 1.0 kPa CO) for each sample.

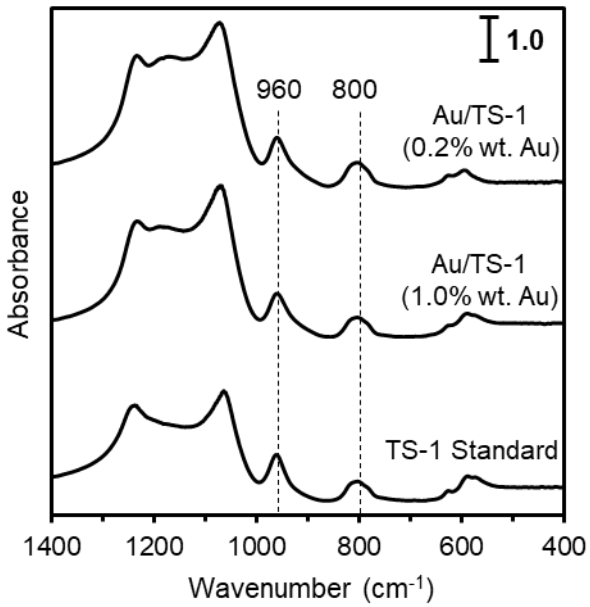

Figure 6.7 IR spectra of post-synthetically treated TS-1 and Au/TS-1 (with 1.0% wt. and 0.2% wt. nominal Au loading) in a He atmosphere at ambient temperature.

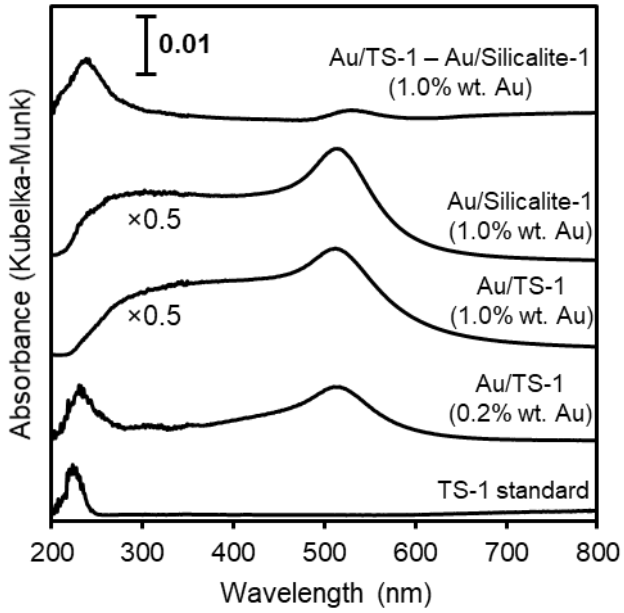

Figure 6.8 UV-vis spectra of post-synthetically treated TS-1, Au/TS-1 (with 0.2% wt. and 1.0% wt. nominal Au loading), and Au/silicalite-1 (1.0% wt. nominal Au loading) in a He atmosphere at ambient temperature. Also shown is the difference spectra resulting from the background correction of the absorbance spectrum of Au/TS-1 with the spectrum of Au/silicalite-1 (both with 1.0% wt. nominal Au loading). $BaSO_4$ is the reference spectrum used for Au/TS-1 and Au/silicalite-1 with 1.0% wt. nominal Au loading. The spectra of TS-1 and Au/TS-1 with 0.2% wt. nominal Au loading were background corrected using silicalite-1 synthesized, crystallized, and post-synthetically treated at conditions identical to those used for TS-1 but without the addition of Ti precursors to the synthesis gel. Samples were treated in He (1.67 $cm^3\ g^{-1}\ s^{-1}$) at 623 K for 1 h prior to spectral acquisition.

Table 6.1 Crystallization temperature, crystallization time, presence of TS-1 seed crystals, stability of ligand-protected Au^{3+} cations, solid yields, and crystallinity of solid products for Au/TS-1 syntheses with 1% wt. nominal Au loading.

Crystallization Temperature (K)[a]	Crystallization Time (h)[b]	% wt. added seed crystals[c]	Au Precursor Stability[d]	% Solid Yield[e]	% Product Crystallinity[f]
448	48	0	Unstable	97	96
438	48	0	Unstable	98	97
423	48	0	Unstable	90	73
413	48	0	Unstable	44	73
413	120	0	Unstable	75	92
393	120	0	Stable	65	93
393	120	10	Stable	85	94

[a]Temperature of synthesis gel during hydrothermal assembly. [b]Duration of hydrothermal assembly. [c]Seed crystals consist of as-synthesized TS-1 crystallized at 448 K for 48 h; % wt. added seeds is based on the yield of TS-1 synthesized at 448 K for 48 h (5.48 g; Section 6.2.2). [d]The presence of Au agglomerates visible in electron micrographs of as-synthesized Au/TS-1 indicates that Au^{3+}-MPS precursors are unstable at the crystallization conditions. [e]Solid product yields are normalized by the yield of TS-1 synthesized at established conditions (448 K; 48 h; 5.48 g; Section 6.2.2) plus the additional weight of any added seed crystals. [f]Calculated from XRD using the integrated intensities of the three most intense diffraction lines, with TS-1 crystallized at 448 K for 48 h as a standard (Section 6.2.2).

Table 6.2 Ethanol ODH turnover rates, inhibition factors, and encapsulation selectivities of Au/TS-1 and Au/SiO_2 samples.

Sample	r_{ODH} (10^{-3} s^{-1} $mol_{surf\text{-}Au}^{-1}$)[a]	Inhibition Factor (λ)[b]	Encapsulation Selectivity (F)[c]
Au/TS-1	10	0.96	0.96
Au/SiO_2	12	0.11	0

[a]EtOH ODH turnover rates of samples agitated in liquid EtOH (300 cm^3 g^{-1}) at ambient temperature for 4 h and then used in reaction (9 kPa O_2, 4 kPa EtOH, and 0.5 kPa H_2O) at 393 K. Turnover rates are defined as the moles of EtOH converted per unit time normalized by the number of exposed metal surface atoms estimated from particle dispersions (Eq. 2).
[b]$r_{ODH,DBT}/r_{ODH}$ (Eq. 5), where $r_{ODH,DBT}$ are EtOH ODH rates measured on similarly treated samples but with DBT dissolved in the EtOH to achieve a 6:1 molar ratio of DBT to Au.
[c]Encapsulation selectivity, defined as the fraction of active Au surface area encapsulated within zeotype crystallites, as estimated from λ values (Eq. 6).

6.6 References

[1] Abad, A.; Corma, A.; García, H. *Chem. Eur. J.* **2008**, *14*, 212-222.
[2] Mallat, T.; Baiker, A. *Chem. Rev.* **2004**, *104*, 3037-3058.
[3] Hutchings, G. J. *Chem. Commun.* **2008**, 1148-1164.
[4] Hayashi, T.; Tanaka, K.; Haruta, M. *J. Catal*. **1998**, *178*, 566-575.
[5] Bravo-Suarez, J. J.; Lu, J.; Dallos, C. G.; Fujitani, T.; Oyama, S. T. *J. Phys. Chem. C* **2007**, *111*, 17427-17436.
[6] Nijhuis, T. A. R.; Visser, T.; Weckhuysen, B. M. *Angew. Chem., Int. Ed*. **2005**, *44*, 1115-1118.
[7] Chowdhury, B.; Bravo-Suarez, J. J.; Mimura, N.; Bando, K. K.; Tsubota, S.; Haruta, M. *J. Phys. Chem. B* **2006**, *110*, 22995-22999.
[8] Farrusseng, D.; Tuel, A. *New J. Chem*. **2016**, *40*, 3933-3949.
[9] Kanungo, S.; Perez Ferrandez, D. M.; d'Angelo, F. N.; Schouten, J. C.; Nijhuis, T. A. *J. Catal.* **2016**, *338*, 284-294.
[10] Ojeda, M.; Iglesia, E. *Chem. Commun.* **2009**, *3*, 352-354.
[11] Perez Ferrandez, D. M.; Fernandez, I. H.; Teley, M. P. G.; de Croon, M. H. J. M.; Schouten, J. C.; Nijhuis, T. A. *J. Catal*. **2015**, *330*, 396-405.
[12] Huang, J.; Akita, T.; Faye, J.; Fujitani, T.; Takei, T.; Haruta, M. *Angew. Chem. Int. Ed*. **2009**, *48*, 7862-7866.
[13] Taylor, B.; Lauterbach, J.; Delgass, W. N. *Catal. Today* **2007**, *123*, 50-58.
[14] Lee, W.-S.; Akatay, M. C.; Stach, E. A.; Ribeiro, F. H.; Delgass, W. N. *J. Catal*. **2012**, *287*, 178-189.
[15] Lee, W.-S.; Lai, L.-C.; Akatay, M. C.; Stach, E. A.; Ribeiro, F. H.; Delgass, W. N. *J. Catal*. **2012**, *296*, 31-42.
[16] Lee, W.-S.; Akatay, M. C.; Stach, E. A.; Ribeiro, F.; Delgass, W. N. *J. Catal*. **2013**, *308*, 98-113.
[17] Joshi, A. M.; Delgass, W. N.; Thomson, K. T. *J. Phys. Chem. C* **2007**, *111*, 7841-7844.
[18] Li, Z.; Zhang, J.; Wang, D.; Ma, W.; Zhong, Q. *J. Phys. Chem. C* **2017**, *121*, 25215-2522.
[19] Lu, J.; Zhang, X.; Bravo-Suárez, J. J.; Fujitani, T.; Oyama, S. T. *Catal. Today* **2009**, *147*, 186-195.
[20] Huang, J.; Takei, T.; Akita, T.; Ohashi, H.; Haruta, M. *Appl. Catal. B* **2010**, *95*, 430-438.
[21] Moreno, I.; Dummer, N. F.; Edwards, J. K.; Alhumaimess, M.; Sankar, M.; Sanz, R.; Pizarro, P.; Serrano, D. P.; Hutchings, G. J. *Catal. Sci. Technol*. **2013**, *3*, 2425-2434.
[22] Ryoo, R.; Cho, S. J.; Pak, C.; Kim, J. G.; Ihm, S. K.; Lee, J. Y. *J. Am. Chem. Soc*. **1992**, *114*, 76-82.
[23] Otto, T.; Zones, S. I.; Iglesia, E. *J. Catal*. **2016**, *339*, 195-208.
[24] Otto, T.; Ramallo-Lopez, J. M.; Giovanetti, L. J.; Requejo, F. G.; Zones, S. I.; Iglesia, E. *J. Catal*. **2016**, *342*, 125-137.
[25] Choi, M.; Wu, Z.; Iglesia, E. *J. Am. Chem. Soc*. **2010**, *132*, 9129-9137.
[26] Otto, T.; Zones, S. I.; Iglesia, E. *Microporous Mesoporous Mater*. **2018**, *270*, 10-23.
[27] Goel, S.; Wu, Z.; Zones, S. I.; Iglesia, E. *J. Am. Chem. Soc*. **2012**, *134*, 17688-17695.
[28] Moliner, M.; Gabay, J. E.; Kliewer, C. E.; Carr, R. T.; Guzman, J.; Casty, G. L.; Serna, P.; Corma, A. *J. Am. Chem. Soc*. **2016**, *138*, 15743-15750.
[29] van der Pol, A.J.H.P.; van Hooff, J.H.C. *Appl. Catal. A* **1992**, *92*, 93-111.
[30] Wang, M.; Zhou, J.; Mao, G.; Zheng, X. *Ind. Eng. Chem. Res*. **2012**, *51*, 12730-12738.
[31] Otto, T.; Zones, S. I.; Hong, Y.; Iglesia, E. *J. Catal*. **2017**, *356*, 173-185.

[32] Wu, Z.; Goel, S.; Choi, M.; Iglesia, E. *J. Catal*. **2014**, *311*, 458-468.
[33] Bratsch, S. G. *J. Phys. Chem. Ref. Data* **1989**, *18*, 1-21.
[34] Bergeret, G.; Gallezot, P. In Handbook of Heterogeneous Catalysis; Ertl, G., Knozinger, H., Schuth, F., Weitkamp, J., Eds.; Wiley-VHC: Weinheim, Germany, 2008; pp 738-765.
[35] Luo, W.; Sankar, M.; Beale, A. M.; He, Q.; Kiely, C. J.; Bruijnincx, P. C. A.; Weckhuysen, B. M. *Nat. Commun.* **2014**, *6*, 1-10.
[36] Burevski, D. *Colloid Polym. Sci.* **1982**, *260*, 623-627.
[37] García-Martinez, J.; Cazorla-Amorós, D.; Linares-Solano, A. *Stud. Surf. Sci. Catal.* **2000**, *128*, 485-494.
[38] Van de Voorde, B.; Hezinova, M.; Lannoeye, J.; Vandekerkhove, A.; Marszalek, B.; Gil, B.; Beurroies, I.; Nachtiqall, P.; De Vos, D. *Phys. Chem. Chem. Phys.* **2015**, *17*, 10759-10766.
[39] C.M. Baerlocher, Database of Zeolite Structures. http://www.iza-structure.org/databases/, 2017 (accessed February 2018).
[40] Nakagawa, Y.; Dartt, C. Pure Phase Titanium-Containing Zeolite Having MEL Structure, Process for Preparing same, and Oxidation Processes using same as Catalyst. U.S. Patent 5,968,474, Oct 19, 1999.
[41] Goel, S.; Zones, S. I.; Iglesia, E. *Chem. Mater*. **2015**, *27*, 2056-2066.
[42] Carabineiro, A. A. C.; Nieuwenhuys, B. E.; *Gold Bull*. **2009**, *42*, 288-301.
[43] Venkov, T.; Fajerwerg, K.; Delannoy, L.; Klimev, H.; Hadjiivanov, K.; Louis, C. *Appl. Catal., A* **2006**, *301*, 106-114.
[44] Dartt, C. B.; Khouw, C. B.; Li, H.-X.; Davis, M. E. *Microporous Mater*. **1994**, *2*, 425-437.
[45] Xiong, G.; Jia, Q.; Cao, Y.; Liu, L.; Guo, Z. *RSC Adv*. **2017**, *7*, 24046-24054.
[46] Peng, S.; McMahon, J. M.; Schatz, G. C.; Gray, S. K.; Sun, Y. *Proc. Natl. Acad. Sci. U.S.A.* **2010**, *107*, 14530-14534.
[47] Chavez, S.; Rao, V. G.; Linic, S. *Faraday Discuss*. **2018**, DOI: 10.1039/C8FD00143J.
[48] Crea, F.; Nastro, A.; Nagy, J. B.; Aiello, R. *Zeolites* **1988**, *8*, 262-267.
[49] Pritchard, J.; Kesavan, L.; Piccinini, M.; He, Q.; Tiruvalam, R.; Dimitratos, N.; Lopez-Sanchez, J. A.; Carley, A. F.; Edwards, J. K.; Kiely, C. J.; Hutchings, G. J. *Langmuir* **2010**, *26*, 16568-16577.

6.7 Supporting Information

Contents

6.S1. Heating procedure used for the post-synthetic oxidative treatment of Au/TS-1

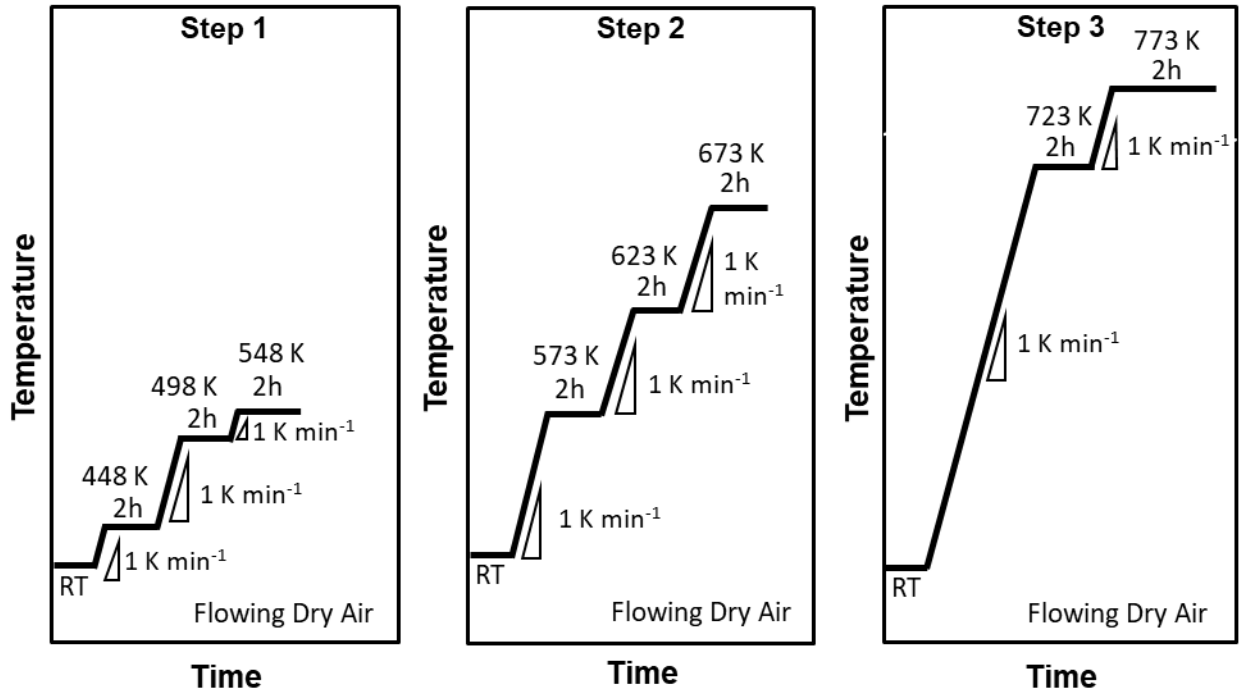

Figure 6.S1. Heating procedure used for the post-synthetic oxidative treatment of as-synthesized Au/TS-1. Samples were heated in flowing dry air (1.67 cm^3 g^{-1} s^{-1}).

6.S2. Sample electron micrograph of as-synthesized Au/TS-1 with 0.2% wt. nominal Au loading

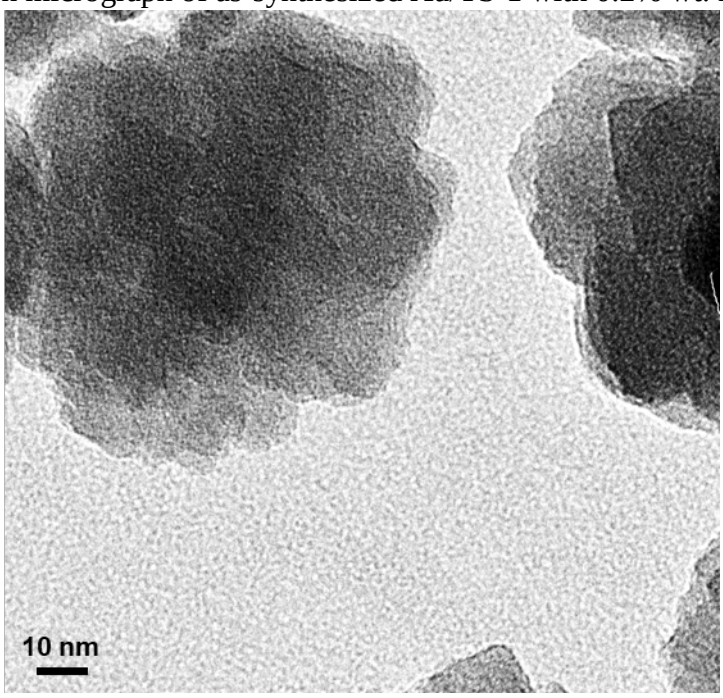

Figure 6.S2. Sample transmission electron micrograph of as-synthesized Au/TS-1 crystallized with 0.2% wt. nominal Au loading and with 10% wt. seed crystals at 393 K for 120 h.

6.S3. CO_2 uptakes at 273 K for TS-1 and Au/TS-1 with 1.0% wt. nominal Au loading

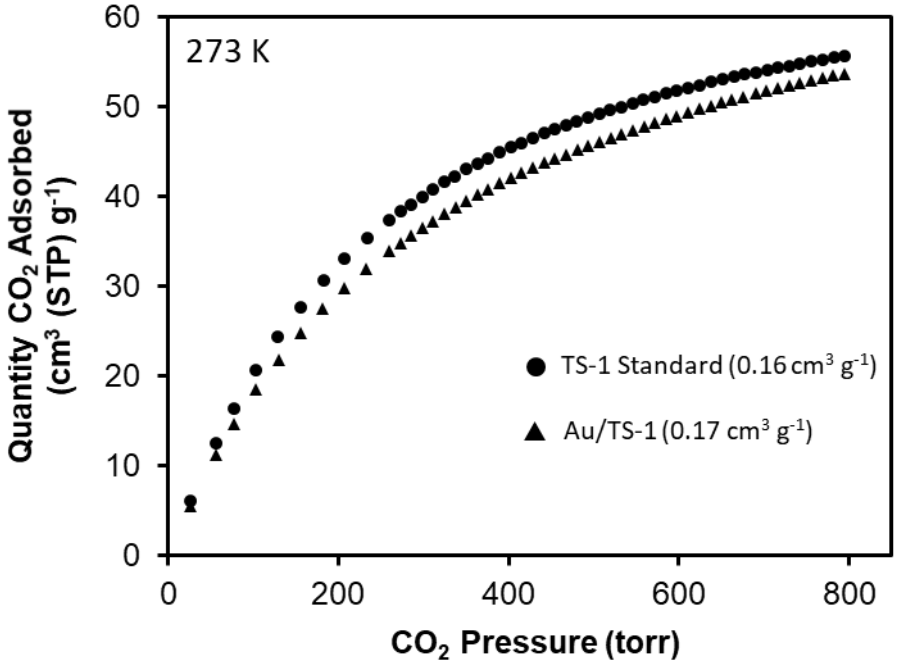

Figure 6.S3. CO_2 uptakes and micropore volumes (calculated by the Dubinin-Astakhov method) of a TS-1 standard sample (crystallized at 448 K for 48 h) treated in air at 823 K for 4 h and an Au/TS-1 sample (0.9% wt. Au) post-synthetically treated in air using the procedure described in Section 6.2.3.